UNIVERSITY OF CALIFORNIA

Santa Barbara

Heterogeneous Silicon III-V Mode-Locked Lasers

A dissertation submitted in partial satisfaction of the

requirements for the degree Doctor of Philosophy in Electrical and Computer Engineering

by

Michael Loehrlein Davenport

Committee in charge:

Professor John Bowers, Chair

Professor Larry Coldren

Professor Nadir Dagli

Professor Rod Alferness

Professor Martijn Heck

September 2017

The dissertation of Michael Loehrlein Davenport is approved.

_____

Martijn Heck

_____

Rod Alferness

_____

Nadir Dagli

_____

Larry Coldren

_____

John Bowers, Committee Chair

July 2017

Heterogeneous Silicon/III-V Mode-Locked Lasers

Michael L. Davenport

Acknowledgements

I would like to begin by acknowledging my advisor, Professor John Bowers, for his persistent support of my work in mode-locked lasers. None of this would have been possible without his technical guidance, patience, and uncanny ability to secure a continuous stream of funding for my outrageous Nanofab recharge bills. It was also a great pleasure associating with Dr. Bowers socially, and I always enjoyed his and Ariel's hospitality on the yearly ski trips, Christmas parties, and summer graduation celebrations.

My professional mentors have been pivotal in the development of my understanding of laser physics and engineering. Prof. Martijn Heck helped provided invaluable insight on mode-locking phenomena and laser physics that helped shape my understanding of the subject. He set an excellent example for me and the other students in Bowers' group with his skillful problem solving. Dr. Hyundai Park taught me how approach the often-obscured laser epitaxy design issue, and how to generate and understand the large data sets that are required to find a solution. I owe the experimental approach to laser optimization used in this dissertation to Dr. Park's methods. Prof. Richard Fork originally sent me down this path by kindling my interest in mode-locked lasers and providing an introduction to Prof. Bowers.

Molly Piels and Jared Bauters, my cohort in Bowers' group, became great friends of mine as we collaborated to solve homework problems, screening exam questions, and finally the SOUL project, which was a graduate school dream team. Bristol Palins was the first place in California that I considered to be "my home" instead of "my apartment."

Many other students, in Bowers' group and others, provided assistance to this work by sharing their knowledge and skills with me. Geza Kurćzveil, Siddharth Jain, and Hui-Wen Chen taught me how to fabricate silicon lasers. Demis John, John Parker, Chong Zhang, and

Andy Carter all provided valuable advice in the cleanroom. Alex Spott and Eric Stanton took on tough problems in process development so I did not have to. Sudha Srinivasan and Tin Komljenovic were great office-mates, always ready to lend a hand with design and testing of the bizarre laser devices that I kept spinning out or have an insightful discussion.

The Nanofab staff provided constant assistance for the fabrication challenges addressed in this work. Brian Thibeault assisted with process development and debugging more times than I can count. Tony Bosch, Don Freeborn, Mike Silva, Adam Abrahamsen, Brian Lingg, Luis Zuzunaga, Tino Sy, and Aidan Hopkins did an excellent job of maintaining the equipment—and repairing it after I jammed it up.

I made many lifelong personal friends during my time in graduate school. Matt Laurent and Joe Nedy made excellent roommates at the Chalet, as well as weight-room partners, along with Alex Wheels and Michael “Little Big Mike” Belt (who could have been in the previous paragraph for his contribution to the tantala project). I had lots of great times with these guys and the rest of the Chalet crew, Myley Dang, Carl Neufeld, Jen Smith, Laura Urbisci, Ann Kim, and Jacquie Dodd. My girlfriend, Lauren Amery, was an outstanding companion throughout the final dissertation-defense-publication panic.

My family was instrumental during the earlier years of my life for helping to develop the skills and attributes that led me to be able to gain admission to and complete a graduate program. I was home schooled, and my mother Evelyn taught me math and geography, but more importantly set an example by continuously teaching herself new things. My father Robert taught me writing, history, and how to be inquisitive about the world around me. My grandfather Earl Loerhlien was my first introduction to electrical engineering; we built hobby electronics projects out of breadboard in his garage. I would not have been able to live by

myself at first without help from my grandmother Elisabeth. Even though I have (hopefully) moved past the Campbells Soup cookbook, I still remember Granny's advice about cooking. The consistent supply of home-made apricot bars at finals time was always a great comfort. My brother John taught me to test my own limits and explore fearlessly. My twin Jerry was my steadfast ally through swim team, the self-taught phase, real high school, and undergraduate.

I owe all of these people a debt of gratitude for their assistance with my education and training.

Dedication

To Mom and Bob

ABSTRACT

Heterogeneous Silicon III-V Mode-Locked Lasers

by

Michael Loehrlein Davenport

Mode-locked lasers are useful for a variety of applications, such as sensing, telecommunication, and surgical instruments. This work focuses on integrated-circuit mode-locked lasers: those that combine multiple optical and electronic functions and are manufactured together on a single chip. While this allows production at high volume and lower cost, the true potential of integration is to open applications for mode-locked laser diodes where solid state lasers cannot fit, either due to size and power consumption constraints, or where small optical or electrical paths are needed for high bandwidth. Unfortunately, most high power and highly stable mode-locked laser diode demonstrations in scientific literature are based on the Fabry-Perot resonator design, with cleaved mirrors, and are unsuitable for use in integrated circuits because of the difficulty of producing integrated Fabry-Perot cavities.

We use silicon photonics and heterogeneous integration with III-V gain material to produce the most powerful and lowest noise fully integrated mode-locked laser diode in the 20 GHz frequency range. If low noise and high peak power are required, it is arguably the best performing fully integrated mode-locked laser ever demonstrated. We present the design methodology and experimental pathway to realize a fully integrated mode-locked laser diode. The construction of the device, beginning with the selection of an integration platform, and proceeding through the fabrication process to final optimization, is presented in detail. The dependence of mode-locked laser performance on a wide variety of design parameters is presented.

Applications for integrated circuit mode-locked lasers are also discussed, as well as proposed methods for using integration to improve mode-locking performance to beyond the current state of the art.

Contents

List of Figures

Given this information, it is clear that using a 400-nm waveguide to eliminate higher order modes will be very costly in terms of loss, as this waveguide has almost 10 dB/cm of propagation loss. Therefore, an 800-nm waveguide will generally be used for straight sections, such as the mode-locked laser passive waveguide, and the waveguide will be tapered to the 400-nm width only for bent waveguides to avoid the need for a waveguide

Chapter 1

Introduction

The mode-locked laser diode has been a recurring matter of interest among laser scientists seeking to produce ultra-short picosecond-scale optical pulses since the first demonstration in 1978 [1] of a single-section GaAs/AlGaAs laser, which was actively modulated to produce a 20-ps pulse. The first demonstration of mode-locking through the use of a saturable absorber–"passive" mode locking, in the absence of a high-speed electronic synthesizer–was demonstrated in 1984 [2], using a bulk-optic external cavity to include the saturable absorber. The development of the multi-segment mode-locked laser, which used a reverse biased section of the gain waveguide in the laser diode as a saturable absorber, in 1989 [3] allowed for compact monolithic cavities which were wholly included on a single substrate. This development enabled generation of optical pulses at much higher repetition rate, 40 GHz in [3], thanks to elimination of the external cavities of [1] and [2] resulting in shorter overall length.

These lasers held the promise of providing millimeter- and microwave sources of short optical pulses for use in optical sampling [4], soliton data transmission [5], optical time domain

multiplexing [6], all-optical clock recovery [7], and optical analog-to-digital conversion [8], with the compact size, low cost, and high reliability of laser diodes. Shortly after these developments, early harmonically mode-locked fiber lasers began to match the mode-locked laser diode in terms of repetition frequency with the demonstration of a 200 GHz fiber laser in 1996 [9], and rapidly outstripped diode lasers in terms of pulse energy. Demonstration of 2.3-nJ pulse energy in 1995 [10] from an erbium-doped fiber mode-locked laser has never been exceeded by even the most energetic monolithic mode-locked laser diode [11] at 58 pJ. Modern commercially available fiber mode-locked lasers have up to 30 μJ of pulse energy. With such a drastic 6-order of magnitude difference in performance, the mode-locked laser diode did not gain a lasting commercial foothold.

The fiber laser is not suitable for some applications, for example, optical time division multiplexing, a technique that uses interleaved ultra-short pulses to produce extremely high bit rate data signals for transmission over optical fiber. Telecommunication systems demand the reliability and low-component-cost of the diode laser. Unfortunately, the rise of coherent data transmission ended the need for optical time division multiplexing as the coherent system is more spectrally efficient. Coherent systems can also compensate for dispersion, which ended the usefulness of soliton transmission over fiber.

The mode-locked laser diode does maintain some advantages over its fiber laser counterpart. The laser diode is smaller, more power efficient, and simpler to operate, as it is self-starting and requires only DC power supplies. The greatest, and currently commercially unrealized, strength of the mode-locked laser diode is the power of photonic integration.

Photonic integration is the process of combining multiple photonic functions onto a single substrate. “Monolithic integration” describes integrated devices which are all single-

crystalline, such as in the case of most indium phosphide (InP) substrate devices, even those with multiple regrowth steps [12]. “Heterogeneous integration” refers to devices that combine different types of material onto a single substrate, in the case of transferring III-V epi layers onto a silicon substrate [13]. “Hybrid integration” is the combination of fully fabricated devices into a single package in close contact, often through soldering onto a sub mount; in some cases the substrate of one device is used as the sub mount, as when a fully fabricated III-V amplifier is flip-chip bonded to a completed silicon photonic chip [14].

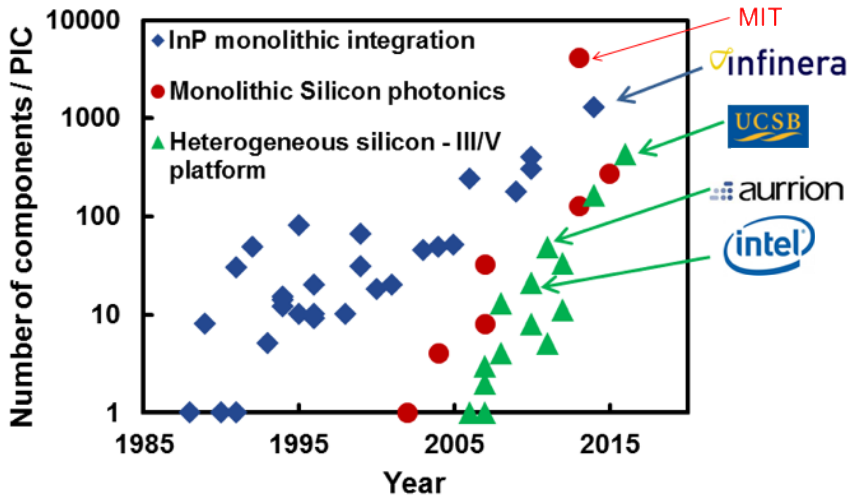

Figure 1-1 Size of photonic integrated circuits versus platform

The scale of photonic integrated circuits on the InP platform has been increasing steadily, with the primary application being telecommunications transmitters and receivers. This progress is shown in Figure 1-1 [15]. The emergence of silicon (specifically silicon-on-insulator, SOI) as a substrate for photonic integrated circuits was followed quickly by the heterogeneous silicon platform, which uses wafer bonding technology to transfer III-V epi layers and other materials to SOI substrates. Heterogeneous integration can offer most of the functions of InP monolithic circuits as well as the advantages of silicon photonics, namely low-

loss high-confinement waveguides, small footprint, and the maturity of the CMOS manufacturing infrastructure.

1.1. Integrated Circuits Using Mode-locked Lasers

Currently, there are few examples of integrated circuits that include mode-locked lasers. The most common example is the addition of a semiconductor optical amplifier (SOA) to a mode-locked laser to increase the output power, such as in [16]. Another common type of mode-locked laser integrated circuit is the inclusion of an electro-absorption modulator (EAM). In this section, two integrated circuits based on emerging mode-locked laser applications will be proposed as examples of technologies that will be enabled by integrated mode-locked lasers.

1.1.1. Microwave Channelizer

A channelizer, or channelized receiver, is a system used to characterize the spectral components of a wide-band radio-frequency (RF) signal in parallel and in real-time. Conventional channelizers consist of large numbers of bulky microwave filters and are limited in operation frequency by the speed of their electronic components. A microwave photonic implementation of a channelizer has a number of advantages: Compact size due to the reduction in wavelength at optical frequencies, extremely broad-band components, and simultaneous access to the phase and amplitude of the signal [17].

The first demonstration of a coherent photonic RF channelizer was in 2001 [18]. The authors proposed optically modulating a single wavelength laser with the incoming RF signal, then separating out the frequency components with a diffraction grating, and finally mixing the signal on a focal-plane array along with a comb of local oscillator wavelengths for coherent detection. The local oscillator in their experiment was provided by the single wavelength laser,

but an earlier publication demonstrated that injection locking of a mode-locked laser can produce a coherent comb of local oscillator wavelengths [19].

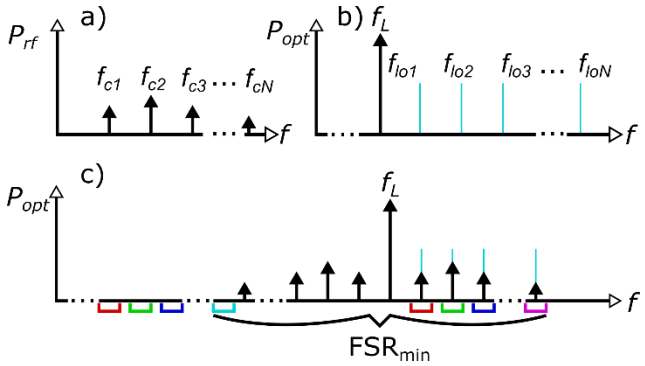

Figure 1-2 a) Frequency components of the incoming RF signal. b) Optical frequency components of the master laser, f_L, and the local oscillator comb, f_{loi}. c) The optical spectrum after modulation and combination of the signals, showing the signal from the modulator (black), the local oscillator lines (cyan), and the position of the channel filters (red, green, blue, magenta), as well as the nearest interfering FSR of the channel filter array.

This architecture can be produced on a photonic integrated circuit. The diffraction grating can be replaced by an array of ring resonators with gradually varying radius. The operating principle is displayed in Figure 1-2. A broad-band microwave signal in (a), with frequency components distributed in N channels at frequencies [f_{c1}, f_{c2}, $f_{c3,}$… f_{cN}], is received by the system. Separate sections of the system produce laser emission at a single wavelength, with optical frequency f_L, and a comb of frequencies at [f_{lo1}, f_{lo2}, $f_{lo3,}$ … f_{loN}] and have the same frequency spacing as the microwave channels. The single-wavelength laser is optically modulated by the RF signal, producing modulation sidebands at the microwave frequency offset from the carrier signal. These modulation sidebands can be filtered individually using an optical filter, and then are mixed with the local oscillator with the corresponding frequency offset from f_L to produce a baseband signal representation of each microwave frequency

channel. A broadband RF signal with a high carrier frequency can be reduced to a series of baseband signals, which can be analyzed by conventional electronics in real time.

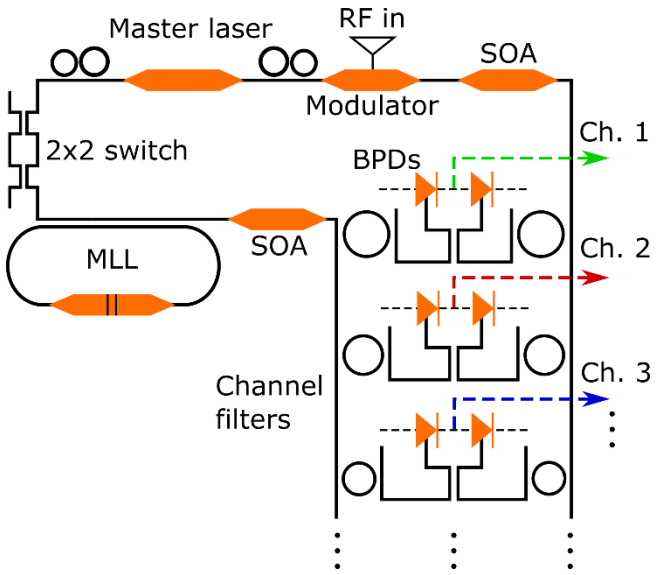

Figure 1-3: A schematic diagram of the channelizer circuit. III-V components are shown as orange, passive silicon circuitry as solid black lines, and electrical connections as dashed lines. The ellipses indicate that the channel filter and detection apparatus may be repeated multiple times to increase the channel number.

We demonstrated a channelizer on the heterogeneous silicon photonic platform, using the combination of single-wavelength lasers with narrow linewidth [20], wideband modulators [21], ring resonator filters [22], and long-cavity mode-locked lasers [23] on a single chip.

A schematic overview diagram is shown in Figure 1-3. The master laser provides the single-wavelength input to the modulator, as well as the seed to phase lock the mode-locked laser. For the single wavelength laser, a coupled-ring resonator cavity design was chosen. This design has demonstrated 160-kHz linewidth and high output power compared to other heterogeneous silicon/III-V single-wavelength lasers at 1550-nm wavelength [20]. The laser is followed by an electro-absorption modulator (EAM), which encodes the incoming RF signal

onto the front-mirror output of the master laser. To compensate for the modulator insertion loss, a high-output power semiconductor optical amplifier (SOA) follows the modulator. The encoded signal passes through a series of ring resonator filters, one for each channel in the device. After the individual channel is selected by the filter, it is split and combined with the oscillator signal with a 50/50 directional coupler and converted into an electrical signal at baseband by a balanced pair of photodetectors.

On the other arm of the circuit, a mode-locked laser with a repetition rate equal to the channel frequency spacing generates a comb of optical lines at each channel wavelength. Phase coherence with the channel signals is enabled by injection locking of the mode-locked laser with the emission from the rear mirror of the master laser. A thermally-tuned 2 x 2 Mach-Zehnder interferometer is used between the master laser and the mode-locked laser to control the injected power, as too high injection will reduce the bandwidth of the mode-locked laser.

In order to prevent the mode-locked laser from injecting multi-mode emission into the master laser, which would cause deterioration of the master laser side-mode suppression ratio, a racetrack cavity design is used. This laser, under injection from the master laser, will only lase in the clockwise direction, emitting high power in the direction of the channel filters.

A second SOA after the mode-locked laser amplifies the local oscillator comb. The output power of the mode-locked laser may not be high—it will have a very long cavity and must have its bias current optimized for comb bandwidth—so the amplifier is necessary to ensure high power and equalization between the local oscillator comb and channel signals.

1.1.2. Dual Comb Spectrometer

Dual comb spectroscopy [24] is a technique for high-sensitivity broad band spectroscopy. It uses two coherent spectral combs with slightly different comb spacing, one to probe the absorption lines of the sample, and the other to act as a comb of coherent local oscillators–in much the same way that the mode-locked laser in the channelizer functions. The comb is split in a 50/50 power splitter, and one arm is directed through the material to be probed. The two pulses are then recombined on a balanced photodetector, which converts the beat signals between the comb lines down to RF frequencies. Recent progress in micro-fluidic waveguides [25] has allowed the co-propagation of light with fluids in hollow core waveguides. This technology could be integrated with a mode-locked laser pulse source to produce an integrated dual comb spectrometer, as depicted in Figure 1-4

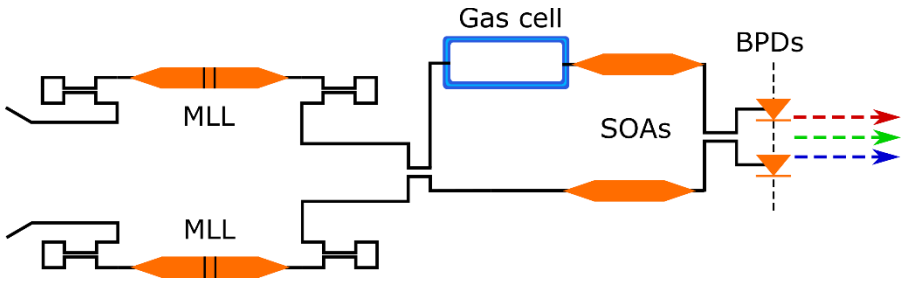

Figure 1-4: Integrated dual comb spectrometer. MLL: Mode-locked laser, SOA: Semiconductor optical amplifier. BPD: Balanced photodetector. Solid lines are waveguides, dashed lines are electrical signals.

1.2. Performance of Integrated Mode-locked Lasers

Most mode-locked laser diodes in the literature are Fabry-Perot (FP) resonator lasers, meaning that they have planar mirrors forming the laser cavity. These mirrors are usually formed by cleaving along the plane parallel to the 110 direction. Not only is this a relatively simple process, but the mirrors have very high performance, owing to the atomically smooth cleaved

surface, the large power reflection coefficient, R ≈ 0.3, and the extremely broad-band nature of the Fresnel reflection between the high-index semiconductor waveguide and air. Cleaved facets limit the use of these types of lasers in photonic integrated circuits, since any other component would have to be cleaved away to form the facet. As such, an integrated mode-locked laser will need some kind of on-chip mirror, such as a distributed Bragg reflector (DBR) mirror. Unfortunately, as shown in Figure 1-5, the pulse width of the mode-locked laser is typically deteriorated by the introduction of an integrated mirror, as shown in Figure 1-5. This figure and the subsequent literature review scatter charts in this chapter and Chapter 2 all draw from this list of references. Note that these are all on-chip lasers; no devices with external free space or fiber optic cavities were included in the comparison.

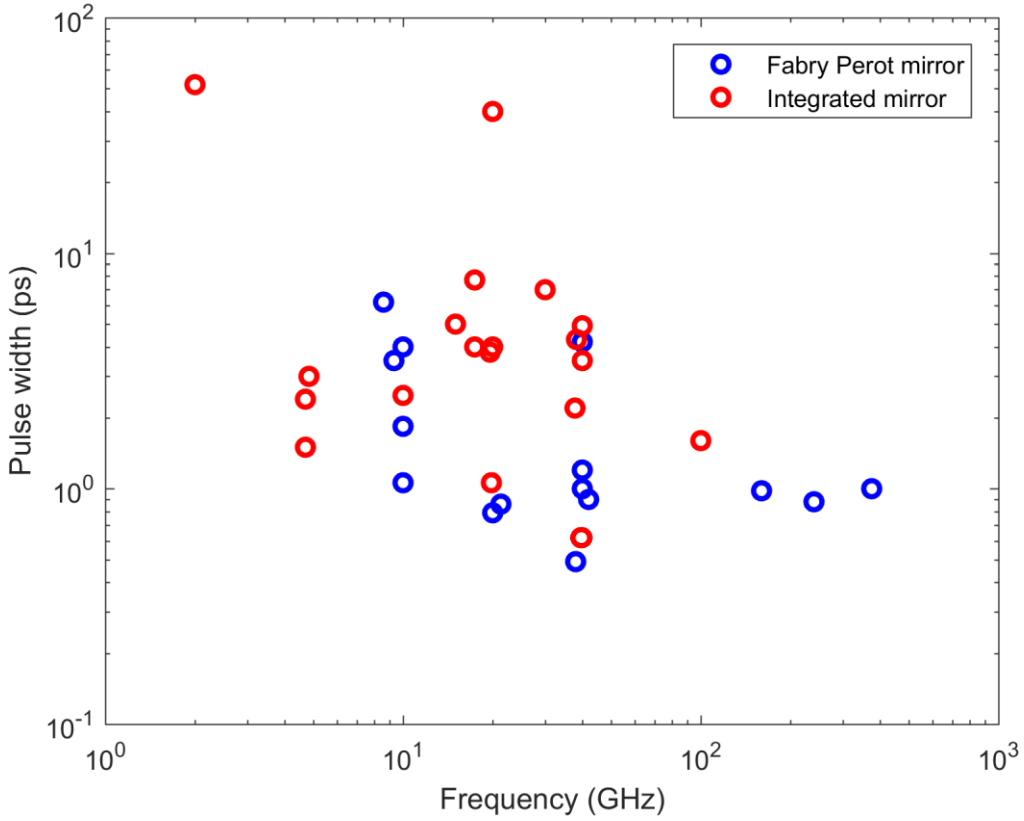

Figure 1-5: Pulse width for a selection of quantum-well mode-locked laser diodes versus repetition rate. References: [26][27][28][29][30][31][32][16][33][34][35][36][37][38]

[39][40][41][42][43][44][45][46][47][48][49][50][51][11][52][53][54][55][56][57][58][59][60]

Pulse width is the most commonly measured metric for mode-locked lasers. The formation of a short pulse, in the case of an amplitude modulated mode-locked laser, will cause a broad spectral output due to the modulation transferring power out into the mode comb. Therefore, it is highly desirable for any mode-locked laser to produce a short pulse. Because of this, and the fact that pulse width is the most common measurement, it is useful to compare the pulse width of mode-locked lasers from literature. According to Figure 1-5, there are 6 examples of sub-1-ps cleaved facet lasers, and only one fully integrated laser [52], which was a fairly sophisticated racetrack-style, regrown-p-cladding, deeply-etched InP-substrate laser with an integrated gain flattening filter.

The reason for this degradation is that the cleaved (or polished) facet, which is source of a large and broad-band reflection in the FP laser, also creates a reflection in the integrated-mirror case, only now it is typically between the output facet and the laser mirror, creating a parasitic cavity. Measures such as a flared and angled facet [61] (see Section 6.1.3) can be taken to reduce this parasitic reflection, but the effect is difficult to eliminate completely. The parasitic cavity creates interference nulls that narrow the lasing spectrum of the device, which affects the pulse width by reducing available bandwidth. This will be shown in Section 5.3. Feedback below −50 dB do not produce easily observable perturbations in the optical spectrum.

In addition to integration of the mirror, the laser must also include a transition from the active amplifier waveguide to a passive waveguide for it to be able to be placed into a complex integrated circuit, such as those shown in Figure 1-3 and Figure 1-4. These circuits contain power splitters and ring resonator filters which are severely complicated by gain in the

waveguide, and so the mode-locked laser must have a passive waveguide as well as an integrated mirror to be useful in a large scale integrated circuit. A mode-locked laser with both of these features will be referred to as a "fully-integrated" mode-locked laser. Unlike the integrated mirror, the integrated passive waveguide is sometimes helpful with regard to the pulse width. This is shown in Figure 1-6. In fact, the shortest pulse width ever demonstrated from a quantum-well mode-locked laser had an integrated passive waveguide. This was thought to be due to a reduction in nonlinear dispersion induced by self-phase modulation [62]. The fully integrated devices in Figure 1-6 therefore can have an advantage in pulse width over the integrated mirror devices. Evidently, the design of the transition between the active and passive waveguide is critical for short pulse width, but perhaps not as difficult as the integrated mirror.

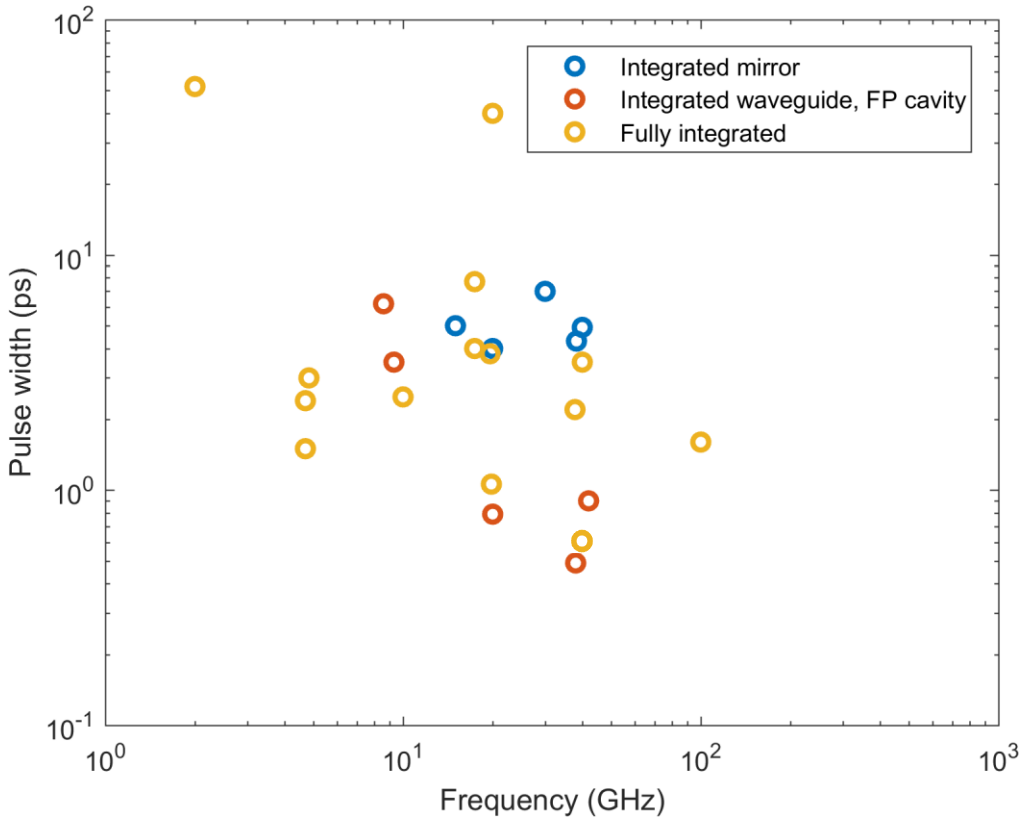

Figure 1-6: Pulse width versus frequency for a selection of lasers from the literature. Note that the "integrated waveguide" devices, denoted by the red dots, have cleaved facets and were considered FP lasers in Figure 1-5. This figure uses the same references as Figure 1-5.

Photonic integration is a powerful tool to reduce cost, size, and power consumption of optical systems. While the erbium-doped fiber laser poses strong competition against the mode-locked laser diode as a source for short optical pulses at high repetition rate, it is not compatible with photonic integration due to its massive size and demand for high pump power [63]. This opens a wide range of new applications for mode-locked f; however, there is a penalty to be paid in performance for integration that must first be overcome.

1.3. Outline of This Work

The objective of this thesis is to develop a fully integrated mode-locked laser diode for use in photonic integrated circuits. This device should have low pulse width, high peak power, high repetition rate, and high timing stability of the optical pulse train. To accomplish this, the laser design will be fully optimized, from the selection of the integration platform, to the active region material, waveguide design, cavity-mirror selection and design, amplifier design, and absorber design. Instead of including all of the mode-locking experiments in a single chapter, these results will be interspersed with the design sections, so that the design process, continuous-wave laser performance, and mode-locking performance will all be co-located to help the reader understand the significance of each design aspect with respect to the final behavior of the mode-locked lasers.

Chapter 2 will be focused on the laser architecture. Due to the difficulty and cost of performing experiments across platforms, the laser architecture selection will be mainly performed through literature survey and thought experiments.

Next, in Chapter 3, the integrated laser fabrication process will be outlined in detail. Considerable effort was put forth during the experimental phase of this dissertation toward producing high-yield and high-performance fabrication. The relative scarcity of mode-locked laser experimental results that include more than a single device indicates that the devices are highly intolerant to fabrication variation. Since there is a lack of workable models for integrated circuit mode-locked lasers, much of the optimization was done experimentally. This requires very repeatable fabrication results.

Chapter 4 contains the design and characterization of the amplifier portion of the device. This mainly focuses on waveguide and gain material design. This development was performed for the most part before the other technologies in Chapters 5 and 6 were viable for mode locking, so there will be few mode-locked laser results in this chapter.

Chapter 5 will focus on the transition between the active and passive waveguide sections. As indicated in Figure 1-6, a poorly designed transition can be quite disastrous for the pulse width performance, and this will be shown experimentally in Chapter 5, along with transition designs that produce high performance mode-locked lasers.

Chapter 6 will present the design of the passive waveguide circuitry that forms the integrated mirrors, as well as the low-reflection waveguide facet. This development was performed after the optimization of the material in Chapters 4 and 5, and thus it contains the best and most thoroughly characterized mode-locking results.

Chapter 7 will conclude with a discussion of the mode-locking behavior, and a proposal for future directions to further improve the performance of the lasers beyond what has already been presented.

References

[1] P. T. Ho, L. A. Glasser, E. P. Ippen, and H. A. Haus, “Picosecond pulse generation with a cw GaAlAs laser diode,” *Appl. Phys. Lett.*, vol. 33, no. 3, pp. 241–242, 1978.

[2] Y. Silberberg, P. W. Smith, and D. J. Eilenberger, “Passive mode locking of a semiconductor diode laser,” vol. 9, no. 11, pp. 507–509, 1984.

[3] P. P. Vasil’ev and A. B. Sergeev, “Generation of bandwidth-limited 2 ps pulses with 100 GHz repetition rate from multisegmented injection laser,” *Electron. Lett.*, vol. 25, no. 16, p. 1049, 1989.

[4] J. Valdmanis, G. Mourou, and C. Gabel, “Subpicosecond electrical sampling,” *IEEE J. Quantum Electron.*, vol. 19, no. 4, pp. 664–667, Apr. 1983.

[5] H. A. Haus and S. G. Evangelides, “Long-Distance Soliton Propagation using Lumped Amplifiers and Dispersion Shifted Fiber,” *J. Light. Technol.*, vol. 9, no. 2, pp. 194–197, 1991.

[6] T. S. Kinsel, “Wide-Band Optical Communication Systems : sources,” vol. 58, no. October, 1970.

[7] S. Arahira, S. Sasaki, K. Tachibana, and Y. Ogawa, “All-optical 160-Gb/s clock extraction with a mode-locked laser diode module,” *IEEE Photonics Technol. Lett.*, vol. 16, no. 6, pp. 1558–1560, 2004.

[8] S. Member, C. E. Woodward, and F. J. Leonberger, “Wide-Band Electrooptic Guided-Wave Analog-to-Digital Converters,” vol. 7, no. 7, 1984.

[9] G. The and R. Gainas, “80~200GHz erbium doped fibre laser using a rational harmonic mode-locking technique,” *Electron. Lett.*, vol. 32, no. 15, pp. 1370–1372, 1996.

[10] B. C. Barnett, L. Rahman, M. N. Islam, Y. C. Chen, P. Bhattacharya, W. Riha, K. V

Reddy, a T. Howe, K. a Stair, H. Iwamura, S. R. Friberg, and T. Mukai, “High-power erbium-doped fiber laser mode locked by a semiconductor saturable absorber.,” *Opt. Lett.*, vol. 20, no. 5, pp. 471–473, 1995.

[11] J. J. Plant, J. T. Gopinath, B. Chann, D. J. Ripin, R. K. Huang, and P. W. Juodawlkis, “250 mW, 1.5 m monolithic passively mode-locked slab-coupled optical waveguide laser,” *Opt. Lett.*, vol. 31, no. 2, pp. 223–225, 2006.

[12] R. Nagarajan, J. Rahn, M. Kato, J. Pleumeekers, D. Lambert, V. Lal, H.-S. Tsai, A. Nilsson, A. Dentai, M. Kuntz, R. Malendevich, J. Tang, J. Zhang, T. Butrie, M. Raburn, B. Little, W. Chen, G. Goldfarb, V. Dominic, B. Taylor, M. Reffle, F. Kish, and D. Welch, “10 Channel, 45.6 Gb/s per Channel, Polarization-Multiplexed DQPSK, InP Receiver Photonic Integrated Circuit,” *J. Light. Technol.*, vol. 29, no. 4, pp. 386–395, Feb. 2011.

[13] M. J. R. Heck, J. F. Bauters, M. L. Davenport, J. K. Doylend, S. Jain, G. Kurczveil, S. Srinivasan, and J. E. Bowers, “Hybrid Silicon Photonic Integrated Circuit Technology,” *IEEE J. Sel. Top. Quantum Electron.*, vol. 19, no. 4, pp. 6100117–6100117, 2013.

[14] N. Kobayashi, K. Sato, M. Namiwaka, K. Yamamoto, S. Watanabe, and T. Kita, “Silicon Photonic Hybrid Ring-Filter External Cavity Wavelength Tunable Lasers,” vol. 33, no. 6, pp. 1241–1246, 2015.

[15] M. L. Davenport, S. Skendzic, N. Volet, J. C. Hulme, M. J. R. Heck, and J. E. Bowers, “Heterogeneous Silicon/III–V Semiconductor Optical Amplifiers,” *IEEE J. Sel. Top. Quantum Electron.*, vol. 22, no. 6, pp. 78–88, Nov. 2016.

[16] J. Akbar, L. Hou, M. Haji, M. J. Strain, J. H. Marsh, a. C. Bryce, and A. E. Kelly, “High-power AlGaInAs mode-locked DBR laser with integrated tapered optical

amplifier," *IEEE Photonics Technol. Lett.*, vol. 25, no. 3, pp. 253–256, 2013.

[17] C.-S. Brès, S. Zlatanovic, A. O. J. Wiberg, and S. Radic, "Reconfigurable parametric channelized receiver for instantaneous spectral analysis.," *Opt. Express*, vol. 19, no. 4, pp. 3531–3541, 2011.

[18] W. Wang, R. L. Davis, T. J. Jung, R. Lodenkamper, L. J. Lembo, J. C. Brock, and M. C. Wu, "Characterization of a coherent optical RF channelizer based on a diffraction grating," *IEEE Trans. Microw. Theory Tech.*, vol. 49, no. 10 II, pp. 1996–2001, 2001.

[19] T. Jung, J. L. Shen, T. Dennis, K. Tong, S. Murthy, M. C. Wu, T. Tanbun-Ek, W. Wang, R. Lodenkamper, R. Davis, L. J. Lembo, and J. C. Brock, "CW injection locking of a mode-locked semiconductor laser as a local oscillator comb for channelizing broad-band RF signals," *IEEE Trans. Microw. Theory Tech.*, vol. 47, no. 7 PART 2, pp. 1225–1233, 1999.

[20] S. Srinivasan, M. Davenport, T. Komljenovic, J. Hulme, D. T. Spencer, and J. E. Bowers, "Coupled-Ring-Resonator-Mirror-Based Heterogeneous III–V Silicon Tunable Laser," *IEEE Photonics J.*, vol. 7, no. 3, pp. 1–8, 2015.

[21] Y. Tang, J. D. Peters, and J. E. Bowers, "Over 67 GHz bandwidth hybrid silicon electroabsorption modulator with asymmetric segmented electrode for 1.3 μm transmission," *Optics Express*, vol. 20, no. 10. p. 11529, 07-May-2012.

[22] W. Bogaerts, P. De Heyn, T. Van Vaerenbergh, K. De Vos, S. Kumar Selvaraja, T. Claes, P. Dumon, P. Bienstman, D. Van Thourhout, and R. Baets, "Silicon microring resonators," *Laser Photon. Rev.*, vol. 27, no. 1, p. n/a-n/a, 2011.

[23] M. J. Heck, M. L. Davenport, H. Park, D. J. Blumenthal, and J. E. Bowers, "Ultra-Long Cavity Hybrid Silicon Mode-Locked Laser Diode Operating at 930 MHz," *Opt. Fiber*

Commun. Conf., p. OMI5, 2010.

[24] W. Coddington, Ian, Newbury, Nathan, Swann, "Dual-comb spectroscopy," *Optica*, vol. 3, no. 4, pp. 414–426, 2016.

[25] H. Schmidt and A. R. Hawkins, "The photonic integration of non-solid media using optofluidics," *Nat. Photonics*, vol. 5, no. 10, pp. 598–604, 2011.

[26] L. Hou, M. Haji, J. H. Marsh, and A. C. Bryce, "10 GHz AlGaInAs/InP 1.55 μm passively mode-locked laser with low divergence angle and timing jitter.," *CLEO SI*, vol. 19, no. 26, pp. B75-80, 2011.

[27] Z. Lu, J. Liu, S. Raymond, P. Poole, P. Barrios, and D. Poitras, "312-fs pulse generation from a passive C-band InAs/InP quantum dot mode-locked laser," *Opt. Express*, vol. 16, no. 14, pp. 10835–10840, 2008.

[28] M. Dontabactouny, C. Rosenberg, E. Semenova, D. Larsson, K. Yvind, R. Piron, F. Grillot, O. Dehaese, N. Chevalier, and S. Loualiche, "10-GHz 1.59-μm quantum dash passively mode-locked two-section lasers," *Proc. SPIE--the Int. Soc. Opt. Eng.*, vol. 7720, no. 1, p. 77201A–77201A–10, 2010.

[29] L. Hou, M. Haji, J. H. Marsh, and A. C. Bryce, "490 fs pulse generation from a passive C-band AlGaInAs / InP quantum well mode-locked laser," *Opt. Lett.*, vol. 37, no. 5, pp. 773–775, 2012.

[30] L. Hou, M. Haji, J. Akbar, B. Qiu, and a C. Bryce, "Low divergence angle and low jitter 40 GHz AlGaInAs/InP 1.55 μm mode-locked lasers.," *Opt. Lett.*, vol. 36, no. 6, pp. 966–968, 2011.

[31] C. Ji, N. Chubun, R. G. Broeke, J. Cao, Y. Du, S. J. B. Yoo, K. Y. Liou, J. R. Lothian, S. Vatanapradit, S. N. G. Chu, B. Patel, W. S. Hobson, and W. T. Tsang, "Synchronized

transform-limited operation of 10-GHz colliding pulse mode-locked laser," *IEEE Photonics Technol. Lett.*, vol. 18, no. 4, pp. 625–627, Feb. 2006.

[32] J. F. Martins-filho, S. Member, E. A. Avrutin, C. N. Ironside, and J. S. Roberts, "Monolithic Multiple Colliding Pulse Mode-Locked Quantum-Well Lasers : Experiment and Theory," *Spectrum*, vol. 1, no. 2, 1995.

[33] S. Keyvaninia, S. Uvin, M. Tassaert, Z. Wang, X. Fu, S. Latkowski, J. Marien, L. Thomassen, F. Lelarge, G. Duan, G. Lepage, P. Verheyen, J. Van Campenhout, E. Bente, and G. Roelkens, "III–V-on-silicon anti-colliding pulse-type mode-locked laser," *Opt. Lett.*, vol. 40, no. 13, p. 3057, Jul. 2015.

[34] C. Gordon, R. Guzman, V. Corral, M. Chieh Lo, and G. Carpintero, "On-chip multiple colliding pulse mode-locked semiconductor laser," *J. Light. Technol.*, vol. 34, no. 20, pp. 4722–4728, 2016.

[35] C. Gordón, R. Guzmán, V. Corral, X. Leijtens, and G. Carpintero, "On-Chip Colliding Pulse Mode-locked laser diode (OCCP-MLLD) using multimode interference reflectors," *Opt. Express*, vol. 23, no. 11, p. 14666, 2015.

[36] L. Hou, M. Haji, J. Akbar, A. C. Bryce, and J. H. Marsh, "160-GHz 1.55-um Colliding-Pulse Mode-Locked AlGaInAs/InP Laser With High Power and Low Divergence Angle," *IEEE Photonics Technol. Lett.*, vol. 24, no. 12, pp. 1057–1059, Jun. 2012.

[37] L. Hou, M. Haji, and J. H. Marsh, "240 GHz pedestal-free colliding-pulse mode-locked laser with a wide operation range," *Laser Phys. Lett.*, vol. 11, no. 11, p. 115804, 2014.

[38] D. Larsson, K. Yvind, and J. M. Hvam, "Wide-band residual phase-noise measurements on 40-GHz monolithic mode-locked lasers," *IEEE Photonics Technol. Lett.*, vol. 17, no. 11, pp. 2388–2390, 2005.

[39] M. J. R. Heck, A. Renault, E. A. J. M. Bente, Yok-Siang Oei, M. K. Smit, K. S. E. Eikema, W. Ubachs, S. Anantathanasarn, and R. Notzel, "Passively Mode-Locked 4.6 and 10.5 GHz Quantum Dot Laser Diodes Around 1.55 um With Large Operating Regime," *IEEE J. Sel. Top. Quantum Electron.*, vol. 15, no. 3, pp. 634–643, Aug. 2009.

[40] V. Dijk, G. Duan, G. Aubin, and A. Ramdane, "Short pulse generation using a passively mode locked single InGaAsP / InP quantum well laser," *Opt. Express*, vol. 16, no. 14, pp. 9007–9012, 2008.

[41] R. Scollo, H.-J. Lohe, F. Robin, D. Erni, E. Gini, and H. Jackel, "Mode-Locked InP-Based Laser Diode With a Monolithic Integrated UTC Absorber for Subpicosecond Pulse Generation," *IEEE J. Quantum Electron.*, vol. 45, no. 4, pp. 322–335, Apr. 2009.

[42] F. Camacho, E. A. Avrutin, A. C. Bryce, and J. H. Marsh, "Passive modelocking in semiconductor lasers with monolithically integrated passive waveguides," *Iee Proceedings-Optoelectronics*, vol. 145, no. 1, pp. 43–46, 1998.

[43] P. B. Hansen, G. Raybon, U. Koren, P. P. Iannone, B. I. Miller, G. M. Young, M. A. Newkirk, and C. A. Burrus, "InGaAsP monolithic extended-cavity lasers with integrated saturable absorbers for active, passive, and hybrid mode locking at 8.6 GHz," *Appl. Phys. Lett.*, vol. 62, no. 13, pp. 1445–1447, 1993.

[44] H. Fan, C. Wu, M. El-Aasser, N. K. Dutta, U. Koren, and A. B. Piccirilli, "Colliding pulse mode-locked laser," *IEEE Photonics Technol. Lett.*, vol. 12, no. 8, pp. 972–973, Aug. 2000.

[45] M. S. Tahvili, Y. Barbarin, X. J. M. Leijtens, T. de Vries, E. Smalbrugge, J. Bolk, H. P. M. M. Ambrosius, M. K. Smit, and E. a J. M. Bente, "Directional control of optical power in integrated InP/InGaAsP extended cavity mode-locked ring lasers.," *Opt. Lett.*,

vol. 36, no. 13, pp. 2462–4, 2011.

[46] S. Joshi, C. Calò, N. Chimot, M. Radziunas, R. Arkhipov, S. Barbet, A. Accard, A. Ramdane, and F. Lelarge, “Quantum dash based single section mode locked lasers for photonic integrated circuits,” *Opt. Express*, vol. 22, no. 9, p. 11254, 2014.

[47] L. Hou, M. Haji, R. Dylewicz, B. Qiu, and A. C. Bryce, “Monolithic 45-GHz mode-locked surface-etched DBR laser using quantum-well intermixing technology,” *IEEE Photonics Technol. Lett.*, vol. 22, no. 14, pp. 1039–1041, 2010.

[48] B. R. Koch, A. W. Fang, O. Cohen, and J. E. Bowers, “Mode-locked silicon evanescent lasers,” *Opt. Express*, vol. 15, no. 18, pp. 11225–11233, 2007.

[49] S. Srinivasan, E. Norberg, T. Komljenovic, M. Davenport, G. Fish, and J. E. Bowers, “Hybrid Silicon Colliding-Pulse Mode-Locked Lasers with On-Chip Stabilization,” *IEEE J. Sel. Top. Quantum Electron.*, vol. 21, no. 6, 2015.

[50] V. Moskalenko, S. Latkowski, S. Tahvili, T. de Vries, M. Smit, and E. Bente, “Record bandwidth and sub-picosecond pulses from a monolithically integrated mode-locked quantum well ring laser,” *Opt. Express*, vol. 22, no. 23, p. 28865, 2014.

[51] S. Arahira, Y. Katoh, and Y. Ogawa, “20 GHz subpicosecond monolithic modelocked laser diode,” *Electron. Lett.*, vol. 36, no. 5, p. 454, 2000.

[52] J. S. Parker, A. Bhardwaj, P. R. A. Binetti, Y. Hung, C. H. Lin, and L. A. Coldren, “Integrated 30GHz passive ring mode-locked laser with gain flattening filter,” *Conf. Dig. - IEEE Int. Semicond. Laser Conf.*, vol. 1, no. 805, pp. 3–4, 2010.

[53] Z. Wang, K. Van Gasse, V. Moskalenko, S. Latkowski, E. Bente, B. Kuyken, and G. Roelkens, “A III-V-on-Si ultra-dense comb laser,” *Light Sci. Appl.*, vol. 6, no. 5, p. e16260, May 2017.

[54] L. Hou, M. Haji, and J. H. Marsh, “Monolithic mode-locked laser with an integrated optical amplifier for low-noise and high-power operation,” *IEEE J. Sel. Top. Quantum Electron.*, vol. 19, no. 4, 2013.

[55] A. W. Fang, B. R. Koch, K.-G. Gan, H. Park, R. Jones, O. Cohen, M. J. Paniccia, D. J. Blumenthal, and J. E. Bowers, “A racetrack mode-locked silicon evanescent laser.,” *Opt. Express*, vol. 16, no. 2, pp. 1393–1398, 2008.

[56] S. Keyvaninia, S. Uvin, M. Tassaert, X. Fu, S. Latkowski, J. Mariën, L. Thomassen, F. Lelarge, G. Duan, P. Verheyen, G. Lepage, J. Van Campenhout, E. Bente, and G. Roelkens, “Narrow-linewidth short-pulse III-V-on-silicon mode-locked lasers based on a linear and ring cavity geometry,” *Opt. Express*, vol. 23, no. 3, p. 3221, Feb. 2015.

[57] Y. Barbarin, E. a J. M. Bente, M. J. R. Heck, Y. S. Oei, R. Nötzel, and M. K. Smit, “Characterization of a 15 GHz integrated bulk InGaAsP passively modelocked ring laser at 1.53microm.,” *Opt. Express*, vol. 14, no. 21, pp. 9716–27, 2006.

[58] R. Kaiser, B. H??ttl, H. Heidrich, S. Fidorra, W. Rehbein, H. Stolpe, R. Stenzel, W. Ebert, and G. Sahin, “Tunable monolithic mode-locked lasers on InP with low timing jitter,” *IEEE Photonics Technol. Lett.*, vol. 15, no. 5, pp. 634–636, 2003.

[59] K. Sato, I. Kotaka, Y. Kondo, and M. Yamamoto, “Actively mode-locked strained-InGaAsP multiquantum-well lasers integrated with electroabsorption modulators and distributed Bragg reflectors,” *IEEE J. Sel. Top. Quantum Electron.*, vol. 2, no. 3, pp. 557–564, 1996.

[60] S. Arahira, Y. Matsui, T. Kunii, S. Oshiba, and Y. Ogawa, “Transform-Limited Optical Short-Pulse Generation at High Repetition Rate over 40 GHz from a Monolithic Passive Mode-Locked DBR Laser Diode,” *IEEE Photonics Technol. Lett.*, vol. 5, no. 12, pp.

1362–1365, 1993.

[61] M. Reed, T. M. Benson, P. C. Kendall, and P. Sewell, “Antireflection-coated angled facet design,” *IEE Proc. - Optoelectron.*, vol. 143, no. 4, pp. 214–220, Aug. 1996.

[62] F. Camacho, E. A. Avrutin, P. Cusumano, A. S. Helmy, A. C. Bryce, and J. H. Marsh, “Improvements in Mode-Locked Semiconductor Diode Lasers Using Monolithically Integrated Passive Waveguides Made by Quantum-Well Intermixing,” *IEEE Photonics Technol. Lett.*, vol. 9, no. 9, pp. 1208–1210, 1997.

[63] M. Belt, T. Huffman, M. L. Davenport, W. Li, J. S. Barton, and D. J. Blumenthal, “Arrayed narrow linewidth erbium-doped waveguide-distributed feedback lasers on an ultra-low-loss silicon-nitride platform.,” *Opt. Lett.*, vol. 38, no. 22, pp. 4825–8, 2013.

Chapter 2

Laser Architecture

The design of integrated mode-locked laser diodes is critical for maintaining high performance in integrated circuits. Fully integrated mode-locked laser diodes show a wide range of quality, with many showing considerable impairments while others have comparable performance to Fabry-Perot lasers (Figure 1-6). The shortest reported pulse widths and the lowest RF line widths typically come from Fabry-Perot lasers. This is because fully integrated lasers, which require an on-chip reflector, passive and active waveguides, and an active-to-passive transition, normally have some additional parasitic loss, reflection, or other effects from the integrated components. It is possible for integration to improve performance if these parasitic effects can be sufficiently reduced. For example, the addition of a passive waveguide can reduce the effect of self-phase modulation [1], and dispersion control in integrated distributed Bragg reflectors (DBRs) can be used to compensate for pulse chirping [2].

This chapter will explain the design of the integrated mode-locked laser diode. It will begin with the selection of the laser amplifier and waveguide material, as a variety of semiconductor materials are available for these purposes at telecommunications wavelengths. Then, the

integration of the passive waveguide will be discussed, as once again there are several techniques for accomplishing active-passive integration. The selection of the type of mode-locked laser cavity will then be detailed, and finally the selection of a reflector design will complete the laser architecture.

2.1. Amplifier Material Selection

For lasers in the telecommunications wavelength bands, around 1.31 μm and 1.55 μm, there are numerous options for amplifier materials. The most common is the InGaAsP quaternary system, which can be latticed matched to InP substrates and provide a range of band gap wavelengths between 0.96 μm and 1.65 μm. All of these alloys have Type I heterointerfaces with InP. In addition, the quaternary alloy allows the specification of lattice constant and band gap wavelength independently, so InGaAsP can produce finely optimized strained multi-quantum well lasers and amplifiers. This material was used to produce the first continuous wave 1.55-μm-band laser diode in 1979 [3] and is the most widely studied in literature, which makes the design of InGaAsP/InP lasers comparatively simple.

AlGaInAs alloys can also be lattice matched to InP, with the first laser demonstration in 1984 [3]. This alloy combination provides a higher range of lattice matched band gap wavelengths than InGaAsP, ranging from 1.65 μm for pure $In_{0.53}Ga_{0.47}As$ to 0.88 μm for $In_{0.53}Al_{0.47}As$. The system was originally proposed because of the higher conduction band offset between an $In_{0.53}Al_{0.47}As$ separate confinement heterostructure (SCH) and an $In_{0.53}Ga_{0.47}As$ quantum well, compared to an InGaAsP SCH and an InGaAs quantum well [4]. From a growth perspective, it is easier to create graded layers in AlGaInAs, since the only group V element is arsenic, which does not need to vary during growth of a graded composition

section. Researchers later fully understood the significance of these advancements for high-temperature laser operation, and used graded AlGaInAs quaternary materials to produce the highest operating temperature lasers at both 1.31 μm (175°C continuous wave [5]) and 1.55 μm (150°C continuous wave [6]). Both of these lasers were practical, compact, single-transverse-mode lasers with low threshold current, high slope efficiency, and high modulation bandwidth. Modeling and experiments have suggested that AlGaInAs has higher differential gain, lower transparency current, and lower linewidth enhancement factor than InGaAsP [7][8].

GaInNAs may be grown on a GaAs substrate and make use of the high-energy band gap AlGaAs ternary to produce high temperature operation lasers [9], but is less suitable for 1.55 μm operation [10]. The performance of lasers made from this material can be quite good at 1.31 μm wavelength [11] in terms of characteristic temperatures and reliability. This material is not currently commercially available, and the design of GaInNAs lasers is complicated by the relative scarcity of material characterization in literature.

Quantum dot gain material, typically consisting of InAs or InGaAs dots grown on GaAs or InP substrates, shows great promise for short pulse lasers, with the two shortest pulses ever generated from an on-chip laser diode coming from quantum dot lasers, 390 fs at 1.31 μm [12] and 312 fs at 1.55 μm [13]. In addition, as explained in [12], quantum dot mode-locked lasers tend to be able to operate with short pulses at higher bias currents, leading to the potential for high peak power.

The AlGaInAs material system has long been favored over InGaAsP for use in high-speed electro-absorption modulators due to the band lineup structure: increased conduction band offset means that there is similarly reduced valence band offset, reducing the depth of the hole well and therefore reducing the escape time of the hole, which limits the recovery time of

reverse biased quantum well absorbers [14][15][16]. This was proven in the context of mode-locked lasers in [17], in which the absorber recovery time was shown to be 5 times faster in AlGaInAs than InGaAsP. The researchers responsible for [17] went on to produce the shortest pulse ever demonstrated from a 1.55 μm quantum well laser, 490 fs, using AlGaInAs. The pulse width versus frequency for 1.55 μm mode-locked lasers for various amplifier materials is shown in Figure 2.1 (see Chapter 1 for references). It is clear that particular gain media do not necessarily result in a short pulse. However, due to the faster absorber recovery time, and the single data point below 500 fs in Figure 2.1, it can be presumed that AlGaInAs is superior to InGaAsP under ideal circumstances.

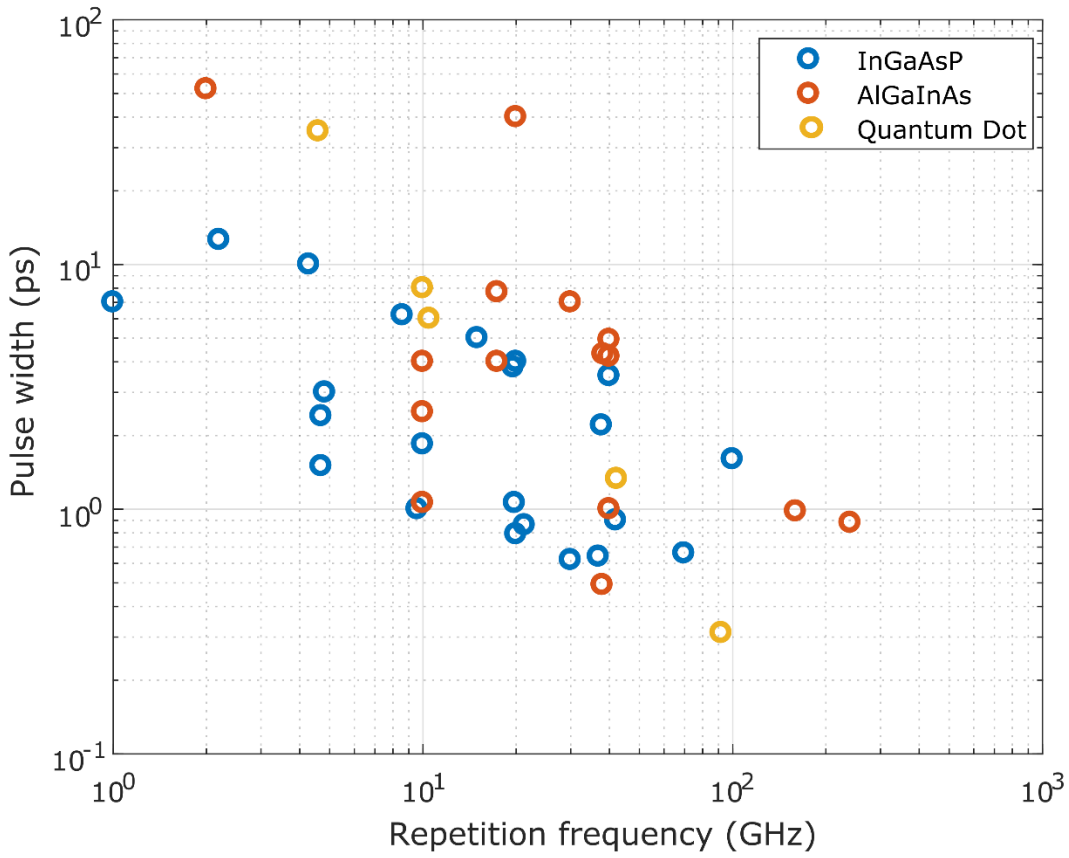

Figure 2.1: Pulse width versus repetition frequency for 1.55 μm lasers based on their gain material, from literature. The references for this figure are in Chapter 1. It must be noted that

few of the authors of these papers considered pulse compression or expansion due to dispersion in the fibers and amplifiers in the measurement apparatus.

Quantum dot mode-locked lasers have been shown to produce very short pulses, likely due to the more inhomogeneous nature of the gain broadening with wavelength allowing quantum dot lasers to produce wider frequency combs. Picosecond recovery time has also been demonstrated for quantum dot semiconductor saturable absorber mirrors [18], and authors have observed that quantum dot material can withstand larger reverse bias than quantum wells, as high as −10 V [12], where quantum well saturable absorbers are normally operated around −5 V. The lasers in this dissertation would fail due to high current density when operated above that voltage. It is likely that the quantum dot gain material has lower responsivity and therefore lower current density at high reverse bias.

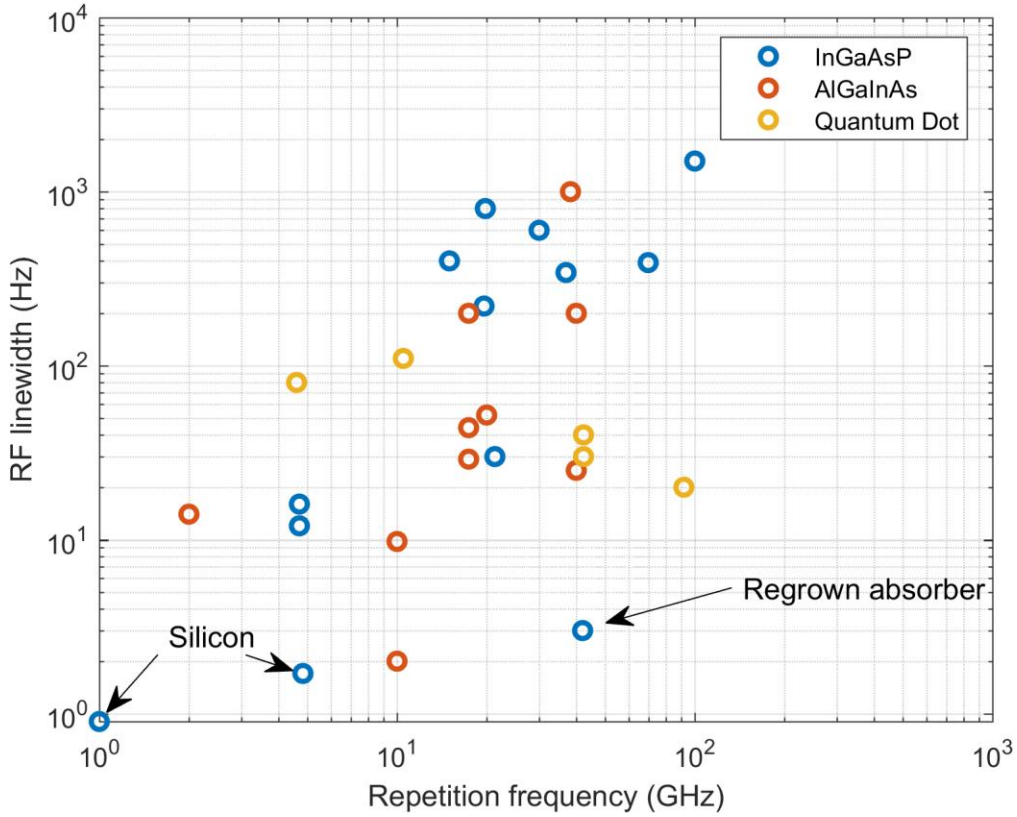

Figure 2.2: RF linewidth versus repetition frequency for mode-locked lasers from the literature. See Chapter 1 for references.

Since one of the original goals of this research was to produce a highly-stable passively mode-locked laser, the RF linewidth results from literature must also be examined. Figure 2.2 shows the RF linewidth versus repetition rate for lasers from the literature. It needs to be emphasized that the RF linewidth is highly dependent on the repetition frequency. Ignoring the 2-kHz AlGaInAs outlier [19] and the InGaAsP result with the regrown absorber [20], there is a roughly linear trend of 15 kHz/GHz. AlGaInAs generally shows lower values than InGaAsP, with quantum dots normally showing higher linewidth than both of the common quantum well materials. AlGaInAs is theorized to have lower linewidth enhancement factor than InGaAsP [8], which contributes to the RF linewidth. Two existing InGaAsP lasers with long heterogeneously integrated silicon waveguides demonstrate the lowest linewidths in the survey

[21][22], with [21] significantly better than the trend. This is most likely due to the reduced amplified spontaneous emission that can be accomplished by shortening the gain section in extremely long cavity mode-locked lasers, as 4.83 GHz corresponds to a cavity length of 8 mm. Once again, the gain material does not necessarily dominate in RF linewidth, but AlGaInAs appears to have an advantage.

Given this information, it is clear that quantum dot material is superior for short pulses and AlGaInAs is superior for low noise. The original motivation of this work was low noise, so AlGaInAs was selected as the gain waveguide material. In addition, there are some practical reasons for avoiding quantum dots. Quantum dot material is commonly grown on GaAs substrates, as forming dots on InP substrates is more difficult. As described in Section 2.2, heterogeneous integration with silicon is highly desirable. This is accomplished with wafer bonding, which is much more difficult when bonding GaAs to silicon compared to InP to silicon due to their thermal coefficient of expansion differences [23]. Lastly, because quantum dots are still an emerging technology, there are very few commercial epi growers compared to quantum wells. For these practical reasons, and the evidence in literature, AlGaInAs was chosen for the gain material.

2.2. Active-Passive Integration

The inclusion of a passive waveguide on InP substrate mode-locked laser diodes is commonly accomplished with three methods. The first (in no particular order) is butt-joint regrowth [24], where the active waveguide is etched and a passive waveguide core is regrown adjacent to it. The second is offset-quantum-well-waveguide overgrowth [25], where the quantum wells are

grown above a passive waveguide and etched away before regrowth of the p-cladding. The third method is quantum well intermixing [26], where defects are selectively diffused into the quantum well to increase the band gap. All of these methods have been commonly shown to produce reflections at the interface below −40 dB, the threshold for usefulness in a laser circuit. However, all three methods result in high-loss passive waveguides, often in the 10 dB/cm range, because the passive waveguide shares the p-type doped InP cladding, which is necessary for current injection in the active waveguide. P-type InP increases the waveguide loss primarily due to intervalence band absorption [27][28][29]. Reduction in loss of InP waveguides to 1-2 dB/cm can be accomplished by incorporating a second regrowth step to grow a separate un-doped cladding for the passive waveguide. Complex epi design, dopant set-back, and hydrogenation can be also used [30], although the effectiveness of hydrogen exposure has been debated [31]. These methods all involve high process temperatures, above 600°C.

Regrowth-free active-passive integration is possible using vertically coupled waveguide layers, normally connected with adiabatic couplers [32]. These have the advantage of being regrowth free, but due to the higher index contrast of the interface compared to regrown or intermixed junctions, the loss and reflection are normally higher. The couplers are often complicated to fabricate and have high sensitivity to variations such as lithographic feature size and misalignment. Heterogeneously integrated InP/Si devices generally rely on this type of integration, since regrowth is difficult because of mechanical degradation introduced by thermal stress at the bonded interface.

Table 2-1: Waveguide properties of different materials at 1550-nm wavelength

Property	InP	Si
Typical propagation loss (dB/cm)	10	1
Best propagation loss (dB/cm)	0.81 [31]	0.06 [33]
Typical minimum bend radius (μm)	80 [34]	2 [35]
Two-photon absorption coefficient (cm/GW)	31 [36]	0.45 [37]

Silicon-on-insulator (SOI) waveguides have many advantages over InP waveguides. The principal one is high index contrast in the vertical direction, commonly $\Delta n = 2$ when $n = 3.47$ silicon is clad with $n = 1.45$ silicon dioxide. This allows much smaller bend radii, as low as 2 μm in Si [35] for a deeply etched waveguide, compared to 80 μm in a deeply etched InP waveguide. The reduced bend radius can produce smaller components, which help reduce total insertion loss (less overall length) and increase device density. Common InP waveguides have p-type doped upper cladding, as discussed earlier, and often have high propagation loss limited by absorption in the p-type material. These loss values are normally 10 dB/cm or more. Since silicon devices are normally doped in selective areas with ion implantation, the absorption due to doping can be extremely low, as commonly available SOI has background doping in the 10^{15} cm^{-3} range, which does not cause significant absorption. The propagation loss in silicon waveguides is limited by scattering from the etched waveguide sidewall, and they usually have loss around 1 dB/cm. The lowest loss InP waveguides, in which the doping profile is carefully managed to reduce absorption, have 0.8 dB/cm loss, which is still limited by absorption [31]; however, the best published result for an SOI waveguide is 0.06 dB/cm [33]. It appears that silicon waveguides typically have roughly an order of magnitude advantage over InP waveguides for propagation loss [38].

Finally, the two-photon absorption (TPA) coefficient of silicon is almost 100 times lower than InP, thanks to the indirect band gap of silicon [37][36]. A summary of relevant waveguide

parameters is shown in Table 2-1. Two-photon absorption is important to consider in mode-locked lasers since the high peak power can cause the two-photon absorption to become significant. The size of the waveguide must also be considered, as TPA is intensity dependent, so waveguides that support modes with small effective area will have increased TPA. Figure 2.3 shows three example waveguides: a) is a common quasi-single mode shallow ridge InP laser waveguide, with effective area A_{eff} = 1.64 μm^2, b) shows a heterogeneous Si/InP waveguide with A_{eff} = 0.88 μm^2 and InP confinement factor Γ_{InP} = 0.378, c) is a 400-nm wide 500-nm tall silicon wire waveguide with A_{eff} = 0.17 μm^2, and d) is a 3.5-μm wide 500-nm tall silicon waveguide. Calculated loss per watt of power is shown in Table 2-2, showing that the passive silicon waveguide has a modest advantage in TPA loss and the heterogeneous silicon waveguide is approximately equal to the InP waveguide despite 61% confinement in silicon due to the reduced mode volume.

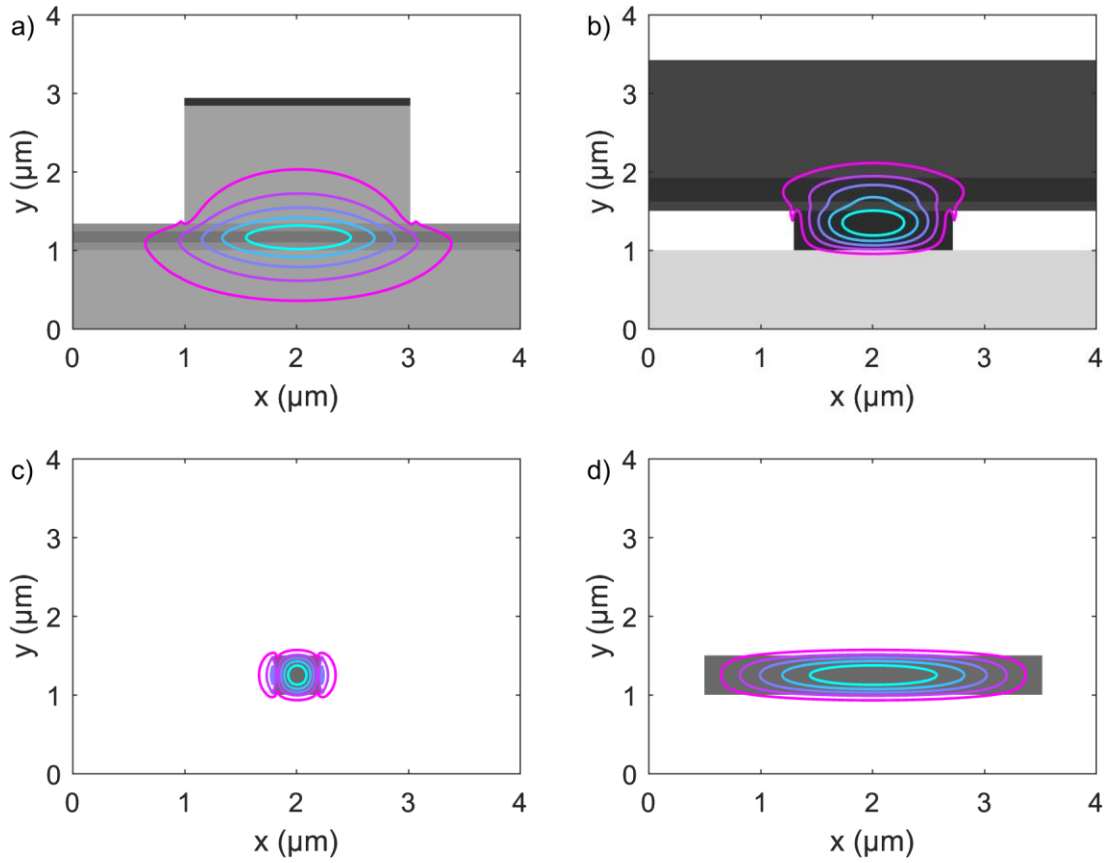

Figure 2.3: Mode E_x profiles of three waveguides, for comparison of their relative mode area; a) shows a 2-μm wide shallow InP laser waveguide, b) shows a 1.4-μm wide silicon heterogeneous waveguide with bonded InP active region, c) shows a 400-nm wide and 500-nm tall Si wire, and d) shows a 3000-nm wide and 500-nm tall Si waveguide. The figures are drawn to scale.

Table 2-2: Two-photon absorption loss for waveguides in Figure 2.3

Waveguide	A_{eff} (μm^2)	Γ_{InP}	Γ_{Si}	Two-photon absorption loss (dB/cm/W)
InP shallow ridge	1.64	0.85	0	7.0
Heterogeneous Si/InP	0.88	0.38	0.61	5.9
400-nm wide Si nanowire	0.17	0	0.89	1.0
3-μm wide Si waveguide	0.93	0	0.96	0.15

As a purely passive waveguide, silicon enjoys considerable advantages. Lower propagation loss allows for higher efficiency lasers and long extended cavities for low repetition rate integrated mode-locked lasers [22]. The extremely low minimum bend radius will be used in this work to produce ultra-compact laser reflectors (Section 6.3). While peak power in typical mode-locked laser diodes is not limited by TPA, it is worthwhile to think ahead as applications will require high power. A mode-locked laser with 1 GHz repetition rate, 0.5 mW continuous wave power and a 7 ps pulse, as [22], has approximately 71 mW of peak power. If this pulse were shortened to 600 fs, the current state of the art for integrated mode-locked lasers, this would increase the peak power to 833 mW. A 1 GHz repetition rate laser requires 40 mm of waveguide, which in this case would have 22 dB of loss from TPA in the InP waveguide shown in Figure 2.1a), making low threshold impossible, while the narrow silicon waveguide in Figure 2.3c) will only have 4 dB of loss from TPA, which is manageable, and increasing the silicon waveguide width to 3 μm, shown in Figure 2.3d), reduces the TPA loss to 0.45 dB. Widening the waveguide to reduce TPA is possible on both waveguide platforms, but the 3-order-of-magnitude difference in TPA coefficient cannot reasonably be overcome on InP without drastic changes to the design. This is in addition to the overall lower propagation loss in silicon waveguides.

Heterogeneous silicon waveguide lasers have already demonstrated the lowest RF linewidth of any mode-locked lasers, as shown in Figure 2.2, thanks to their ability to produce long low-loss extended cavities. With proper engineering to achieve short pulses, silicon lasers should be able to demonstrate the best overall performance of any integrated mode-locked laser.

2.3. Cavity Design

As mentioned in Chapter 1, the reflector has a strong impact on the performance of mode-locked laser diodes, particularly the pulse width. The cleaved-facet mirror that is commonly used in InP-based laser diodes creates an excellent ultra-broad band and low loss mirror, properties which are desirable for generation of short pulses and high peak power. There are many ways to integrate a cavity on a chip with a laser, too many to cover here. An "integrated cavity," in this document, refers to a laser cavity which is fully on-chip, can be partially transmitting, and outputs into a waveguide which can connect to other integrated circuit components.

2.3.1. Reflector selection

The three most common integrated mode-locked laser cavity designs are shown in Figure 2.4. The racetrack laser, in Figure 2.4a, consists of a ring cavity and a power splitter/combiner, such as a directional coupler, to interface with external circuitry. Racetrack lasers often demonstrate very short pulse width, as shown in Figure 2.5a, and indeed the shortest pulse from an integrated mode-locked laser was a racetrack laser. The design and fabrication of the output coupler can be challenging, and it does not allow for a high reflection/low reflection type of cavity, so high slope efficiency in racetrack lasers is rare and they tend to have lower peak power as a result, as shown in Figure 2.5b.

The second type of integrated mode-locked laser cavity, and the most common in literature, uses a distributed Bragg reflector (DBR) to form the cavity, an example of which is shown in Figure 2.4b. The DBR may be part of the amplifier waveguide, in which case it is an "active DBR", or part of the passive waveguide, in which case it is a "passive DBR". DBR mode-

locked lasers inherit mature design and fabrication technology from single-wavelength lasers, and so tend to have very high continuous-wave power. Because the DBR designs are related to single-wavelength lasers, they often have low index contrast between the grating gap and tooth, and so they typically have transform limited pulses in the few picosecond range, as shown in Figure 2.5a. Additionally, the grating side lobes can impair the mode-locking operation and create RF tones at unintentional frequencies. Despite this, due to their high continuous wave power, the highest peak power fully integrated mode-locked lasers use DBR-based cavities, as shown in Figure 2.5b.

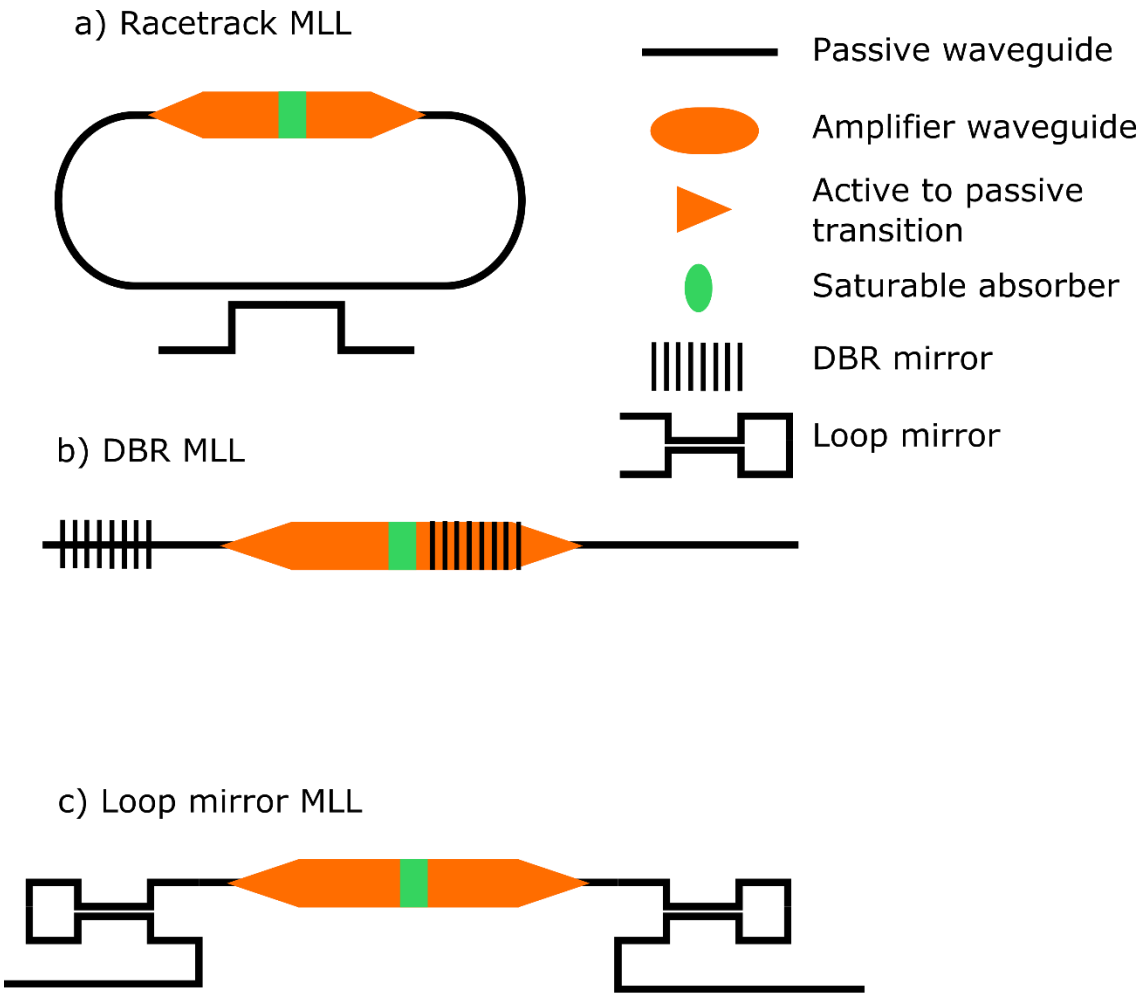

Figure 2.4: Common integrated mode-locked laser cavity designs.

The third design, which is relatively new compared to the other two, is the loop mirror-based mode-locked laser, shown in Figure 2.4c and was first demonstrated in [39]. It is based off of a Sagnac loop mirror [40]. This cavity design has the advantage of the broad-band operation, like the racetrack, but has a linear cavity geometry which can direct the power out of a single side by using high reflection/low reflection mirrors, and does not have the bidirectional instability of the racetrack laser. There are comparatively few examples in literature of these lasers, and while the pulse widths have thus far been poor (Figure 2.5a), peak power has been reasonably high (Figure 2.5b). Because of the wide bandwidth (see Section 6.3), it is expected that with proper design optimization these lasers could produce sub-picosecond pulses.

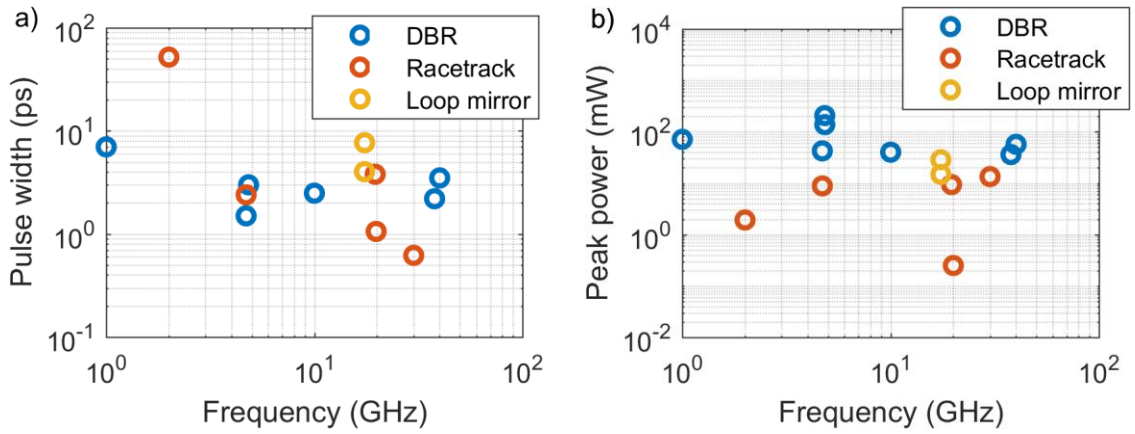

Figure 2.5: Pulse width (a) and peak power (b) plotted against repetition frequency for three common fully integrated mode-locked laser cavity designs shown in Figure 2.4. The references for these figures can be found in Chapter 1.

The loop mirror has additional advantages. On silicon, they are very simple to fabricate, as the dimensions of the power splitter/combiner (usually a directional coupler or MMI) are relatively large, >400 nm, when compared to a DBR, <150 nm. There is no side-lobe, as with

a DBR, and the reflectivity of the mirror can be easily controlled by varying the splitting ratio of the power splitter/combiner. More information about the design of the loop mirror will be presented in Section 6.3.

2.3.2. Absorber placement

The last design element to be considered is the saturable absorber positioning. The DBR has an advantage over the other two designs presented here in that it is possible to place the absorber directly beside one of the reflectors, so that the cavity will be fundamentally mode-locked. The racetrack laser and the loop mirror laser can both support multiple pulses inside the cavity under passive mode-locking operation, in what is referred to as "colliding-pulse mode locking." This is in contrast to harmonic mode locking, where an actively mode-locked laser is modulated at an integer multiple of the cavity fundamental frequency. It has been claimed that colliding-pulse operation can result in shorter pulses, but this has not been effectively established experimentally [41], and in fact the shortest pulses in on-chip mode-locked lasers are from fundamentally mode-locked lasers [42][13]. It has been suggested that multiple-pulse mode locking creates additional phase noise in the form of supermode noise [43]. For high frequency colliding-pulse lasers there is only one supermode spur, and it is far from the carrier frequency. Colliding-pulse mode-locking was adopted for the devices in this work out of practical necessity, since the loop mirror design does not allow for fundamental mode locking and the advantages of the loop mirror are expected to outweigh increased noise of the colliding pulse design.

2.4. Conclusion

The final cavity design is an extended cavity, meaning it includes a passive waveguide, to allow selection of the repetition rate without affecting the length of the amplifier section. Therefore, the gain and transparency current can be optimized separately from the repetition rate. The passive waveguide, due to the advantage in propagation loss, bend radius, and two-photon absorption, is an SOI waveguide. The amplifier section, to be compatible with the passive waveguide, must be heterogeneously integrated as there is no efficient manner to produce light from a silicon waveguide. AlGaInAs quantum wells provide the best performance for mode-locked lasers, and so these are integrated with the SOI waveguide through direct bonding. The reflector is a Sagnac loop mirror, chosen for its wide bandwidth, controllable reflection, and ease of fabrication. The absorber is in the center of the cavity, out of necessity due to the design of the loop mirror. The final cavity design is shown schematically in Figure 2.6. The following chapters will discuss the fabrication (Chapter 3), component development (Chapter 4 and Chapter 5), and experimental characterization of these devices (Chapter 6).

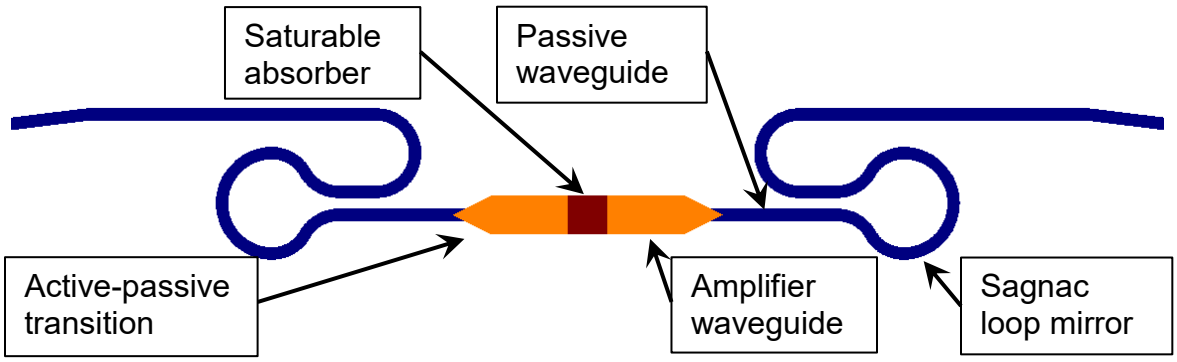

Figure 2.6: Schematic of the final laser design.

References

[1] L. Hou, M. Haji, J. Akbar, B. Qiu, and a C. Bryce, "Low divergence angle and low jitter 40 GHz AlGaInAs/InP 1.55 μm mode-locked lasers.," *Opt. Lett.*, vol. 36, no. 6, pp. 966–968, 2011.

[2] J. M. Xie, S. Bouchoüle, J. M. Lourtioz, E. Brun, and D. Lesterlin, "Chirp compensation in mode-locked DFB laser diodes with extended cavity," *J. Light. Technol.*, vol. 14, no. 2, pp. 179–186, 1996.

[3] Y. Kawamura, H. Asahi, and K. Wakita, "InGaAs/InGaAlAs/InAlAs/InP SCH-MQW laser diodes grown by molecular-beam epitaxy," *Electron. Lett.*, vol. 20, no. 11, p. 459, 1984.

[4] R. People, K. W. Wecht, K. Alavi, and A. Y. Cho, "Measurement of the conduction-band discontinuity of molecular beam epitaxial grown In0.52Al0.48As/In0.53Ga 0.47As, N-n heterojunction by C-V profiling," *Appl. Phys. Lett.*, vol. 43, no. 1, pp. 118–120, 1983.

[5] H. Wada, K. Takemasa, T. Munakata, M. Kobayashi, and T. Kamijoh, "Effects of well number on temperature characteristics in 1.3-μm AlGaInAs-InP quantum-well lasers," *IEEE J. Sel. Top. Quantum Electron.*, vol. 5, no. 3, pp. 420–427, 1999.

[6] R. Paoletti, M. Agresti, D. Bertone, L. Bianco, C. Bruschi, A. Buccieri, R. Campi, C. Dorigoni, P. Gotta, M. Liotti, G. Magnetti, P. Montangero, G. Morello, C. Rigo, E. Riva, G. Rossi, D. Soderstrom, A. Stano, P. Valenti, M. Vallone, and M. Meliga, "Highly reliable and high-yield 1300-nm InGaAlAs directly modulated ridge fabry-Perot lasers, operating at 10-gb/s, up to 110/spl deg/C, with constant current swing," *Journal of Lightwave Technology*, vol. 24, no. 1. pp. 143–149, 2006.

[7] J. Minch, S. H.-H. Park, T. Keating, and S. L.-L. Chuang, “Theory and Experiment of In Ga As P and In Ga Al As Long-Wavelength Strained Quantum-Well Lasers,” *Quantum Electron. IEEE J.*, vol. 35, no. 5, pp. 771–782, 1999.

[8] D. P. Sapkota, M. S. Kayastha, and K. Wakita, “Analysis of linewidth enhancement factor for compressively strained AlGaInAs and InGaAsP quantum well lasers,” *Opt. Quantum Electron.*, vol. 45, no. 1, pp. 35–43, Jan. 2013.

[9] B. Borchert, A. Y. Egorov, S. Illek, and H. Riechert, “Static and dynamic characteristics of 1.29-mu m GaInNAs ridge-waveguide laser diodes,” *Ieee Photonics Technol. Lett.*, vol. 12, no. 6, pp. 597–599, 2000.

[10] H. D. Sun, A. H. Clark, H. Y. Liu, M. Hopkinson, S. Calvez, M. D. Dawson, Y. N. Qiu, and J. M. Rorison, “Optical characteristics of 1.55 μm GaInNAs multiple quantum wells,” *Appl. Phys. Lett.*, vol. 85, no. 18, pp. 4013–4015, 2004.

[11] J. Mitomo, M. Yokozeki, Y. Sato, Y. Hirano, T. Hino, and H. Narui, “1.30-um GaInNAs laser diode with lifetime over 1000 hours grown by MOCVD,” *IEEE J. Sel. Top. Quantum Electron.*, vol. 11, no. 5, pp. 1099–1102, 2005.

[12] E. U. Rafailov, M. A. Cataluna, and W. Sibbett, “High-power picosecond and femtosecond pulse generation from a two-section mode-locked quantum-dot laser,” *October*, pp. 5–7, 2005.

[13] Z. G. Lu, J. R. Liu, S. Raymond, P. J. Poole, P. J. Barrios, and D. Poitras, “312-fs pulse generation from a passive C-band InAs / InP quantum dot mode-locked laser,” *Opt. Express*, vol. 16, no. 14, pp. 10835–10840, 2008.

[14] T. H. Wood, T. Y. Chang, J. Z. Pastalan, C. A. Burrus, N. J. Sauer, and B. C. Johnson, “Increased optical saturation intensities in GaInAs multiple quantum wells by the use of

AlGaInAs barriers," *Electron. Lett.*, vol. 27, no. 3, p. 257, 1991.

[15] B. J. Hawdon, T. Tütken, A. Hangleiter, R. W. Glew, and J. E. A. Whiteaway, "Direct comparison of InGaAs/InGaAlAs and InGaAs/InGaAsP quantum well modulators," *Electron. Lett.*, vol. 29, no. 8, p. 705, 1993.

[16] K.-B. Kim and D.-S. Shin, "Comparison of Quantum Wells based on InGaAs(P)/InP and InGa(Al)As/InAlAs Material Systems in View of Carrier Escape Times for High-Saturation-Optical-Power Electroabsorption Modulators," *J. Opt. Soc. Korea*, vol. 11, no. 3, pp. 133–137, Sep. 2007.

[17] R. P. Green, M. Haji, L. Hou, G. Mezosi, R. Dylewicz, and A. E. Kelly, "Fast saturable absorption and 10 GHz wavelength conversion in Al-quaternary multiple quantum wells," *Opt. Express*, vol. 19, no. 10, pp. 700–705, 2011.

[18] E. U. Rafailov, S. J. White, A. A. Lagatsky, A. Miller, W. Sibbett, D. A. Livshits, A. E. Zhukov, and V. M. Ustinov, "Fast Quantum-Dot Saturable Absorber for Passive Mode Locking of Solid-State Lasers," *IEEE Photonics Technol. Lett.*, vol. 16, no. 11, pp. 2439–2441, 2004.

[19] L. Hou, M. Haji, J. H. Marsh, and A. C. Bryce, "10 GHz AlGaInAs/InP 1.55 μm passively mode-locked laser with low divergence angle and timing jitter.," *CLEO SI*, vol. 19, no. 26, pp. B75-80, 2011.

[20] R. Scollo, H.-J. Lohe, F. Robin, D. Erni, E. Gini, and H. Jackel, "Mode-Locked InP-Based Laser Diode With a Monolithic Integrated UTC Absorber for Subpicosecond Pulse Generation," *IEEE J. Quantum Electron.*, vol. 45, no. 4, pp. 322–335, Apr. 2009.

[21] S. Keyvaninia, S. Uvin, M. Tassaert, Z. Wang, X. Fu, S. Latkowski, J. Marien, L. Thomassen, F. Lelarge, G. Duan, G. Lepage, P. Verheyen, J. Van Campenhout, E.

Bente, and G. Roelkens, “III–V-on-silicon anti-colliding pulse-type mode-locked laser,” *Opt. Lett.*, vol. 40, no. 13, p. 3057, Jul. 2015.

[22] Z. Wang, K. Van Gasse, V. Moskalenko, S. Latkowski, E. Bente, B. Kuyken, and G. Roelkens, “A III-V-on-Si ultra-dense comb laser,” *Light Sci. Appl.*, vol. 6, no. 5, p. e16260, May 2017.

[23] O. Moutanabbir, *Heterogeneous Integration of Compound Semiconductors*. .

[24] Y. Barbarin, E. a J. M. Bente, C. Marquet, E. J. S. Leclère, J. J. M. Binsma, and M. K. Smit, “Measurement of reflectivity of butt-joint active-passive interfaces in integrated extended cavity lasers,” *IEEE Photonics Technol. Lett.*, vol. 17, no. 11, pp. 2265–2267, 2005.

[25] B. Mason, J. Barton, G. A. Fish, L. A. Coldren, and S. P. DenBaars, “Design of sampled grating DBR lasers with integrated semiconductor optical amplifiers,” *IEEE Photonics Technol. Lett.*, vol. 12, no. 7, pp. 762–764, 2000.

[26] J. H. Marsh, “Quantum well intermixing,” *Semicond. Sci. Technol.*, vol. 8, no. 6, pp. 1136–1155, 1993.

[27] G. N. Childs, S. Brand, and R. a Abram, “Intervalence band absorption in semiconductor laser materials,” *Semicond. Sci. Technol.*, vol. 1, no. 2, pp. 116–120, 1986.

[28] I. Joindot and J. L. Beylat, “Intervalence band absorption coefficient measurements in bulk layer, strained and unstrained multiquantum well 1.55 μm semiconductor lasers,” *Electron. Lett.*, vol. 29, no. 7, p. 604, 1993.

[29] H. C. Casey and P. L. Carter, “Variation of intervalence band absorption with hole concentration in p-type InP,” *Appl. Phys. Lett.*, vol. 44, no. 1, p. 82, 1984.

[30] E. V. K. Rao, Y. Gottesman, M. Allovon, E. Vergnol, D. Sigogne, A. Talneau, H. Sik,

S. Slempkes, B. Theys, and J. Chevallier, “A significant reduction of propagation losses in InGaAsP-InP buried-stripe waveguides by hydrogenation,” *IEEE Photonics Technol. Lett.*, vol. 10, no. 3, pp. 370–372, 1998.

[31] A. Bhardwaj, M. Larson, M. Moewe, and Y. Feng, “Low-Loss InGaAsP/InP Surface Ridge Waveguides for Photonic Integrated Circuits,” *IEEE Photonics Technol. Lett.*, vol. 28, no. 13, pp. 1403–1405, 2016.

[32] I. Moerman, P. P. Van Daele, and P. M. Demeester, “A review on fabrication technologies for the monolithic integration of tapers with III-V semiconductor devices,” *IEEE J. Sel. Top. Quantum Electron.*, vol. 3, no. 6, pp. 1308–1320, 1997.

[33] A. Biberman, M. J. Shaw, E. Timurdogan, J. B. Wright, and M. R. Watts, “Ultralow-loss silicon ring resonators,” *IEEE Int. Conf. Gr. IV Photonics GFP*, vol. 37, no. 20, pp. 39–41, 2012.

[34] X. Leijtens, “JePPIX: the platform for Indium Phosphide-based photonics,” *IET Optoelectron.*, vol. 5, no. 5, pp. 202–206, 2011.

[35] W. Bogaerts and S. K. Selvaraja, “Compact Single-Mode Silicon Hybrid Rib/Strip Waveguide With Adiabatic Bends,” *IEEE Photonics J.*, vol. 3, no. 3, pp. 422–432, Jun. 2011.

[36] D. Vignaud, J. F. Lampin, and F. Mollot, “Two-photon absorption in InP substrates in the 1.55μm range,” *Appl. Phys. Lett.*, vol. 85, no. 2, pp. 239–241, Jul. 2004.

[37] H. K. Tsang, C. S. Wong, T. K. Liang, I. E. Day, S. W. Roberts, A. Harpin, J. Drake, and M. Asghari, “Optical dispersion, two-photon absorption and self-phase modulation in silicon waveguides at 1.5??m wavelength,” *Appl. Phys. Lett.*, vol. 80, no. 3, pp. 416–418, 2002.

[38] M. J. R. Heck, J. F. Bauters, M. L. Davenport, D. T. Spencer, and J. E. Bowers, “Ultra-low loss waveguide platform and its integration with silicon photonics,” *Laser Photonics Rev.*, vol. 8, no. 5, pp. 667–686, 2014.

[39] M. L. Davenport, S. Srinivasan, M. J. R. Heck, and J. E. Bowers, “A Hybrid Silicon / InP Integrated Feedback Stabilized Mode- Locked Laser,” *Opt. Fiber Commun. Conf.*, pp. 8–10, 2014.

[40] X. Sun, L. Zhou, J. Xie, Z. Zou, L. Lu, H. Zhu, X. Li, and J. Chen, “Tunable silicon Fabry-Perot comb filters formed by Sagnac loop mirrors.,” *Opt. Lett.*, vol. 38, no. 4, pp. 567–9, 2013.

[41] K. A. Williams, M. G. Thompson, and I. H. White, “Long-wavelength monolithic mode-locked diode lasers,” *New J. Phys.*, vol. 6, pp. 179–179, 2004.

[42] L. Hou, M. Haji, J. H. Marsh, and A. C. Bryce, “490 fs pulse generation from a passive C-band AlGaInAs / InP quantum well mode-locked laser,” *Opt. Lett.*, vol. 37, no. 5, pp. 773–775, 2012.

[43] C. M. Depriest, T. Yilmaz, and P. J. Delfyett, “Ultralow noise and supermode suppression in an actively mode-locked external-cavity semiconductor diode ring laser,” *Opt. Lett.*, vol. 27, no. 9, pp. 719–721, 2002.

Chapter 3

Fabrication

The greatest advantage of integrated circuit mode-locked lasers is drawn from the technology of semiconductor manufacturing. The capability to produce fully solid-state electrically pumped lasers with sub-micrometer precision simultaneously across a semiconductor wafer, thousands to tens of thousands at a time, is what differentiates the semiconductor laser from its bulk and fiber laser counterparts. Single devices can be manufactured at immense scale: the 20 GHz mode-locked laser detailed later in Chapter 6 only occupies 0.4 mm^2, meaning that 11,000 can fit on a single 75-mm-diameter InP substrate, or 80,000 on a 200 mm Si substrate. Multiple circuit functions can be combined in a single device, much like electronic integrated circuits. Light emission, routing, filtering, modulation, detection, and isolation can all be integrated in a single device and fabricated simultaneously.

Accessing this advantage requires utmost attention to the manufacturing process. Optical devices are highly sensitive to manufacturing process induced impairments. The term “process impairment” in the context of photonic integrated circuit fabrication, and in this work, refers to an unintentional change to the physical structure of the device that causes a deviation in the

desired performance. Some common process impairments in semiconductor lasers are listed below:

- Growth defect: A dislocation or defect in the semiconductor, often a small physical defect, which creates a source of electrical leakage. These can originate from the substrate, as they are normally present with small density in III-V wafers, or from particles deposited on the wafer during growth.
- Lithographic misalignment: Alignment between layers normally has a nonzero error, which can be introduced by a number of factors, such as stretching of the wafer after thermal processing or thin film deposition ("scale factor"), warping of the wafer due to nonuniform strain fields ("orthogonality", often a problem with chips and wafer quarters), inadequate precision in the alignment strategy, and inherent inaccuracy of the alignment measurement system in the lithography tool. Different photonic components have varying degree of sensitivity to misalignment. For example, the taper used in the heterogeneous transition Chapter 5 is highly sensitive to misalignment.
- Lithographic exposure: The amount of energy delivered to the photosensitive resin ("photoresist") and deviation from the focal point of the lens in the imaging system can alter the physical size and shape of photoresist patterns. This will change the optical properties of waveguides by altering the effective index, and thereby change the behavior of phase sensitive components such as Bragg gratings or directional couplers (see Section 6.3).
- Sub-microscopic contamination: Unintentional contamination of the semiconductor with a foreign material, often a metal, which degrades the optical or

electrical properties. One famous example is the contamination of silicon by sodium, which gives rise to increased leakage current in CMOS transistors. Metallic contamination in silicon has also been shown to increase absorption loss substantially in optical waveguides [1].

- Microscopic particulates: Sub-millimeter particulates which are deposited on the wafer surface during processing and handling. These produce unintentional masking on the wafer, degrade photoresist uniformity, and can cause absorption or scattering if they are deposited on waveguide cores. These often come from humans in fabrication facilities where wafers are handled manually, but can also come from wet processing if particles are in the liquid, or from plasma processing, specifically film deposition where the deposited films build up and flake off.
- Laminar contamination: Unintentional thin films which may or may not be thick enough to be easily visible. These can be caused by interfacial native oxides forming on the semiconductor, by insufficient etching, insufficient cleaning of photoresist, or deposition of polymer by plasma processing, such as dry etching with fluorine containing process gasses.
- Macroscopic particulates: Large particles visible to the naked eye. These can be a small problem if spotted early enough, as they are often easy to remove, or a large problem if they are not. A piece of hair can create a large-scale disturbance in photoresist thickness if it is present during spin coating, for example, or a large scorch mark if it is present during a high temperature process.

These impairments often reduce the performance of the device, ranging from relatively minor to extremely severe. A microscopic particle on the outside of the waveguide cladding

may make a small reflection, which could affect the operating wavelength range of a tunable laser. The same particle on a waveguide core could create a noticeable amount of loss, reducing the output power of the device. Wafer-wide gold contamination on silicon photonic waveguides might render every device on the wafer inoperable due to elevated propagation loss.

Careful management of these impairments is required for production of high performance photonic devices because the yield of integrated circuits scales geometrically with the number of components. For example, a component yield of 90% in a PIC with 10 components will mean, assuming the failures are randomly distributed, that the PIC yield will be $(0.9)^{10} = 0.34$, so indeed 90% yield is quite poor in this context.

Some of the impairments may be unavoidable, for example, most lithography systems available for processing III-V devices have lower bounds on the layer alignment accuracy that are a sizeable fraction of a micrometer. For example, the GCA Autostep200 at UCSB normally has misalignment of no better than 150 nm. In these cases, the components must be designed so that they can tolerate this level of misalignment. Particulate contamination is also related to the physical facility that the devices are fabricated in, and more sophisticated clean rooms can have extremely low particulate contamination. State-of-the-art CMOS facilities store wafers in sealed cassettes that are only opened inside of enclosed process tools.

Most contamination can be avoided by proper cleaning and handling procedures, but in the case of particulates, they accumulate on the wafer gradually over time. Heterogeneous integrated circuits are often difficult to clean due to the range of materials included in the device. For example, after n-metal deposition, the heterogeneous lasers detailed in this chapter have exposed InGaAs (no phosphoric acid), InP (no hydrochloric acid), AlGaInAs (no sulfuric

acid), silicon, silicon dioxide (no hydrofluoric acid), and germanium (no hydrogen peroxide or hot water), thus many well-known semiconductor cleaning procedures, such as RCA cleaning or Piranha cleaning, cannot be performed. Therefore, when designing a manufacturing process, simply reducing the amount of time that the wafer spends in fabrication can help reduce the accumulation of particulates. In addition, shorter and simpler processes have less exposure to random failures like machine breakdown or process drift. Adding steps to improve the yield must be weighed carefully, since additional processing can degrade yield.

This chapter is divided into four sections: Silicon processing, bonding, III-V processing, and metallization. Each section will detail the process flow, selection process, and decision criteria for each fabrication step and its relevance to the photonic performance and yield of the resulting device. The final process recipe used for the best performing devices will be listed in an appendix.

3.1. Silicon

The silicon portion of the device in this work was used for passive waveguide components only. In theory, silicon may be used to produce PN-junction phase modulators and germanium-based photodetectors. Producing these components in a research environment, particularly at UCSB where non-CMOS compatible materials are allowed in the facility, is extremely difficult. Ideally the silicon processing would be performed at a CMOS foundry, but low-volume research scale production is prohibitively expensive at these facilities.

As explained in Chapter 6, the silicon waveguide is fully etched down to the buried oxide to assist with repeatability of the directional coupler. At the beginning of development for this work, etch-rate monitoring was not available in any of the systems used for silicon etching,

and so this was a necessity. Recent upgrades to the deep RIE system could render this requirement obsolete.

Another concern during silicon processing is that with the deep UV lithography, the antireflection (AR) coating underlayer (AR2 or DUV42P) is difficult to remove, and repeated lithography can create some laminar contamination that degrades the surface quality, reducing bond yield and increasing waveguide loss. For the best performance and yield, it is preferable to limit the number of deep UV lithography steps on the silicon wafer if the AR coating is required. Adhesion is normally poor between deep UV resists and silicon, even with HMDS adhesion promoter, but holes and > 1 μm lines can be produced for dry etching or deposition without difficulty when HMDS is used instead of the AR coating. For this reason, and the overall requirement for reduced process complexity, only a single silicon etch step is performed. The bonding outgassing structure and the waveguide trench are formed in the same layer.

3.1.1. Process Flow

The process flow of the silicon waveguide etch is shown in Figure 3.1. The bare silicon wafer is normally coated with resin to protect it during the coring process when the 200-mm wafer is sized down to 100 mm for use in the UCSB cleanroom, so this resin is cleaned using 1165 solvent (Figure 3.1a). Then the wafer is coated with an antireflection (AR) layer, AR2-600 in this case. This has been replaced in the UCSB Nanofab with DUV42p. Specific thickness control is required for optimum reflection reduction. 60 nm is optimal and is attained with 4000 rpm spin speed. The AR layer is then baked at 220°C (Figure 3.1b); note that a lower bake temperature, say 190°C, may help reduce footing. Extreme care must be taken regarding the cleanliness of the wafer at this point, as particles on the wafer will create non-uniform

thickness of the AR layer that will then fail to be fully removed in the AR etch step. The imaging resist, UV-6 0.8, is then applied (Figure 3.1c). The thickness of this resist is determined by the silicon dry etch selectivity: 500 nm of silicon etching with the Si DRIE recipe (detailed later) will consume 200 nm of resist, so the thinner UV-220 resist is risky. The UV-6 is spun at 5000 RPM, so that it is as thin as possible, about 400 nm. This leaves a comfortable margin of 200 nm of resist remaining after the etch. The resist is then exposed and developed in 2.38% TMAH developer, AZ300MIF (Figure 3.1d). The AR coating is not photosensitive and must be dry etched using O_2 RIE plasma etching (Figure 3.1e) in RIE #5, using 20 sccm of O_2 flow, 10 mT of pressure, and 100 W of RF power, for 30 seconds.

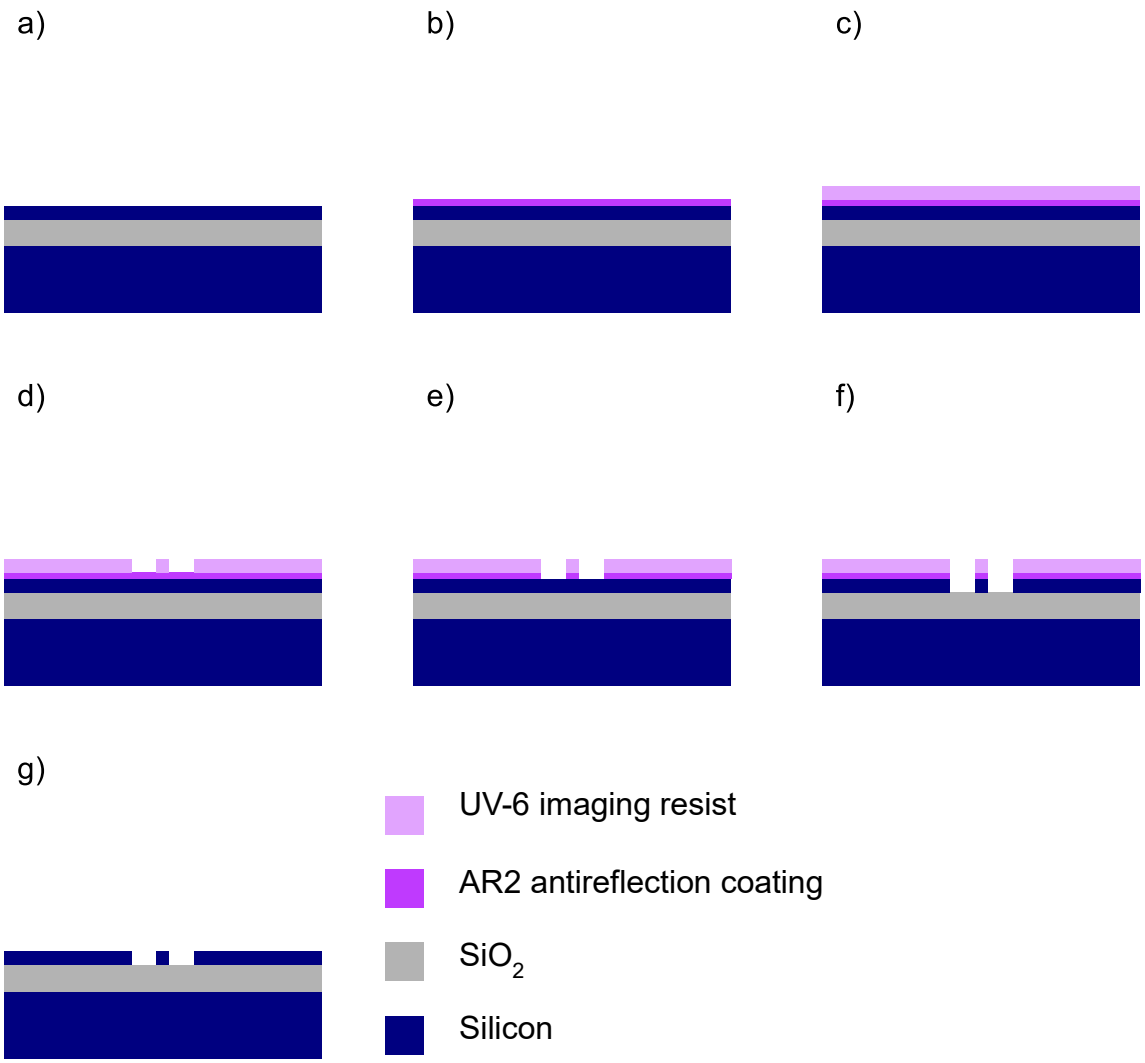

Figure 3.1: Process flow for the deep etched silicon waveguide.

Over-etching of the AR layer etch must be avoided as there is a pattern effect on the directional coupler–the linewidth reduction on the outside of the structure is more rapid than in the gap–so linewidth narrowing by over-etching cannot be corrected by adjustment of the exposure. The AR layer appears to be fully etched after 20 seconds, so 30 seconds is a 50% over etch. The wafer is then etched in the Si deep RIE tool, sometimes called the "Bosch" etcher, using a single step etch developed at UCSB [2] (Figure 3.1f). This work uses a slight

modification of the recipe [2] to produce more vertical sidewalls on SOI wafers and is shown in Table 3-1.

Table 3-1: Silicon etch recipe

C_4F_8 flow	56 sccm
SF_6 flow	24 sccm
Ar flow	20 sccm
Chamber pressure	19 mT
ICP[1] power	825 W
CCP[2] power	15 W
Source temperature	40°C
Electrode temperature	10°C

[1]Inductively-coupled plasma.
[2]Capacitively-coupled plasma

For a reason that never became clear, better sidewall quality is produced when etching silicon with the above recipe (and many permutations of that recipe) if the etched sample is seated on a carrier wafer. This was discovered by accident, as the first attempt to form narrow spot size converter tapers on 100 mm wafers failed, as the thin 125-nm patterns were completely undercut. Attempts to optimize the dry etch recipe on pieces failed to reproduce the problem, as they always looked pristine and vertical. Adjustments to the recipe did not fix the problem: variation was explored in gas flows, source temperature, electrode temperature, ICP power, pressure, and CCP power. The undercut persisted. The only solution that could be found was to stick the device wafer onto an oxide-coated carrier wafer with a loop of Kapton tape (oil was not allowed by the staff since it could squeeze out into the clamp). The impact of the carrier wafer approach is shown in Figure 3.2: a) shows a 100-nm taper tip which was etched with the recipe in Table 3-1 on a carrier wafer, and b) shows a larger feature (the 100-

nm tapers were completely undercut during the process) which was etched with no carrier wafer and has significant undercut.

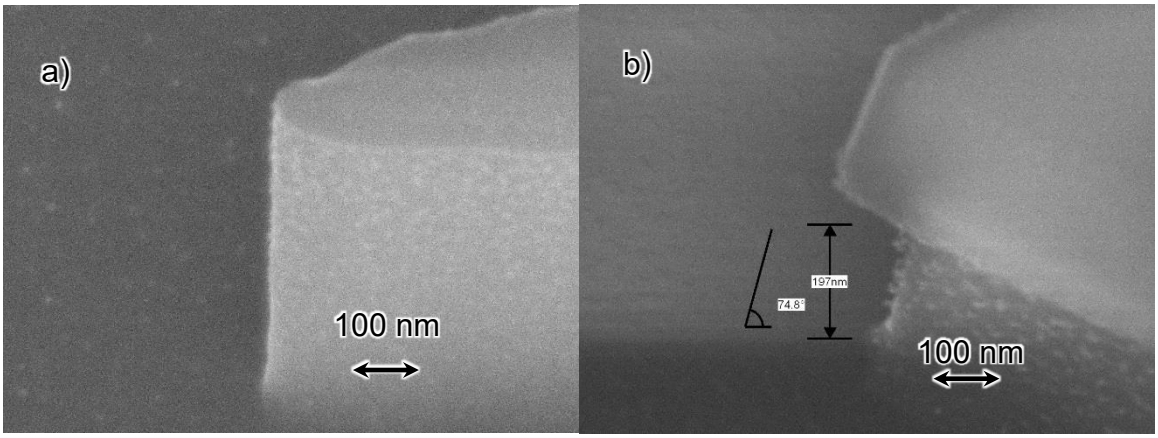

Figure 3.2: Electron micrograph of the tip 500-nm tall silicon ridge. The photoresist is still on top of the pattern. a) shows a bulk silicon wafer that was etched on top of a carrier wafer; the impact of AR2 footing can be seen, as the Si pattern is larger than the imaging resist pattern. b) shows a wafer that was etched by itself. The silicon undercut the resist by almost 100-nm, and the quality of the sidewall is visibly degraded.

Lastly the imaging resist was stripped in 1165 and then the AR layer was removed with 3:1 H_2SO_4:H_2O_2 ("Piranha") on an 80°C hot plate. While the cleaning process was used frequently without issue, other users have reported some difficulty with removing the resist, a problem which emerged after this work was completed. It is likely that an O_2 plasma ash before the solvent clean is necessary.

Careful optimization of the lithography process is required, mainly for the directional coupler, which will be detailed in Section 6.2. A multitude of factors affect the final linewidth of the etched devices: the exposure and focus setting of the lithography tool, pattern effect in lithography, the AR layer foot, pattern effect in the RIE O_2 plasma etch of the AR layer, linewidth bias in the silicon etch, and grid snapping in the photomask production all contribute

to impaired feature size in the directional coupler. Most of these can be corrected by performing the lithography exposure optimization with the production mask on a production wafer (an SOI wafer with the same device design as the device wafer). Pattern effect in RIE etching is mitigated but not completely resolved by reducing the etch time; decreased chamber pressure or reduced AR layer baking temperature might help resolve this issue. Linewidth bias in the Si etch can be corrected by performing the Si etch on the exposure optimization wafer. The best achieved directional coupler is shown in Figure 3.3: the line width is 3% off the designed value of 400-nm and the gap is 0.5% off the designed value of 400-nm. Note that exposure optimization cannot compensate for this error, as it will widen the gap as it shrinks the waveguide. In addition, isolated lines designed at 400-nm width were 390-nm wide, due to the RIE O_2 etch pattern effect: the outside of the waveguide in the directional coupler is etched laterally faster than the inside of the waveguide in the directional coupler, while the isolated line is etched fast on both sides. Introducing a mask bias would correct for this: reducing the width of the waveguide on the mask in the directional coupler by 12 nm would allow the error to be compensated by exposure control. However, this type of process correction normally requires a large collection of statistical data and is impractical for a research setting. The performance of these directional couplers was ultimately satisfactory.

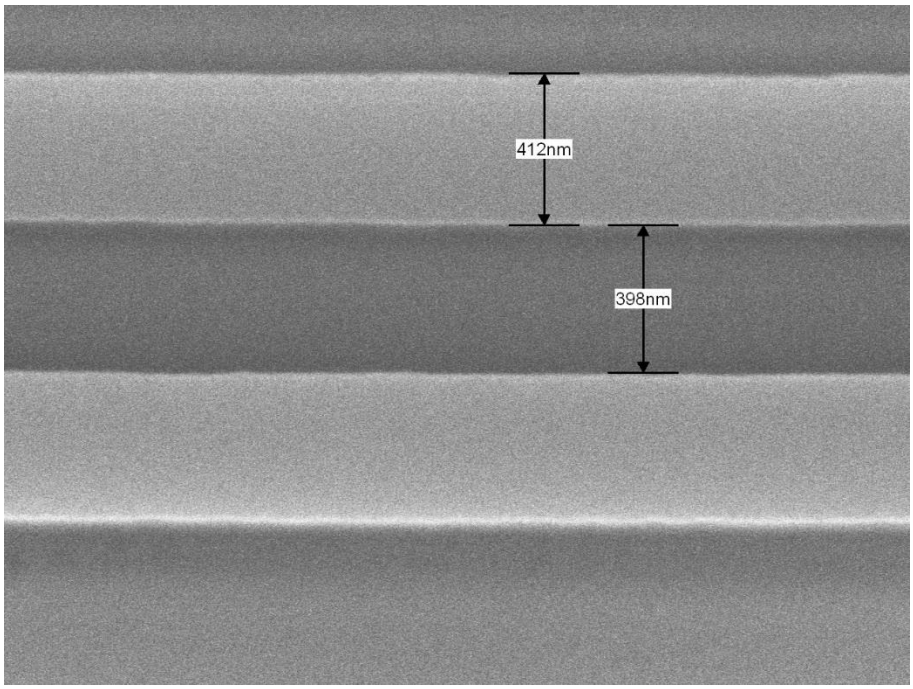

Figure 3.3: Electron micrograph of a deeply etched silicon directional coupler. The intended dimensions are 400-nm for the waveguide and 400-nm for the gap.

3.1.2. Bonding Outgassing Structure

The surface of the silicon must also be patterned with an outgassing structure, since trapped water vapor at the bonded interface can form voids during the bonding anneal. In the past, a matrix of square holes was etched into the silicon device layer [3] to allow the gas to diffuse into the buried oxide. This was normally successful; however, some devices showed a micro-bubble phenomenon, where small voids, smaller than the outgassing channel, would form in between the channels. Additionally, some of the film overhanging the outgassing channels would burst during processing, and the broken flake would land on the surface, masking it. It was hypothesized that the interfacial gas did not always diffuse all the way to an outgassing channel, and that the gas trapped in the channel did not diffuse into the buried oxide. To solve these problems, a grid of channels was implemented instead of isolated squares. The grid has

the same fill factor as the vertical channel, but the distance between suspended bonded film and the anchor point is smaller in the grid, which helps reduce bursting of the channels. Figure 3.4 shows that the grid design eliminates the microbubbles.

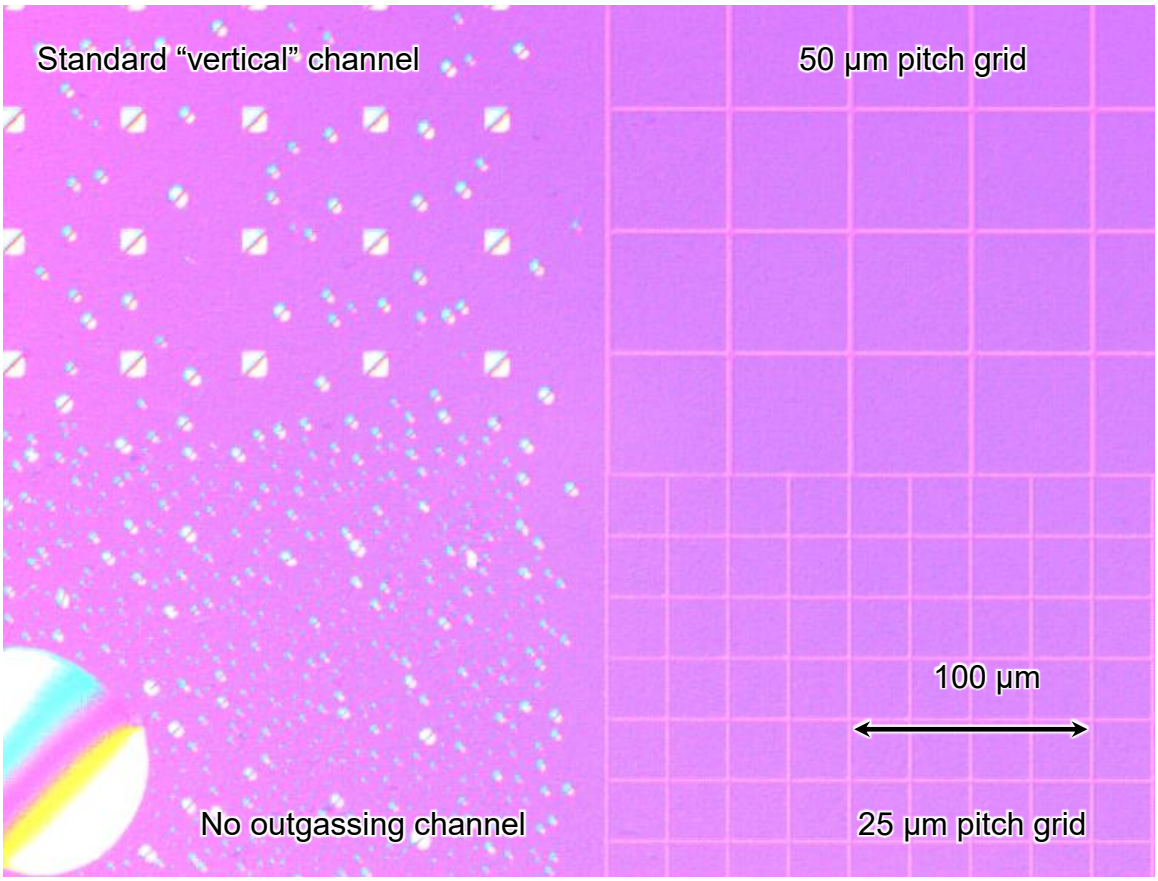

Figure 3.4: Micrograph of a 150-nm InP film bonded to an SOI wafer with various outgassing channel designs. Large voids are eliminated by the square vertical channel, and the microbubbles are eliminated by the grid-style channel.

Although wet chemicals did not penetrate into the grid in tests, paranoia won out, and the final design was a plus shape so that it would be impossible for chemicals, particularly the HCl used during the bonding substrate removal, to penetrate into the grid and lift away the bonded film. 500-nm wide trenches with a pitch of 25 µm were selected as the final design, and are shown in Figure 3.5. More details on the bonding process are in the following section.

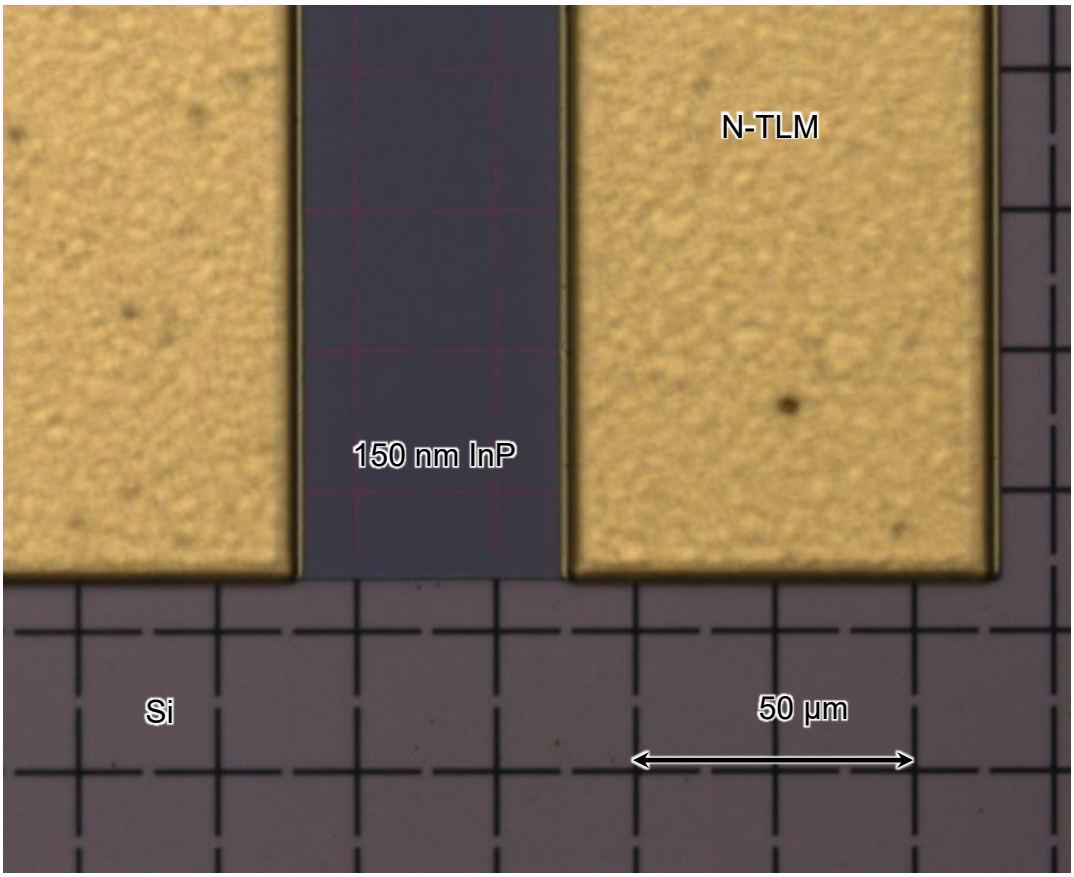

Figure 3.5: The final outgassing channel design. The figure shows an n-type TLM structure, which often demonstrated microbubbles with the vertical outgassing channel that disrupted characterization. This device has been completed through all the InP etching, so the silicon is exposed. A thin film of the n-type InP remains between the two metal pads. This film is free of microbubbles.

3.2. Bonding

The heart of the heterogeneous silicon/III-V technology is the bonding process: it allows the combination of multiple materials on a single wafer. While a heterogeneous wafer is not technically monolithic, it brings many of the advantages of monolithic integration. All of the semiconductors can be single-crystalline and have low defect density, since they are originally

manufactured on their native substrate. Post bonding, the fabrication of the heterogeneous materials can be completed at wafer scale, with lithographic alignment precision.

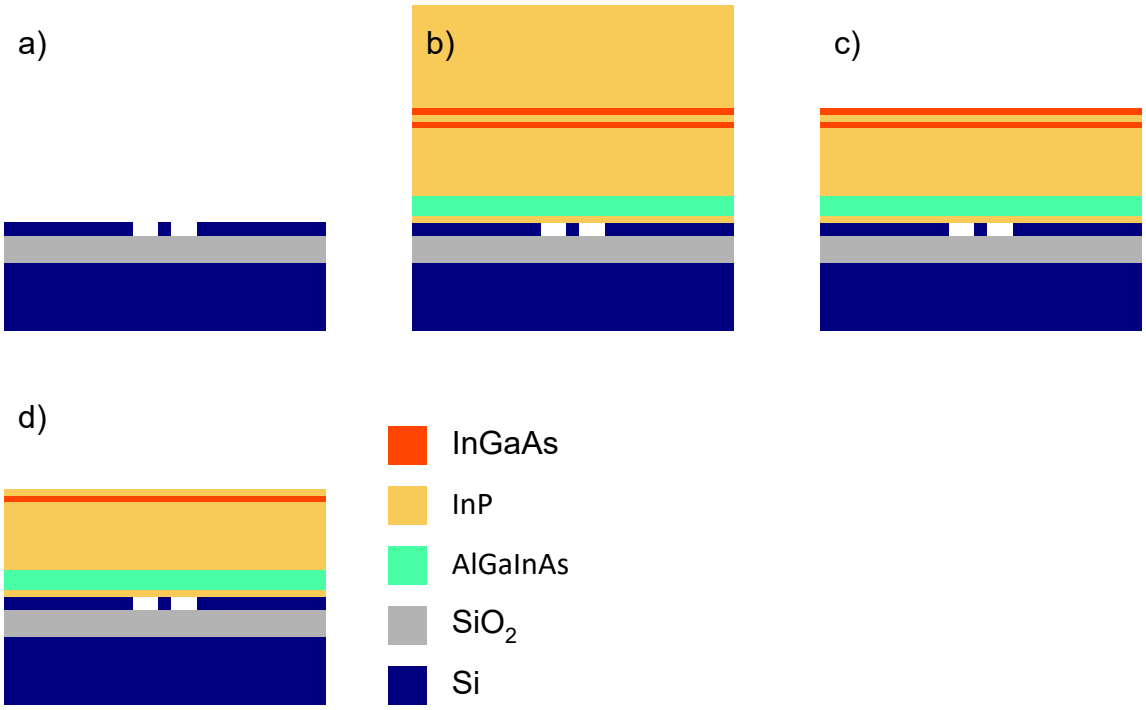

Figure 3.6: Bonding process flow. A) shows the wafer after completion of the silicon etching process; b) is after the III-V die is bonded; c) is after substrate removal; d) is after the InGaAs etch stop layer removal.

The bonding process flow is shown in Figure 3.6. After completing the silicon etching (Figure 3.6a), the InP die is bonded to the silicon wafer (Figure 3.6b). The substrate of the InP wafer is then removed with a combination of mechanical polishing for the first 300 μm of the normally 375 μm substrate, and then wet etching in 3:1 HCl:H_2O (Figure 3.6c). The process is done partially mechanically because removing the entire substrate with the wet etch would take ~2 hours, which would allow for significant undercut of the InP in bond-fail regions. Removing most of the substrate mechanically reduces the amount of time that the HCl can flow into exposed trenches in bond-fail regions. The wet etch stops against an InGaAs etch

stop (the top layer in Figure 3.6c) with >1000:1 selectivity, so the roughness and nonuniformity of the mechanical polishing is completely removed, leaving only the intended epitaxial layers with a smooth planar surface. Finally, the etch stop layer is removed, with 1:1:38 H_3PO_4:H_2O_2:H_2O (Figure 3.6d). This process also has nearly infinite selectivity for etching InGaAs away from InP. The exposed layer at the top of the epi stack is now the InP sacrificial layer. At this stage, there is a tall triangular ridge on either side of the die where the 110 and 11-0 planes, which etch slowly in HCl, become exposed. These are removed manually by first coating the wafer with photoresist (to later lift off the particulates), and then the mountain is scratched away with a razor blade. Steady hands are recommended; the operator is advised to have a nominal amount of caffeine level in his blood before attempting this part of the process. After stripping the resist, some fine particulates may remain from the substrate removal process. Swabbing the chip with Tergitol will remove most of this particulate and will not harm the bonded film except in regions where a void has formed, which are going to fall away in the subsequent steps anyway. These mountains are typically about 2/3rd the height of the substrate after mechanical polishing. It is possible that precise leveling and a finer grit polishing film could reduce the thickness after polishing to 30-40 μm. The usual 20-minute HCl etch would then fully remove the mountains.

The bonding process is quite simple. An EVG 810 plasma activator is used to activate both the Si and InP wafer surfaces prior to bonding. The pieces are then placed in contact, orienting the waveguide perpendicular to the InP wafer major flat, to ensure that the “mountain” that remains after wet etch substrate removal is above and below the die. This can be done manually in the case of a non-aligned bond or with a flip-chip bonder in cases when alignment is required. The spontaneously-bonded parts and are then placed in a graphite clamp and annealed

at 300°C for 1 hour (some have suggested 2 hours may have higher bond strength). The bonding pressure is normally 200 kPa, but careful calibration of the bonding clamp was not performed, and satisfactory bonds were shown between 100 and 800 kPa, so it is evidently insensitive to this parameter. No ozone, ammonium hydroxide, dehydration baking, O_2 descum, etc. is required. The bond yield will then essentially be limited by vertically protruding defects on the InP chip (the silicon wafer will be virtually free of surface defects), and by particulate contamination on both parts.

Die-sized pieces of InP epi wafers that are free of defects that cause significant bond yield problems can be found by cleaving up the InP wafer and discarding the few pieces that have defects. The cleaving process itself can add a significant amount of InP particulate that adheres strongly to the InP chip surface, which is hard and inorganic and may create bond yield problems. To avoid this, it is critical that the InP chip be coated with resist (SPR 955 1.8CM with no HMDS is used) before cleaving–by these means, the InP particles generated by cleaving will be lifted away.

The silicon wafer, which has just been cleaned with Piranha (Figure 3.1g), is normally clean at this point. HF removal of the native oxide formed by the Piranha clean is not necessary. If the experimenter is unlucky and a large sticky particle has fallen on either piece, gentle swabbing with a low-particulate swab and inorganic detergent (such as Tergitol) is effective at removing even low-lying adherent-particulate contamination. The O_2 plasma in the bonding activation will remove the organic film that remains from the detergent.

As with all nanofabrication, simpler is better, and attempts to clean chip surfaces often will only make them dirty. It was also found that InGaAs protective cap layers are unhelpful with bonding yield and only offer another opportunity to add particulates to the InP chip. Since

commercially grown InP epi is produced in a cleanroom environment, the material is usually clean upon arrival at UCSB and it is best to simply coat it, cleave it, remove the resist, and bond. Extremely high yield, nearly 100%, can be attained in lucky cases when no small particles fell on the chips while loading into the activator and performing the initial bond.

3.3. III-V Mesa Formation

Thanks to the nature of heterogeneous integration, the fabrication process for the III-V components can largely be copied from existing methods for fabricating pure InP lasers. The only caveat is that the underlying silicon waveguide must be protected from damage during the III-V processing. In the event of partial die bond (where only part of the silicon die is covered by III-V) or in the case where the silicon has been exposed unintentionally (such as a bond yield failure), the silicon may be exposed and needs to be considered. Silicon is impervious to the common wet etches used in InP processing (H_2SO_4, H_3PO_4, and HCl), but is unfortunately quite vulnerable to dry etching, as silicon-halides are commonly volatile under the conditions inside of a plasma etch chamber. Since halides (CF_4, $SiCl_4$, BCl_3, HBr, HI) are the most frequently used process gases in dry etching due to their high electronegativity, the use of dry etching must be considered carefully to ensure the underlying silicon devices are not damaged.

Luckily, InP can be etched in a methane hydrogen mixture, usually combined with argon and referred to as “MHA” [4]. MHA does not etch silicon, and in fact deposits a protective polymer over silicon, so even the mechanical attack from ion bombardment is limited. Unfortunately, because the InP mesa must be etched very deeply (1.8 μm, see Chapter 4 for

epi layers), a hard mask is required. Common hard mask materials are dielectrics such as SiO_2 and Si_3N_4, which must be dry etched for definition of micron-scale features. Smooth and vertical dry etching of these materials is usually accomplished with CF_4 and CHF_3 chemistry, which etches silicon very rapidly. Hard masks must be over-etched to compensate for etch nonuniformity, and this over-etch will attack exposed silicon. Even a few nanometers of etch into the surface of a silicon waveguide can produce significant insertion loss and reflection. For this reason, the hard mask for the InP mesa etch is deposited with a lift-off process. A bi-layer resist using PMGI as the under-layer and a simple single-step develop allows the deposition of a thin SiO_2 hard mask using electron-beam evaporation. Features down to 500-nm with i-line lithography and down to 300 nm with 248-nm-DUV lithography can be achieved with this process if the thickness of the oxide is kept below 300 nm, as thicker films allow more diffusion of the adatoms underneath the undercut imaging resist.

The process flow for the III-V mesa formation is shown in Figure 3.7. After the bonding substrate removal is complete (Figure 3.7a), the mesa etch hard mask is deposited using liftoff (Figure 3.7b). Since the Si wafer is still intact, DUV lithography may still be used (the machine only accepts 100 mm wafers). PMGI SF-15, the thickest available, is used as the under layer, since thinner under layers will not planarize the 2 μm tall epi layer at the edge of the bonded die, resulting in unintentional deposition of hard mask material along the edge of the epi layers. UV-6 0.8 is used for the imaging resist. The PMGI is absorptive in the ultra-violet and has good adhesion to the III-V and the UV-6, so no AR layer is needed. The “single step” develop process, in which the imaging resist is developed in the same step as the PMGI, is used to ensure large undercut in the taper tip. Since PMGI is developed isotropically in the photoresist developer, the undercut is normally > 2μm and has a wet-etched profile. Careful inspection of

the taper tips should be conducted to ensure they are fully undercut. Often the undercut rate in the taper tip is slower than the rest of the pattern because it is so narrow. A short 30 second etch in phosphoric acid 1:1:38 H_3PO_4:H_2O_2:H_2O is conducted after the hard mask deposition to remove the InP native oxide, which can interfere with the MHA dry etch, as a thin layer of polymer forms on any surface that does not contain indium. The p-mesa is then formed with MHA dry etch (Figure 3.7c). The etch rate of this tool depends on the size of the InP chip, the fill factor of the lithographic pattern, and the phase of the moon: it varies between 0.5 nm/s and 1.5 nm/s. The system in the UCSB Nanofab is equipped with a laser etch-rate monitor, and it must be used for accurate etch depth. MHA will etch InGaAs at about half the speed of InP, but AlGaInAs is much slower, about five times slower, depending on the Al content. The mesa can be over-etched considerably to level out the etch nonuniformity, which is 10% in the tool used for this process. This corresponds to 180 nm of nonuniformity. After etching into the AlGaInAs, this nonuniformity is divided by the selectivity, so it can be reduced to about 36 nm, which is acceptable. It is important to place the etch rate monitor on the center of the etched area, since that etches the slowest. Then, the AlGaInAs is patterned with thick DUV resist (PEK 162c) and wet etched with 1:5:15 H_3PO_4:H_2O_2:H_2O (Figure 3.7d).. The etch rate of the AlGaInAs is approximately 300-nm/min downward and evidently approximately the same laterally. As described in Chapter 5, the AlGaInAs is undercut in this step by over-etching. The selectivity against the underlying n-type InP is extremely high, so over etching with the phosphoric acid mixture does not damage the InP. The active region etch pattern overhangs the III-V mesa by 500 nm, and it is desired to “dead sharp” the p-mesa taper tip, which is 300 nm wide, so the undercut should be (500 + 300)/2 on either side. This normally takes 1 minute and 10 seconds. While definitive establishment of the width requirement of the active

region taper could not be established, it appears that any width below 300 nm is suitable for low-reflection transitions. Currently the reflection is dominated by the n-layer taper as long as the active region taper is less than 300 nm. Dead sharpening the active region taper is risky as excessive over-etch can shorten the active region taper.

Also note that the SiO_2 hardmask is left on for this step, as the phosphoric acid mixture also etches InGaAs, so in the event of poor adhesion between the photoresist and the III-V, the attack on the InGaAs will be limited to a few hundred nanometers of undercut. The active region etch has typically been done with the SPR-955 1.8CM resist in the i-line stepper until recently. HMDS+SPR 955 has very good adhesion to InP. The process was moved to the DUV stepper for better alignment accuracy, but the PEK 162c resist is more troublesome, and forms a scum layer when HMDS is used. Without HMDS, some undercutting of the InGaAs was observed. More development is required, but for now it has proven to be satisfactory.

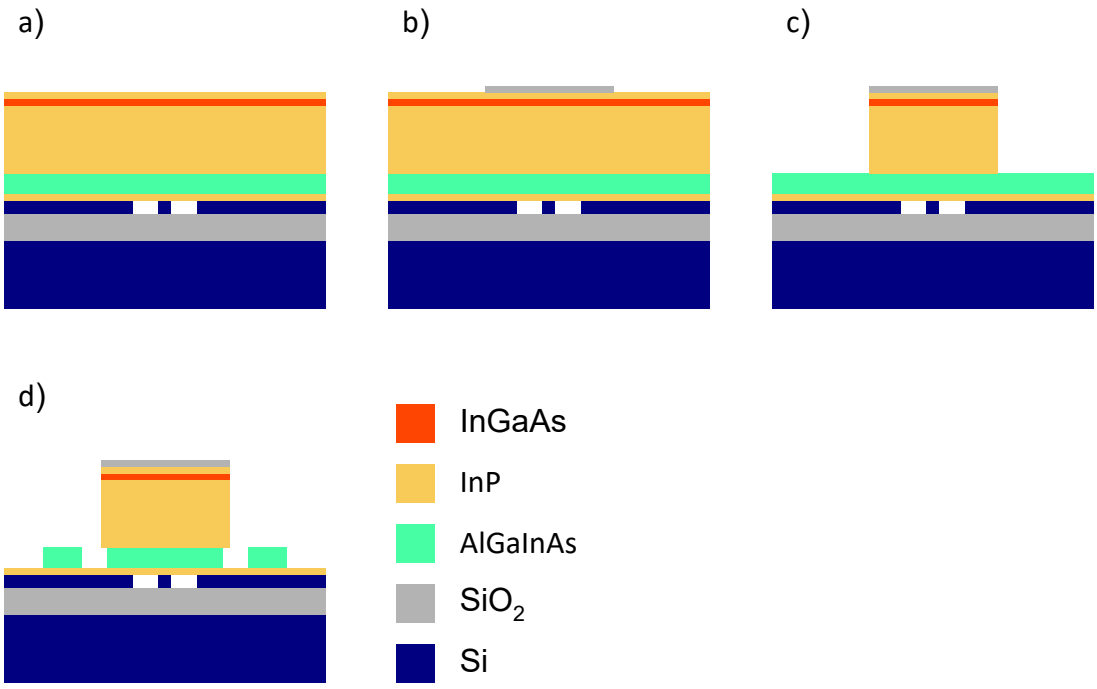

Figure 3.7: Process flow for the III-V mesa formation. A) shows the wafer after completion of the substrate removal step; b) shows the deposition of the SiO_2 hard mask; c) shows the dry etch through the top InGaAs and p-cladding; d) shows the wet etch through the AlGaInAs active region.

Thanks to the smooth line edge of DUV lithography, and the natural smoothing effect of the inhibited MHA etch, the sidewall of the III-V waveguide is nice and clean and vertical. Extremely small p-mesa taper tip size (below 200 nm) have been achieved with DUV lithography, but experiments showed that the best laser slope efficiency came from p-mesa taper tip sizes of 300 nm and 500 nm, so 300 nm was chosen for lowest reflection. The actual width at the bottom of the mesa that is achieved with this process is slightly wider because of the slope of the sidewall. This is shown in Figure 3.8a, and is normally around 500 nm. The AlGaInAs layer is undercut and sometimes visible underneath the p-mesa if the sample is tilted, as shown in Figure 3.8b. The reason that the wide p-mesa tip and narrow AlGaInAs taper tip has the best performance will be covered in more detail in Chapter 5.

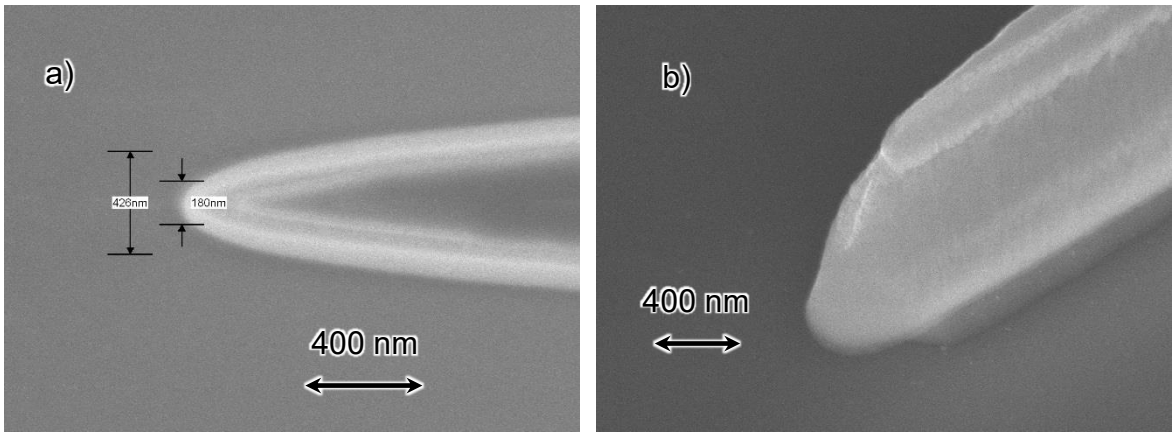

Figure 3.8: Etched III-V mesas. A) shows a plan view of the taper tip after the MHA dry etch. The oxide hard mask is still on the mesa. The mask is narrowed by erosion from 300 nm to 180 nm. The MHA etch normally has an 86° sidewall angle, and this combined with the

erosion results in a bottom width of the taper of 428 nm. The p-mesa must be below 500 nm for low reflection. Figure b) shows a 35° tilted view of the taper after the AlGaInAs active region is etched. The AlGaInAs taper can be seen underneath the p-mesa, slightly narrower and shorter.

The majority of the III-V laser mesa is the implanted type, which is wide enough that the III-V sidewall does not interact with the laser mode Chapter 4. The heterogeneous transition is highly sensitive to manufacturing deviation, as it consists of a very narrow waveguide and so is susceptible to scattering loss from rough waveguide sidewalls. Accurate definition of the taper features, both in feature size (since too small features will elevate loss, where too large features will elevate reflection) is critical for a low loss heterogeneous transition.

3.4. Back End

The back-end process consists of the metallization, oxide cladding, isolation etch, ion implantation, and probe metal deposition steps. These are grouped together because there are no more critical lithography steps after the end of the III-V mesa definition, and the isolation, cladding, and contact steps are interspersed with one another. While the feature sizes are all >500 nm and alignment tolerances all >200 nm, these steps are all critical to a successful device. A failure at either contact metallization step will result in high resistance and low efficiency. Grass or incomplete etching of the n-contact will elevate the waveguide loss, potentially preventing lasing or reducing slope efficiency. Insufficient isolation will prevent mode-locking operation. Probe metal with whiskers can cause short circuits, or if it does not adequately coat the mesa sidewall the devices can be impossible to test. The experimenter is advised to remain stressed out over fabrication until the entire process is completely finished.

3.4.1. N-contact formation

This phase of the fabrication process forms the n-contact metal and etches the n-contact InP away from the passive waveguides. During the active region etch, a strip of the active region AlGaInAs is left behind over the area where the n-contact metal will be deposited; this is referred to as the n-type sacrificial layer (Figure 3.9a). The n-contact metal lithography uses PMGI SF-15 and SPR 955 1.8 as the under layer and imaging resist, respectively. This lithography uses the cap-on bilayer process, where the imaging resist is exposed and developed, then the wafer is flood exposed with DUV light to expose the underlying PMGI. The exposed PMGI can then be developed with a different chemical (tetraethyl ammonium hydroxide, TEAH, brand name XAL 101A in the Nanofab). The cap-on bilayer process produces a smaller undercut, typically 1 μm or less, than the single-step developer process used in the p-mesa etch hard mask liftoff (Figure 3.7b). This is necessary for the n-metal formation to prevent metal vapor from coming in contact with the adjacent active region sidewall, which can shunt the diode. The cap-on bilayer resist after flood-expose development of the PMGI is shown in Figure 3.9b.

The n-type sacrificial layer is etched using the n-contact metal photoresist pattern, so that the metal deposition can take place immediately after the sacrificial-layer etch. Normally the imaging photoresist is hydrophobic and the wet etch (the same as the active region wet etch, 1:5:15 H_3PO_4:H_2O_2:H_2O) is viscous and will not penetrate into the opened photoresist patterns, and so an O_2 plasma ash is used to roughen the resist to turn the surface hydrophilic. This is conducted in the Technics PE2 system at 300 mT and 100 W, for 4 minutes. After the wet etch is complete (Figure 3.9c), the wafer should be inspected carefully in a microscope to ensure that all the sacrificial layers have been removed. Usually the outgassing structure will become

visible after the active region has been removed, so it is helpful to be sure that an outgassing structure is underneath all the n-contact metal patterns. Prompt loading into the evaporator is recommended to limit the formation of a native oxide; however, delays of 1-2 hours do not appear to produce a drastic increase in the contact resistance. The contact metal stack used is 10-nm palladium, 110-nm germanium, 25-nm palladium, 1-µm gold, and 25-nm titanium (to improve adhesion of the subsequent via oxide) deposited in E-beam 4 (Figure 3.9d). This recipe was taken from [5] by the recommendation of the author S. Jain. 10/60/25 was superior for n-type InP contacts annealed at 350°C in [5], but subsequent experiments did not show this to be the case.

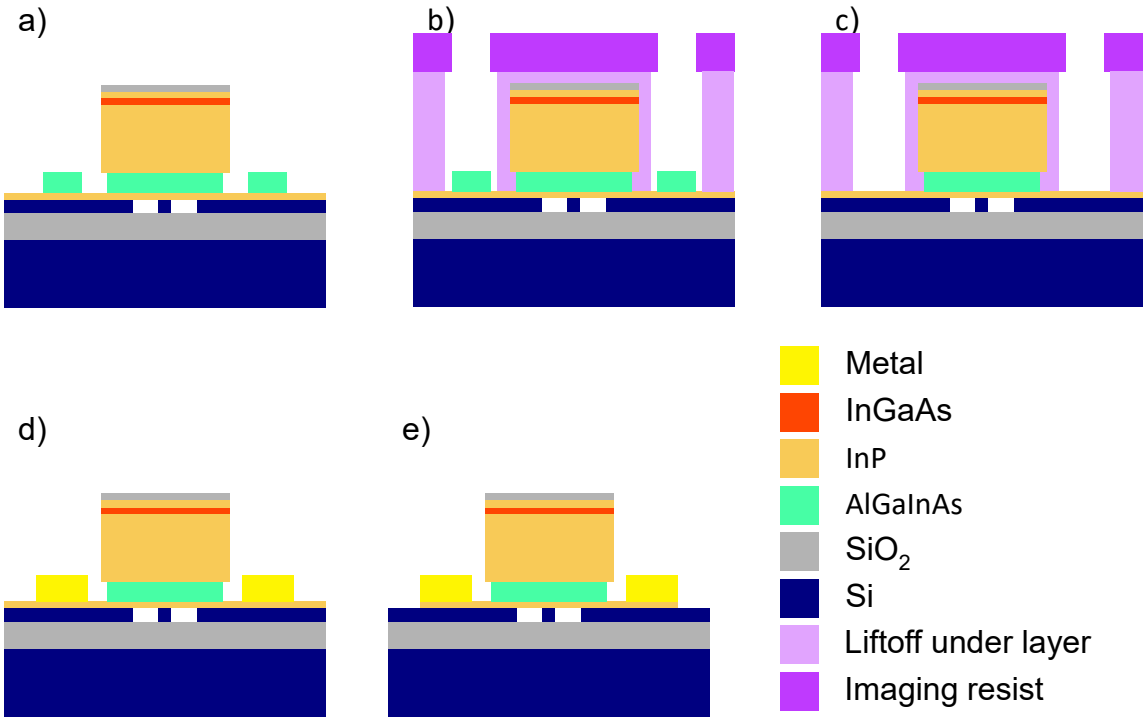

Figure 3.9: The n-contact formation. Figure a) is the device condition after the III-V mesa etching; b) is after the flood expose development of the PMGI underlayer; c) is after the n

sacrificial layer etch; d) is after the n-contact metal deposition; e) is after the n-contact InP etch.

Because of the germanium, extreme care after this stage must be taken to avoid undercutting the gold pad by etching the germanium, which is sensitive to wet chemical etching. Germanium etches rapidly in H_2O_2 and hot water. While it evidently is not etched by n-methyl pyrrolidone (the solvent used in 1165 and AZ NMP to remove PMGI), small amounts of water contaminating the solvent bath can attack the germanium. Therefore, it is critical to avoid leaving the wafer for a long time in the liftoff bath. For the n-contact metal liftoff, acetone is used to remove the imaging resist. Acetone does not dissolve PMGI, so the germanium is protected even if the solvent is contaminated with water. Then, using carefully dried glassware, two 5-minute baths of heated 1165 are used to remove the PMGI.

During evaporation of the n-contact metal, spitting of larger particles of gold can create spikes on the metal pad that may not be adequately covered by SiO_2 in the via step, allowing short circuits to form where the probe metal overlaps with the n-contact metal. The addition of tantalum to the gold melt (in E-beam #4) is used to prevent spitting. The staff normally maintains the gold melt, but this can be devastating, so a test deposition should be done first to ensure that a smooth film is deposited. Or the fabricator may simply add a tantalum pellet and ask for forgiveness later.

The thin n-type InP contact, which is 150 nm in total thickness (see Table 4-1: Epi J), is very fragile when it is not structurally bolstered by the thicker p- and i-type layers, so it is best to remove it from the passive silicon waveguides. In addition, unscientific experiments suggest that the loss introduced by the n-type InP may be higher than projected by literature. This step cannot be performed with a wet etch, as the etchant will be able to penetrate into the waveguide

trench after the etch is complete and attack the underside of the active region mesa. As mentioned before, dry etching must be done with caution due to the sensitivity of silicon to common dry etchants. A hard mask is not an option, since the fragile n-InP normally has higher levels of bond failure than the full epi stack, especially over passive Si devices like star couplers (where no outgassing trench is allowed) or directional couplers (where the waveguide trench is widened beyond the design rule of 3 μm when the waveguides merge), and these will be attacked by the over-etch if a hard mask is used. Because it does not etch silicon, MHA is again selected as the dry etch chemistry for the n-InP contact. Since the n-InP is thin, and the verticality of the structure is less critical, a photoresist mask can be used for the etch. Liftoff hardmask is impossible because of the topography of the p-mesa and n-contact metal: the directionality of electron beam evaporation that allows it to be lifted off also prevents it from conforming over topography.

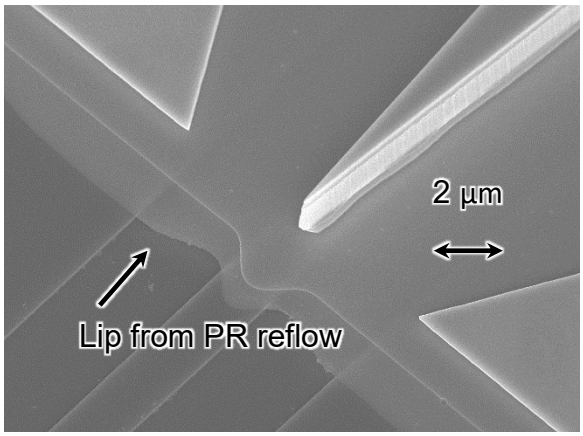

Figure 3.10: Heterogeneous laser after n-InP contact etch at 500 V and photoresist strip, showing the thin flake of n-InP that results from photoresist melting during the dry etch.

Three problems emerged during the development of the photoresist n-InP etch. The first was photoresist melting. The MHA system at UCSB has a heated chuck, which normally operates at 50°C, but thermal sticker measurement shows that the normal process for deep

etching InP raises the temperature at the surface of the wafer to over 100°C. This causes the photoresist to reflow. The photoresist, again SPR-955 1.8CM, is hard baked at 135°C to help prevent it from flowing during the MHA dry etch. Then, the RIE voltage is reduced from 500 V to 200 V.

Stripping the resist after MHA etching was the second issue that needed to be addressed. The MHA etch process deposits a polymer on any surface which is not chemically etched, so the polymer builds up on the photoresist mask. Removing the resist with solvent is then impossible. Normally, an O_2 etch is performed in the MHA system to remove the polymer; however, since this is at low pressure, the etch is highly directional and does not remove the polymer on the sidewall of the resist. The polymer on the sidewall will then collapse (Figure 3.11), and puzzlingly become impossible to remove in O_2 plasma, as is often the case for collapsed polymer sheets.

The third was the longest lasting and ultimately the simplest to resolve. HMDS is not designed for InP, and thick layers of scum are often left behind after development, especially in dense features or narrow openings. These are normally too thick to be removed with O_2 ashing. Removal of the HMDS resolves the problem but then the exposed silicon areas do not have good photoresist adhesion. Ultimately, changing the design of the n-InP taper to an angle, which is insensitive to lithography, allowed a drastic increase in exposure dose, from 0.56 seconds to 1 second, which ended the scum problem.

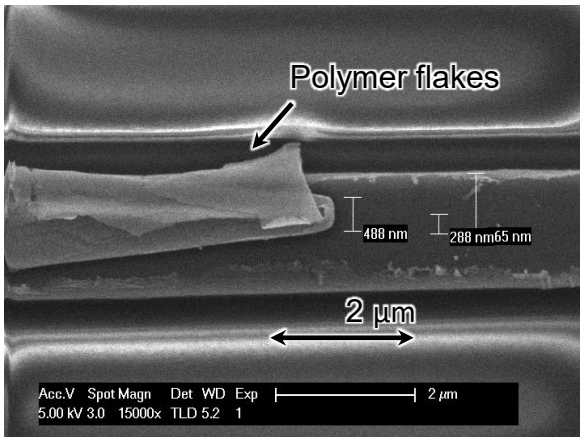

Figure 3.11: Polymer flakes over the n-InP taper after RIE #2 O_2 ash and solvent strip.

Performing the O_2 ash in a higher pressure system, such as the Technics PE2 (300 mT as opposed to 125 mT in RIE #2), is more isotropic and successfully removes the polymer from the photoresist sidewall. The final cleaning procedure is to use the standard O_2 clean in RIE #2 (125 mT, 300 V, 20 sccm O_2) out of paranoia, then move to Technics PE2 (300 mT, 100 W) for 1 minute, then 2 baths of 10 minutes in 1165 at 80°C. Once again, care should be taken to ensure that the glassware is dry and no water can contaminate the solvent bath. The solvent clean needs to be revisited in view of the germanium etch issue. Shorter strip time or stripping in acetone should be explored. A scanning electron micrograph of the final photoresist-masked etch and clean is shown in Figure 3.12.

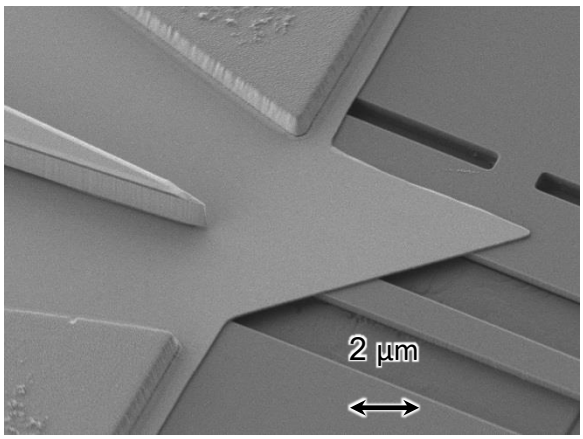

Figure 3.12: Etched n-InP layer showing vertical sidewall and absence of residue after photoresist stripping.

Other options for cleaning the photoresist that were explored and subsequently abandoned were using ICP O_2 ashing in the ICP #1 ashing chamber, which did not have sufficient forward power to attack the polymer (see the dissertation of J. Schramm), using a heated downstream asher (Gasonics), which lacks forward power and also hard-bakes the underlying photoresist, and using buffered hydrofluoric acid, which is extremely effective at removing the MHA buildup but also penetrates the waveguide trench and can damage the bonded interface (which is SiO_2).

This order of fabrication–n-metal contact first, then n-InP etch–is used because the n-InP protects the underlying silicon from contact with the gold during liftoff, and also because the exposed waveguide trench leading out from underneath the heterogeneous waveguide allows escaping air to blow holes in the photoresist during the lithography process. Bond failures can still allow metal contact with silicon and bubbles to be blown, however. It was established near the end of this work that using a 200°C oven bake for 30 minutes instead of a 200°C hot plate for the PMGI prevents the bubble blowing. It may be advantageous to shift the n-contact metal process to be after the via process, and then add a second layer of SiO_2 to protect the n-metal germanium from subsequent processing.

3.4.2. Via and p-contact metal

The silicon dioxide via layer serves multiple purposes in these devices. The probe pad layer needs to be able to overlap the n-contact metal so that the p-pad can have a low resistance connection to the p-contact metal, and the via layer allows this by being lithographically etched only where the metal needs to connect through it. The via is composed of silicon dioxide with

n = 1.45, which forms the waveguide upper cladding layer, protecting the waveguide from further processing impairments and allowing it to be routed under probe pad metal. It provides a passivation layer for the AlGaInAs active region sidewall. Finally, it is used as part of the "conformal via" process (detailed below) to allow lithographic alignment to the 300-nm taper tips for the p-contact metal to ensure that the taper is fully electrified. For this reason, the via process and the p-contact metal process are interrelated.

First, the p-mesa etch hard mask needs to be removed (Figure 3.13a). This is left on during the active region etch and n-sacrificial layer etch out of paranoia, in case the photoresist does not adequately protect the InGaAs, which can be etched in the H_3PO_4 solutions used in these processes. In the event of problems with the p-mesa etch, a contaminated layer may remain on the SiO_2 surface, which can be impervious to dry etch and prevent the via opening dry etch from functioning correctly. Buffered hydrofluoric acid etches both SiO_2 and the MHA polymer contamination, so the hard mask is removed using this chemical (Figure 3.13b). A lithography must be performed to protect the exposed buried oxide in the waveguide trench. This is done using the via mask. The hydrofluoric acid fluorinates the photoresist and leaves behind a thin insoluble layer, which needs to be ashed in the Technics PE2 for 1 minute before solvent stripping to avoid the deposition of the collapsed polymer layer on the chip. While the ash can be done after the solvent strip, since the layer is very thin, this is not always successful in removing the collapsed film.

The SiO_2 cladding layer is then deposited using reactive ion sputtering in the AJA Sputter #3 system, using 2.5 sccm O_2 flow, 25 sccm Ar flow, 250 W of power on the Si target, and 20 W of power on the substrate RF generator. The gas flows are selected for high deposition rate, and the substrate RF is used to densify the film, which reduces roughness, increases

conformation, and improves density of the film. Approximately 900 nm is deposited (Figure 3.13c), at a deposition rate of about 4.5 nm/min. This deposition rate depends on the target age and varies by about 20% over the life of the target. The exact thickness is not critical, but it needs to be known accurately for the via etch timing, so a monitor chip must be included. A small piece of silicon can fit on the chuck next to the major flat of the device wafer.

The via etch lithography is performed using SPR 955 1.8 CM, spun on at about 2.2 μm thickness (2500 rpm). Thinner resist is helpful for opening the narrow via over the taper tip. A CHF_3 etch in Panasonic ICP #2 is used to remove the SiO_2, using 40 cm^3/min CHF_3, 0.5 Pa pressure, 900 W ICP power, and 25 W RIE power (Figure 3.13d). This etch chemical combines with photoresist to produce an insoluble polymer, which enhances the selectivity to about 2:1 and is helpful for etching the thick SiO_2 via layer with a relatively thin photoresist. However, it will adhere to the wafer surface after stripping the resist with solvent, which ruins the wafer. To prevent this, anisotropic ashing at low temperature (to prevent the hard-baking of the resist) is conducted in the Panasonic ICP #1 ashing chamber using recipe 306 for 20 minutes, then the remaining photoresist is removed with 1165 stripper heated to 80°C.

Similar to the n-contact metal process, a sacrificial layer is used to protect the p-InGaAs contact from lithography residue, oxidation, and dry etch damage during processing. The sacrificial layer in this case is made from 50-nm of InP, since InGaAs etches in H_3PO_4 but not HCl. A cap-on bilayer process (flood-expose develop) is used (Figure 3.13e), purely out of superstition since it has always been done that way, while a simple bilayer process (single-step develop) would likely be appropriate. As with the n-sacrificial layer, a 4 minute etch is conducted in the PE2 Technics O_2 descum to render the photoresist hydrophilic. The sacrificial

layer is then etched in 1:2 HCl:H_2O, which has a 45-nm/min etch rate, for 2 minutes to guarantee the etch is successful (Figure 3.13f).

Again, as with the n-sacrificial layer, the wafer should be transferred into the evaporator as rapidly as possible. Electron beam evaporator #4 is used. The metal layer stack deposited is 10-nm palladium, 20-nm titanium, 20-nm palladium, then 1500-nm gold (Figure 3.13g). The thickness of the gold layer is important for the upcoming hydrogen implantation, as it is used as a mask to protect the underlying current channel. The chip is then annealed at 350°C in nitrogen for 30 seconds in a rapid thermal annealer. This metal stack originated from [6], and was selected specifically for its optimal resistance at low annealing temperature. The mechanism for the use for Pd/Ti/Pd/Au instead of the more common Pt/Ti/Pt/Au is explained in [7], in which a similar structure is used to form ohmic contacts to GaAs. The first 10-nm palladium layer forms a Pd-Ga-As compound upon deposition, and can be ohmic without annealing. Bonded heterogeneous Si/InP devices are sensitive to high temperature processes due to the difference in coefficient of thermal expansion causing optical degradation, so the reduction in anneal temperatures from 400°C for Pt/Ti/Pt/Au, or 450°C for Ti/Pt/Au, to 350°C for Pd/Ti/Pd/Au, was thought to be helpful. Strict comparisons are difficult, but some process runs annealed at 420°C exhibited similar performance to the standard 350°C anneal, so switching to Pt/Ti/Pt/Au and using a 400°C anneal may improve the p-contact resistance [8]. Other useful contact-resistance papers are: [9][10][11][12][13][14].

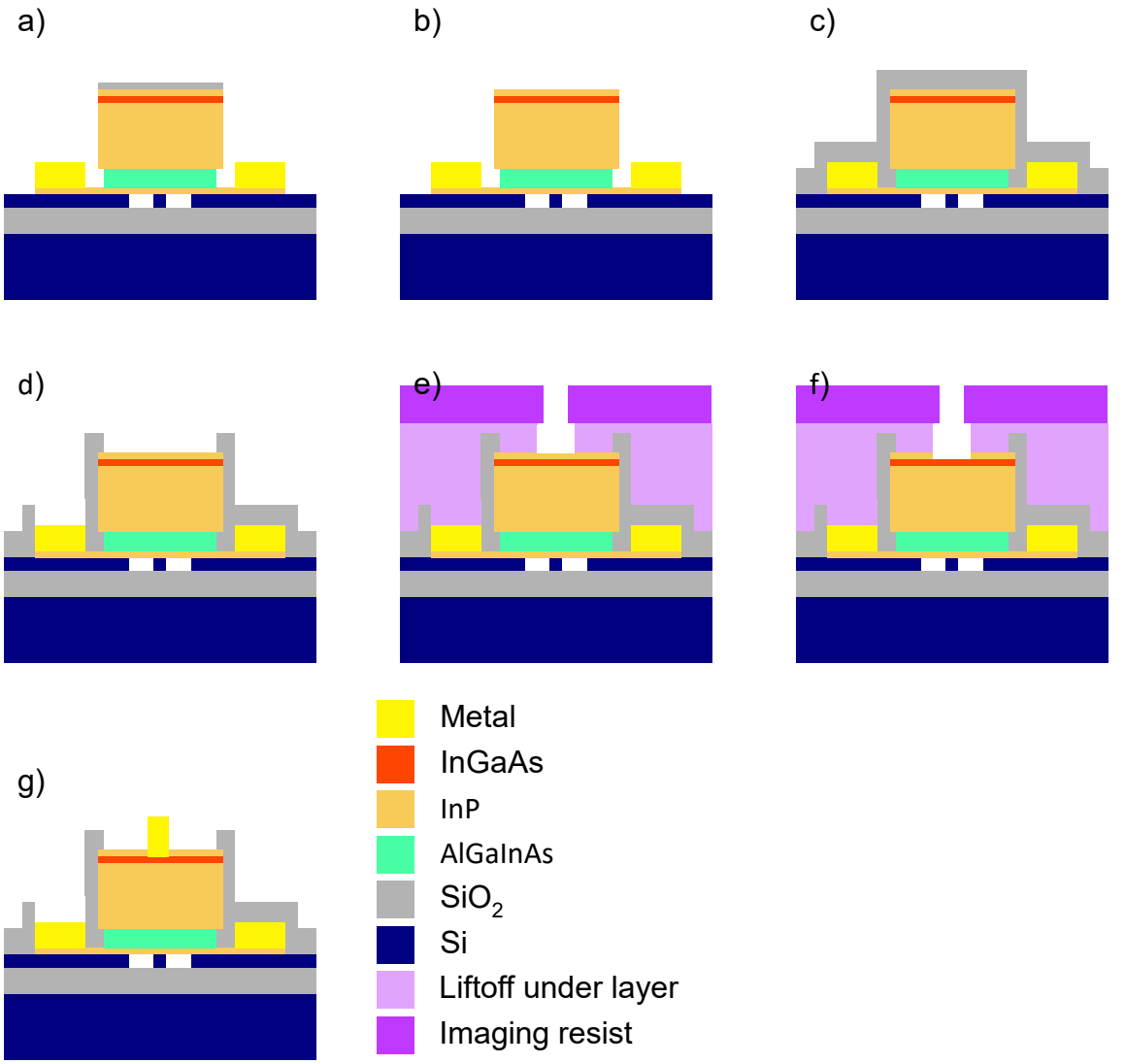

Figure 3.13: The via and p-contact metal process flow for the amplifier waveguide section. Figure a) shows the device after via oxide deposition; b) after the via etch; c) after application of the p-contact liftoff lithography development; d) after the p-type sacrificial layer etch; e) after liftoff of the p-contact metal.

This process was originally designed to ensure contact metallization and thick electrode deposition all the way out to the tip of the narrow III-V mesa in the heterogeneous transition section. This was initially considered to be extremely important, since early transition designs

exhibited more than 3 dB of loss. The loss was assumed to be partially due to inadequate pumping: these early designs used the "self-aligned" process, in which the p-contact metal was deposited before the p-mesa etch [15][16]. This metal layer was only 150 nm thick, while the taper was 100 μm long. The self-aligned process was used because of the difficulty of alignment and lithographic accuracy when attempting to overlay the p-contact metal pattern on the 300-nm taper tip. In the autostep200 system, ± 150 nm is the best alignment accuracy that can be obtained. Due to the large topography after the mesa etching (~2 μm), a thick photoresist must be used, which limits the lithographical accuracy. Exposure and focus optimization to better than ± 200 nm has proven to be challenging. In the worst case, a shrink of the pattern by 200 nm and misalignment of 150 nm will cause the tip of the taper to be completely uncovered by metal.

To solve this problem, a thick layer of SiO_2 is use for the via oxide. The sputter tool (and most of the PECVD tools as well) have about 40% of the top surface thickness deposited on the sidewall of the III-V mesa, so a 900-nm SiO_2 on the planar top surface will correspond to 360 nm on either side of the mesa, effectively widening the size of the taper feature that must be overlaid onto in the via lithography to 1020 μm (Figure 3.14a). The via pattern is widened so that it overhangs the III-V mesa by 200 nm on either side to ensure that misalignment will not cause the metal to miss the p-InGaAs contact, and the pattern is overexposed, eliminating the chance that the opening is too small for the taper tip.

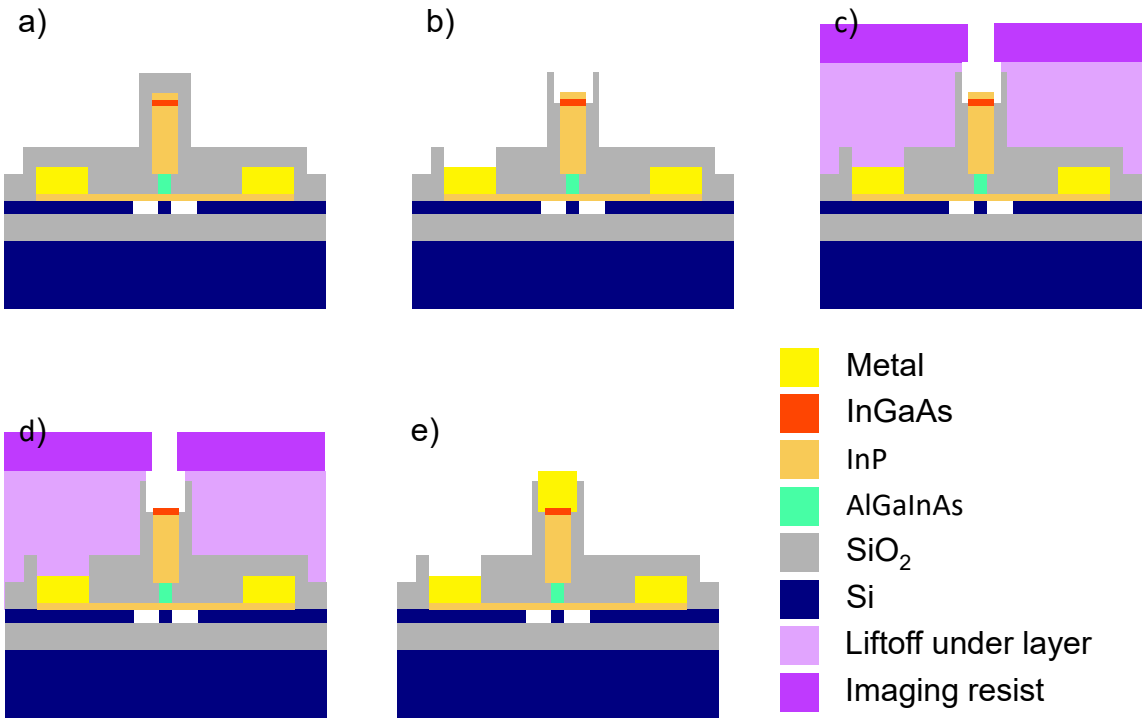

Figure 3.14: The via and p-contact metal process flow for the heterogeneous transition section, showing the conformal via process. Figure a) shows the device after via oxide deposition; b) after the via etch; c) after application of the p-contact liftoff lithography development; d) after the p-type sacrificial layer etch; e) after liftoff of the p-contact metal. Note that the via oxide etch must not be etched past the InGaAs contact, or else the sacrificial layer etch will attack the p-InP cladding.

The widened via opening after etching is shown in Figure 3.14b. There is a “bat ear” type of cross section in the oxide, which will require that planetary rotation be used in the probe metal deposition step. It can be adequately coated with this method. Figure 3.14c shows the sacrificial layer removal. This is the difficult part of the conformal oxide process: over etching of the via oxide will expose the p-InP cladding to the sacrificial layer removal etch, which can undercut the InGaAs contact. The total amount of allowed over-etch is 150 nm, the sum of the

p-sacrificial layer and p-InGaAs contact thicknesses. This allows for 16% over etch, whereas 10% is normally considered to be a requirement, so it is achievable, but the process must be executed carefully. Typically, the fabricator will etch the wafer in steps, starting with 4 minutes, then etching in 15 second steps until the via is visibly clear, then add on the 10% over etch. This normally takes about 5 minutes. Increasing the thickness of the sacrificial layer would ease this part of the process. SEM inspection and scratching the n-metal TLM pad with a needle are often helpful to ensure that the oxide is completely gone. While only 50 nm is being etched, in theory, which would leave a bit of a connection at the taper tip, normally 3-dimensional structures etch faster in wet chemicals than the planar etch rate would suggest. Subsequently, the p-metal process is shown on the taper tip: liftoff lithography (Figure 3.14c), sacrificial layer etch (Figure 3.14d), and p-contact metal deposition (Figure 3.14e).

A focused ion beam (FIB) cross section scanning electron micrograph (SEM) is shown in Figure 3.15. This is near the end of a taper. The "bat ear" of SiO_2 is visible and despite the large misalignment the taper is still fully covered with the p-contact metal. Note that this device had a damaged n-contact layer due to intentional over etch of the p-mesa dry etch (perfect devices are seldom FIB cross sectioned).

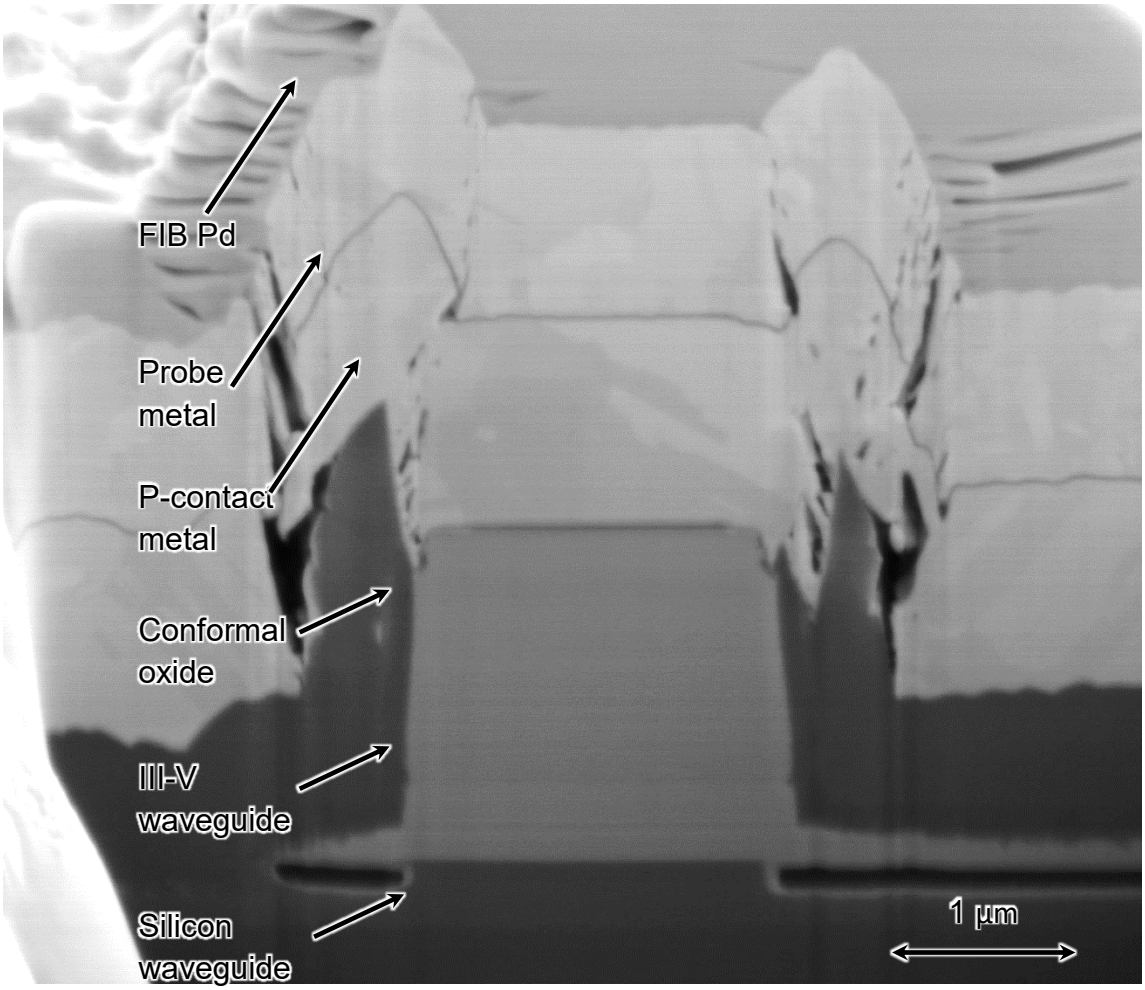

Figure 3.15: FIB SEM cross section near the end of a III-V taper in the heterogeneous transition. Despite suffering from almost 250-nm of misalignment, the p-InGaAs is 100% covered with metal. Adequate coverage of the sidewall with probe metal can also be seen.

The conformal oxide process was important because it allowed the conduction of an experiment to determine whether full metallization of the taper with thick metal is necessary. Two identical 3-section lasers were produced with the contact metal covering all the way to the end of the taper on one laser and the contact stopping 5 μm back from the end of the taper. The result of this experiment is shown in Figure 3.16. There is no impact on threshold current and a small reduction in slope efficiency. This was a 7 QW Epi F laser, so small changes in

loss may not be reflected in the threshold. The conclusion is that there is a small benefit to metallizing the entire taper, but it is likely that a setback of 500 nm would have no impact. Therefore, in the future, it is probably possible to partially abandon the conformal via process in favor of a via design which does not overhang the mesa on the taper to allow for over etching of the oxide without risking the p-InP during the sacrificial layer etch.

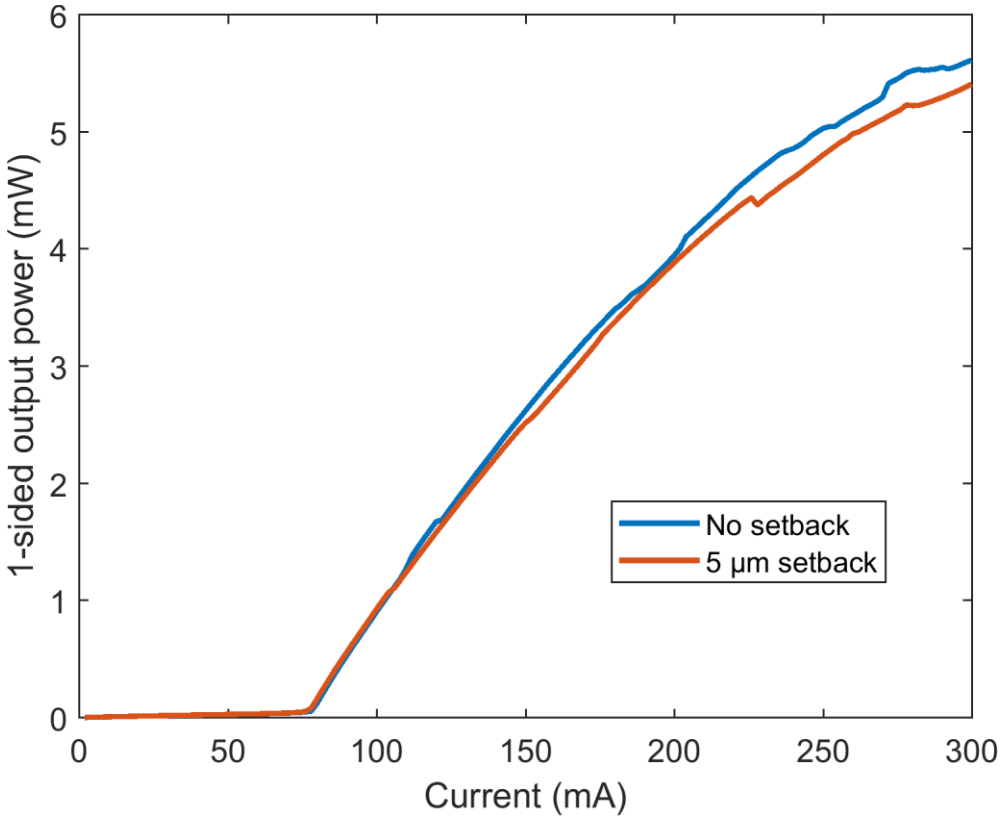

Figure 3.16: LI characteristics of two lasers showing the impact of fully metallizing the taper, and halting the metallization 5 μm from the end of the taper. There is no impact on threshold and a small impact on maximum power.

The selection of the via oxide is an extremely important one. A thick layer is required to prevent absorption loss when the waveguide is routed underneath pad metal–over 400 nm at least–and the conformal via process requires 900 nm, so the film must be fairly thick by thin film deposition standards. The obvious first choice would be plasma-enhanced chemical vapor

deposition (PECVD), which is known for high deposition rate, in the ~2-nm/s range. The UCSB Nanofab has several options for PECVD: two capacitively coupled RIE PECVD systems operating at 300°C, and an inductively coupled (ICP) PECVD which can operate between 50°C and 300°C. All three systems use the same silicon precursor: Silane, SiH_4. Hydrogen is known to contaminate p-type InGaAs [17] and compensate the doping, which is highly problematic for the formation of ohmic contacts. Because of this, it is not advisable to use plasma processes that contain hydrogen on the exposed p-InGaAs.

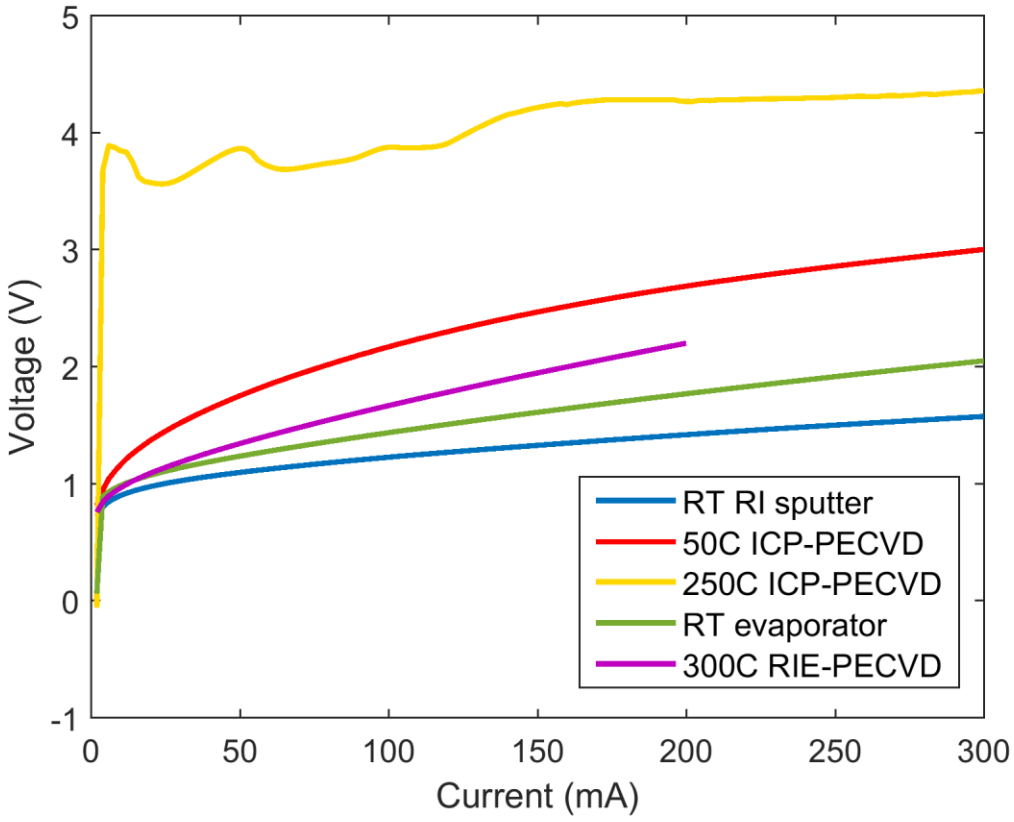

Figure 3.17: IV curves from identical 1 mm long laser diodes fabricated in similar processes, with various deposition techniques used for SiO_2 deposition on the exposed p-InGaAs. All devices used the same process tool for the p-mesa etch hard mask and the oxide via except for the "Evaporated" curve, which used electron beam evaporator #2 for the hard mask and reactive ion (RI) sputter #3 for the via oxide. RT stands for "room temperature,"

although the substrate temperature was not controlled and probably reached 80°C due to heating from exposure to the deposition source

Exposure of the p-InGaAs contact to hydrogen in PECVD machines, for either the p-mesa hard mask or the via oxide, can degrade the forward IV characteristic of the laser diodes, which degrades the wall-plug efficiency of the devices, or prevents them from operating at all. The effect of the various SiO_2 deposition techniques is shown in Figure 3.17. The high temperature ICP PECVD, which operates at higher pressure than the RIE PECVD, created the largest disturbance, rendering devices that were practically open circuit upon screening. The strange shape to the IV curve on the 250°C ICP PECVD curve is due to self-heating in the device annealing away the hydrogen contamination. A second IV sweep will look more like the 50°C ICP PECVD curve, which exhibits a "slow turn on" characteristic that indicates a non-ohmic contact. The RIE PECVD simply has higher resistance, indicating that it is ohmic but still has reduced carrier concentration in the p-type InGaAs. The evaporated hard mask has slightly higher resistance than the sputtered hard mask even though the evaporator does not use hydrogen as a process gas. This could be because the sputtered film is densified by the RF substrate bias, which may help prevent the diffusion of hydrogen through the hard mask during the MHA process. The difference in resistance is not large and may simply be due to process variation.

On native substrate devices, the hydrogen can be driven out with a high temperature anneal. >450°C, to restore the conductivity. This will degrade the optical performance of heterogeneous lasers due to mismatched thermal expansion of the two materials at the bonded interface. To test the thermal sensitivity of these lasers to thermal annealing, completed laser chips were produced with no hydrogen implantation, since this may also be altered by

annealing. These lasers have 14 μm-wide "implanted style" mesas, but the implant process was skipped. The standard contact anneal, 350°C for 30 seconds was sufficient to produce low enough operating voltage that the laser threshold could be achieved, as shown in Figure 3.18a. Annealing the device at 420°C for 2 minutes causes the threshold, slope efficiency, and below threshold spontaneous emission to deteriorate. Above threshold, the 420°C annealed laser has less than half the output power at the same drive current. At the same time, the "high turn on" in the IV curve was corrected, as shown in Figure 3.18b). The second kink at around 75 mA is believed to be due to hydrogen contamination forming a thin p- layer at the surface, resulting in a Schottky barrier in addition to the diode turn on voltage. This device used an RIE PECVD hard mask.

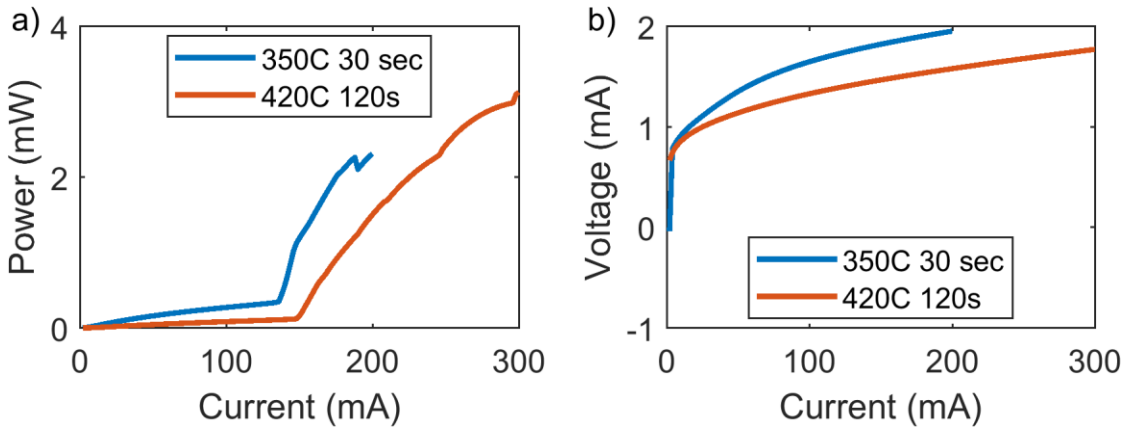

Figure 3.18: Effect of thermal annealing on non-implanted wide mesa lasers. Figure a) shows the LI characteristics deteriorating while the IV characteristic in Figure b) improves.

Three very important lessons can be learned from Figure 3.17 and Figure 3.18. First, hydrogen plasma must be avoided where possible, particularly when the p-doped surface is exposed. Second, high temperature processes should also be avoided. Degradation under rapid thermal annealing at 420°C also means that longer thermal treatment at lower temperatures could degrade the laser, and experiments show that even at 250°C, annealing time should be

limited to 2 hours or less. The bonding anneal, critically, may be degrading the device performance. The third lesson is that the sacrificial layer (20-nm thick in these devices) is too thin to block the in-diffusion of hydrogen. In response, the later epi designs use a 50-nm sacrificial layer. Repeating this experiment with the thicker sacrificial layer would be interesting, and increasing the thickness further may have additional value.

3.4.3. Isolation, implant, probe metal

The remaining fabrication steps are somewhat unrelated and are bunched into this section together for that reason. They are the current channel formation, isolation etch, and probe metallization.

After the contact anneal, the wafer is coated with a cap-on bilayer resist (SPR 955 1.8CM and PMGI SF-15) and flood-expose developed to form the implant pattern. The bilayer resist is used because the imaging resist becomes very difficult to remove after ion implant. The cap-on bilayer process is used to prevent excessive undercut from allowing the protons to reach the n-type InP layer on either side of the mesa. As an added layer of protection, there is 1 μm alignment and lithography tolerance on either side of the mesa. It is unlikely that this un-implanted section allows any leakage current because of the hydrogen passivation from the MHA, the active region undercut, and the limited sheet resistance of the implanted InGaAs. The current channel is not masked with photoresist; instead, the 1500-nm gold layer on the p-contact metal is used for the mask, so that the p-contact metal and the current channel are self-aligned. The cross section in the amplifier is shown in Figure 3.19a. A series of hydrogen implantations are used. The implants are done in order of highest to lowest energy, to prevent the higher energy doses from penetrating deeper than expected due to the disordered material

introduced by the lower energy doses. The wafer is rotated 7° through the plane formed by the normal vector of the wafer surface and the propagation direction of the amplifier waveguide to reduce channeling. The implants are performed at room temperature by Leonard Kroko, Inc. The implantation schedule is shown in Table 2-2. It is designed to have $2.5 \cdot 10^{18}$ ion concentration in the p-InP and less than $1 \cdot 10^{17}$ cm^3 in the quantum well, as detailed in the dissertation "Silicon Evanescent Lasers" by A. Fang.

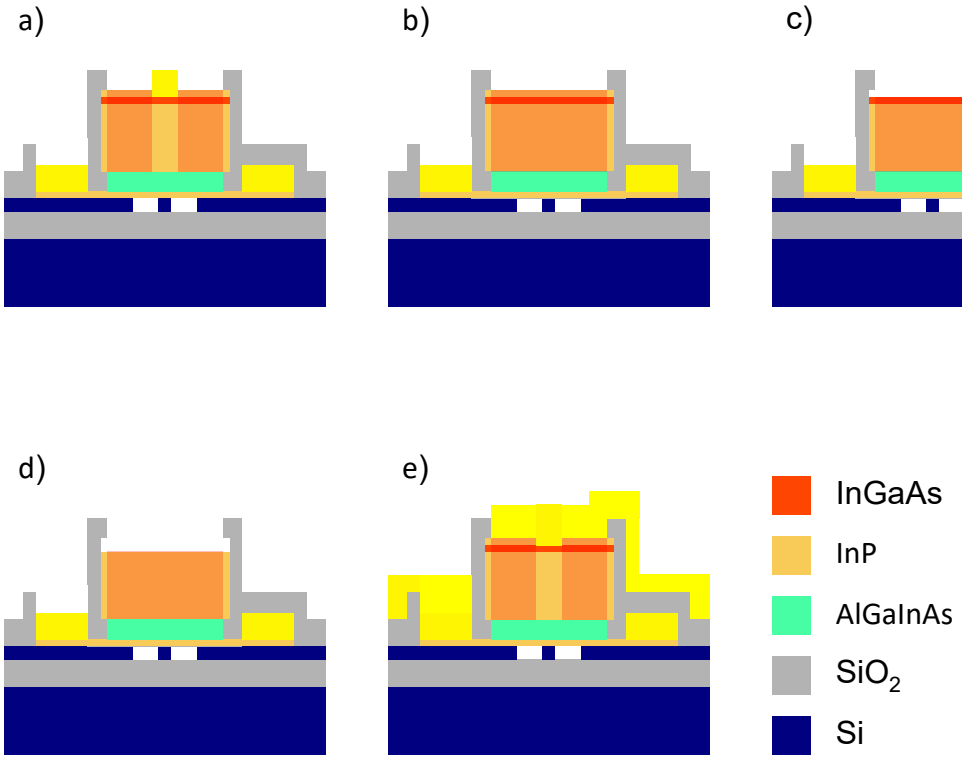

Figure 3.19: The final fabrication steps. Figure a) is the proton implant; b) shows the isolation section during implant; c) is after the isolaton p-sacrificial layer removal; d) is after the isolation InGaAs removal; e) is after the probe metal.

Table 3-2: Hydrogen ion implantation schedule

Implant order	Energy (keV)	Dose ($1/cm^2$)

7	10	$5 \cdot 10^{13}$
6	35	$8 \cdot 10^{13}$
5	70	$9 \cdot 10^{13}$
4	110	$1 \cdot 10^{14}$
3	150	$8 \cdot 10^{13}$
2	170	$8 \cdot 10^{13}$
1	180	$8 \cdot 10^{13}$

For the isolation sections, there is a gap 3 μm wide between the p-contact metal on either side of the saturable absorber. This allows for a 1 μm wide isolation section and 1 μm of tolerance on either side to account for lithography variation. This gap is shown in Figure 3.1Figure 3.19b. A lithography using SPR 955 1.8CM and a 4 minute O_2 descum open the isolation section, which is then etched in 1:2 HCl:H_2O for 2 minutes to remove the sacrificial layer (Figure 3.19c). HCl undercuts the photoresist rapidly, however. The sacrificial layer underneath the p-contact metal has already been etched, so the HCl will not lift off the p-contact metal, but it does defeat the adhesion of the photoresist, allowing the subsequent H_3PO_4 etch to undercut the InGaAs p-contact and lift off the p-contact metal. To prevent this, the photoresist should be stripped and the lithography repeated. Then a 1:5:15 H3PO4:H2O2:H2O etch for 40 seconds is used to remove the InGaAs in the isolation section (Figure 3.19d). The etched and implanted isolation section provides about 10 kΩ/μm, while implanted only isolation sections provided only 10 Ω/μm. This is because the p-InGaAs is only rendered partially insulating by the proton implant.

The final step is the application of the probe pad metal. This must be conformal over the side of the mesa and the oxide bat ear, so the planetary rotation system is used in E-beam evaporator #4. For liftoff to be successful, a simple bilayer resist scheme is used, once again with PMGI SF-15 and SPR 955 1.8CM. The simple bilayer resist develops the imaging resist with 2.38% TMAH developer, and is left in the developer for an extra 1.5 minutes. The

developer isotropically etches the PMGI, leaving a large undercut, 3 μm or more. This prevents the coating of the underlayer resist by the conformal planetary deposition. The minimum space between probe metal pads, however, must be quite large to avoid being lifted off during the single-step development. Normally 10 μm is used as a safe minimum.

3.4.4. Discussion and Outstanding Issues

The process outlined in the previous sections is very mature, and high yield fabrication is possible under normal circumstances. There are still a few intermittent problems that occasionally take down an entire chip at once, and a few opportunities to potentially realize higher efficiency lasers.

Normally the electrical contacts are to blame when an entire wafer fails, and four times out of five, it is the p-type contact that fails. This is generally because the positive charge carrier– the hole–has much higher effective mass than the electron. P-type semiconductors also are commonly susceptible to hydrogen contamination, which is very common. Switching to a reactive ion sputtered hard mask could help protect the p-InGaAs from hydrogen contamination during the p-mesa etch. It may be possible to lift off a sputtered hard mask if the chip was aimed at the gun. Dry etching a moat around the mesa and then wet etching the bulk of the p-InP with a wet etch would allow dry etching the hard mask without attacking the bond-fail regions. Ion-assisted electron-beam evaporators exist, which would be ideal, but the UCSB Nanofab does not have such a machine.

Contamination of the Pd source used for the p-type Pd/Ti/Pd contact is a common hypothesis for a failed contact, and indeed, Pd does form an opaque green oxide layer. The impact of this has not been addressed in literature. As mentioned in Section 3.4.2, switching to

Pt/Ti/Pt may help resolve this problem, as Pt does not form a native oxide. Because the p-contact failure is intermittent, it will be hard to prove that it is defeated forever.

Switching to a Cl_2-Ar-N_2 based dry etch for the p-mesa dry etch would also remove some of the hydrogen exposure introduced by the MHA etch. This would require a similar dry-etched moat and wet-etched field to protect the bond-fail silicon areas, as it will etch silicon very quickly. The MHA etch prevents the realization of narrow-mesa lasers by passivating the exposed sidewalls of narrow mesas, and likely is responsible for some of the loss in the heterogeneous transition (see Section 5.2.3). The relative instability of the heated Cl_2 etcher in the UCSB Nanofab prevented this researcher from considering switching, as the MHA etch is highly stable, exhibiting similar sidewall profile and etch rates since the early 90s.

The occasional n-contact failure is usually due to intermittent attack of the germanium allowing the n-contact to be lifted off, as described in Section 3.4.1. Normally a small amount of undercut is present, but occasionally the entire contact falls off and the devices fail. Beyond using acetone and developer for the n-contact liftoff, a slight rearrangement of the process and the addition of another layer of oxide would prevent the germanium from being exposed to the n-contact etch process as well, potentially reducing the incidence of n-contact liftoff. Using the 200°C oven bake allows the n-contact etch to be performed before the n-contact metal deposition, since it eliminates the PMGI bubble issue that would normally occur at the exposed waveguide trench.

Part of dual via process is shown in Figure 3.20. The steps before Figure 3.20a and after Figure 3.20h are not affected. The concept is to rearrange the process so that the n-metal contact can be protected immediately by being encapsulated by the dense sputtered SiO_2, so the mesa and n-contact etches need to be completed before the n-metal contact. However, the silicon

needs to be protected against contamination with gold from the n-contact metal liftoff, so a protective oxide layer needs to be deposited in between the n-contact etch and n-contact metal, which then immediately needs a second layer to protect the germanium. The wafer condition after the active region etch is shown in Figure 3.20a. Instead of the n-metal contact deposition, the n-contact is etched (Figure 3.20b), and then the p-mesa hard mask is removed (Figure 3.20c) and the first 450-nm oxide layer is deposited (Figure 3.20d). The first oxide layer then needs to be etched away to open the n-metal contact region. Thinking ahead, the p-via also needs to be opened, otherwise during the second via etch the p-via will need to be etched for twice as long, which may damage the n-metal, which will be exposed to the dry etch for a long time. Combination of the via mask and the n-metal mask allows this, without needing another mask plate. This is shown in Figure 3.20e. Then, the n-contact metal lithography is performed (not shown), which can now be simple bilayer single step develop for process simplicity since the intrinsic region of the diode is not exposed (Figure 3.20f). Now the second 450-nm layer of oxide is deposited, protecting the n-layer from further chemical processes. The original via mask can now be etched and the process may continue from the via etch step in Figure 3.13g.

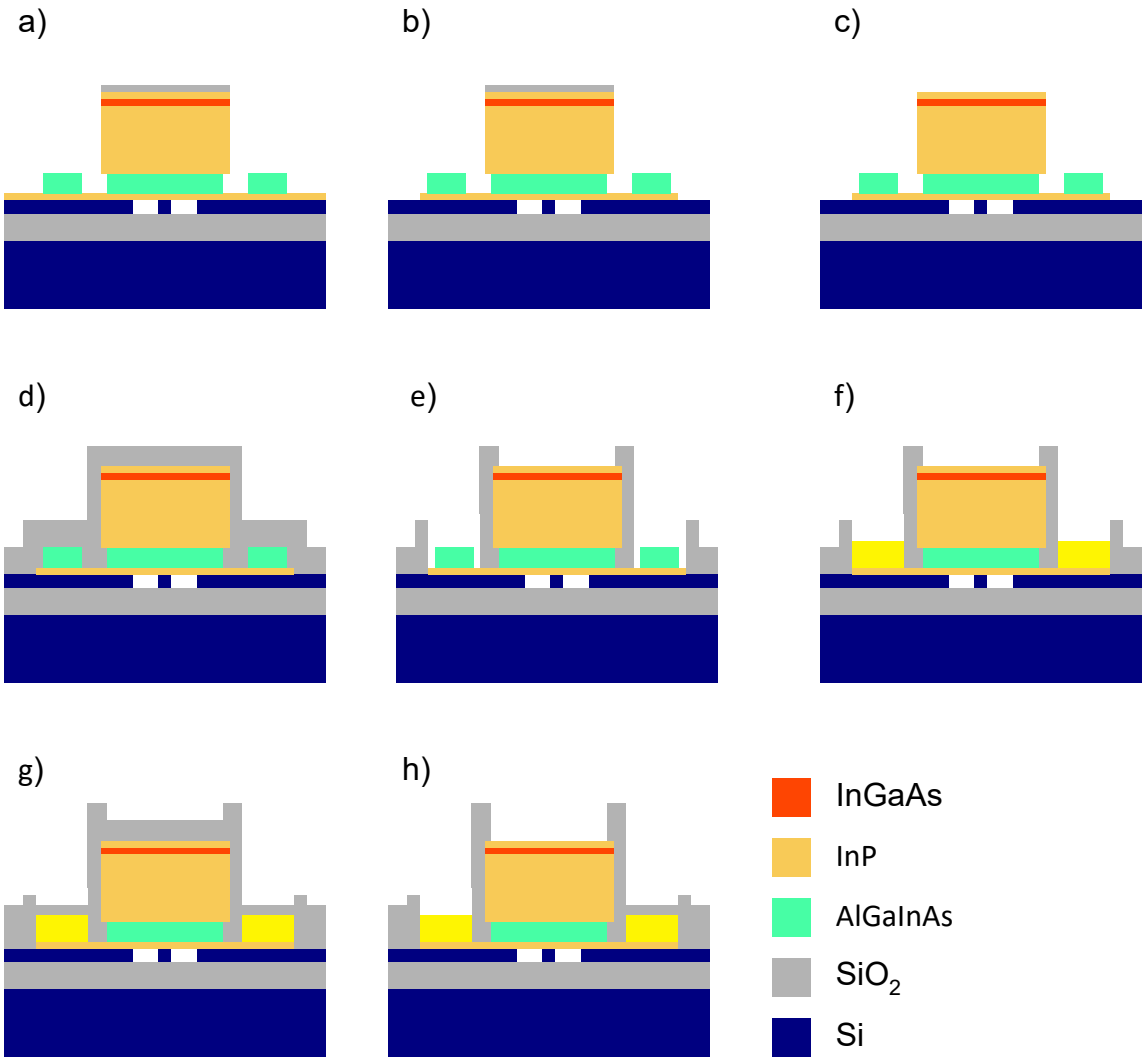

Figure 3.20: Dual via oxide process to avoid n-contact lifting. Figure a) shows the device after the active region etch Figure 3.7d; b) shows the n-contact etch; c) shows the p-mesa etch hard mask removal; d) shows the first via oxide deposition; e) shows the contact opening of via 1; f) shows the n-metal deposition; g) shows the second via oxide deposition; h) shows the via opening.

The additional processing, an extra deposition, lithography, dry etch, ash, and strip exposes the wafer to more chances to accumulate particulate contamination, but the extra processing is after the first via deposition when the waveguide is protected and the impact of particulate

contamination begins to be reduced. In fact, the length of the process before the via oxide is reduced, which could improve yield despite the lengthened overall process. The two via lithographies may impair the conformal oxide process, since now there are two via mask alignments; however, as mentioned in Section 3.4.2, the conformal oxide process could potentially be eliminated.

Much of this process development was conducted before UCSB's deep UV stepper was online, or before thick DUV photoresists were available at UCSB. Consequently, only the processes using thin photoresist were generally done with the DUV stepper: the silicon etches, and the p-mesa hard mask. Because the DUV stepper requires a 100-mm wafer, multiple die bonded wafers were usually separated before the p-mesa dry etch, since that step used to eat an occasional wafer. After the addition of the H_3PO_4 etch before the dry etch to shorten the process, this researcher has run 13 wafers without having RIE #2 eat one, so the wafer can remain together. This, along with the introduction of thick DUV resist, means that much more of the process could be migrated to the DUV lithography system. The DUV lithography tool is specified to have alignment accuracy better than 50 nm, and in practice has been shown to have accuracy better than 25 nm, which eliminates the need for the conformal oxide process completely.

Currently, the active region etch is conducted using PEK 162C DUV photoresist, for the improved alignment accuracy. This photoresist is quite difficult to work with, and it is not recommended to switch to it unless specifically necessary. The Nanofab now stocks UV-26 a thicker formulation of UV-6. The UV-6 resist is very easy to work with, and the thick photoresist processes could likely be migrated to UV-26 without much redevelopment, with the exception of the active region etch and the n-layer etch, which are difficult because

photoresists are often less compatible with InP than they are with Si, and, in the case of the n-layer, the polymerization of the resist in the MHA dry etch complicates removal.

In conclusion, this chapter demonstrated a manufacturing procedure for high yield and high performance integrated circuit lasers. The length of the process has been minimized to reduce exposure to random failures, and to increase the spin rate for more rapid development of experimental characterization. There are a few remaining problems with the fabrication that may be able to be resolved without an excessive amount of effort

References

[1] T. Barwicz, C. W. Holzwarth, P. T. Rakich, M. A. Popović, E. P. Ippen, and H. I. Smith, "Optical loss in silicon microphotonic waveguides induced by metallic contamination," *Appl. Phys. Lett.*, vol. 92, no. 13, p. 131108, 2008.

[2] Y. J. Hung, S. L. Lee, B. J. Thibeault, and L. a. Coldren, "Fabrication of highly ordered silicon nanowire arrays with controllable sidewall profiles for achieving low-surface reflection," *IEEE J. Sel. Top. Quantum Electron.*, vol. 17, no. 4, pp. 869–877, 2011.

[3] D. Liang and J. E. Bowers, "Highly efficient vertical outgassing channels for low-temperature InP-to-silicon direct wafer bonding on the silicon-on-insulator substrate," *J. Vac. Sci. Technol. B Microelectron. Nanom. Struct.*, vol. 26, no. 4, p. 1560, 2008.

[4] J. E. Schramm, "Fabrication of high-aspect-ratio InP-based vertical-cavity laser mirrors using CH4/H2/O2/Ar reactive ion etching," *J. Vac. Sci. Technol. B Microelectron. Nanom. Struct.*, vol. 15, no. 6, p. 2031, 1997.

[5] S. Jain, M. Sysak, M. Swaidan, and J. Bowers, "Silicon fab-compatible contacts to n-InP and p-InGaAs for photonic applications," *Appl. Phys. Lett.*, vol. 100, p. 201103, 2012.

[6] W. K. Chong, E. F. Chor, C. H. Heng, and S. J. Chua, "(Pd, Ti, Au) - Based Ohmic Contacts to p- and n-doped In0.53Ga0.47As," *Compd. Semicond. 1997*, vol. 156, pp. 171–174, 1998.

[7] E. F. Chor, D. Zhang, H. Gong, W. K. Chong, and S. Y. Ong, "Electrical characterization, metallurgical investigation, and thermal stability studies of (Pd, Ti, Au)-based ohmic contacts," *J. Appl. Phys.*, vol. 87, no. 5, pp. 2437–2444, 2000.

[8] H. Kim, I. Kim, J. S. Yu, S. H. Kim, and T. I. Kim, "PtTiPtAu and PdTiPtAu ohmic

contacts to p-InGaAs," *Compd. Semicond. 1997. Proc. IEEE Twenty-Fourth Int. Symp. Compd. Semicond.*, pp. 175–178, 1998.

[9] T. C. Shen, G. B. Gao, and H. Morkoc, "Recent developments in ohmic contacts for III-V compound semiconductors," *J. Vac. Sci. Technol. B*, vol. 10, no. 5, pp. 2113–2132, 1992.

[10] A. . Baca, F. Ren, J. . Zolper, R. . Briggs, and S. . Pearton, "A survey of ohmic contacts to III-V compound semiconductors," *Thin Solid Films*, vol. 308–309, pp. 599–606, Oct. 1997.

[11] P. Jian, D. Ivey, R. Bruce, and G. Knight, "Ohmic contact formation in palladium-based metallizations to n-type InP," *J. Electron. Mater.*, vol. 23, no. 9, 1994.

[12] A. Szerling, P. Karbownik, A. Łaszcz, K. Kosiel, and M. Bugajski, "Low-resistance p-type ohmic contacts for high-power InGaAs/GaAs-980nm CW semiconductor lasers," *Vacuum*, vol. 82, no. 10, pp. 977–981, 2008.

[13] P. Ressel, K. Vogel, D. Fritzsche, and K. Mause, "Nonalloyed ohmic contacts for p+-type InGaAs base layer in HBTs," *Electron. Lett.*, vol. 28, no. 24, p. 2237, 1992.

[14] A. M. Crook, E. Lind, Z. Griffith, M. J. W. Rodwell, J. D. Zimmerman, A. C. Gossard, and S. R. Bank, "Low resistance, nonalloyed Ohmic contacts to InGaAs," *Appl. Phys. Lett.*, vol. 91, no. 19, pp. 3–5, 2007.

[15] G. Kurczveil, P. Pintus, M. J. R. Heck, J. D. Peters, and J. E. Bowers, "Characterization of Insertion Loss and Back Reflection in Passive Hybrid Silicon Tapers," *IEEE Photonics J.*, vol. 5, no. 2, pp. 6600410–6600410, 2013.

[16] G. Kurczveil, M. J. R. Heck, J. D. Peters, J. M. Garcia, D. Spencer, and J. E. Bowers, "An integrated hybrid silicon multiwavelength AWG laser," *IEEE J. Sel. Top. Quantum*

Electron., vol. 17, no. 6, pp. 1521–1527, 2011.

[17] M. Moehrle, “Hydrogen passivation of Zn acceptors in InGaAs during reactive ion etching,” *Appl. Phys. Lett*, vol. 56 (6), no. February 1990, pp. 542–544, 1989.

Chapter 4

Amplifier Waveguide

The core of any laser device is the optical amplifier waveguide. It is the single most critical aspect of the entire design, as it contains the gain material, current injection, carrier confinement, optical confinement, and electrical contact structures. It is simultaneously an optical and electronic device. High-wall-plug efficiency, which is highly desirable in practical applications, is defined as $\eta_{wp} = P_{opt}/P_{elec}$. High optical power, P_{opt}, relies on low material transparency, low waveguide loss, and high differential gain. Minimal electrical power consumption, P_{elec}, at the laser operating condition will require high gain and low waveguide loss to reduce threshold, high slope efficiency for low bias current, and on low device series resistance and turn-on voltage. The purely electrical characteristics are often in opposition to high optical performance, specifically the waveguide loss, as increasingly conductive epitaxial layers have increased absorption due to free carrier and inter-valence band absorption [1]–[6].

One of the objectives of this work is to produce as high output power as possible, which is normally interchangeable with a high wall-plug efficiency laser, as output power is limited in long-wavelength lasers by self-heating [7]. Lasers with high slope efficiency will then reach

higher power before the thermal rollover point, and reduced operating voltage will delay the onset of the rollover. With that in mind, the design process can follow these steps:

- Create a device cross section which supports a single transverse mode, or is at least quasi-single mode (only one mode has positive net gain) in the lowest order fundamental mode. This is crucial as the subsequent passive circuits can usually only be designed to operate correctly on one mode, and the eventual output coupling–be it to a free-space collimating lens or an optical fiber–will be very inefficient for higher order modes. The device cross section should keep the thermal constraints in mind, because the waveguide is also part of the current injection structure and must be able to dissipate heat. Using an extremely narrow waveguide will increase the series resistance R_s and thermal impedance Z_t.
- Select a gain material which will provide the highest performance for the given application. For lasers in general, this will depend on the operating temperature and the desired cavity length, since higher numbers of wells are optimal for high temperature operation [8], and lower numbers of wells are optimal for very long cavities such as pump lasers where J_{tr} can limit the threshold current. In the case of mode-locked lasers, this means maximizing the gain coefficient, as operation at low confinement factor may be required to minimize gain saturation [9], and minimizing the linewidth enhancement factor, since the convolution of optical lines will define the minimum passively mode-locked RF linewidth.
- Design the optical waveguide to maintain the desired confinement factor in the quantum well and to have as low propagation loss as possible while maintaining quasi-single mode operation.

- Consider how the heterogeneous transition is affected by the previous design stages. An integrated laser must have a transition from the amplifier to a fully passive waveguide to reap the benefits of integration, and so the transition must have low loss, low reflection, and low parasitic higher-order-mode emission. This criterion will be covered in more detail in Chapter 5.

4.1. Cross Section

The cross section is dictated partially by the fabrication technology employed to introduce the III-V epi layers. The prevailing methods fall broadly into two categories: those directly bonded to Si, and those bonded to a planarizing interlayer, such as the polymer divinylsiloxane-bis-benzocyclobutene (DVS-BCB) or chemical-mechanically polished silicon dioxide (SiO_2) [10]. Directly bonded devices may be bonded through a hydrophobic process, sometimes referred to as wafer fusion, allowing for conduction through the layers [11], or by hydrophilic bonding, which utilizes a thin oxide layer—normally only a few nanometers thick—to attach the heterogeneous materials [12]. Low temperature hydrophilic bonding is typically accomplished with an oxygen plasma activation to form the thin oxide layer, and allows bonding of materials with larger mismatch of the coefficient of thermal expansion. This method is widely used since InP and Si have a considerable mismatch in their coefficients of thermal expansion. For comparison, hydrophobic bonding in [11] required a bonding anneal temperature of 650°C, while hydrophilic bonding of InP to Si is normally conducted at 300°C. Bonding with DVS-BCB can also be conducted at low temperatures, such as 280°C [13]. High process temperatures degrade Si/III-V light emitting devices rapidly, except in the case of thin films [14].

For high output power applications, the directly bonded approach is superior because of increased thermal contact between the laser mesa and the thermally conductive silicon device layer. Interlayer bonded materials normally suffer a penalty in thermal performance because of the low thermal conductivity of common interlayer materials.

Direct bonding introduces a design complication of its own. The thickness of the silicon layer is fixed by the heterogeneous transition at 500 nm. Since the waveguides are in very close proximity, it creates large coupling between the unperturbed modes of the two waveguide systems. This is advantageous for the heterogeneous transition, but it creates essentially a directional coupler, and the device will support two modes. This is displayed in Figure 4.1: the symmetric mode in Figure 4.1a and the antisymmetric mode in Figure 4.1b. The waveguides depicted in Figure 4.1 are 1-μm wide. Decreasing the thickness or width of either waveguide will not eliminate the antisymmetric mode until one of the waveguides is impractically small. Several attempts were made to produce such narrow waveguide devices and all led to failure. The principle reason was electrical, since the narrow P-type InP mesa was electrically degraded by the mesa dry etch (see Section 5.2.3). Even after repairing this with a burn-in process, the antisymmetric mode had higher confinement factor than the symmetric mode, and with no overlap with a mode in the silicon waveguide, it was radiated in the heterogeneous transition.

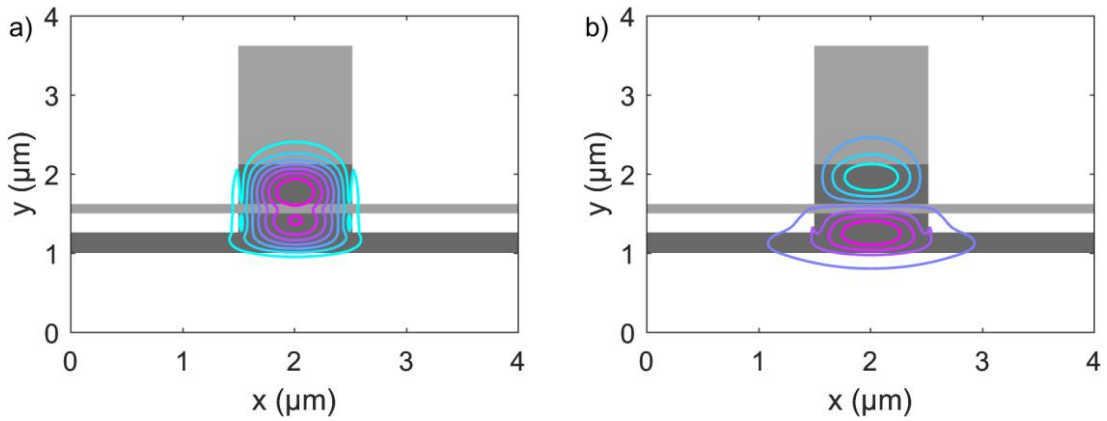

Figure 4.1: Cross section of a hypothetical twin waveguide, with a silicon rib underneath and a III-V waveguide, with current injection layers, on the top. Index is qualitatively shown as the gray scale background (darker represents higher index), and the contours are the E_x field. a) symmetric mode and b) antisymmetric mode of the coupled waveguide.

The behavior of modes in twin waveguides offers a solution to this problem. The silicon waveguide has an effective index n_{eff} = 3.2 in a typical 500-nm-tall 800-nm-wide waveguide, while the III-V waveguide shown in Figure 4.1 in the absence of the silicon waveguide has n_{eff} = 3.15, due to the lower index of the III-V quaternaries used in typical laser waveguide cores: 3.38 in this case, compared to silicon at 3.47. In a twin waveguide system, the antisymmetric mode will have larger confinement in the lower effective index waveguide, in this case the III-V waveguide. By manipulating the widths of the two waveguides, specifically widening the III-V mesa, the antisymmetric mode can be expanded so that its overlap with the symmetric mode is reduced. This reduces directional coupling by increasing the mismatch between the propagation constants of the waveguides. Furthermore, if the carriers can be confined to the central region of the mesa, then the relative confinement factor in the pumped region can be much larger for the symmetric mode than the antisymmetric mode. Figure 4.2a shows the

tightly confined symmetric fundamental mode, while Figure 4.2b shows the now enlarged antisymmetric mode.

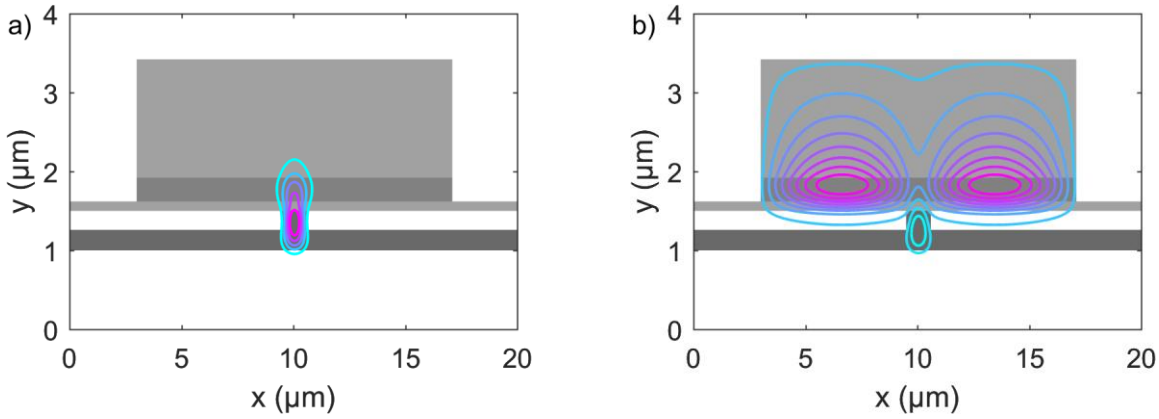

Figure 4.2: Cross section of the hypothetical twin waveguide, with widened III-V mesa to expand the antisymmetric mode. Index is shown as the gray scale background, and the contours are the E_x field of the (a) symmetric mode and (b) antisymmetric mode of the coupled waveguide.

The III-V mesa is now expanded to be relatively large, and in addition to the antisymmetric mode, there are several even symmetric higher-order transverse modes that may have some overlap with the pumped region. As long as the silicon waveguide is kept below a certain width, the higher order modes will be mostly confined in the III-V waveguide. The addition of a waveguide trench design, where the un-etched silicon slab is brought underneath the III-V mesa, can further reduce the impact of the higher order modes in the III-V waveguide by coupling them to radiation modes in the waveguide slab. Figure 4.3a shows the still tightly confined higher order mode, and Figure 4.3b shows the leaky antisymmetric mode. Oscillating electric field profile in the cladding layer signifies large coupling to radiation modes. In this case the loss is extremely high, over 1 dB/um. All the higher order transverse modes have similar coupling to radiation modes and spread-out mode profiles. The combination of the

mode expansion (to reduce confinement factor), and radiation loss (to reduce the net gain of the higher order modes) results in a waveguide which is resolutely quasi-single mode.

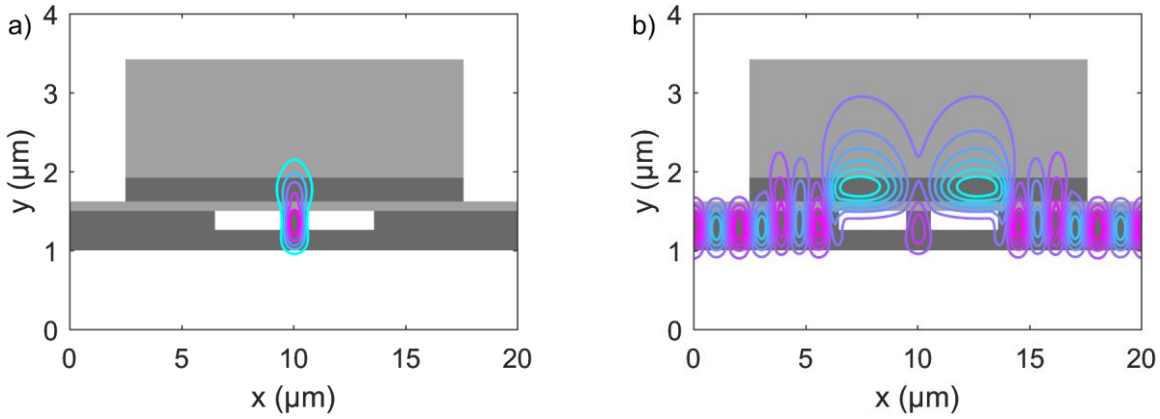

Figure 4.3: Cross section of the hypothetical widened twin waveguide, with the silicon slab introduced to cause radiation in the antisymmetric mode. Index is shown as the gray scale background, and the contours are the E_x field of (a) symmetric mode and (b) antisymmetric mode of the coupled waveguide.

Increasing the width of the III-V waveguide has a few other effects which bear mentioning. It can now have an extremely wide P-contact, which reduces the electrical resistance. The wide III-V waveguide also acts as a heat sink, and has increased contact with the thermally conductive silicon slab. The increased width does increase the transparency current by increasing the volume of gain material that must be pumped. This can be addressed by using a hydrogen ion implantation to selectively increase the resistance of the P-type InP [15]. This is shown schematically in Figure 4.4. Now that the sides of the mesa are not pumped with carriers, any higher order mode with significant overlap in that region will have interband absorption loss, suppressing them even further.

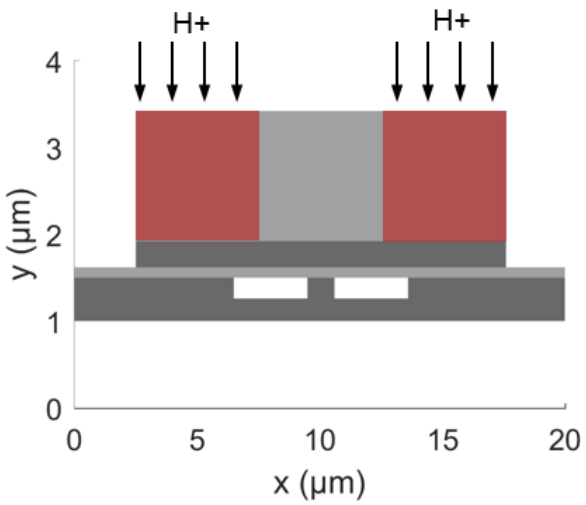

Figure 4.4: Hydrogen implantation of the III-V mesa for current isolation.

With this method, a waveguide which allows for quasi-single mode operation and has low electrical and thermal resistances can be produced for the amplifier waveguide. The III-V slab can be wide and still only lase in a single transverse mode because of the lateral index confinement afforded by the silicon waveguide. Then the carrier profile can be controlled by the dimensions of the hydrogen implantation, giving the designer an additional degree of freedom over single waveguide systems.

4.2. Quantum Wells

The design of the quantum well in heterogeneous silicon/III-V lasers is not fundamentally different from the design of quantum wells in InP substrate III-V lasers, since the structure is grown epitaxially on an InP substrate. Therefore, one can simply copy the design of a quantum well from an optimized InP substrate laser and expect to have high performance, as long as the additional zinc diffusion due to the structure being grown upside down can be properly accommodated for in the growth (Landmark Optoelectronics, the grower used in this work, can perform this adjustment). At the telecommunications wavelengths (1310 nm and

1550 nm), the designer has several options for gain region materials: the most mature InGaAsP quantum well, the AlGaInAs quantum well, the GaInNAs quantum well, and the InAs quantum dot. GaInNAs has the advantage of being grown on a GaAs substrate and can thus employ extremely wide bandgap AlGaAs layers for vertical carrier confinement, but is complicated by the growth of dilute nitride materials. Although it has been shown to have high performance and reliability [16], it has not been widely adopted and is unavailable from commercial growers. It also has only shown high performance in the 1310-nm band. Quantum dots are an emerging technology that may be of considerable interest for mode-locked laser applications. Currently the shortest pulse on-chip mode-locked laser diode ever demonstrated is 312 fs, from a single section quantum dot mode-locked laser [17]. Like GaInNAs, the technology is less mature, but is beginning to be available from commercial growers. Due to the nature of the quantum dot growth, the surface roughness is elevated compared to quantum wells, which will create difficulty for direct bonding.

This leaves InGaAsP and AlGaInAs quantum wells. InGaAsP is more mature and offers a larger wealth of information in the literature to allow for more accurate quantum well design, but AlGaInAs reportedly has higher differential gain and lower linewidth enhancement factor [18]. It is most famous for having larger conduction band offset than InGaAsP, which allegedly increases the high temperature performance [7]. While this is fairly well accepted at 1310-nm wavelength, it does not seem to have much of an advantage at 1550-nm wavelength. This is likely due to the fact that at 1550 nm the hole well is extremely shallow, which may allow holes to thermally escape.

For mode-locked laser applications, AlGaInAs has a clear advantage. Due to the aforementioned hole well depth, the recovery time of the saturable absorber is reduced

significantly, by a factor of 5 [19] compared to InGaAsP. This, coupled with a reduction in linewidth enhancement factor [18], results in considerably better mode-locked laser performance in the pulse width and line width metrics, as shown in Section 2.1. For these reasons, AlGaInAs was chosen as the quantum well material for this work.

To design a laser quantum well, the designer must first select a desired photoluminescence wavelength. The proximity of the photoluminescence wavelength to the operating wavelength depends on the application. Higher gain coefficient, a fitting parameter described in Chapter 4 which represents the rate of increase in gain versus the increase in current or carrier density, can be found near the photoluminescence peak, along with increased propagation loss. A short-cavity, directly modulated laser would be designed to operate near the photoluminescence peak, but long-cavity high-output-power lasers will tend to have better performance red-shifted by 20 nm or so from the photoluminescence peak, due to lower propagation loss. Lasers that are intended to have a wide operating wavelength range, such as mode-locked lasers and tunable lasers, operate primarily on the red side of the photoluminescence wavelength peak.

Once the operating wavelength is set, the depth of the quantum well is selected. This will determine the number of bound electron energy levels in the well. The quantum well should be as deep as possible to reduce thermal carrier escape, but shallow enough that only a single state is bound to prevent band-to-band recombination at the higher energy level. The well depth is the flat-band difference between the conduction band energy level in the quantum barrier and the quantum well conduction band. The best performing lasers in literature [20] normally have quantum wells around 6 nm in thickness, so then the designer should only change the depth of the well. The flat-band well depth used in this work is 0.1 eV.

Then, the designer must determine the well and barrier alloy compositions. The AlGaInAs quaternary can access a broad range of energy-band gaps and lattice constants, as shown in Figure 4.5. The band gap and lattice constant for the three binaries, AlAs, GaAs, and InAs are shown as blue circles. The ternary alloys InAlAs, AlGaAs and InGaAs are represented by black lines. The quaternary may have any band gap and lattice constant combination enclosed by the lines; however, the most relevant alloy compositions are those which are lattice matched or nearly lattice matched to InP. Selection of the quantum well alloy is done by first adjusting the quantum well band gap–while remaining latticed matched to the substrate–to the desired energy level, in this case 0.8 eV (shown by the arrow marked "a" in Figure 4.5). The alloy is then adjusted to produce the desired strain. Quantum well lasers are almost always compressively strained, which reduces carrier-dependent loss introduced by intervalence band absorption from the hole population injected into the quantum well [3]. Most experimentally developed diode lasers using the AlGaInAs quaternary use between 0.8% and 1.5% compressive strain, for example: 1.37% [20], 0.8% [21], 1.44% [8]. This work primarily used 1% strain. The strain is introduced by a modification to the lattice constant, which can be applied to quaternary materials without changing the energy gap, as shown in Figure 4.5 as the arrow marked b). Typically, the barrier is tensile strained to compensate for the compressive strain in the barrier. The strain does produce a small change in the valence band energy of both the barrier and the well.

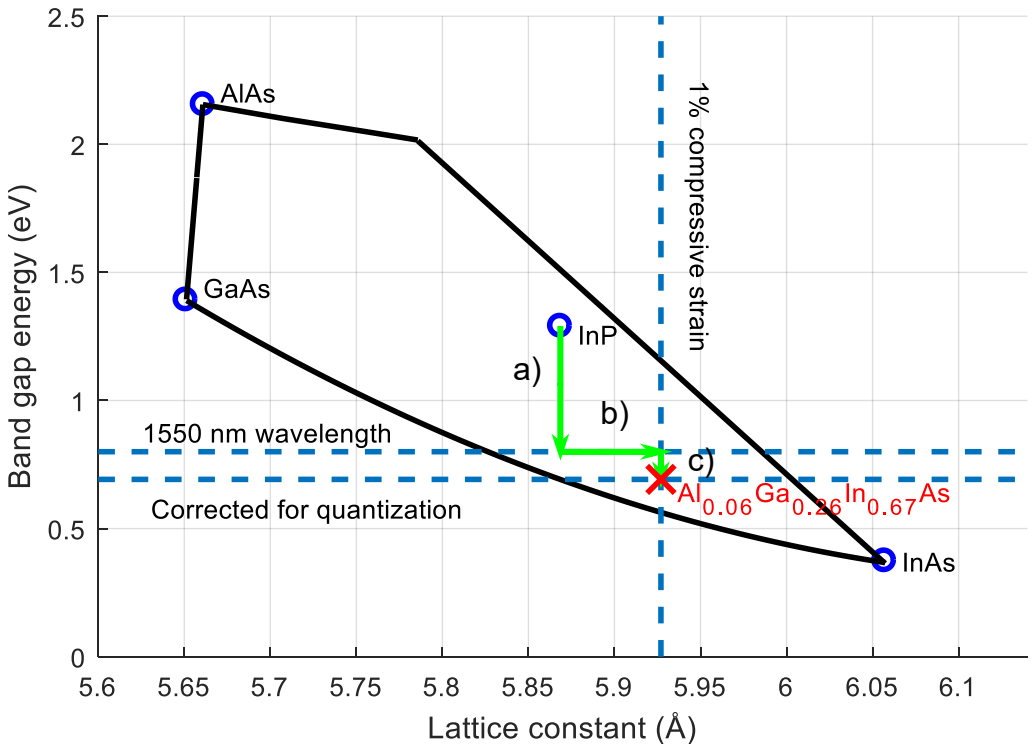

Figure 4.5: Band gap versus lattice constant for the AlGaInAs system. Figure reproduced from [22].

Finally, the energy gap of the quantum well must be adjusted slightly downward to compensate for the quantization effect. Since the lowest bound state in the electron well has higher energy than the conduction band, another adjustment to the alloy composition, shown as the arrow marked c) Figure 4.5, must be made to achieve the desired lasing wavelength.

In practice, these calculations are somewhat approximate, as the material parameters given in literature for the AlGaInAs system are not all in agreement. The approximate design is usually corrected by the commercial grower, in this case LandMark Optoelectronics.

Once the quantum well and barrier are designed, another design aspect to consider is the number of quantum wells. This is also application specific, as thicker multi-quantum well stacks have increased modal gain coefficient through larger modal overlap with the increased

cross-sectional area of gain material but similarly increased transparency current density due to the larger volume of gain material. This is illustrated in Figure 4.6. Given that the mode field amplitude, shown in the figure plotted to the left of the figure, remains approximately the same, a gain medium with length L and thickness $2t$ (Figure 4.6a) pumped with current I, should have the same amount of material gain as the same gain medium having length $2L$ and thickness t (Figure 4.6b) if it is also pumped with current I.

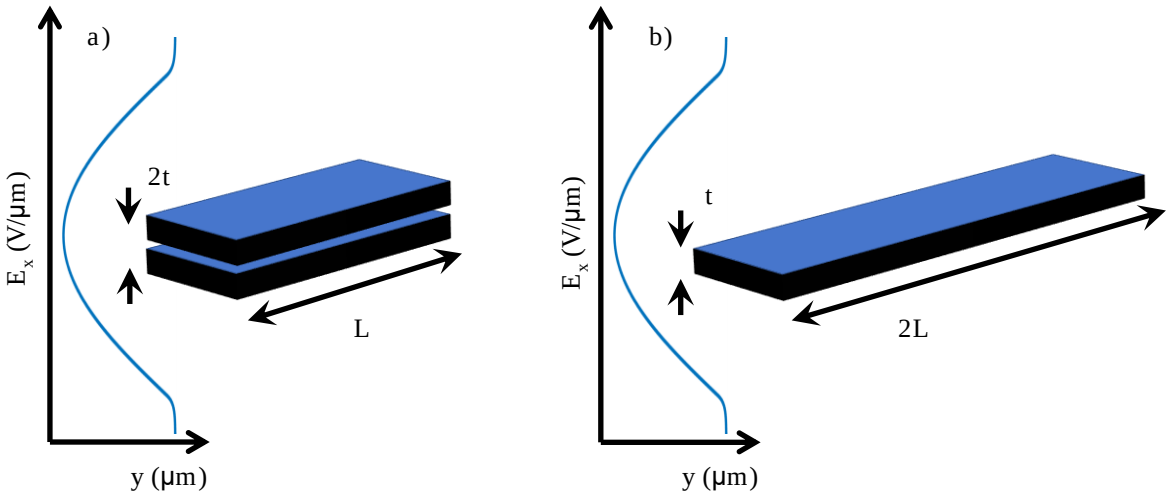

Figure 4.6: Illustration of the dimensions of two hypothetical gain media.

While this seems like a straightforward trade-off, there are three secondary factors to consider. The first is that the overlap with the hole population in the quantum well is an unavoidable source of propagation loss, as intervalence band absorption is still possible. Increased modal overlap in larger numbers of quantum wells increases the propagation loss. The second and third factors arise from similar origins: the electrical series resistance of the diode, $R_s \approx \rho_c / wL$ when it is dominated by the p-contact resistance (as it commonly is), and the thermal resistance $Z_t = h / \zeta wL$, assuming vertical heat flow, both scale inversely with the

mesa width w and length L. In this case ρ_c is the contact resistivity, h is the height above the heat sink, and ζ is the material thermal resistivity.

Because of this, it is normally beneficial in terms of maximum output power and wall plug efficiency to reduce the number of quantum wells and increase the length, since there will be lower operating voltage thanks to reduced series resistance and lower self-heating due to reduced thermal resistance while maintaining low transparency current. The additional benefit of reduced loss from overlap with the carrier population in the quantum wells can increase the laser slope efficiency. There are limits: lower numbers of quantum wells are less capable of compensating for fixed internal losses, and laser designs that call for high mirror loss, such as short cavity lasers, benefit from a higher number of quantum wells. This is shown with a calculation of the gain/current relation for two-quantum well configurations, 3 wells and 6 wells, for a low loss waveguide in Figure 4.7a, and a high loss waveguide in Figure 4.7b. For the low loss waveguide, mirror loss below 10 cm^{-1} provides an advantage in threshold current density for the 3-quantum well structure, while above that value the 6-quantum well device will have lower threshold. For the higher loss waveguide in Figure 4.7b, there is no scenario where the 3-quantum well laser has lower threshold current density. In general, lower internal loss will allow for reduced number of quantum wells.

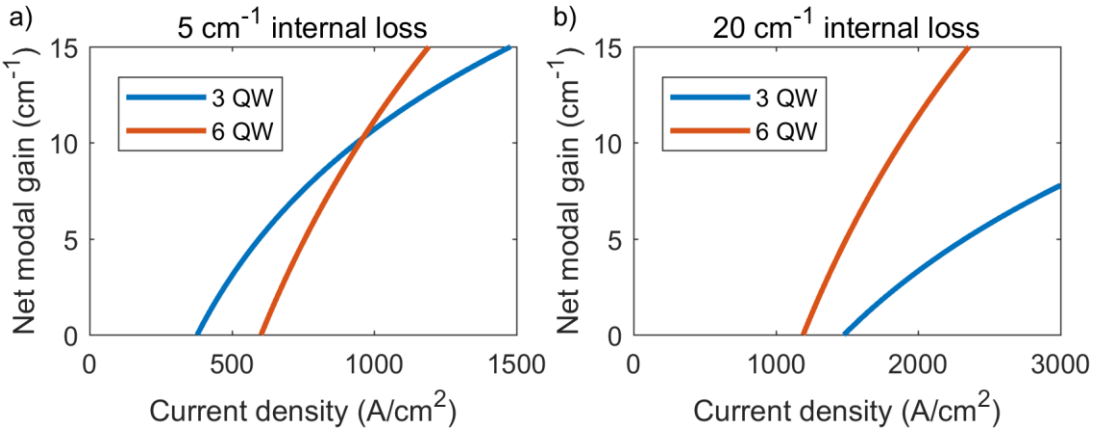

Figure 4.7: Calculation of the gain-current relation between two hypothetical lasers with a) 5 cm^{-1} internal loss, and b) 20 cm^{-1} internal loss.

If other factors are held constant, the lower quantum well laser will have better output power due to the reduced overlap with the lossy quantum well. However, the longitudinal confinement factor must increase–the relative length of the active waveguide to the total cavity length–which increases the total cavity loss in the case of silicon lasers, where the passive waveguide has 5-10 times lower loss than the active waveguide. The principal benefit of reduced quantum wells is that the thermal and electrical resistances can be reduced and provide the same amount of gain.

4.3. Waveguide

The configuration of the III-V layers must be carefully considered for use in a heterogeneous amplifier. Many elements of the design can be copied from monolithic III-V amplifiers, but the effect of the Si waveguide on the optical mode and the inability to extract current through the bonded region with the present level of technology requires modification to the design of the epitaxial waveguide layers.

The addition of the Si waveguide presents the advantage of allowing control of the confinement factor by varying the width of the Si ridge, as the effective index of this portion of the waveguide increases relative to the effective index of the III-V waveguide. This allows integration of low and high confinement factor waveguide sections on a single chip, enabling the combination of high gain and high saturation power amplifiers with low-threshold lasers. Decreasing the confinement factor in the III-V layers will also decrease the propagation loss,

as the mode overlap increases with the low-doped Si. Low-doped silicon typically has very low absorption, which helpful for the production of high slope efficiency lasers.

However, the proximity of the Si, which has relatively high refractive index compared to most InP alloys, requires special consideration. If the indices and thicknesses of the III-V layers are too low, it requires a very narrow or thin Si layer. This increases the scattering loss due to the narrow Si waveguide. Balancing the size of the two waveguides is critical for ensuring high performance. Typical separate confinement heterostructure (SCH) layers in AlGaInAs/InP lasers are often very thin, such as 60 nm used in [23]. Because the III-V waveguide must compete against the high index silicon waveguide, a thicker III-V SCH must be introduced.

The optimization of the III-V SCH layer thickness was carried out by numerical simulation of the transverse optical mode in the gain region waveguide. The confinement factor Γ_{xy} and modal internal propagation loss $<\alpha_i>$ can be extracted from this simulation. Both values vary as a function of waveguide width. These can be used with a known or assumed material gain value to compute the net modal gain coefficient, $g_{\mathrm{net,m}}$, using the following equation:

$$g_{\mathrm{net,m}}(w) = \Gamma_{xy}(w) g_{\mathrm{p,0}} - \langle \alpha_{\mathrm{i}}(w) \rangle \,. \tag{4.1}$$

A value of 1650 cm^{-1} was used for material gain $g_{\mathrm{p,0}}$, which was extrapolated based on small-signal measurements of Fabry-Perot lasers; this represents the maximum attainable gain after an estimation of thermal effects are included, which will produce the worst-case propagation loss from the carrier population in the quantum well. Loss values are computed based on known relationships between the doping level and the absorption in InP [4][24][25]. There is some disagreement in literature [5][3] on the absorption level in the quantum well. Using the value from [1], and calculating the carrier density [28] based on Equation 4.2:

$$N = \sqrt{\frac{J\eta_i}{qN_w t_w B}}, \qquad 4.2$$

while assuming J = 3400 A/cm^2 for the current density (this calculation was done at the bias condition used for maximum gain in a traveling wave amplifier, see Section 4.4), η_i = 0.6 for the injection efficiency, knowing the thickness of the well t_w = 7 nm and the number of wells N_w = 3 from Table 4-2: Epi E, and B = $10 \cdot 10^{-10}$ cm^3/s for the bimolecular recombination rate, the absorption coefficient in the quantum well is calculated to be 83 cm^{-1}.

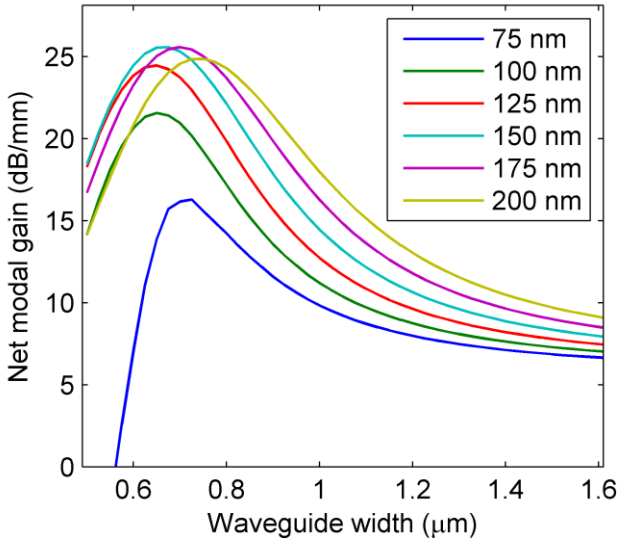

Figure 4.8: Simulated net modal gain as a function of silicon waveguide width, for various thicknesses of the SCH. The legend indicates the thickness of a single SCH layer.

The real refractive indices are calculated using [26] for AlGaInAs and [27] for InGaAsP. The refractive index for the quantum wells and barriers, which are not lattice matched to the substrate, was inferred by comparing measured mode width values to simulations. The net modal gain for a variety of SCH thicknesses versus Si waveguide width is shown in Figure 4.8.

The maximum achievable gain increases with increasing SCH thickness, peaking around 25 dB/mm for the 150-nm SCH.

This is driven mainly by the transverse quantum well confinement factor Γ_{xy}, which increases for decreasing waveguide width and increasing SCH thickness. After 150-nm SCH thickness, the mode expands vertically with the expanding SCH thickness and the confinement factor begins to decline. This is shown in Figure 4.9, along with the confinement factor of the first higher order mode in the 125-nm SCH. The emergence of the higher order mode imposes a minimum value of confinement factor, since the higher order mode will lase first if it has higher confinement than the fundamental mode.

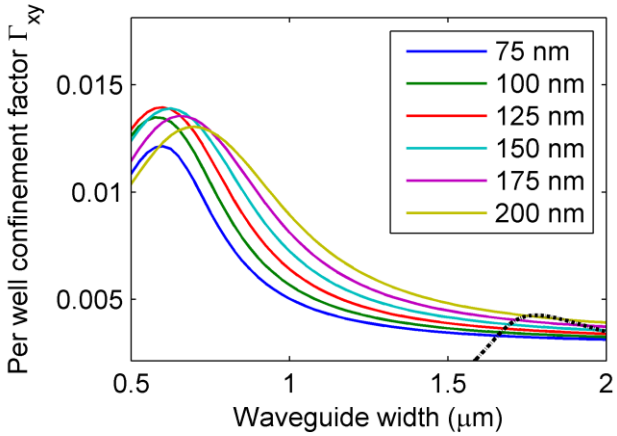

Figure 4.9: Variation in the quantum well confinement factor versus waveguide width for various SCH thicknesses. The confinement factor for the first higher order mode in the 125-nm SCH, TE10, is shown as a black dotted line.

Higher attainable maximum gain in the 150-nm and 175-nm SCH waveguides and lower maximum gain in the 75-nm SCH waveguide in Figure 4.8 are driven by differences in the propagation loss. The total simulated loss for the different SCH designs versus waveguide width is shown in Figure 4.10a (note that the y-axis has a logarithmic scale). The loss increases

dramatically for thin SCH layers and narrow waveguide widths. Figure 4.10b shows the loss contribution from the various sources, considering loss from interband absorption in the InGaAs contact layer, loss from doping in the p- and n-claddings, loss from the carriers in the active region, loss due to radiation into the slab (such as in Figure 4.3b), and the total loss, in a 125-nm SCH waveguide. The loss depends strongly on waveguide width, as the mode expands into the III-V layers when the silicon waveguide is narrow, increasing its overlap with the lossy p-InP and InGaAs layers. The mode leakage begins to increase rapidly below 0.8 μm, and eventually dominates. The loss contributions for a fixed waveguide width (850 nm) are shown versus SCH thickness in Figure 4.10c. The onset of radiation loss increases for larger SCH thickness, since the light is coupled more strongly across the trench. Thinner SCH designs provide less vertical confinement, increasing the loss due to the p-type InP and InGaAs layers. The minimum total loss for this waveguide width comes at 125-nm SCH thickness, so while the net modal gain at narrow waveguides in Figure 4.8 is lower for this SCH design than the 150-nm and 175-nm designs, lower propagation loss is desirable for high slope efficiency lasers, so 125-nm is the value that was chosen.

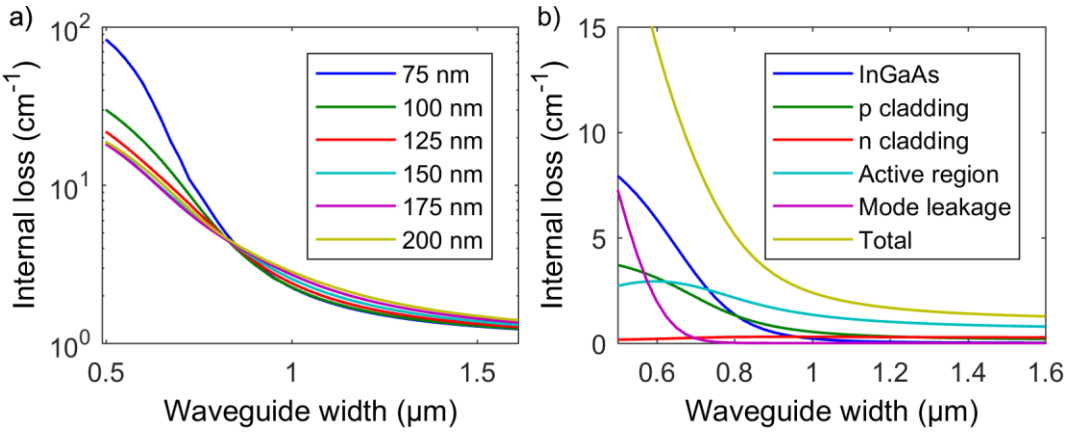

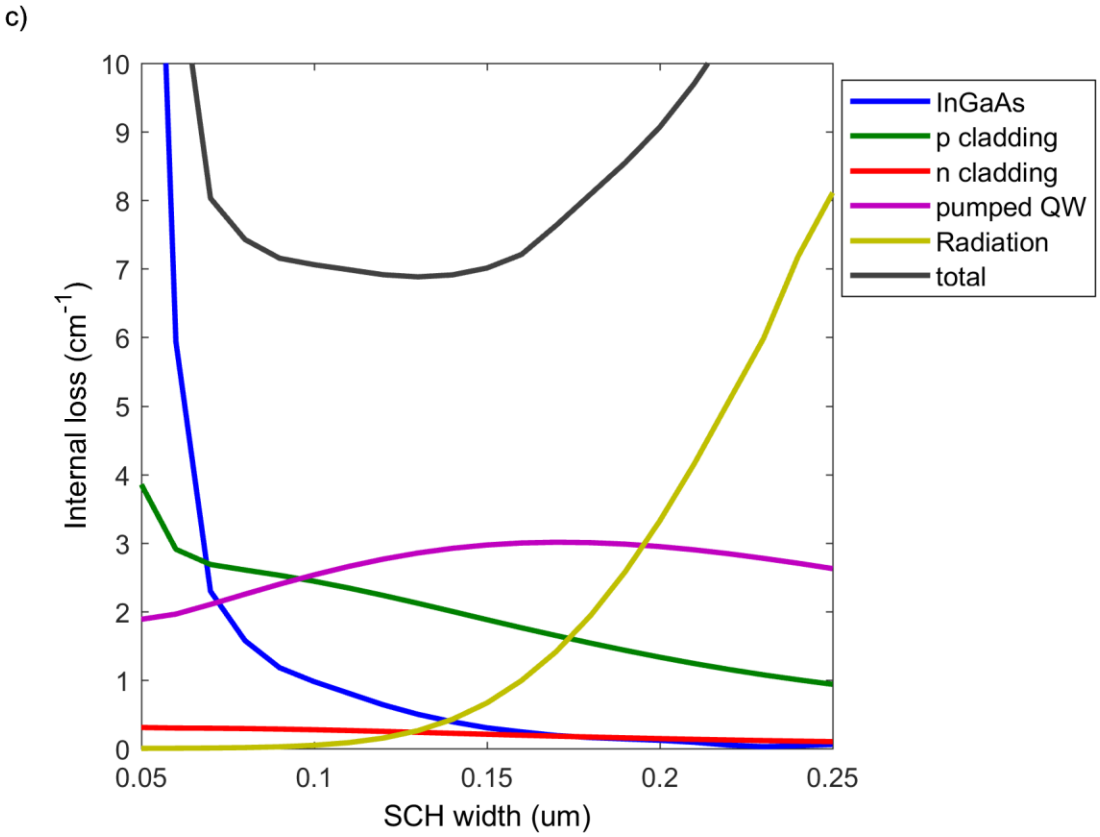

Figure 4.10: Losses for various Si waveguide and III-V SCH dimensions. a) Total loss versus waveguide width for various SCH thicknesses. b) Loss from all sources in a 125-nm-thick SCH versus silicon waveguide width, and c) loss from all sources versus SCH thickness with an 850-nm Si waveguide.

A final factor that must be considered is the minimum attainable confinement. As can be seen in Figure 4.9, thicker SCH layers have higher confinement factor at the onset of multimoding than thinner layers. For amplifier designs where low confinement factor is desired, for example to increase saturated output power or to reduce self-phase modulation in a mode-locked laser, it is worth considering how low a confinement factor can be achieved. This is shown in Figure 4.11. While 150–175 nm has the highest net gain, 125 nm has the

highest attainable difference in confinement factor $\Delta\Gamma_{xy}$. This combined with the generally lower propagation loss led to the selection of 125 nm for the SCH thickness.

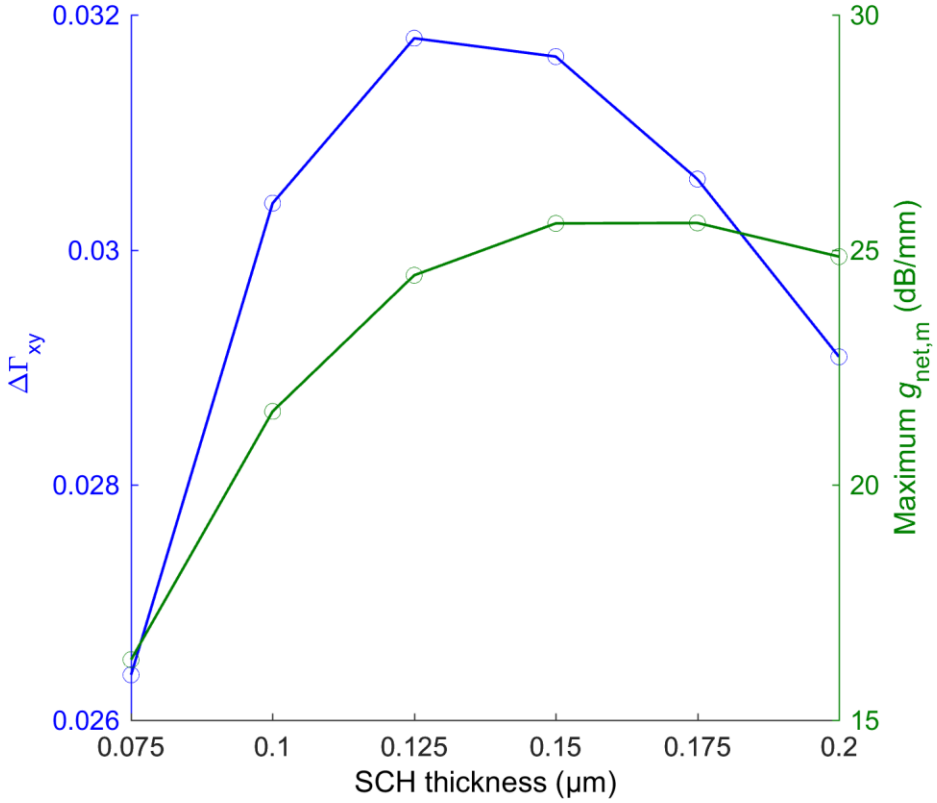

Figure 4.11: Attainable difference between maximum and minimum confinement factor, $\Delta\Gamma_{xy}$, and maximum net modal gain $g_{net,m}$, plotted vs SCH thickness.

TABLE 4-1: EPI J
RELEVANT PROPERTIES OF THE HETEROGENEOUS WAVEGUIDE

	Material	Thickness (nm)	Doping (cm^{-3})	Band Gap Wavelength (μm)	Strain[a]	Refractive Index	Loss (cm^{-1})
1	$In_{0.53}Ga_{0.47}As$	100	p $1.5 \cdot 10^{19}$	1.65	0	3.65	10,000
2	$In_{0.59}Ga_{0.41}As_{0.89}P_{0.11}$	25	p $3.0 \cdot 10^{18}$	1.50	0	3.52	66
3	$In_{0.73}Ga_{0.27}As_{0.59}P_{0.41}$	25	p $3.0 \cdot 10^{18}$	1.30	0	3.38	66
4	InP	1000	p $1.5 \cdot 10^{18}$	0.92	0	3.17	33
5	InP	250	p $8.0 \cdot 10^{17}$	0.92	0	3.17	17.6
6	InP	250	p $5.0 \cdot 10^{17}$	0.92	0	3.17	5.5
7	$In_{0.53}Al_{0.18}Ga_{0.29}As$	125	u.i.d.	1.20	0	3.38	1.1
8	3x $In_{0.68}Al_{0.06}Ga_{0.26}As$	6	u.i.d.	1.70	+1%	3.41	83[b]
	4x $In_{0.44}Al_{0.09}Ga_{0.47}As$	9	u.i.d.	1.35	-0.6%	[c]	[c]
9	$In_{0.53}Al_{0.18}Ga_{0.287}As$	125	n $1.0 \cdot 10^{17}$	1.20	0	3.38	0.1
10	InP	110	n $2.0 \cdot 10^{18}$	0.92	0	3.17	1.0
11	2x $In_{0.85}Ga_{0.15}As_{0.33}P_{0.67}$	7.5	n $1.0 \cdot 10^{18}$	1.11	0	3.28	1.0
	2x InP		n $1.0 \cdot 10^{18}$	0.92	0	3.17	
12	InP	10	n $1.0 \cdot 10^{18}$	0.92	0	10	1.0
13	Bonding SiO_2	7	N/A	N/A	0	1.45	0
14	Si	500	u.i.d.	1.10	0	3.47	0
15	Buried SiO_2	1000	N/A	N/A	0	1.45	0

[a]Positive indicates compressive, negative indicates tensile. [b]This value depends on the carrier density; this is under high injection current (J = 3400 A/cm2). [c]Loss and index from the barrier is contained in the loss value used for the well.

The final epitaxial layer design is shown in Table 4-1. The table lists the alloy compositions and thicknesses for all the epi layers, as well as the doping, band gap wavelength, strain, refractive index, and absorption coefficient. It should be noted that considerable experimental optimization contributed to this final design. This process is detailed in Section 4.5.

4.4. Semiconductor Optical Amplifier

The capability to vary the quantum well confinement factor with a simple lithography mask dimension (the silicon waveguide width, see Figure 4.9) presents an interesting opportunity. Amplifier waveguides, when used as a traveling wave amplifier (commonly referred to as a semiconductor optical amplifier or SOA), can be used to amplify optical signals. The total amount of gain for small input power signals can be quite large, 30 dB or more, but tends to decline as the input power increases, according to Equation 4.3:

$$G = G_0 \frac{1 + P_{in} / P_s}{1 + G_0 P_{in} / P_s}, \quad 4.3$$

where G is the gain factor, G_0 is the unsaturated gain factor, P_{in} is the input power, and P_s is the material gain saturation power.

The material gain saturation power can be derived from the laser rate equations [28], and is equal to:

$$P_s = \frac{hc}{\lambda_{xy}} \frac{\sigma_{xy}}{a \tau \Gamma_{xy}}, \quad 4.4$$

where σ_{xy} is the quantum well cross-sectional area, λ is the photon wavelength, a is the differential gain, Γ_{xy} is the modal overlap with the pumped region of the quantum well, τ is the carrier lifetime, h is Planck's constant, and c is the speed of light in vacuum. Reducing a and τ increases the input saturation power, and this can be accomplished by operating the device at high carrier density. Reducing Γ_{xy} increases $P_{in,s}$, but also reduces G_0 according to Equation 4.5. A reduction in the number of quantum wells reduces the cross-sectional area A, which reduces P_s, but it also reduces Γ_{xy} and increases the carrier density at a given current bias, for a net increase in P_s. Taking this measure reduces the modal gain coefficient, so the tradeoff between gain and saturation power must be considered carefully for the design of the amplifier. The effect of confinement factor on the unsaturated gain factor G_0 is shown in Equation 4.5:

$$G_0 = \exp(g_{p,0} L \Gamma_{xy}). \quad 4.5$$

where $g_{p,0}$ is the peak gain coefficient and L is the length of the amplifier.

The three-section laser of Figure 4.16 can be modified to operate as an SOA by applying an anti-reflection coating to the polished facet. Light can be launched into the amplifier input with a lensed fiber, and collected from the output in the same manner. In this case, a CW tunable laser was used, along with an erbium doped fiber amplifier (EDFA) to amplify the

power sufficiently to overcome the large 9 dB fiber-to-chip coupling loss and ensure the amplifier could be saturated for the input signal. The laser power after amplification by the EDFA was controlled with a variable optical attenuator. Because the SOA has compressively-strained quantum wells, it has the highest gain for TE polarized light. A fiber spool polarization controller was used to adjust the polarization of the input light. After the SOA, a band-pass filter was used to filter out ASE, to prevent it from being counted as signal power at low input levels. The light was finally collected on a photodetector. A schematic of the measurement apparatus is shown in Figure 4.12.

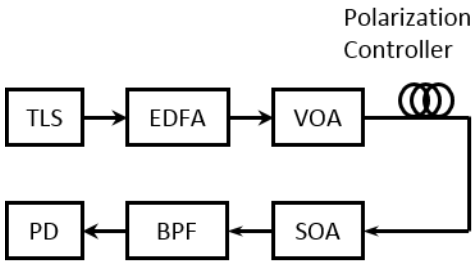

Figure 4.12: The measurement apparatus used for the characterization of the gain and saturation power. TLS: Tunable laser source. EDFA: Erbium doped fiber amplifier. VOA: Variable optical attenuator. SOA: Semiconductor optical amplifier. BPF: Band pass filter. PD: Photodetector.

The SOAs tested here used Epi H and the basic 2-μm flare 20-μm-long heterogeneous transition with an n-InP taper (described in Chapter 5). The amplifier section was 2 mm in length, and there were 500-μm-long passive Si waveguides on either side. A series of otherwise identical SOAs were produced with various waveguide widths to vary the confinement factor. The characterization of the gain versus input power for extraction of the gain saturation behavior was performed at 1.55 μm wavelength, where the gain was at its maximum. All of the measurements were performed with 280 mA of bias current. The operating voltage at this

bias value was 2.3 V. The variation of the gain with respect to input power is shown in Figure 4.13.

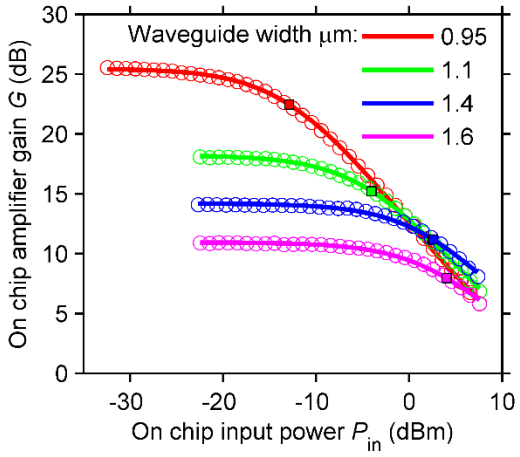

Figure 4.13: Gain versus on-chip input power for all for SOA designs. The measurement data is shown as circles, and the curve fits are shown as lines. The 3 dB saturation points are shown as squares.

Equation 4.3 was used to fit the measurement data in Figure 4.13 to extract P_s and G_0. The resulting fit parameters are shown as symbols in Figure 4.14. Equations 4.4 and 4.5 were used to fit the fit parameters, and are shown as solid lines. The resulting gain coefficient fitted from the data is $g_{p,0} = 1.49 \cdot 10^3$ cm^{-1}.

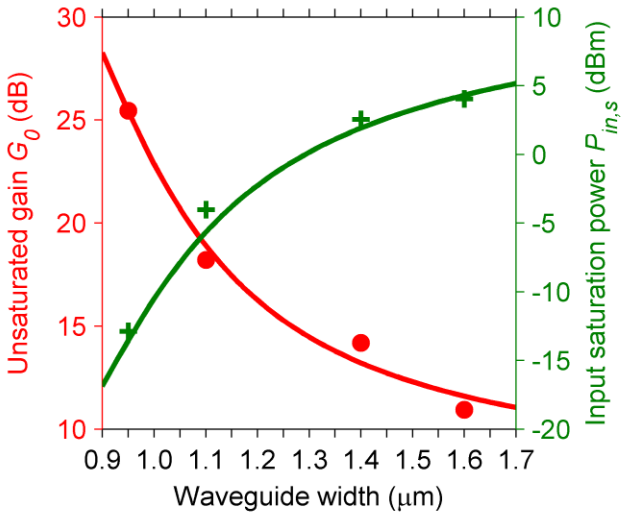

Figure 4.14: Unsaturated gain G_0 (red) and input saturation power $P_{in,s}$ (green) extracted from the data in Figure 4.13 (markers), and curve fits (lines).

The spectral bandwidth of the SOA was also tested. Because S- and L-band EDFAs with high enough output power were not available, this test was performed in the small signal regime with −12 dBm input power. The wavelength spectra of the various SOA devices were similar, so only the data from the highest output power 1.4 μm SOA is shown, in Figure 4.15.

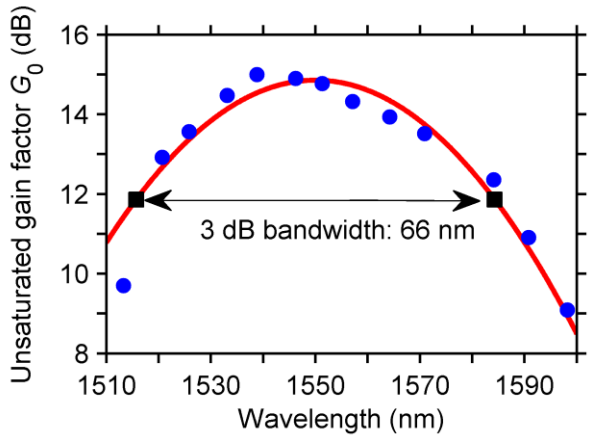

Figure 4.15: Unsaturated gain G_0 versus wavelength for the 1.4 μm device under 280 mA bias current. The blue circles are data, while the red line is the curve fit using Equation 4.6.

The data are shown as dots, while the red line is a curve fit using:

$$G \propto \exp[-\Gamma_{xy} a_2 L(\lambda - \lambda_p)^2]. \quad 4.6$$

where the constant a_2 is the spectral gain coefficient from [29], and is 31 $cm^{-1} \cdot nm^{-2}$ in this case.

Control of the confinement factor tradeoff between the gain and saturation power can be achieved by a lithography mask design only, as opposed to varying the physical composition of the epitaxial material. Unsaturated gain of 25.5 dB and input saturation power of 4.25 dBm were respectively demonstrated with the narrowest and with the widest waveguide SOA. These results were achieved with a 65-nm wide 3-dB gain bandwidth. One device showed 16 dBm of saturated output power, which is the highest that has been demonstrated in heterogeneous Si/III-V SOA. Careful waveguide design allowed for low propagation loss (< 5 cm^{-1}) across a range of confinement factors (1.2-2.6 %) while ensuring single transverse mode operation. Selection of a three quantum well active region increases the carrier density, which improves P_s and increases the gain bandwidth. Very low parasitic reflection from the Si/III-V transition allows for operation of long amplifiers at high drive current, which increases the gain and saturation power. Because the input and output are both passive Si waveguides, these amplifiers can be seamlessly integrated with other heterogeneous Si/III-V devices. Examples include a power amplifier for a narrow-linewidth laser, a channel amplifier for an optical phased array beam steering chip, or a high-gain amplifier for an integrated photodetector.

4.5. The Epi Wafer Development Trajectory

While many types of epi material were fabricated and tested, direct experimental comparisons are frustratingly difficult due to a major confounding factor: a simple cleaved facet ridge laser is impractical to fabricate on the heterogeneous Si/III-V platform, due to the poor facet preparation yield caused by the polishing process used to form the laser mirror. Silicon is difficult to cleave, and SOI more so, due to its higher hardness than InP and tendency to cleave on the 011 plane, which is oriented 45 degrees from the desired facet angle. Polishing the facet, as is normally done for Si devices, is extremely difficult in presence of bonded III-V material as the bonded films can delaminate under the mechanical force used for polishing.

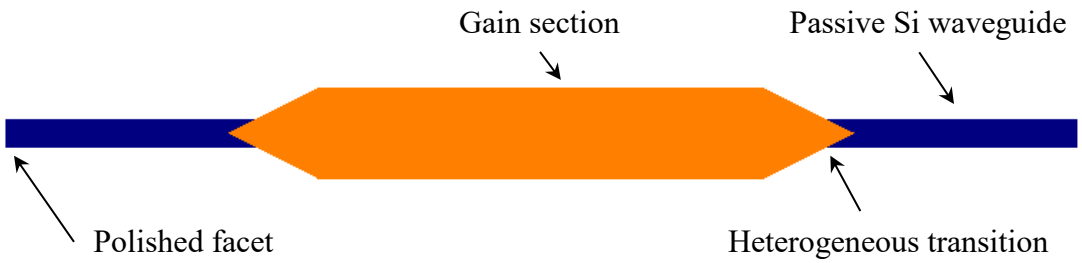

Figure 4.16: Schematic of a 3-section laser

Most of the successful device comparisons in this work are done with 3-section lasers, meaning that they include two passive waveguides as outputs from a central active amplifier waveguide, along with the two necessary heterogeneous transitions. This is shown schematically in Figure 4.16. Variation in the heterogeneous transition was found to be lower than variation in polished facets; however, as the technology level of the heterogeneous transition improved, it made comparing lasers across generations impossible. In addition,

experimental yield prevented some of the epi wafer designs from being realized. The process to the optimized Epis J and K in Table 4-1 is shown in Figure 4.17.

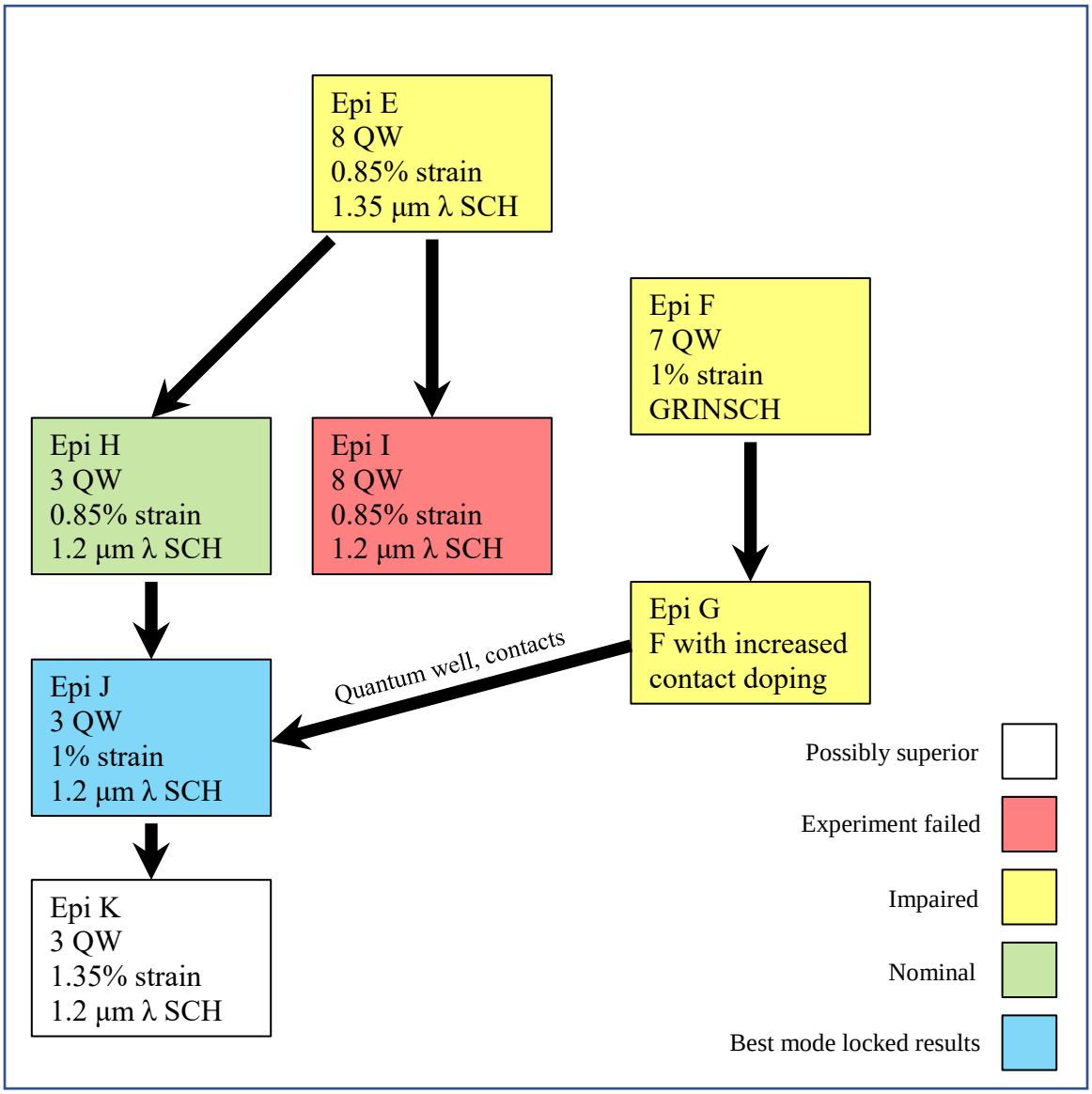

Figure 4.17: Optimization path of epi designs.

Epi E was based off the epi material used in the work of G. Kurczveil [30]. All 1550-nm-wavelength heterogeneous laser results from UCSB published up until [30] used variants of this material, with the only difference being the relative thickness of the SCH layers; the original work by H. Park and A. Fang had 250-nm top SCH and no bottom SCH, while

Kurczveil had 125-nm bottom SCH and 125-nm top SCH. There were 8 quantum wells, each 7-nm-thick with 0.85% compressive strain, as shown in Table 4-2. There is no connection in literature to the source of this quantum well design. The performance of these devices was poor in terms of both threshold and slope efficiency, as could be expected of early prototypes demonstrating a new platform. In addition, because of the complications in separating the heterogeneous transition loss from the laser epi performance, it was unclear what the cause of the poor laser performance was.

TABLE 4-2: EPI E

	Material	Thickness (nm)	Doping (cm^{-3})	Band Gap Wavelength (μm)	Strain[a]
1	$In_{0.53}Ga_{0.47}As$	200	p $1.5 \cdot 10^{19}$	1.65	0
2	$In_{0.59}Ga_{0.41}As_{0.89}P_{0.11}$	25	p $3.0 \cdot 10^{18}$	1.50	0
3	$In_{0.73}Ga_{0.27}As_{0.59}P_{0.41}$	25	p $3.0 \cdot 10^{18}$	1.30	0
4	InP	1000	p $1.5 \cdot 10^{18}$	0.92	0
5	InP	250	p $8 \cdot 10^{17}$	0.92	0
6	InP	250	p $5 \cdot 10^{17}$	0.92	0
7	$In_{0.65}Al_{0.13}Ga_{0.34}As$	125	p $1 \cdot 10^{17}$	1.36	0
8	8x $In_{0.65}Al_{0.055}Ga_{0.29}As$	7	u.i.d.	1.75	+0.85%
	9x $In_{0.45}Al_{0.089}Ga_{0.46}As$	10	u.i.d.	1.29	-0.55%
9	$In_{0.65}Al_{0.13}Ga_{0.34}As$	125	n $1 \cdot 10^{17}$	1.36	0
10	InP	110	n $2 \cdot 10^{18}$	0.92	0
11	2x $In_{0.85}Ga_{0.15}As_{0.33}P_{0.67}$	7.5	n $1 \cdot 10^{18}$	1.11	0
	2x InP		n $1 \cdot 10^{18}$	0.92	0
12	InP	10	n $1 \cdot 10^{18}$	0.92	0
13	Bonding SiO_2	7	N/A	N/A	0
14	Si	500	u.i.d.	1.10	0
15	Buried SiO_2	1000	N/A	N/A	0

The assumption made with the prototype material was that high internal loss was impairing the laser performance, since the material showed good gain characteristics when operated as an amplifier [31]. So, a p-type doping setback was introduced: the 250 nm of P-InP cladding above the SCH was reduced in doping to $5 \cdot 10^{17}$, and the 250 nm above that was reduced to $8 \cdot 10^{17}$ (Layers 5 and 6 in Table 4-2). As stated before, direct comparisons are difficult, but two very similar devices were fabricated with the prototype epi and Epi E. The comparison of

the LI curves is shown in Figure 4.18. The author acknowledges G. Kurzcveil for the fabrication of the device with no doping setback.

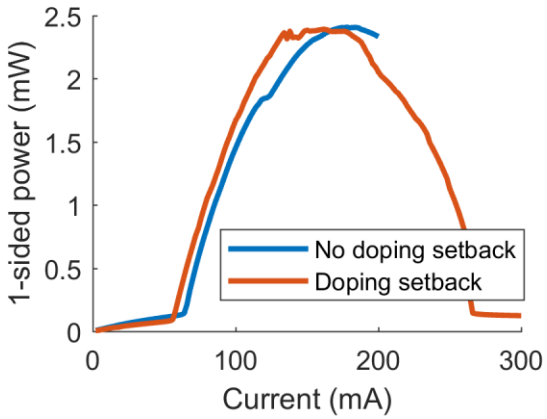

Figure 4.18: LI comparison of 3-section lasers, 800-µm long, with 80-µm deeply etched (through the QW) heterogeneous transitions, and a 1-µm-wide by 700-nm-thick silicon waveguide.

Epi E, with the doping setback, is slightly superior in terms of threshold; it still has high threshold and low maximum output power, signifying that the p-type doping was not the root cause of the high threshold.

Removal of the heterogeneous transition by facet polishing showed that the transition was a major source of output power impairment, as seen in Figure 4.19. Removal of the transition resulted in a 3-fold increase in output power, and a reduction in threshold current of about 25%. However, the threshold current of 44 mA translates to a current density of 1,300 A/cm^2, which is perhaps 4 times the state of the art for quantum well lasers. The development of the heterogeneous transition is detailed in Chapter 5.

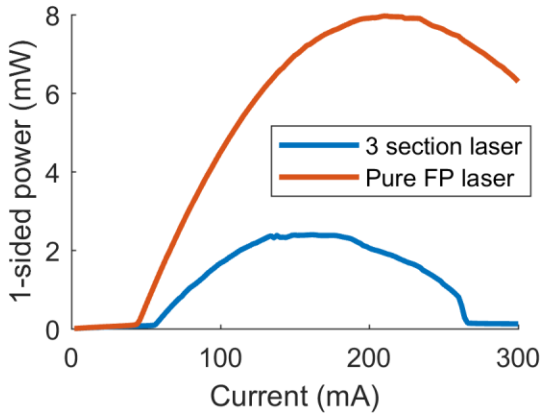

Figure 4.19: Comparison of a 3-section laser with Epi E, and then a pure FP laser with polished facets and no heterogeneous transition or passive waveguide. Both are 840 μm in length.

Experimental investigation of the gain current relation of the FP laser of Figure 4.19 revealed that the threshold current was limited by high modal transparency current. The net modal gain spectra were extracted from the FP laser by using Cassidy's method [32]. The extracted net modal gain spectrum for increasing bias current is shown in Figure 4.20a. The gain value is plotted versus current density (the device is 840 μm long and has a 4-μm-wide current channel), showing a zero crossing at 1017 A/cm^2 in Figure 4.20b. This is the modal transparency current–the terminal current at which the gain has compensated both the material gain and the internal loss of the cavity. The internal loss was extracted using the long-wavelength loss method [33] to be 6 cm^{-1} at zero bias for a device with a 1 μm wide silicon waveguide. To extract the material terminal transparency current, this loss value must be subtracted from the peak modal gain in Figure 4.20b, resulting in the terminal material transparency current $J_{tr,t}$. Then, $J_{tr,t}$ must be multiplied by the injection efficiency of the device to attain the material transparency current density at the quantum well. The injection efficiency is assumed to be 0.61, after measurements taken by H. Park in his dissertation, *Silicon*

Evanescent Devices for Optical Networks and Buffers. The resulting material quantum well transparency current density is 574 A/cm^2, or 71 A/cm^2 per well.

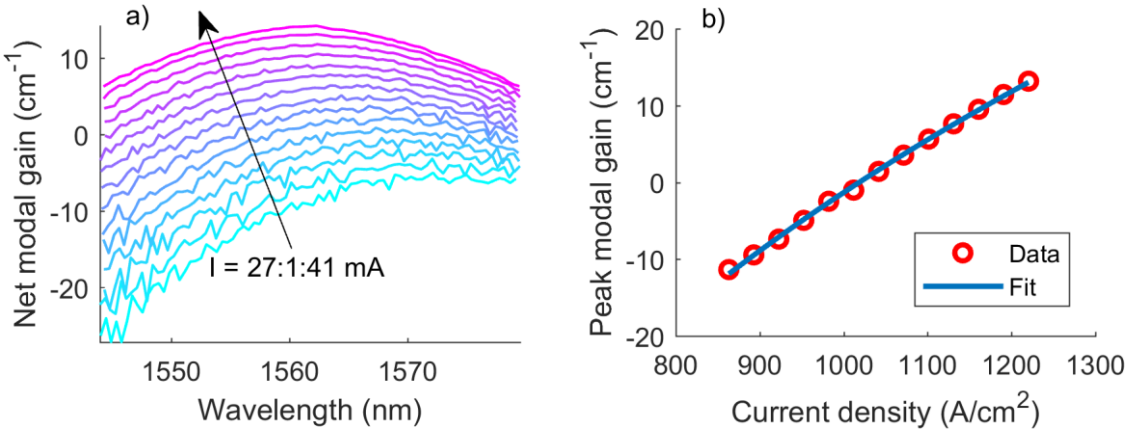

Figure 4.20 a) modal gain spectra from the Epi E FP laser, and b) the gain value at the lasing wavelength (1565 nm) versus injected current density.

This value of transparency current density is inadequate, as good-performing lasers should have terminal threshold current densities near this value. The per-well density is reasonably low, so the clear first step would be to simply reduce the number of wells, except that the modal gain coefficient per well is not particularly high at 9 cm^{-1} per well. Simply reducing the number of quantum wells to 3, for example, using the formula

$$J_{\text{th}} = \frac{J_{\text{tr,well}}}{\eta_{\text{i}}} e^{\frac{\alpha_m + \alpha_i}{\Gamma g_0}} \qquad 4.7$$

and η_{i} = 0.61, $J_{\text{tr,well}}$ = 574 A/cm^2, α_{i} = 6 cm^{-1}, α_{m} = 14 cm^{-1}, and Γg_0 = 71.7 cm^{-1}, yields J_{th} = 1,244 A/cm^2, only a minor improvement over the 1,300 A/cm^2 demonstrated by the 8 QW FP laser. So, for reduction of quantum wells to be a viable solution, first other improvements must be made.

The internal loss was the first point to investigate. Although 6 cm^{-1} is a good value for a laser waveguide, measurement of the device in the long wavelength regime–in this case

1640 nm–while it was forward biased revealed a different picture. The extracted long wavelength loss increased drastically with increasing forward bias. This measurement could not be applied above transparency, as the FP fringes begin to take on a sawtooth shape as the tunable laser is swept across them due to injection locking, but according to the trend in Figure 4.21, the loss at threshold may be as high as 32 cm^{-1}, which does explain the low slope efficiency of the FP laser device in Figure 4.19. This complicates the model in Equation 4.7, as the loss is assumed to be fixed in that case. Leaving Equation 4.7 in its ignorant current form, the increasing loss with increasing bias will simply reduce the gain coefficient g_0, so this explains the poor gain slope as well as low slope efficiency.

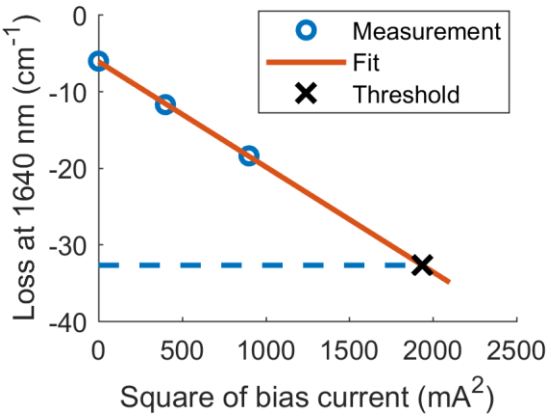

Figure 4.21: Measurement of long-wavelength loss versus the square of the bias current. The measurement data is open circles, while a linear fit is plotted as a line. The X represents the loss at the threshold value of the laser.

This increasing loss is likely due to modal overlap with the hole population in the quantum well. Compressive strain is supposed to reduce or eliminate this loss, so evidently 0.85% strain is insufficient. Therefore, the strain was increased from 0.85% in Epi E to 1% in Epi J and 1.35% in Epi K.

The 1.35-μm band gap AlGaInAs SCH for Epi E was presumably chosen because the extremely high index of refraction (compared to other InP alloys) of this material, 3.45, is very close to silicon and would allow for high confinement factor. A calculation of the flat band lineups of Epi E is shown in Figure 4.22a, showing that the band gap of the SCH is too narrow to act as a carrier confinement layer. An increase in the band gap of the SCH corrects this. While the lower index may reduce the confinement factor, this can be compensated by adjusting the silicon waveguide width. This was presumed to be the source of the low injection efficiency η_i.

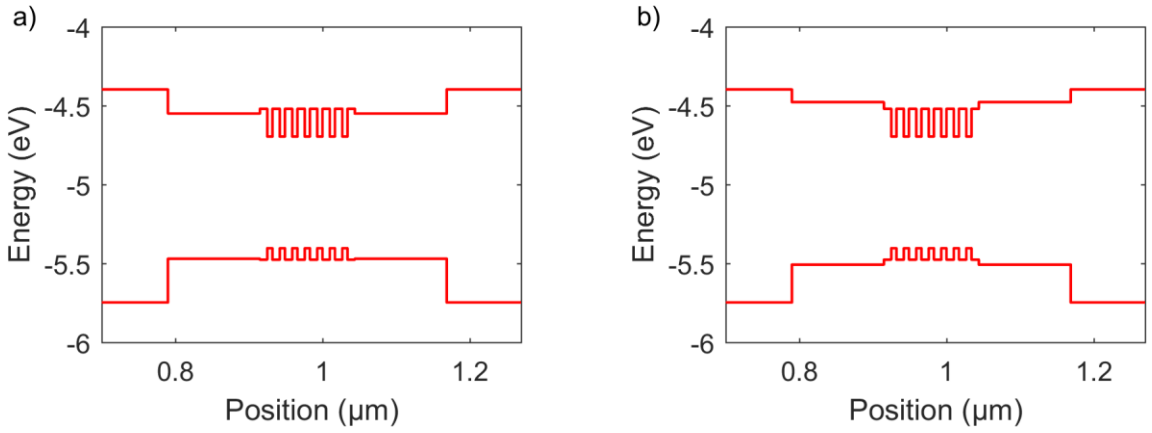

Figure 4.22: Flat band lineup for Epi E (a) and Epi I (b).

Along with Epi E, a researcher named Yongbo Tang in the Bowers group developed Epi F (There were only 3 epi designs before E. E and F were ordered together and labeled this way by the grower), which incorporated the doping setback, but replaced the entire active region waveguide with a completely redesigned graded index SCH (GRINSCH), and 7 quantum wells with 1% strain, which were taken from a Taiwanese Ph.D thesis and were supposedly recommended to the Taiwanese group by Landmark Optoelectronics. This design is shown in Table 4-3. Epi F FP lasers were found via cutback (the only successful cutback measurement ever completed by the author) to have $\eta_i = 0.4$ and $\alpha_m = 8$ cm^{-1} for a 750-nm-wide waveguide,

which has equivalent confinement factor to the 1 μm waveguide devices on Epi E. This loss value represents loss at threshold, since it is extracted from fitting inverse slope efficiency of above threshold lasers, which presumably have their carrier density clamped at the threshold carrier density.

TABLE 4-3: EPI F

	Material	Thickness (nm)	Doping (cm^{-3})	Band Gap Wavelength (μm)	Strain[a]
1	$In_{0.53}Ga_{0.47}As$	200	p $1.5 \cdot 10^{19}$	1.65	0
2	$In_{0.59}Ga_{0.41}As_{0.89}P_{0.11}$	25	p $3 \cdot 10^{18}$	1.50	0
3	$In_{0.73}Ga_{0.27}As_{0.59}P_{0.41}$	25	p $3 \cdot 10^{18}$	1.30	0
4	InP	1000	p $1.5 \cdot 10^{18}$	0.92	0
5	InP	250	p $8 \cdot 10^{17}$	0.92	0
6	InP	250	p $5 \cdot 10^{17}$	0.92	0
7	$In_{0.53}Al_{0.34}Ga_{0.13}As$ => $In_{0.53}Al_{0.15}Ga_{0.315}As$	100	u.i.d.	1.36	0
8	7x $In_{0.68}Al_{0.06}Ga_{0.26}As$	6	u.i.d.	1.75	+1%
	8x $In_{0.44}Al_{0.09}Ga_{0.47}As$	9	u.i.d.	1.35	-0.6%
9	$In_{0.53}Al_{0.15}Ga_{0.315}As$ => $In_{0.53}Al_{0.34}Ga_{0.13}As$	100	n $1 \cdot 10^{17}$	1.36	0
10	InP	110	n $2 \cdot 10^{18}$	0.92	0
11	2x $In_{0.85}Ga_{0.15}As_{0.33}P_{0.67}$	7.5	n $1 \cdot 10^{18}$	1.11	0
	2x InP		n $1 \cdot 10^{18}$	0.92	0
12	InP	10	n $1 \cdot 10^{18}$	0.92	0
13	Bonding SiO_2	7	N/A	N/A	0
14	Si	500	u.i.d.	1.10	0
15	Buried SiO_2	1000	N/A	N/A	0

Despite the apparently poor injection efficiency, the change in loss from 34 cm^{-1} to 8 cm^{-1} above threshold provided a considerable improvement in laser efficiency, shown in Figure 4.23a. The threshold current was reduced to 29 mA, or 882 A/cm^2, and the terminal modal J_m improved to 793 A/cm^2. The gain coefficient at 1565-nm-wavelength increased to 91 cm^{-1}, or 13 cm^{-1}/well, almost 50% higher that of the material in Epi E. This can be adjusted for internal loss, corrected for confinement factor (although the designs are intentionally similar with Γ_{xy} = 8.0% for Epi E and 8.8% for Epi F) and normalized to the number of wells to be compared to Epi E. This is shown in Figure 4.23b, which is the material gain versus the terminal *J*. The increasing advantage of Epi F at higher bias current was presumed to be due to the higher strain

reducing carrier dependent loss in the quantum well; this will be contested later in a more tightly controlled experiment.

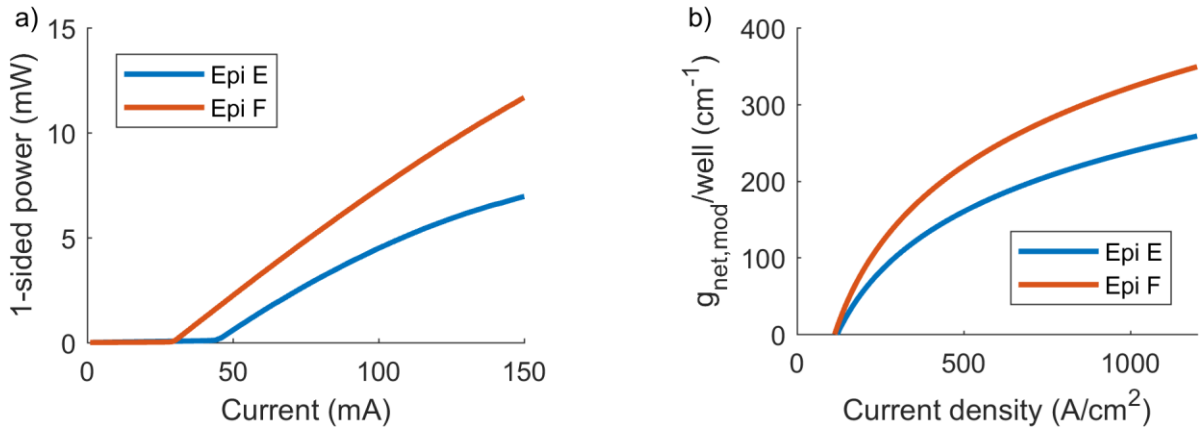

Figure 4.23: Comparison between 840-μm long FP lasers with Epi E and Epi F. a) is the LI behavior, and b) is the per-well modal gain vs terminal current.

The carrier dependent loss hypothesis can be confirmed with another measurement, such as the one carried out in [3], where the loss is extracted from the laser below threshold ASE with a Hakki-Paoli method or derivative (in this case Cassidy's method). Gain spectra from the Epi E and Epi F FP lasers are shown in Figure 4.24. Notice the decreasing gain at 1590 nm in Figure 4.24a, which corroborates the result shown in Figure 4.21. This loss increase is absent in the Epi F gain spectra in Figure 4.24b; in fact, the Epi F device has only increasing gain even out to 1620 nm wavelength.

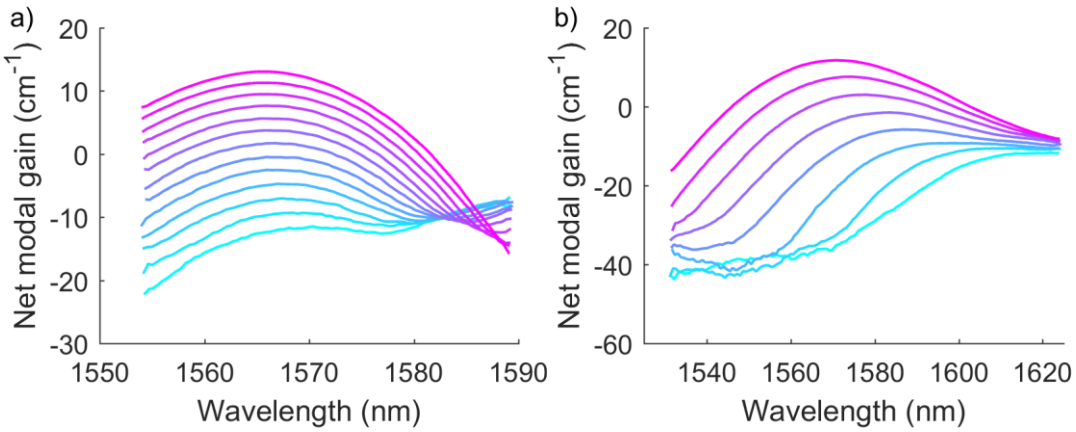

Figure 4.24: Gain spectra from FP lasers made with a) Epi E and b) Epi F. The Epi F laser is 434-μm long, while the Epi E laser is the same 840-μm-long laser as before.

After this development, it was decided to attempt a more scientific approach. As mentioned before, Epi F has worse injection efficiency, 0.4, than Epi E, 0.61, which already was not particularly high. The reason for this may be the narrow band gap of the Epi F GRINSCH near the quantum well not providing adequate carrier confinement, or it may be related to a defect between the high aluminum content layer 7 and the N-type InP [34]. It is also possible that the redesigned GRINSCH, which was designed to have higher index by lowering the overall band gap, may not provide the quasi-electric field that is normally expected from a graded band gap structure. So, the first step was to keep the Epi E design, and widen the band gap in the SCH from 1.35-μm-wavelength band gap quaternary ("1.35Q") to a 1.2-μm-wavelength band gap ("1.2Q") to investigate the effect of correcting the flawed SCH design from Epi E. This is Epi I, which does not need its own table as only the SCH layers, 7 and 9, were changed from Epi E in Table 4-2, to $Al_{0.21}Ga_{0.25}In_{0.54}As$. Unfortunately, as indicated by the red shade in Figure 4.17, this laser failed due to a fabrication error degrading its p-contact.

The step after Epi I, which was fabricated together with I, was Epi H. H was further modified from I, by reducing the number of quantum wells to 3. The combination of the reduced number of quantum wells and increased SCH band gap resulted in a dramatic improvement in laser output power compared to Epi E, which shares the same quantum well design. Since the Epi I fabrication failed, it is unclear what the individual contributions from the two changes were. The Epi H lasers were produced in later runs with more reliable heterogeneous transitions, and so comparisons could be made between 3-section lasers, which

have polished Si facets and are more repeatable (Figure 4.25a compares performance of 3-section lasers).

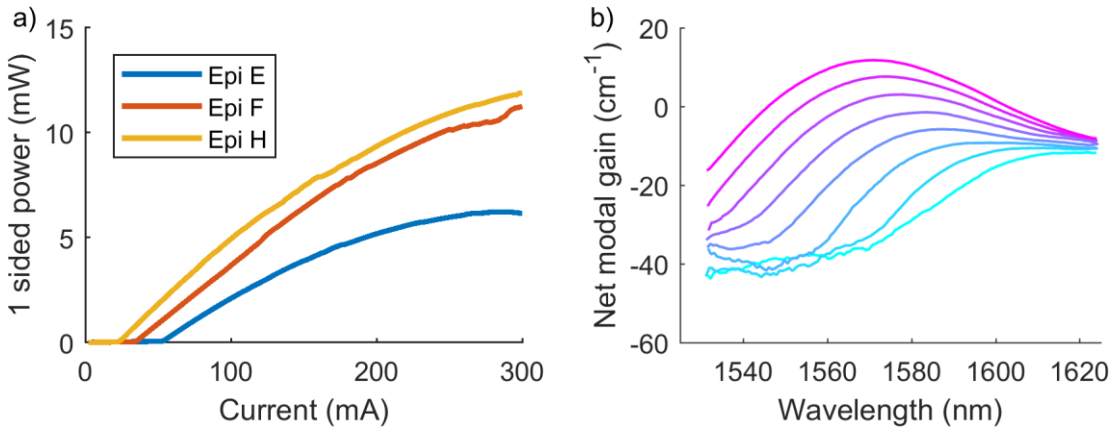

Figure 4.25: a) Comparison of LI characteristics of 3-section lasers based on 8 QW, 1.35Q SCH Epi E, 7 QW GRINSCH Epi F, and 3 QW 1.2Q Epi I, and b) Gain spectra from an Epi H FP laser, showing no increased loss at long wavelength as injection current increases.

The LI performance of 3-section lasers with 1000-µm-long gain sections, 20-µm-long heterogeneous transitions, and 500-µm-wide passive waveguide sections is shown in Figure 4.25a. The Epi H laser has comparable slope efficiency to the Epi F laser and lower threshold current due to the reduced gain material volume accorded by the lower number of quantum wells. Based on the gain spectra shown in Figure 4.25b, it does not appear that Epi H was affected by the injection level dependent propagation loss that deteriorated the performance of Epi E (Figure 4.21), so evidently this loss increase was due to the SCH design, and not the strain in the quantum wells. The full epi design of Epi H is shown in Table 4-4.

TABLE 4-4: EPI H

	Material	Thickness (nm)	Doping (cm^{-3})	Band Gap Wavelength (μm)	Strain[a]
1	$In_{0.53}Ga_{0.47}As$	200	p $1.0 \cdot 10^{19}$	1.65	0
2	$In_{0.59}Ga_{0.41}As_{0.89}P_{0.11}$	25	p $3 \cdot 10^{18}$	1.50	0
3	$In_{0.73}Ga_{0.27}As_{0.59}P_{0.41}$	25	p $3 \cdot 10^{18}$	1.30	0
4	InP	1000	p $1.5 \cdot 10^{18}$	0.92	0
5	InP	250	p $8 \cdot 10^{17}$	0.92	0
6	InP	250	p $5 \cdot 10^{17}$	0.92	0
7	$In_{0.53}Al_{0.18}Ga_{0.29}As$	125	p $1 \cdot 10^{17}$	1.36	0
8	3x $In_{0.65}Al_{0.055}Ga_{0.29}As$	7	u.i.d.	1.75	+0.85%
	4x $In_{0.45}Al_{0.089}Ga_{0.46}As$	10	u.i.d.	1.29	-0.55%
9	$In_{0.53}Al_{0.18}Ga_{0.29}As$	125	n $1 \cdot 10^{17}$	1.36	0
10	InP	110	n $1 \cdot 10^{18}$	0.92	0
11	2x $In_{0.85}Ga_{0.15}As_{0.33}P_{0.67}$	7.5	n $1 \cdot 10^{18}$	1.11	0
	2x InP		n $1 \cdot 10^{18}$	0.92	0
12	InP	10	n $1 \cdot 10^{18}$	0.92	0
13	Bonding SiO_2	7	N/A	N/A	0
14	Si	500	u.i.d.	1.10	0
15	Buried SiO_2	1000	N/A	N/A	0

The gain-current characteristic of FP lasers with the three epi designs is shown in Figure 4.26a. The 3 quantum well Epi H has a considerable advantage in transparency current, as well as lower net modal gain coefficient $g_{net,modal}$, as expected. As predicted in the calculation shown in Figure 4.7, since these are relatively low loss waveguides, there is a clear advantage in threshold for mirror loss below 30 cm^{-1} for the 3-quantum-well epi. It was impossible to adjust the silicon waveguide width in Epi H to produce a similar confinement factor to the higher number of well epi designs, so instead the material gain must be compared. Assuming 5 cm^{-1} for Epi H (from simulation, Figure 4.10), and that the injection efficiency was the same as Epi E (maybe incorrect), the material gain can be calculated using the fitting parameters shown in Table 4-5. The results of the calculation are shown in Figure 4.26b. Epi E and Epi H have similar transparency current density, as expected given that they have the same well and barrier designs, but Epi H has significantly higher gain coefficient g_0, likely owing to the carrier dependent loss impairment shown to be unique to Epi E. The quantum well design in Epi F is obviously superior, with both higher gain coefficient and lower material transparency current.

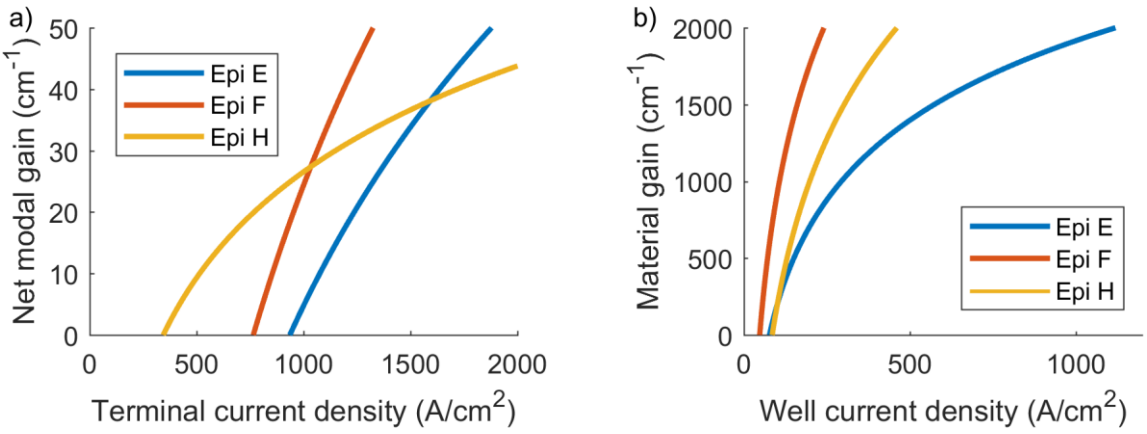

Figure 4.26: Gain comparison between the three epi designs that have FP data available. a) is the net modal gain, b) is the material gain after adjusting for confinement factor, loss, and injection efficiency.

TABLE 4-5: PARAMETERS USED IN MATERIAL GAIN CALCULATION

Epi Design	$g_{net,modal}$ (cm^{-1})	$J_{tr,t}$ (A/cm^2)	α_i	η_i	Γ_{xy}
E	71.7[a]	1017[a]	6[a]	0.61[c]	9.6%[b]
F	91.1[a]	793[a]	8[a]	0.4[a]	7.4%[b]
H	24.9[a]	420[a]	5[b]	0.61[c]	2.1%[b]

a: Measured; b: Calculated; c: Assumed

TABLE 6: MATERIAL GAIN CURVE PARAMETERS

Epi Design	g_0 (cm^{-1})	J_{tr} per well (A/cm^2)
E	746	77
F	1230	47
H	1183	85

Because of the information in Figure 4.26, the final epi design, Epi J, was essentially the 3-quantum-well wide-band gap SCH design of Epi H with the quantum well from Epi F and the contact design from Epi G. Epi J produced the best performing integrated mode-locked laser diodes detailed in Chapter 6, and as such have not been sectioned into simpler lasers for comparison. However, fully integrated lasers do show a smaller than expected benefit from the 1% strained quantum well, as can be seen in Figure 4.27. Two mode-locked lasers, which have Type 1 spline curve mirrors (See Section 6.3) with identical cavity designs and were co-

fabricated on the same wafer, were compared, and Epi J showed slightly higher slope efficiency (5.2% for J and 4.2% for H) and lower threshold (35.5 mA for J, 36.9 mA for H)

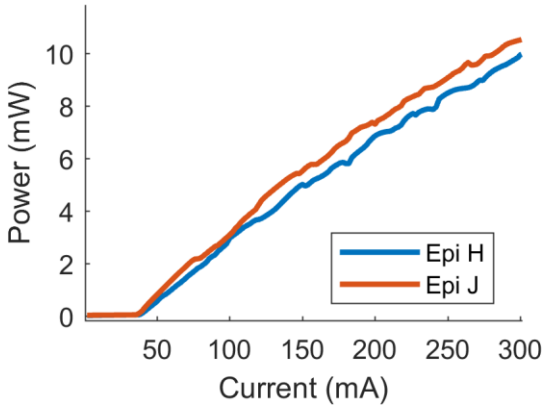

Figure 4.27: Comparison of LI characteristics of two otherwise identical integrated mode-locked lasers made with Epi H and Epi J.

The amplifier waveguide design has an immense impact on the performance of an integrated laser. Simple changes, such as decreasing the silicon waveguide width by a few hundred nanometers (Figure 4.8), can increase the net gain by a factor of 2.5. More complicated optimization of the quantum well and III-V waveguide design–which simultaneously confine charge carriers as well as light–can yield a similar increase in laser output power (Figure 4.25). These parameters must be closely controlled to produce high power fully integrated lasers.

4.6. Mode Locking

While the influence of the laser amplifier design on the continuous wave performance of the laser is clear, the impact of amplifier design on mode-locking behavior is not as well understood. Comparison between mode-locked lasers with different epi is difficult because of the multitude of factors that are free to vary between epi designs. Also, the different materials generally must be fabricated separately on different chips, or at least different dies, introducing

the complication of manufacturing variation into the experiment. In addition, changing the amplifier design normally changes the absorber design as well, so studying the impact of the amplifier waveguide design separately from the absorber is normally impossible. Even when it is possible, it adds another degree of freedom to the experimental space.

It is well accepted in literature that a lower number of quantum wells produces lower noise [9][35][36][37], allegedly due to reduced coupling of amplified spontaneous emission into the waveguide mode. The shortest pulses from on-chip in-plane quantum well lasers have one [9], three [38][39], four [40][41], and six [42] wells, so this parameter may be coupled with another, such as mirror loss.

4.6.1. Confinement factor

The optical confinement factor in the active region, both the transverse confinement factor Γ_{xy} and the longitudinal confinement factor Γ_z can have a strong impact on the pulse width. The shortest on-chip mode-locked laser pulse from a quantum well laser, 490 fs, was produced by exploiting an offset waveguide 3 quantum well laser with a quantum well intermixed passive waveguide to reduce Γ_z [38]. This was allegedly due to reduced self-phase modulation thanks to the lower Γ_{xy} and Γ_z.

The heterogeneous silicon waveguides described in this chapter have the capacity to control confinement factor by varying the waveguide width, making straightforward comparisons possible since devices can be fabricated on the same wafer and compared directly. Four lasers with Type 1 spline curve mirrors, 100-μm saturable absorbers, and 30-μm conformal-index heterogeneous transitions with the angled n-layer were characterized. The shortest pulse width attained from the four devices is shown in Figure 4.28. Unlike [38], the pulse width in these lasers is not limited by self-phase modulation. Instead, increasing

confinement factor yields a shorter pulse. Based on this, it appears that the pulse width is limited by low amplification at the high-power peak of the pulse. Several other pieces of evidence, shown later in Figure 4.31, Figure 4.32, and Section 7.2, will lend additional credence to this hypothesis.

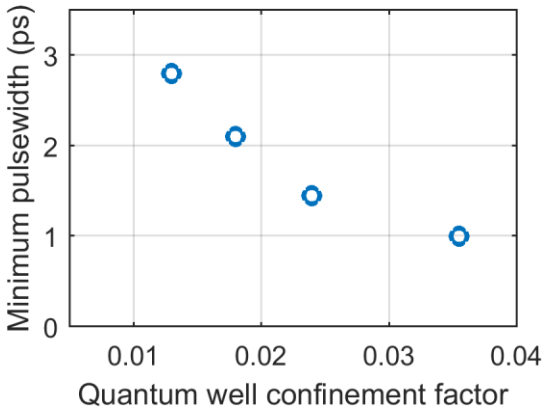

Figure 4.28: Shortest attainable pulse width for four otherwise identical mode-locked lasers with different Si waveguide width in the amplifier and absorber sections. This shows the impact of the confinement factor on pulse width.

Note that the absorber waveguide and the amplifier waveguide were the same in this experiment. It is possible that the increased saturable absorption results from higher confinement, but data on devices with fixed Γ_{xy} and increasing Γ_z in the absorber show that increased absorption does not necessarily yield shorter pulses.

4.6.2. Absorber Design

The length of the absorber is a crucial parameter, and can be varied with a lithographic mask dimension in most mode-locked laser designs. Figure 4.29 shows the impact of shortening the absorber length in four lasers, again with Type 1 spline mirrors, a 1-μm-wide Si waveguide ($\Gamma_{xy} = 0.016$ in Figure 4.28), and the 30-μm-long conformal-index angled n-layer transition. The absorber lengths varied from 50 μm (2.5%) to 200 μm (10%). The pulse width

decreases with decreasing absorber length, and the data suggests that a 30- or 40-μm-long absorber may have produced an even shorter pulse.

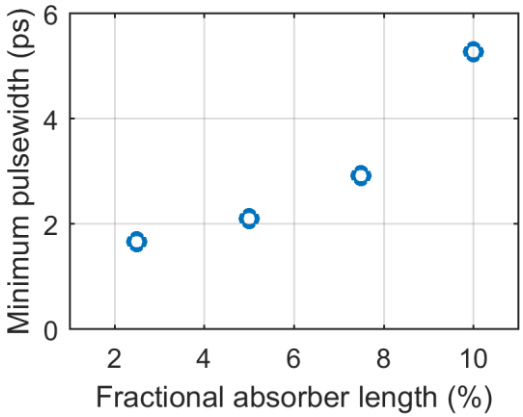

Figure 4.29: Shortest attainable pulse width for four otherwise identical mode-locked lasers with different length saturable absorber sections, plotted as a percentage fraction of the 2-mm-long overall length of the active waveguide.

The reason for this behavior is that the longer absorbers have higher loss when compared to shorter absorbers at the same reverse voltage. The long absorbers can prevent multi-mode laser action when biased at higher (less negative) voltage, whereas the shorter absorbers can be biased at lower (more negative) voltage with the same overall loss (due to less length). At more negative voltage, the recovery time is increased.

In addition to the reverse bias and recovery time, the parasitic capacitance and space-charge effects begin to become relevant at these speeds, so it may be that the longer absorbers also have their recovery slowed down further.

The largest negative voltage bias on the higher transverse confinement absorbers was −5 V, while the voltage on the lower confinement designs was −9 V; beyond these values, the electrical characteristics of the absorber would degrade, becoming strongly shunted diodes, and the LI characteristic of the laser would also suddenly deteriorate. It is likely that the high

photocurrent, as much as 50 mA, caused the metal contact to sinter and short circuit the diode while simultaneously increasing the absorption in the waveguide to beyond what could be overcome by the amplifier. For reference, the contact in the 50-μm-long absorber was 4-μm-wide, so 50 mA corresponds to 25,000 A/cm^2. This was particularly problematic at high forward bias in the amplifier, when the intra-cavity power was high. A shorter absorber, for example 30 μm, would need to have the p-contact design changed. Simply eliminating the proton implant in the absorber section, which is unnecessary, and expanding the contact to cover the entire mesa, 26-μm-wide instead of 4 μm, would reduce the current density by 6.5 times. Addition of refractory metals such as tungsten [43] or molybdenum [44] to the contact metal stack have been shown to increase the reliability of the contact metallization. It is likely that these measures will have to be taken to reduce the pulse width and peak power further, as highly reverse biased (below −5 V) absorbers with high intra-cavity power will produce increasingly damaging current spikes in the absorber contacts. More drastic measures, such as using a specialized structure for the absorber [39] may become necessary.

4.6.3. Quantum Well Design

Unfortunately, the III-V epitaxy design was conducted concurrently with the heterogeneous transition development in Chapter 5. Many of the early epitaxial layer designs had inferior heterogeneous transitions that inhibited mode locking. Only the final device run with the most advanced heterogeneous transition design had mode-locked lasers which could be compared to one another. This device run only had designs H, J, and K. Mode-locked lasers with epi G and epi E were functional, but had impaired operating regimes–they would only mode-lock at a small range of gain current and absorber voltage settings.

Epi H, Epi J, and Epi K are identical, with the exception of the quantum well design. The differences between the three devices is the well composition and thickness, which is 7 nm thick with 0.85% compressive strain in Epi H, 6nm thick with 1% compressive strain in Epi J, and 6-nm thick with 1.35% compressive strain in Epi K. The increased strain is believed to reduce the intervalence band absorption from the carrier population in the quantum well, which increases the differential gain by eliminating the carrier dependent loss, as discussed in Section 4.2.

To compare the mode-locking behavior of the three epi designs, a group of identical integrated mode-locked lasers was prepared. They have the Type 1 spline curve mirror (Section 6.3), 60-µm saturable absorbers, 30-µm conformal-index p-InP tapers, and the angled n-layer transition. This was the second-best design, with the Type 2 spline mirror being superior. The Type 2 spline mirrors did not yield on the Epi H and K chips, so these nominal devices were used for comparison.

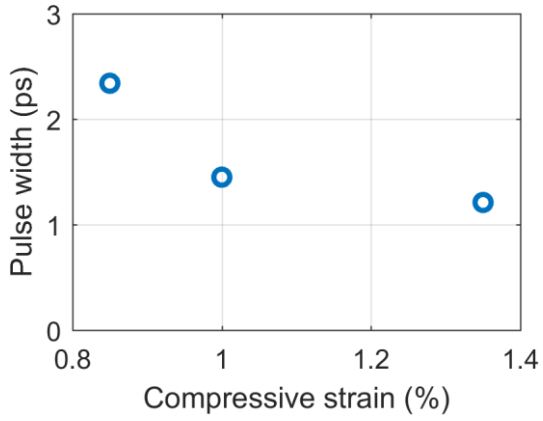

Figure 4.30: The impact of compressive strain on the pulse width of mode-locked lasers with 2-mm amplifier sections, 60-µm saturable absorbers, and Type 1 spline curve mirrors.

The minimum obtainable pulse width for the more highly-strained Epi J laser was significantly shorter than the Epi H laser, at 1.45 ps for Epi J, compared to 2.34 ps for Epi H.

This is due to the higher differential gain of the 1% strained quantum well (Figure 4.26), which allows the amplifier to tolerate higher reverse bias in the saturable absorber. The effect of increasing the compressive strain to 1.35% in Epi K is less pronounced, but does reduce the pulse width further to 1.17 ps. More highly reverse biased absorbers have faster recovery time but likewise higher loss. As shown in Figure 4.31, the shortest pulse width from Epi H comes at 106 mA and −2.96 V. Higher currents do not produce short pulses, which will be discussed in Chapter 7, and at higher negative reverse voltage, the laser becomes single-mode as the absorber reduces the intra-cavity power below the level required to induce spectral hole burning and broaden the emitted mode comb.

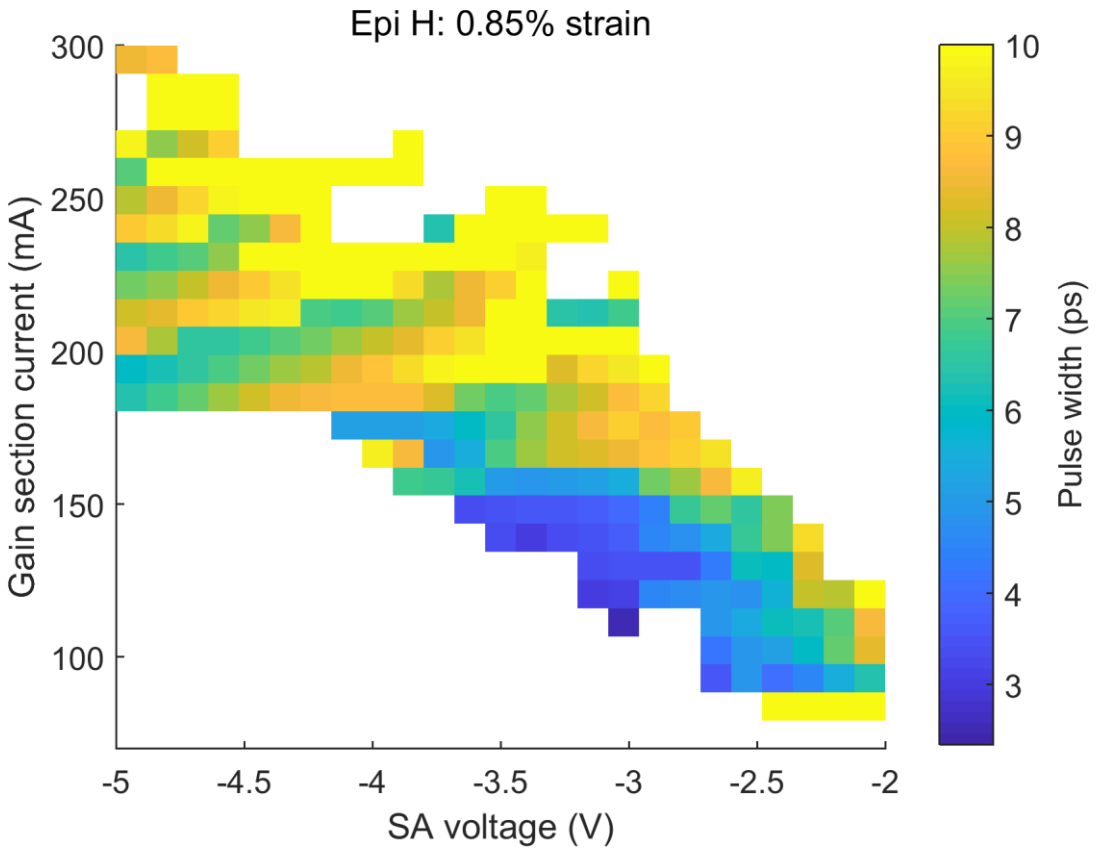

Figure 4.31: Mode locking operating regime for the 0.85% strain 3 QW Epi H. The minimum pulse width achieved from this device was 2.34 ps.

By contrast, the Epi J laser has its optimum bias condition at much more negative reverse voltage, as shown in Figure 4.32. The optimum bias condition is 79 mA and −4.28 V. Mode locking does not occur at negative bias voltage below than −3.5 V, because the loss in the absorber is insufficient to induce mode locking against the higher gain of the 1% strain epi. Naturally, these comparisons are difficult to make accurately because of the multitude of factors that influence the mode-locking behavior, but generally shorter pulses were produced by the 1% strain lasers.

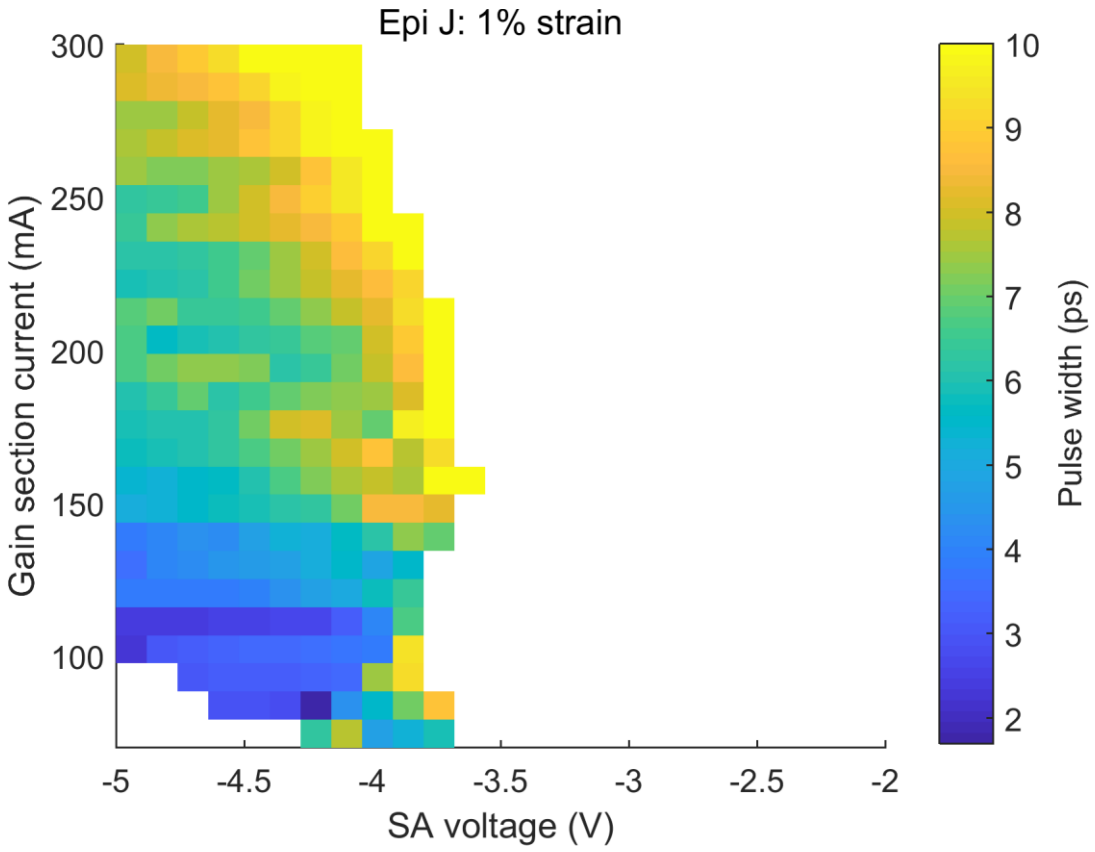

Figure 4.32: Mode locking operation regime for an integrated laser with the 1% strain QW Epi J design. The minimum pulse width obtained from this device was 1.45 ps at 80 mA and −4.52 V.

The design of the amplifier waveguide is of critical importance to the performance of the laser. Practically every detail ultimately affects the mode-locking performance. These devices were optimized experimentally, and so it is unlikely that another large leap in pulse width is possible without making drastic changes. However, higher strain apparently has enough differential gain to permit the device to operate in the multimode regime at lower (more negative) voltage bias. Reducing the length of the absorber may also bring the pulse width down slightly. These changes will produce higher photocurrent from the absorber, and will require redesign of the absorber p-contact. Increasing the amplifier gain may also reduce the pulse width. Accomplishing this by increasing the transverse confinement factor Γ_{xy} may not be practical, as the 700-nm-wide waveguide ($\Gamma_{xy} = 0.035$ in Figure 4.28) is already demonstrating increased propagation loss (see Figure 4.10), which degrades the continuous wave slope efficiency. It may be more practical to increase Γ_z by increasing the relative length of the amplifier section, or to increase Γ_{xy} by increasing the number of quantum wells. Additionally, re-running the fabrication to produce a working Epi K and Type 2 spline mirror would likely produce an even shorter pulse.

References

[1] S. Kakimoto, “Intervalence band absorption loss coefficients of the active layer for InGaAs/InGaAsP multiple quantum well laser diodes,” *J. Appl. Phys.*, vol. 92, no. 11, pp. 6403–6407, 2002.

[2] I. Joindot and J. L. Beylat, “Intervalence band absorption coefficient measurements in bulk layer, strained and unstrained multiquantum well 1.55 μm semiconductor lasers,” *Electron. Lett.*, vol. 29, no. 7, p. 604, 1993.

[3] G. Fuchs, J. Horer, A. Hangleiter, V. Horle, F. Scholz, R. W. Glew, and L. Goldstein, “Intervalence band absorption in strained and unstrained InGaAs multiple quantum well structures,” *Appl. Phys. Lett.*, vol. 60, no. 2, pp. 231–233, 1992.

[4] H. C. Casey and P. L. Carter, “Variation of intervalence band absorption with hole concentration in p-type InP,” *Appl. Phys. Lett.*, vol. 44, no. 1, p. 82, 1984.

[5] G. N. Childs, S. Brand, and R. a Abram, “Intervalence band absorption in semiconductor laser materials,” *Semicond. Sci. Technol.*, vol. 1, no. 2, pp. 116–120, 1986.

[6] L. P. Gonzalez, J. M. Murray, and S. Krishnamurthy, “Wavelength dependence of two photon and free carrier absorptions in InP,” *Opt. Express*, vol. 17, no. 11, pp. 8741–8748, 2009.

[7] J. Piprek, S. Member, J. K. White, and A. J. Springthorpe, “What Limits the Maximum Output Power of Long-Wavelength AlGaInAs / InP Laser Diodes ?,” *IEEE J. Quantum Electron.*, vol. 38, no. 9, pp. 1253–1259, 2002.

[8] G. a. E. Sandra R. Selmic, Tso-Min Chou, Jieh Png Sih, Jay B. Kirk, Art Mantie, Jerome K. Butler, David Bour, “Design and characterization of 1.3 um AlGaInAs-InP Multiple -Quantum-Well Lasers,” *IEEE J. Quantum Electron.*, vol. 7, no. 2, pp. 340–349, 2001.

[9] V. Dijk, G. Duan, G. Aubin, and A. Ramdane, “Short pulse generation using a passively mode locked single InGaAsP / InP quantum well laser,” *Opt. Express*, vol. 16, no. 14, pp. 9007–9012, 2008.

[10] G.-H. Duan, C. Jany, A. Le Liepvre, A. Accard, M. Lamponi, D. Make, P. Kaspar, G. Levaufre, N. Girard, F. Lelarge, J.-M. Fedeli, S. Messaoudene, D. Bordel, and S. Olivier, “Hybrid III-V on silicon lasers for photonic integrated circuits on silicon,” *SPIE Photonics West 2014-OPTO Optoelectron. Devices Mater.*, vol. 9002, no. 4, p. 90020X, 2014.

[11] A. R. Hawkins, W. Wu, P. Abraham, K. Streubel, and J. E. Bowers, “High gain-bandwidth-product silicon heterointerface photodetector,” *Appl. Phys. Lett.*, vol. 70, no. 1997, p. 303, 1997.

[12] D. Liang, D. C. Chapman, Y. Li, D. C. Oakley, T. Napoleone, P. W. Juodawlkis, C. Brubaker, C. Mann, H. Bar, O. Raday, and J. E. Bowers, “Uniformity study of wafer-scale InP-to-silicon hybrid integration,” *Appl. Phys. A Mater. Sci. Process.*, vol. 103, no. 1, pp. 213–218, 2011.

[13] S. Keyvaninia, M. Muneeb, S. Stanković, P. J. Van Veldhoven, D. Van Thourhout, and G. Roelkens, “Ultra-thin DVS-BCB adhesive bonding of III-V wafers, dies and multiple dies to a patterned silicon-on-insulator substrate,” *Opt. Mater. Express*, vol. 3, no. 1, p. 35, Jan. 2013.

[14] S. Matsuo, T. Fujii, K. Hasebe, K. Takeda, T. Sato, and T. Kakitsuka, “Directly modulated buried heterostructure DFB laser on SiO_2/Si substrate fabricated by regrowth of InP using bonded active layer,” *Opt. Express*, vol. 22, no. 10, p. 12139, 2014.

[15] H. Boudinov, H. H. Tan, and C. Jagadish, “Electrical isolation of n-type and p-type InP layers by proton bombardment,” *J. Appl. Phys.*, vol. 89, no. 10, pp. 5343–5347, 2001.

[16] J. Mitomo, M. Yokozeki, Y. Sato, Y. Hirano, T. Hino, and H. Narui, “1.30-um GaInNAs laser diode with lifetime over 1000 hours grown by MOCVD,” *IEEE J. Sel. Top. Quantum Electron.*, vol. 11, no. 5, pp. 1099–1102, 2005.

[17] Z. G. Lu, J. R. Liu, S. Raymond, P. J. Poole, P. J. Barrios, and D. Poitras, “312-fs pulse generation from a passive C-band InAs/InP quantum dot mode-locked laser.,” *Opt. Express*, vol. 16, no. 14, pp. 10835–40, 2008.

[18] D. P. Sapkota, M. S. Kayastha, and K. Wakita, “Analysis of linewidth enhancement factor for compressively strained AlGaInAs and InGaAsP quantum well lasers,” *Opt. Quantum Electron.*, vol. 45, no. 1, pp. 35–43, Jan. 2013.

[19] R. P. Green, M. Haji, L. Hou, G. Mezosi, R. Dylewicz, and A. E. Kelly, “Fast saturable absorption and 10 GHz wavelength conversion in Al-quaternary multiple quantum wells,” *Opt. Express*, vol. 19, no. 10, pp. 700–705, 2011.

[20] Chia-Chien Lin, Meng-Chyi Wu, Hung-Ping Shiao, and Kuo-Shung Liu, “High-temperature, low threshold current, and uniform operation 1×12 monolithic AlGaInAs/InP strain-compensated multiple quantum well laser array in 1.5 μm,” *IEEE Trans. Electron Devices*, vol. 46, no. 8, pp. 1614–1618, 1999.

[21] R. Paoletti, M. Agresti, D. Bertone, L. Bianco, C. Bruschi, A. Buccieri, R. Campi, C. Dorigoni, P. Gotta, M. Liotti, G. Magnetti, P. Montangero, G. Morello, C. Rigo, E. Riva, G. Rossi, D. Soderstrom, A. Stano, P. Valenti, M. Vallone, and M. Meliga, “Highly reliable and high-yield 1300-nm InGaAlAs directly modulated ridge fabry-Perot lasers, operating at 10-gb/s, up to 110/spl deg/C, with constant current swing,” *Journal of*

Lightwave Technology, vol. 24, no. 1. pp. 143–149, 2006.

[22] I. Vurgaftman and J. R. Meyer, "Band parameters for III – V compound semiconductors and their alloys," *J. Appl. Phys.*, vol. 89, no. 11, 2001.

[23] P. M. Stolarz, J. Javaloyes, G. Mezosi, L. Hou, C. N. Ironside, M. Sorel, A. C. Bryce, and S. Balle, "Spectral dynamical behavior in passively mode-locked semiconductor lasers," *IEEE Photonics J.*, vol. 3, no. 6, pp. 1067–1082, 2011.

[24] J. D. Robert and E. Kapon, "Low-Loss III-V Semiconductor Optical Waveguides," *IEEE J. Quantum Electron.*, vol. 27, no. 3, pp. 626–640, 1991.

[25] M. S. Alam, M. S. Rahman, M. R. Islam, A. G. Bhuiyan, and M. Yamada, "Refractive index, absorption coefficient, and photoelastic constant: Key parameters of InGaAs material relevant to InGaAs-based device performance," *Conf. Proc. - Int. Conf. Indium Phosphide Relat. Mater.*, no. May, pp. 343–346, 2007.

[26] C. Grasse, G. Boehm, M. Mueller, T. Gruendl, R. Meyer, and M. Amann, "Empirical modeling of the refractive index for (AlGaIn)As lattice matched to InP," *Semicond. Sci. Technol.*, vol. 25, no. 4, p. 45018, 2010.

[27] M. Amiotti and G. Landgren, "Ellipsometric determination of thickness and refractive index at 1.3, 1.55, and 1.7 μm for In (1− x) Ga x As y P (1− y) films on InP," *J. Appl. Phys.*, vol. 73, no. 6, pp. 2965–2971, Mar. 1993.

[28] S. W. Corzine and M. Mashanovich, *Diode Lasers and Photonic Integrated Circuits*. 2012.

[29] M. J. O'Mahony, "Semiconductor laser amplifiers for future fiber systems," *IEEE J. Light. Tech.*, vol. 6, no. 4, pp. 531–544, 1988.

[30] G. Kurczveil, M. J. Heck, J. D. Peters, J. M. Garcia, D. Spencer, and J. E. Bowers, "An

Integrated Hybrid Silicon Multiwavelength AWG Laser," *IEEE J. Sel. Top. Quantum Electron.*, vol. 17, no. 6, pp. 1521–1527, Nov. 2011.

[31] H. Park, A. W. Fang, O. Cohen, R. Jones, M. J. Paniccia, and J. E. Bowers, "A hybrid AlGaInAs-silicon evanescent amplifier," *IEEE Photonics Technol. Lett.*, vol. 19, no. 4, pp. 230–232, 2007.

[32] D. T. Cassidy, "Technique for measurement of the gain spectra of semiconductor diode lasers," *J. Appl. Phys.*, vol. 56, no. 11, p. 3096, 1984.

[33] G. E. Shtengel, R. F. Kazarinov, G. L. Belenky, M. S. Hybertsen, and D. A. Ackerman, "Advances in Measurements of Physical Parameters of Semiconductor Lasers," *Int. J. High Speed Electron. Syst.*, vol. 9, no. 4, pp. 901–940, 1998.

[34] C. Schramm, H. G. Bach, H. Künzel, and J. P. Praseuth, "Molecular Beam Epitaxy Grown Al(Ga)InAs: Schottky Contacts and Deep Levels," *J. Electrochem. Soc.*, vol. 138, no. 9, p. 2808, 1991.

[35] K. Yvind, D. Larsson, L. J. Christiansen, C. Angelo, L. K. Oxenløwe, J. Mørk, D. Birkedal, J. M. Hvam, and J. Hanberg, "Low-jitter and high-power 40-GHz all-active mode-locked lasers," *IEEE Photonics Technol. Lett.*, vol. 16, no. 4, pp. 975–977, 2004.

[36] K. Yvind, D. Larsson, L. J. Christiansen, L. K. Oxenlowe, J. Mork, J. M. Hvam, and J. Hanberg, "Design and evaluation of mode-locked semiconductor lasers for low noise and high stability," *Opto-irel. 2005 Optoelectron. Photonic Devices, Opt. Networks*, vol. 5825, pp. 37–48, 2005.

[37] K. Yvind, D. Larsson, J. Mørk, J. M. Hvam, M. Thompson, R. Penty, and I. White, "Low-noise monolithic mode-locked semiconductor lasers through low-dimensional structures," *Proc. SPIE*, vol. 6909, p. 69090A–69090A–9, 2008.

[38] L. Hou, M. Haji, J. H. Marsh, and A. C. Bryce, “490 fs pulse generation from a passive C-band AlGaInAs / InP quantum well mode-locked laser,” *Opt. Lett.*, vol. 37, no. 5, pp. 773–775, 2012.

[39] R. Scollo, H.-J. Lohe, F. Robin, D. Erni, E. Gini, and H. Jackel, “Mode-Locked InP-Based Laser Diode With a Monolithic Integrated UTC Absorber for Subpicosecond Pulse Generation,” *IEEE J. Quantum Electron.*, vol. 45, no. 4, pp. 322–335, Apr. 2009.

[40] H. Fan, C. Wu, M. El-Aasser, N. K. Dutta, U. Koren, and A. B. Piccirilli, “Colliding pulse mode-locked laser,” *IEEE Photonics Technol. Lett.*, vol. 12, no. 8, pp. 972–973, Aug. 2000.

[41] V. Moskalenko, S. Latkowski, S. Tahvili, T. de Vries, M. Smit, and E. Bente, “Record bandwidth and sub-picosecond pulses from a monolithically integrated mode-locked quantum well ring laser,” *Opt. Express*, vol. 22, no. 23, p. 28865, 2014.

[42] S. Arahira, Y. Katoh, and Y. Ogawa, “20 GHz subpicosecond monolithic modelocked laser diode,” *Electron. Lett.*, vol. 36, no. 5, p. 454, 2000.

[43] A. Katz, B. E. Weir, D. M. Maher, P. M. Thomas, M. Soler, W. C. Dautremont-Smith, R. F. Karlicek, J. D. Wynn, and L. C. Kimerling, “Highly stable W/ p -In 0.53 Ga 0.47 As ohmic contacts formed by rapid thermal processing,” *Appl. Phys. Lett.*, vol. 55, no. 21, pp. 2220–2222, Nov. 1989.

[44] U. Singisetti, M. A. Wistey, J. D. Zimmerman, B. J. Thibeault, M. J. W. Rodwell, A. C. Gossard, and S. R. Bank, “Ultralow resistance in situ Ohmic contacts to InGaAs/InP,” *Appl. Phys. Lett.*, vol. 93, no. 18, pp. 2008–2010, 2008.

Chapter 5

The Heterogeneous Transition

The heterogeneous amplifier waveguide described in the previous chapter allows efficient generation of light on a silicon photonic integrated circuit. As explained in Chapter 2, the passive silicon waveguide is normally superior to InP waveguides in terms of propagation loss, bend radius, and two-photon absorption, but there is a drastic difference in the mode profile and volume of the proposed inverted slab heterogeneous amplifier waveguide and a typical silicon wire waveguide. To integrate the amplifier with passive waveguide components requires a transition between the heterogeneous waveguide and the passive waveguide.

This heterogeneous transition should have low loss, low unintentional reflection, low transmission into higher order waveguide transverse modes, and high wavelength bandwidth to allow high performance lasers, since the transition must be inside the laser cavity if the architecture proposed in Chapter 2 is to be realized. The loss will increase the laser threshold and reduce its slope efficiency. This loss value should be as low as possible, but 0.25 dB per taper would have a relatively limited impact on the laser performance. Unintended parasitic reflection must be reduced to below −40 dB to prevent the formation of multiple pulses in the

cavity and Fabry-Perot modulation with larger free spectral over the fundamental cavity resonance, which limits the optical bandwidth available to the mode comb. Parasitic multi-mode emission can also produce modulation over the mode comb if the higher order mode is reflected from the laser mirror, since the passive waveguide section then forms an unbalanced Mach-Zehnder interferometer. −30 dB transmission into higher order modes appears to be sufficient for mode-locked lasers, but this effect is believed to place the ultimate limit on the peak power, as explained in Chapter 7, so −40 dB transmission into higher order modes is likely necessary as well. This is evidently difficult to achieve, so the addition of a mode filter, such as a bent or shallowly etched waveguide, may ultimately be required.

This chapter will detail the design and implementation of the heterogeneous transition. Multiple generations of this device were produced, beginning with the design used in [1]. The design of the transition is a multi-dimensional problem that depends on the thickness of the silicon layer, the thickness and index of refraction of the quaternary separate confinement heterostructure (SCH) layers (which depend on the alloy composition), the multi-quantum well design, the distance between the silicon waveguide and the III-V waveguide, and the lateral dimensions of the silicon and III-V waveguides. In addition, the final transition design included the critical dimension of the entire circuit, a 300-nm-wide and 1.8-μm-tall III-V ridge, so the device is vulnerable to fabrication impairment which the design must consider. Because of the variety of factors, a simple design optimization was impractical, and so the final design was advanced gradually through convergence of experimental optimization, numerical simulation, and fabrication improvement.

The first section will explain the general concept of the type of transition used: a system of lateral tapers. The second section is the first experimental shock: the initial simulations failed

to accurately capture the dominant loss and parasitic reflection mechanisms, and so these factors had to be optimized experimentally. After the suppression of the parasitic reflection, the parasitic multimode emission, which had been overlooked due to the relatively small magnitude compared to the parasitic reflection in the initial design, is corrected by a novel taper design method. The final experimental shock was the thin n-layer transition, which was initially assumed to be inconsequential, but was able to impair mode locking operation nonetheless. The chapter will be concluded with the impact of the transition design on mode-locked laser pulse width.

5.1. Architecture

Regrowth is challenging on heterogeneous silicon/InP lasers because the thermal expansion coefficient mismatch between the InP and silicon substrates. Thin (sub 250 nm) films are more resistant to thermal damage, and regrown lasers with extremely low thresholds have been demonstrated [2]. However, regrowth increases the cost and manufacturing complexity of the device. Heterogeneous integration is ultimately similar to regrowth in terms of outcomes: an added critical process step allows the inclusion of additional epitaxial layers. It is redundant to use both regrowth and bonding if the desired characteristic can be attained with only one of the processes. For this reason, and to avoid the design limitation on the epi layer thickness imposed by regrowth, it is desirable to avoid using regrowth for the heterogeneous transition.

The amplifier waveguide discussed in Chapter 4 is essentially a twin waveguide system in which only the symmetric mode is excited by the amplifier medium. To accomplish a transition into the passive waveguide, the mode must be transferred into the silicon waveguide. This may

be accomplished in a number of ways, including a lateral [3] directional coupler, vertical directional coupler [4], a grating assisted codirectional coupler [5], or an adiabatic coupler [6].

Directional couplers have some wavelength sensitivity and very poor tolerance to fabrication variation. In the case of the devices described in this dissertation, which use the inverted ridge waveguide Chapter 4, the beta mismatch between the III-V slab waveguide and the Si ridge waveguide is too high for an efficient directional coupler. Beta mismatch $\Delta\beta$ is the difference in the propagation constant between the two waveguides, and $\Delta\beta > 0$ reduces the maximum coupling strength of the coupler. This can be an advantage, in the case of [3], when low output coupling is desirable for low lasing threshold, but for the transition envisioned in Chapter 2, near 100% coupling (or as close as practical) is required.

Grating assisted directional couplers can overcome the problem of beta mismatch, but the grating has even more limited wavelength bandwidth than the directional coupler. The addition of the grating also adds parasitic reflection, which is intolerable in laser devices, especially broad-band lasers like mode-locked or tunable lasers.

The adiabatic directional coupler presents the best option for the laser active-passive transition. It does not have an intrinsic parasitic reflection, and can be designed to have extremely large wavelength bandwidth, much larger than most semiconductor laser emission bandwidths; [7] demonstrated an adiabatic coupler-based MZI with extinction ratio better than 20 dB over 300 nm of wavelength bandwidth.

The term “adiabatic” refers to the fact that there is no coupling between modes, unlike the directional coupler which launches the fundamental mode of the input waveguide into a superposition of the symmetric and antisymmetric modes. The mode is instead transformed gradually into one of the modes of the coupled waveguide system, usually the symmetric mode.

The symmetric mode has higher confinement in the waveguide with higher effective index, so changing the dimensions of one or both waveguides transfers the mode by this mechanism. The operating principle of a 2 x 2 adiabatic coupler that is designed to transfer 100% of the power from the input waveguide to the opposite waveguide at the output is shown in Figure 5.1. The splitting ratio can be selected by ratio of the widths of the two output waveguides: equal widths will make a 50/50 coupler, and varying the width from equal up to a large difference (800 nm vs. 400 nm in Figure 5.1) would be considered large for these high confinement waveguides) can select an arbitrary splitting ratio.

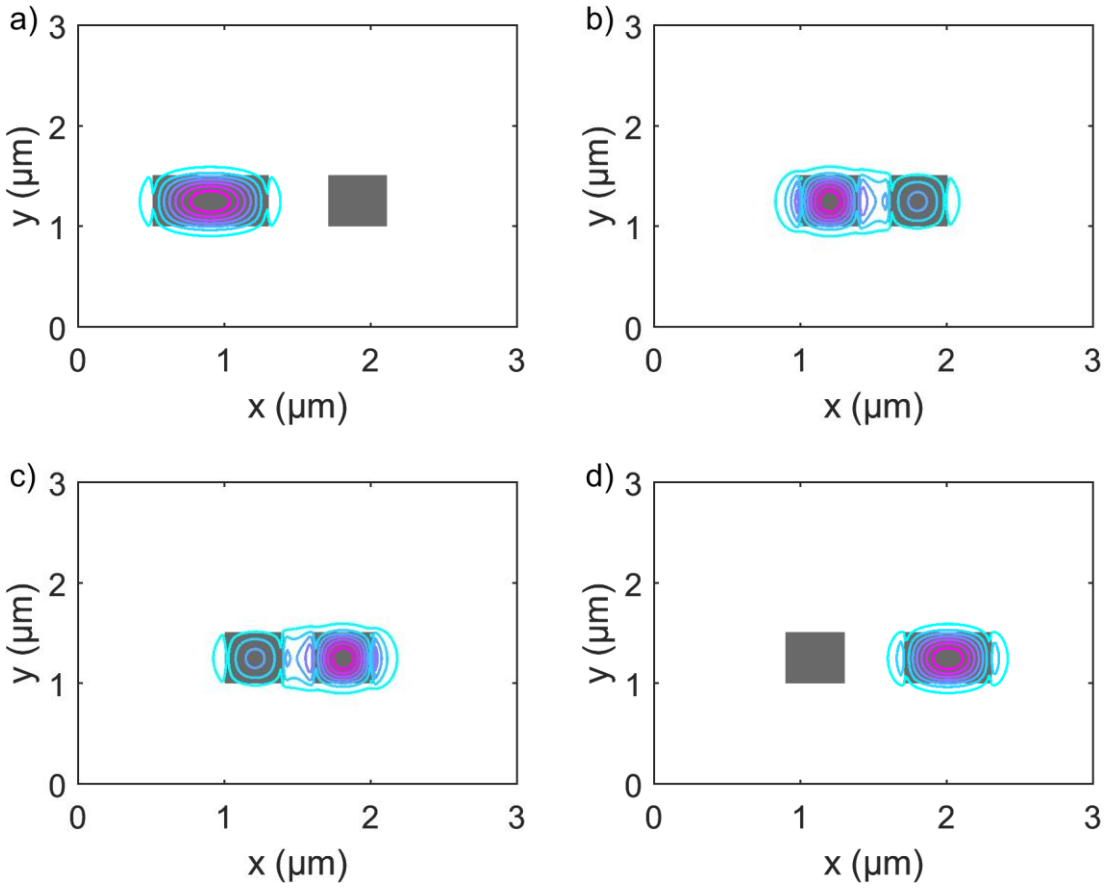

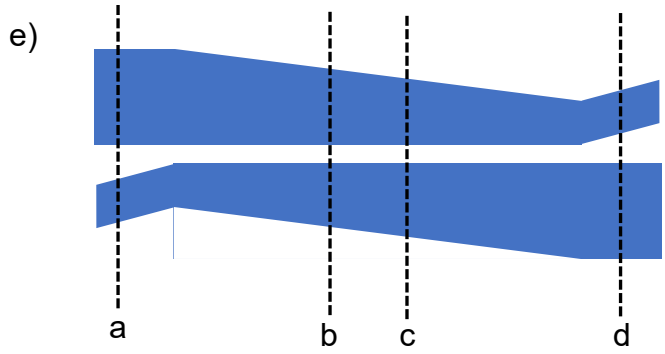

Figure 5.1: Operating principle of a 100% 2 x 2 adiabatic coupler. Figures (a) through (d) show the mode E_x profile (contours) superimposed over the waveguide index of refraction (greyscale). Figure (e) shows a plan view schematic of the coupler. The slices are labeled corresponding to Figures (a)-(d). Figure (a) is the mode profile at the input, showing the mode confined mostly in the left side/upper waveguide. The waveguides are brought to 200-nm apart and are tapered, from 400 nm to 800 nm for the right hand/lower waveguide and from 800 nm to 400 nm for the left hand/upper waveguide. Part of the way through the taper, in Figure (b), the mode begins to exchange between waveguides; in Figure (c), the majority of the mode area has transferred to the right hand/lower waveguide. By the time the right hand/lower waveguide has reached 800 nm, the confinement in the left hand/upper waveguide is very small and the upper waveguide can be curved away, completing the coupling, in Figure (d).

For the heterogeneous transition in the laser cavity, the situation is simplified slightly, as it is in essence a 1 x 1 device. There is an antisymmetric mode, but all the laser light is emitted into the symmetric mode. The concept of using a variation in the dimensions of the waveguides to alter the beta mismatch $\Delta\beta$ and thereby increase the confinement in the silicon waveguide before terminating the III-V waveguide can be applied to the heterogeneous transition. This is done in two stages: first, by widening the silicon waveguide from the high III-V confinement geometry used for the laser amplifier waveguide (Figure 5.2a) to a wide silicon waveguide

which maximizes confinement in silicon (Figure 5.2b), in the “flare.” Then, the III-V structure is necked from the 26-μm-wide slab to the 4-μm-wide beginning of the III-V taper in the “neck”. This has no effect on the mode, as the lateral index guiding from the silicon waveguide prevents any interaction with the III-V width for values larger than 4 μm. The III-V taper then reduces to 300-nm width (the “III-V taper”), adiabatically transforming the mode from the heterogeneous hybrid mode into a mode similar to the silicon waveguide mode. The III-V mesa can then be terminated without creating much of a perturbation, leaving only the silicon waveguide and thin n-contact layer (Figure 5.2d). The thin n-contact layer can in theory be tapered in a similar manner (“n-transition”), however, due to a problem with the fabrication tolerance, this is not the optimal method to execute this transition. This will be discussed in more detail in Section 5.4. Finally, the silicon waveguide is tapered down to the narrow waveguide for bending, either 800 nm for shallow or 400 nm for deep waveguides (the “silicon taper”)

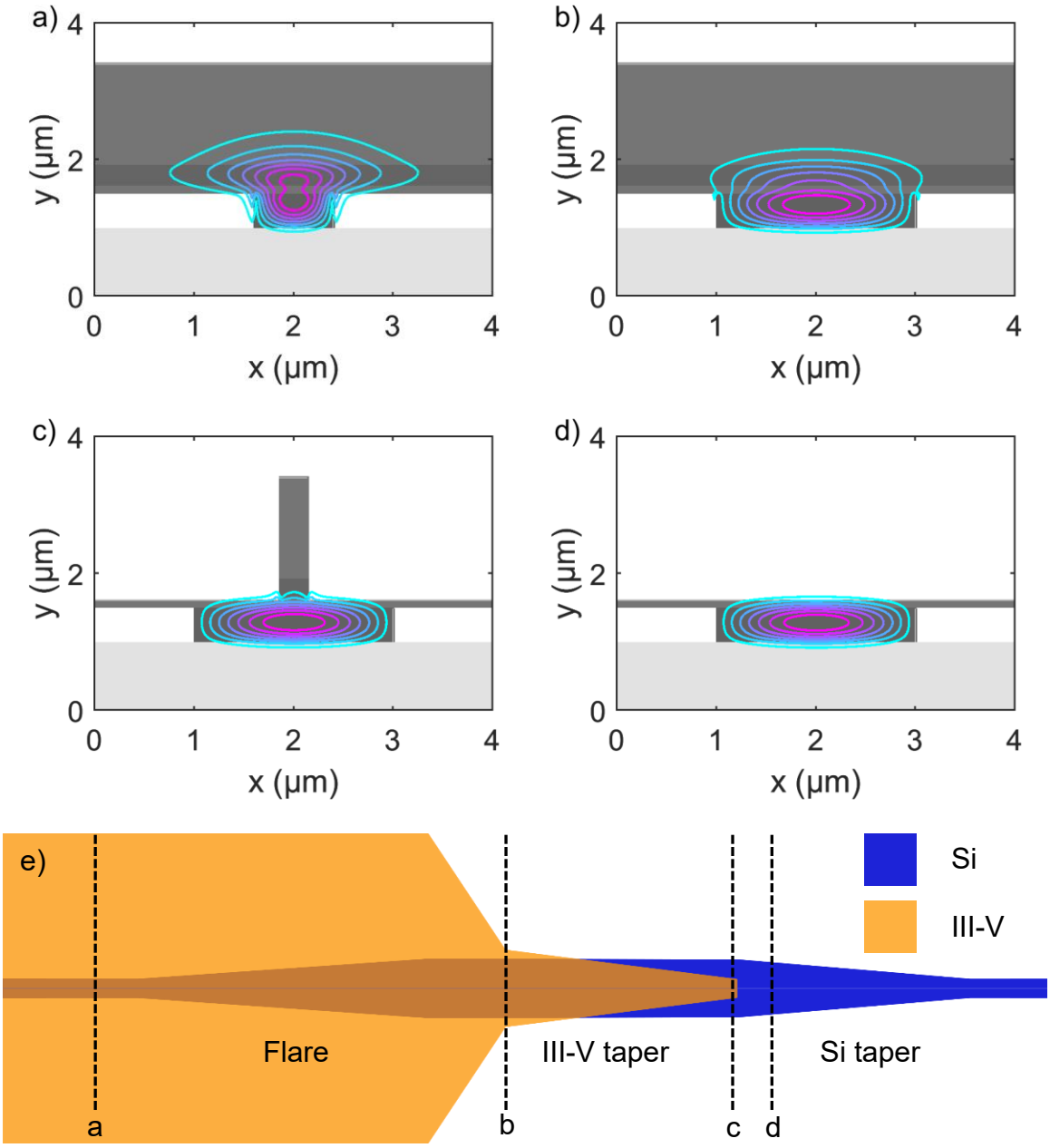

Figure 5.2: Operation principle of the 1 x 1 adiabatic mode converter used for the III-V to silicon heterogeneous transition. Figures a-d are the mode E_x fields of the corresponding slices in Figure (e). Figure (a) shows the mode profile in the amplifier section, which is designed for high confinement in the III-V active region. The silicon waveguide is widened to increase the confinement in the silicon in Figure (b), as the III-V mesa is rapidly necked down to begin the III-V taper. This neck does not have any effect on the mode profile of the fundamental mode.

The III-V mesa then tapers to the small tip in Figure (c), which is abruptly terminated in Figure (d).

This principle allows for low loss and low reflection transformation of the mode from the amplifier waveguide to the passive silicon waveguide, and vice versa. The specifics of the layer thicknesses are limited by the design of the amplifier waveguide, but designing the amplifier for large $\Delta\Gamma$ with respect to the silicon waveguide width (Figure 4.11) for high gain vs. high saturation power amplifiers is also helpful for the heterogeneous transition. Too much thickness in the silicon layer will prevent high confinement factor in the III-V, and too thin silicon will prevent high confinement factor in the silicon. The 500-nm silicon thickness was originally chosen to improve III-V confinement factor, but optimization of the waveguide design for the 500-nm silicon thickness eventually included a reduction in the index of the III-V waveguide layers that compensated for this.

5.2. Loss

The fundamental design of the transition outlined in Section 5.1 represents the concept that was used in the final devices described in Chapter 6, however, many of the dimensions had to be optimized experimentally. Common photonics simulation techniques failed to accurately represent the performance of the early taper prototypes. The beam propagation method assumes that the beam is paraxial, which is not true for all taper geometries given the high index contrast involved in these devices. Eigenmode expansion drastically under-estimated the reflection from the tip of the III-V taper, where residual perturbation to the mode still exists from the III-V mesa due to the requirement that the normal electric flux remain constant across a boundary causes a small reflection even when the confinement in the III-V is minimized. A

commercial solver using the Eigenmode expansion method, FIMMPROP, estimated −50 dB reflection in transitions that had −20 dB reflection in measurement of fabricated devices. The FDTD method was able to capture these relatively large reflections, but due to noise from imperfect mode injection and back reflection from grids, it could not accurately represent tapers with very small tip sizes; this noise floor was about −33 dB. Later generation tapers had reflections below −40 dB. Loss due to scattering and absorption in the tapers requires separate modeling that is not typically included in photonics simulation packages.

5.2.1. Taper Length

The original designs for the heterogeneous transition are detailed in [1] and [8] were both 80 μm in length and claimed below 0.6 dB of loss. In simulation, longer tapers normally have lower loss, as illustrated in Figure 5.6a and b, which show the loss versus length for the III-V taper and flare, respectively. 80 μm was used as a safe length for the III-V taper.

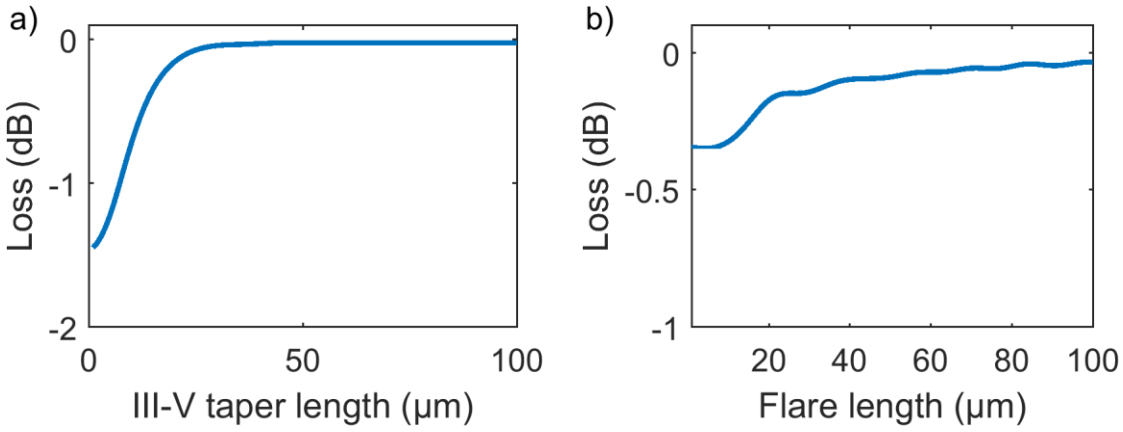

Figure 5.3: Loss for the flare and III-V taper versus length. Figure a) is the III-V taper, and Figure b) is the flare. See Figure 5.2e for a diagram.

A number of devices were built using this design [9][10][11], which curiously exhibited lasing wavelengths near 1600 nm despite the multi-quantum well having photoluminescence

wavelength of 1545 nm. The measurement techniques used in [1] and [8] neglected the absorption in the forward biased taper at the lasing wavelength. Directly measuring the transition loss under forward bias proved to be challenging, as inferring it from the slope efficiency requires knowledge of the passive silicon waveguide loss, the amplifier internal loss, and amplifier injection efficiency at the lasing wavelength. Simply removing the transition and measuring the slope efficiency before and after removal is complicated by the fact that the polished heterogeneous facet does not have repeatable reflection.

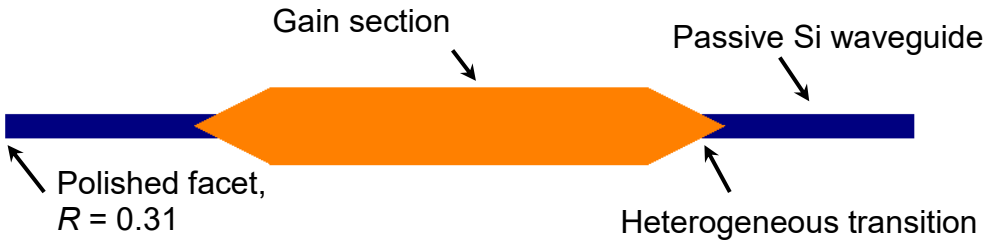

Figure 5.4: Schematic of the 3-section laser used in most of the taper loss comparisons.

For the early part of the taper development, test lasers consisting of a heterogeneous gain section with a transition to a passive waveguide on each side (Figure 5.4) were used to characterize the transitions by simply comparing the threshold and slope efficiency of different designs. Loss could not be extracted directly with this method but accurate comparisons between designs that were fabricated together could be made. Later, for more mature transition designs, a method for quantifying the spectral loss in the transition was employed, which will be covered in Section 5.2.5.

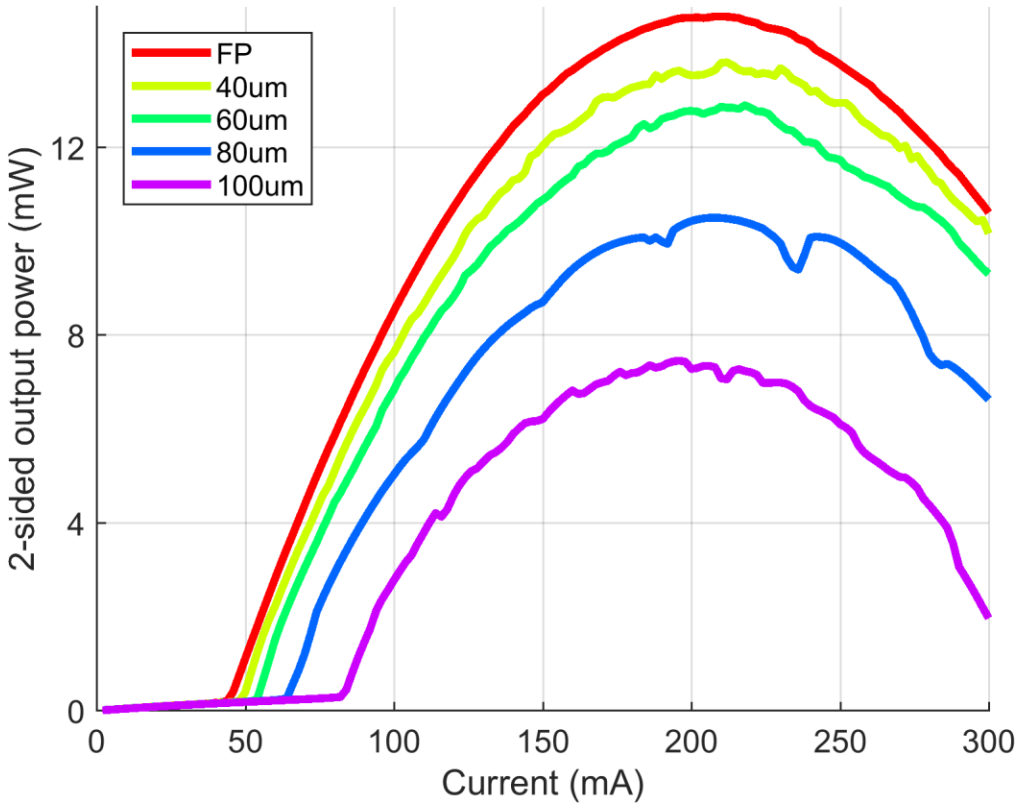

Figure 5.5: LI characteristic of 3-section lasers with varying III-V taper length.

A fabricated set of three-section test lasers with varying taper lengths was produced using Epi E (see Table 4-2: Epi E) and tested. The effect of the taper length on laser performance is shown in Figure 5.5. A pure FP laser with the same active region length is shown in red, with lower threshold and higher slope efficiency. Increasing taper length deteriorates the efficiency rapidly. It should be noted that the FP laser facets are imperfect and have some loss due to damage to the bonded interface at the facet during polishing. Improved taper designs have lower loss than the polished heterogeneous facet.

The excess loss in the III-V taper was originally hypothesized to be due to scattering loss. The tapers in [1][9][10][11] used a complicated hard mask that consisted of a dry etched silicon nitride layer, then a wet etched gold layer, and an ICP Cl_2 dry etched Ti/Pd layer that produced fairly poor quality sidewalls. The lasers shown in Figure 5.5 used an early version of the

process described in Chapter 3, and the III-V and silicon sidewalls were both visibly very smooth. Absorption in the quantum well in the III-V taper was considered as the next possible source of loss.

To examine this hypothesis, the 3-section laser lasing wavelength right above threshold was observed using an optical spectrum analyzer. Lasing wavelength versus the III-V taper length is shown in Figure 5.6a; it increases rapidly with increasing length. This suggests absorption, since the loss on the blue side of the gain peak of an unpumped section of quantum well increases rapidly with decreasing wavelength. However, the lasing wavelength is a complicated matter, since the threshold carrier density, which would be related to the threshold current since the device dimensions are all similar, will affect the lasing wavelength by band filling, and the device self-heating will affect the lasing wavelength by shifting the band gap.

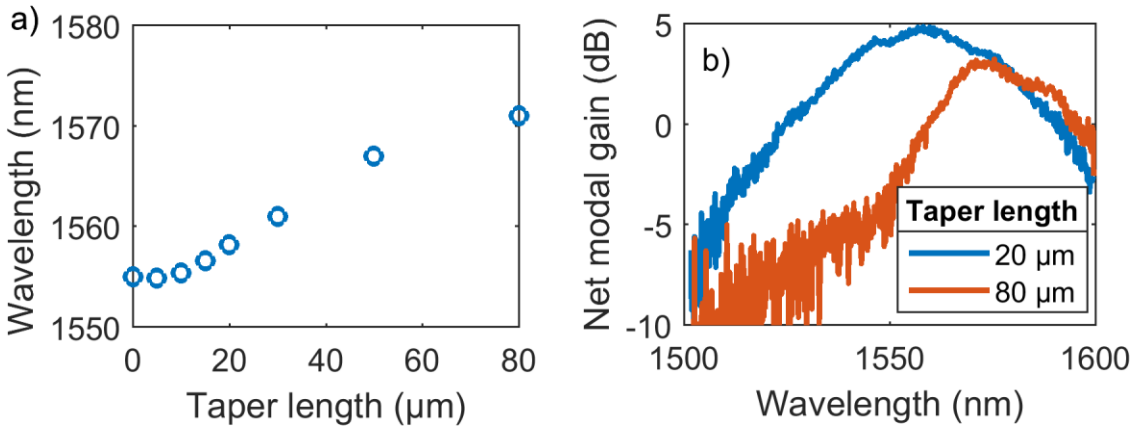

Figure 5.6: The taper length test that revealed the impact of absorption. Figure (a) shows the lasing wavelength of 3-section FP laser test structures. Figure (b) shows the net modal gain of two different taper lengths, displaying the large difference in loss at the PL wavelength and relatively small difference in loss at wavelengths far on the red side of the PL.

For a more conclusive test, gain spectra from the lasers was extracted by examining sub-threshold amplified spontaneous emission spectra using Cassidy's method [12], a variant of the Hakki-Paoli method [13]. In this manner, the spectral gain of the devices can be determined at a fixed current value, which can be small enough that self-heating is negligible. The results of this test on two different taper lengths are shown in Figure 5.6b. Note that this is the net modal gain for the entire device, so all the losses are included: the silicon waveguide loss, the transition loss, and the amplifier internal loss. Because the amplifier and silicon waveguide sections are identical in the two devices, the difference in gain should then be only due to the loss in the heterogeneous transition. The gain at wavelengths above 1580 nm is comparable in the two devices, and even slightly higher in the 80 μm device, because the longer taper is more adiabatic and has less passive loss (Figure 5.3a). But at 1550 nm, the typical desired operating wavelength, the difference in loss is over 7 dB. This explains why the previous examples of lasers using this design had highly red-shifted lasing wavelength.

5.2.2. Sidewall Recombination

Evidently, the III-V taper section of the device is not pumped to the same carrier density as the amplifier section, despite the fact that great care was taken to ensure that the taper is fully metallized. Two hypotheses were developed to explain this effect. The first was sidewall recombination. Due to the narrow III-V ridge in the taper, carriers may diffuse to the sidewall and recombine nonradiatively at surface state defects. A design split on the width of the quantum well etch was produced. In the "Wide QW" design, the etched sidewall of the quantum well is tapered from the full width of the slab (14 μm in this case) so that for most of the transition, the sidewall is far away from the carrier population. In the "Narrow QW" design,

the etched sidewall follows the III-V mesa, with only a 500-nm alignment tolerance on either side. These are 80-μm-long tapers.

The LI characteristics of the two lasers are shown in Figure 5.7a, and a schematic of the two taper designs is shown in Figure 5.7b. Near threshold, the wide QW design has slightly lower threshold (89 mA vs 91 mA) and similar slope efficiency. The difference in maximum power is because the narrow QW device has a wider (24 vs 14 μm) p-mesa in the amplifier section that increases the thermal conductivity. Evidently, the proximity of the active region sidewall does have a small impact on the transition loss, but not enough to explain the 2-times increase in threshold versus the FP laser shown in Figure 5.5.

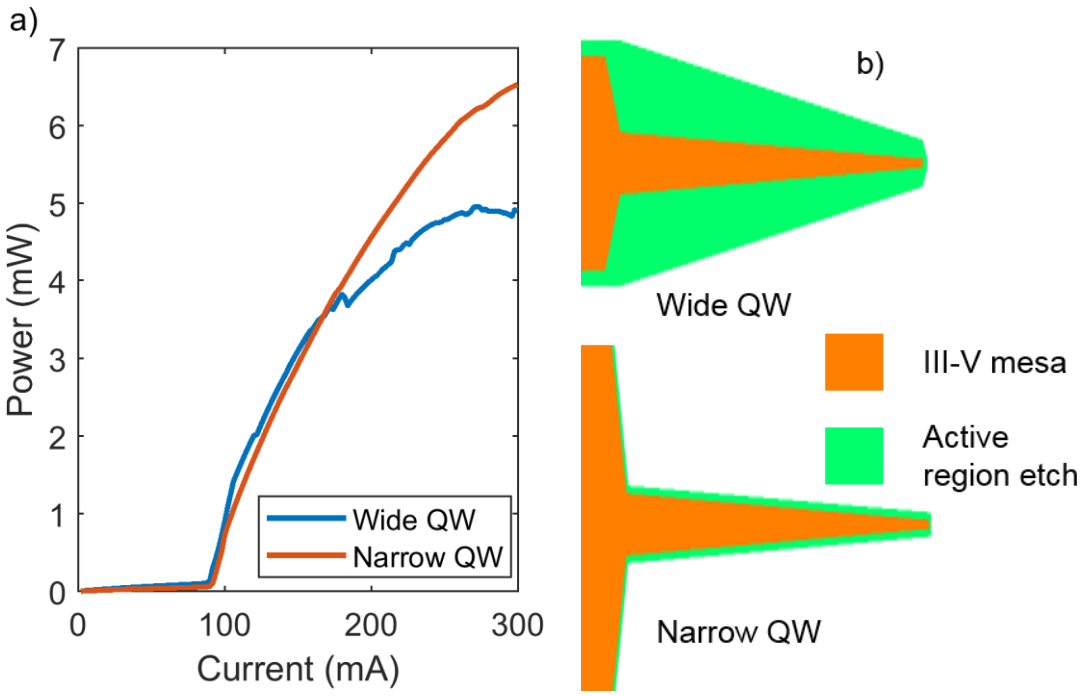

Figure 5.7: Results of the wide QW pattern experiment. Figure (a) is the LIV characteristic of the two lasers, and (b) shows the plan view layout of the wide QW transition, top, and the narrow QW transition, bottom.

5.2.3. Hydrogen Passivation

The second hypothesis is that the narrow III-V mesa in the taper has been contaminated with hydrogen. The p-mesa etch process is conducted using methane-hydrogen-argon RIE (see Chapter 3). The dopant in most p-type III-V semiconductors is compensated by hydrogen contamination, reducing the conductivity. Research into this phenomenon dates back to 1986, when it was described in p-type GaAs [14], and was shortly thereafter discovered in Zn-doped p-type InP [15] in 1988, and then Zn-doped InGaAs in 1989 [16]. Less common p-type dopants, such as beryllium and carbon, have fewer studies available in literature but they are known to be compensated by hydrogen in GaAs [17][18], and carbon doping is known to be compensated by hydrogen in InGaAs [19]. More information on the subject can be found in [20] and [21] and the book, *Hydrogen in Crystalline Semiconductors.*

Reduction in the doping of the p-InP is problematic because it will increase the forward series resistance of the device. Since lasers are typically quite large by electronic device standards (the ultimate devices in this work were 4 μm x 2000 μm) and the p-InP layer is only 1.5 μm thick, the bulk resistance of this layer does not have a large impact on the device performance. More problematic is the p-type InGaAs. Normally, 1.55 μm wavelength lasers grown on InP substrates use a p-type InGaAs layer as the p-contact, since it has a narrower band gap. The InGaAs layer is normally highly doped, as high as possible ($1.5 \cdot 10^{19}$ typical for MOCVD grown epi, higher possible with MBE), to reduce the barrier height at the metal-semiconductor interface. Compensating for the doping in this layer can cause the contact to form a Schottky diode instead of an ohmic contact, which can elevate the operating voltage by 1 V+ even at low bias current, which is disastrous for the laser wall-plug efficiency.

Hydrogen diffuses rapidly in semiconductors, even near room temperature [22], and diffuses much more slowly through SiO_2. The diffusion coefficient of hydrogen in SiO_2 is almost six orders of magnitude higher, so the InGaAs which is protected by the hard mask during the dry etch is similarly protected from hydrogen diffusion. However, as the mesa sidewall becomes exposed to the plasma during the dry etch, hydrogen can diffuse laterally several micrometers [23]. The problem of p-InGaAs passivation does not present itself in the bulk of the amplifier waveguide because the p-InP mesa is very wide, 26 μm, to improve heat sinking and eliminate the antisymmetric mode (See Section 4.1). The hydrogen does not diffuse laterally far enough to impact the central 4 μm current channel, and cannot diffuse vertically through the SiO_2 hard mask. In the III-V taper section, since the III-V ridge is narrow (between 4 μm and 300 nm), some or all of the structure is likely to be impacted by in-diffused hydrogen.

To test the hypothesis that narrow mesa structures suffer from increased operating voltage, a set of lasers was fabricated with successively narrower p-InP mesa widths. The forward IV characteristic of the three diodes is shown in Figure 5.8. The 8-μm-wide diode shows a sharp turn-on at 0.9 V, but the 4-μm- and 2-μm-wide devices have elevated operating voltage, even though the slope of the curve at high bias is similar to or lower than the 8-μm-wide diode, because the of reduced spreading resistance in the n-contact sheet (the n-contact metal is a fixed 2 μm from the p-mesa). The narrow mesas exhibit a slow turn on, and a second kink in the curve is evident at 1.7 V in the 2-μm-wide-mesa curve. This is believed to be due to a Schottky barrier formed at the p-contact because of reduced carrier density at the surface, which adds its turn-on voltage to that of the PN junction. The width of the hydrogen-contaminated region in the mesa can be inferred to be more than 2-μm wide, and probably

significantly less than 4-µm wide, since the 8-µm-wide mesa shows no evidence of contamination. A second kink might have been observed above 300 mA bias current as the electrode voltage increased above the turn on voltage for contaminated section of the contact.

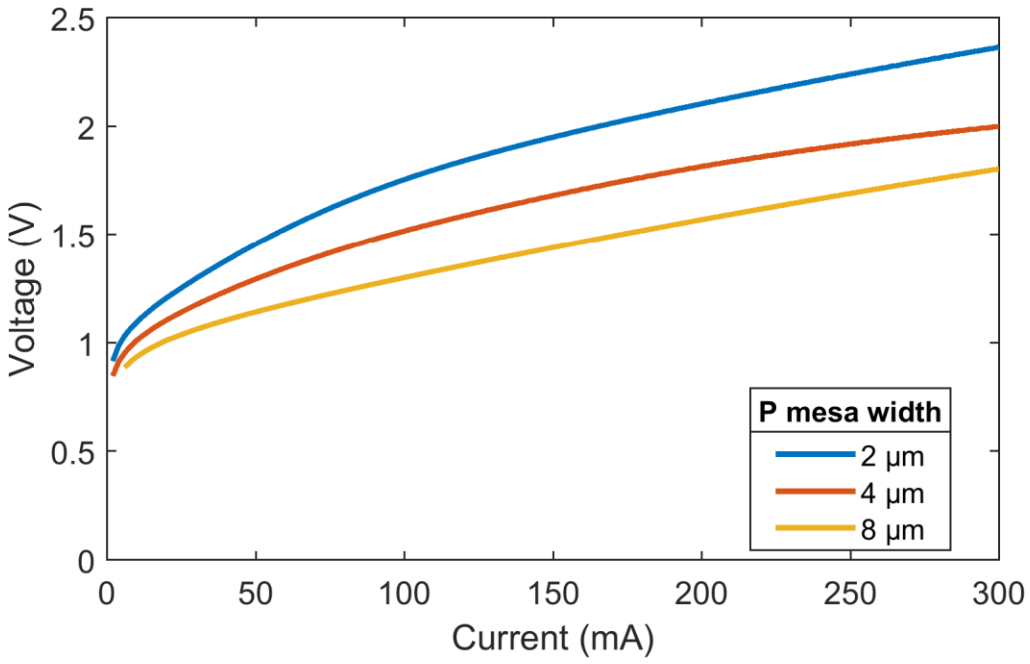

Figure 5.8: IV characteristics of 3-section lasers with various p-InP mesa widths. Narrower mesas exhibit elevated turn on voltage due to hydrogen passivation affecting the ohmic contact. Note that the standard mesa width in this work is 26 µm.

Annealing of the sample can drive out hydrogen and restore conductivity. [24] shows a 3-dimensional plot of conductivity versus time and temperature for hydrogen removal anneals. In InP, the carrier concentration can be restored to within 80% of the original value by annealing the chip for 2 minutes at 520°C, or within an order of magnitude by 2 minutes at 340°C. Unfortunately, heterogeneously integrated devices are damaged by thermal annealing at this temperature, as shown in Figure 3.18, so this option is unavailable.

Switching to a Cl_2-based dry etch could allow the removal of hydrogen from the recipe, but then the mesa dry etch has the chance to attack silicon in the areas which are not protected

by the bonded film, as discussed in Chapter 3. An ICP-based MHA etcher with higher etch rate might also reduce the etch time and therefore lower the amount of time that the hydrogen can diffuse through the semiconductor.

Since the turn-on voltage in the passivated section is higher than the desired operating voltage of a high efficiency laser, the III-V taper section will never pass the second turn-on voltage during normal operation, and so will be pumped at a lower current density than the rest of the laser. This explains the gain spectra shown in Figure 5.6, and the conclusion is that the transition must be designed such that the length and optical mode overlap in the III-V taper section is minimized.

5.2.4. Reduction in Length

This can be accomplished by increasing the relative propagation constant in the silicon waveguide compared to the III-V waveguide by decreasing the index of refraction and thickness of the III-V SCH layers, which can be controlled within the range of 3.18 and 3.65 by changing the alloy composition. Indices above 3.5, however, are absorbing at 1550 nm, and above 3.45 are impractical for MQW lasers because the band gap will then be narrower than that of the quantum barrier. The effect on the simulated loss versus length of moving from 8 QW epi with $In_{0.65}Al_{0.13}Ga_{0.34}As$ SCH, n = 3.46, and a 3 QW epi with $In_{0.54}Al_{0.21}Ga_{0.25}As$ SCH, n = 3.38, (these are Epi E and Epi H in Table 4-2 and Table 4-4), is shown in Figure 5.9, with the higher index design shown in blue and the lower index design shown in red. For example, to achieve passive loss below 0.1 dB, the high index design requires a 35-μm taper, while the low index design requires only 20 μm.

Similarly, the propagation constant of the silicon waveguide scales with the thickness and width of the silicon core. The width can be varied by simply changing mask dimensions. This

is the purpose of the flare shown in Figure 5.2e. The flare width in the "High index III-V" and "Low index III-V" simulations shown in Figure 5.9 was 1 μm. Widening the silicon waveguide to 2 μm reduces the length of the III-V taper further, only requiring a 13 μm length to attain passive loss below 0.1 dB.

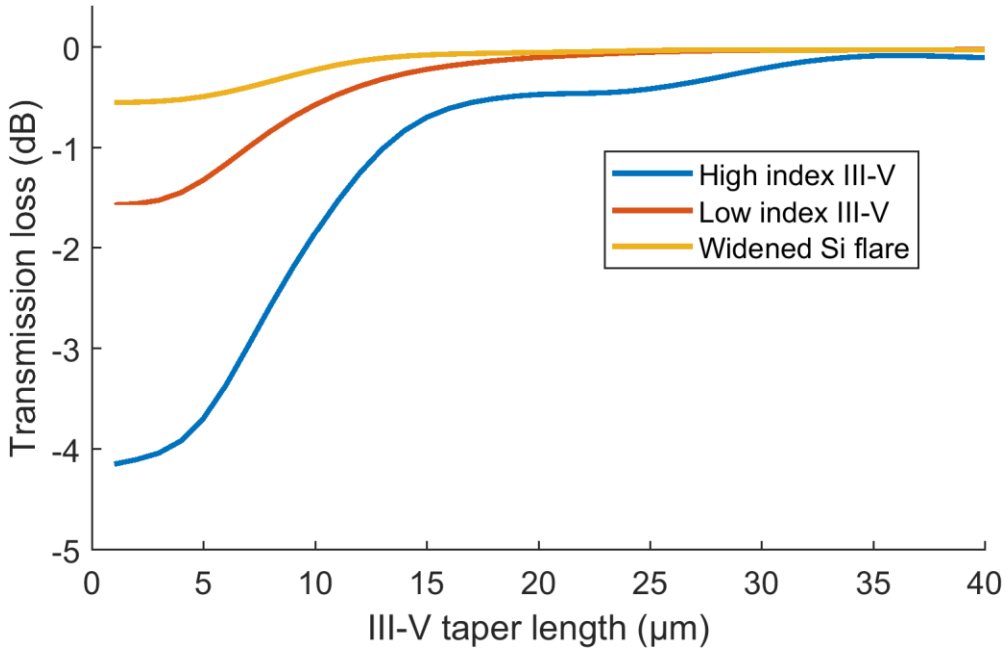

Figure 5.9: The impact of the silicon waveguide flare width on the taper passive loss. Low passive loss can be attained for shorter tapers when lower index and thinner III-V layers are used, and by widening the silicon waveguide flare.

Table 5-1: Dimensions of the heterogeneous transition

Dimension	Size (μm)
Si_{w1}	0.850[1]
Si_{w2}	2
Si_{w3}	0.8
Si_{L1}	100
Si_{L2}	100
InP_{w1}	26
InP_{w2}	4
InP_{w3}	0.5[2]

InP_{L1}	4
InPL2	20[3]

[1]varies, 850 nm typical.
[2]p-mesa width; active region width varies, was 150 nm on best devices.
[3]varies, 20 μm typical.

The dimensions of the basic linear flared transition are shown in Table 5-1. The labels indicated on the table are shown on a plan view schematic of the transition in Figure 5.10a. A 3-dimensional mock-up is shown in Figure 5.10b.

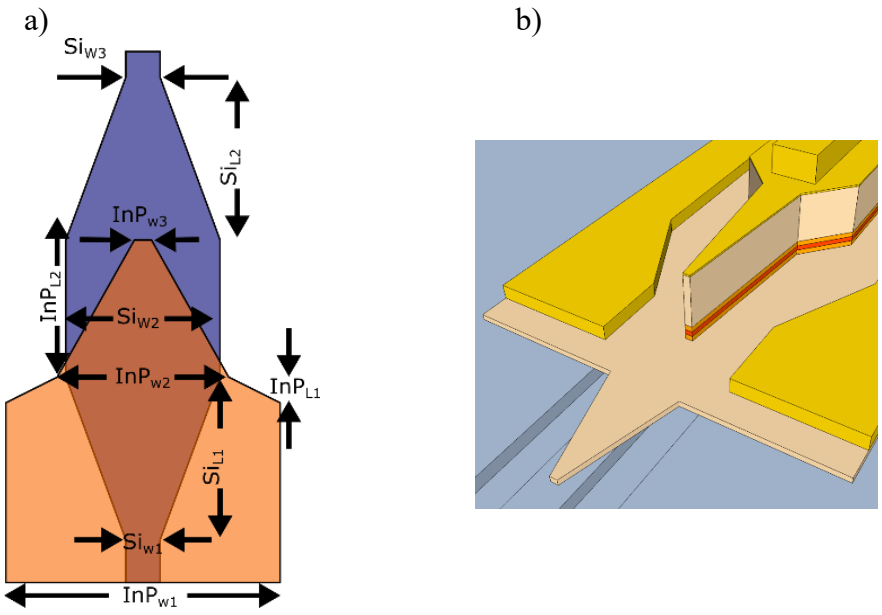

Figure 5.10: Schematics of the heterogeneous transition. Figure (a) shows a plan view with the dimensions indicated in Table 5-1. Figure (b) shows a 3-dimension mock-up of the transition, with the layer heights expanded in 4:1 scale relative to the feature widths.

To test the above transition design, a set of 3-section lasers was fabricated with a range of taper lengths and the slope efficiency was measured using an integrating sphere. The slope efficiency is tied to the losses inside the laser cavity, and other than the III-V taper length, the

lasers were identical, so variation in the slope efficiency can be attributed solely to the loss in the transition. The results of this experiment are shown in Figure 5.11. Shorter tapers have lower slope efficiency due to increased passive loss. As the taper length approaches 20 μm, the slope efficiency reaches its maximum, before beginning to decline again as absorption from the long, narrow, differentially-pumped taper section begins to increase.

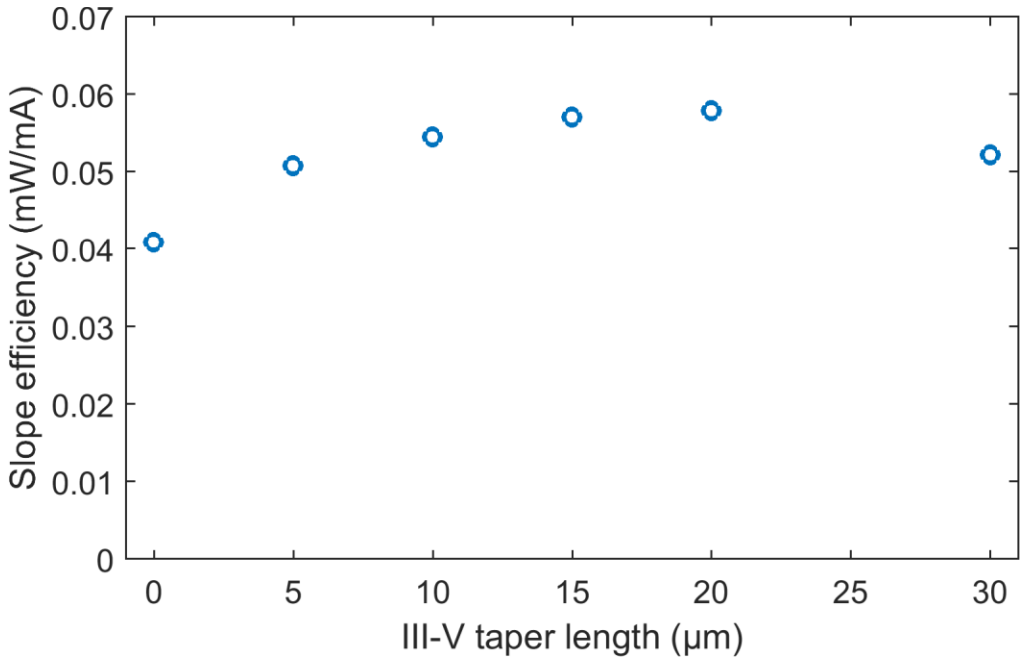

Figure 5.11: 1-sided slope efficiency of 3-section lasers with low index III-V (Epi H) and 2 μm-wide Si flare transitions, with various lengths of III-V taper. The 0 μm device was flat and angled at 15° to reduce reflection. The devices are identical other than the III-V taper length, so the change in slope efficiency can be attributed to the transition loss alone.

5.2.5. Spectral dependence of loss

To characterize the loss in the taper under forward bias and inside a working amplifier structure, a pair of 3-section lasers with identical design except for the gain section length were devised, shown schematically in Figure 5.12. These transitions use Epi H and a 2-μm-wide

silicon flare. The lengths of the active regions, not including the taper, were L_1 = 800 μm and L_2 = 1200 μm. Both devices have polished Si facets with power reflectivity of R = 0.28. Each laser was biased below threshold at the same current density, 375 A/cm^2, or 12 mA and 18 mA, respectively. The spectral gain was measured using an optical spectrum analyzer and the mode-sum minimum method [12]. Neglecting device heating, which should be minimal at this current density, one can assume that the spectral gain should have similar peak wavelength and bandwidth, with the smaller laser producing less gain proportionally to the difference in length. Any difference must be ascribed to fixed losses inside the cavity because fiber-to-chip coupling loss is ignored in the calculation of gain using this method. Only the spectral shape of the Fabry-Perot modes is required. In this case the dominant source of fixed loss is the taper loss l_t. Using:

$$l_t = \frac{L_1 g_2 - L_2 g_1}{2(L_2 - L_1)} - \alpha_{si} L_2 \qquad 5.1$$

where g_1 and g_2 are the net modal gain values versus wavelength of device 1 and 2 and α_{Si} is the propagation loss coefficient of the extra length of Si waveguide on the shorter device. The Si waveguide loss must be captured with a separate measurement. In this case it was only 0.02 dB over the length of 400 μm. The result of the calculation can be seen in Figure 5.12. The taper has loss as low as 0.25 dB / taper at 1600-nm wavelength, but the loss increases to 1 dB at 1550 nm. The increasing loss as the wavelength decreases is believed to be due to absorption caused by unequal pumping of the taper versus the gain section. This increases the loss at 1550 nm to 1 dB / taper.

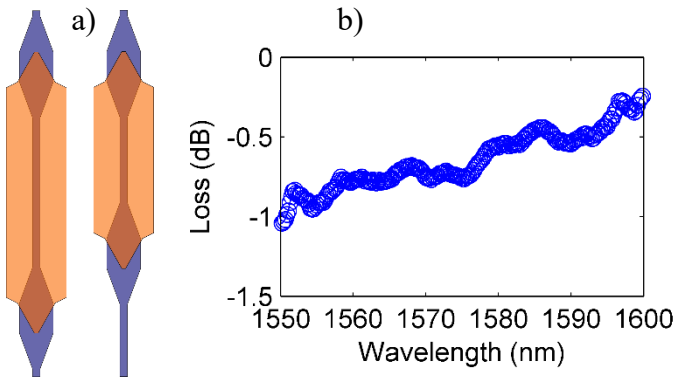

Figure 5.12: (a) Schematic of the two devices used for the taper loss measurement. (b) Loss versus wavelength from a single heterogeneous transition.

At 1550 nm, the total loss from the transitions is 2 dB. According to the simulations in Chapter 4, the propagation loss in the amplifier section is 4 cm^{-1}, which, in the case of the lasers discussed in Chapter 6 with 2 mm-long amplifier sections, amounts to 3.47 dB of loss. The silicon waveguides and loop mirrors (again see Chapter 6) add only 1.1 dB of loss. At this performance level, the loss in the heterogeneous transition will no longer have as large an impact as the earlier 80-μm-long tapers, which may have had > 7 dB of loss, since it is no longer the dominant source of loss. Naturally, the loss in the taper should be as low as possible for the best performance, but a prudent engineer at this point would be wiser to focus on the loss in the amplifier section.

5.3. Reflection

In addition to loss, waveguide transitions normally have an unintended parasitic reflection back into the waveguide mode. This reflection creates a standing wave with the forward propagating field between the unintended reflection and the intentional reflectors (normally the laser mirrors), and is subject to wavelength-dependent interference fringes, similar to a Fabry-Perot

interferometer. This is highly problematic in lasers which are intended to operate over a broad wavelength range, since the laser threshold will be elevated at wavelengths where a transmission null exists. In a tunable laser, this will degrade the side-mode suppression when tuned onto a wavelength null, or prevent lasing entirely at that wavelength. In a mode-locked laser, which is meant to lase in multiple modes simultaneously, the parasitic cavity will impose a super-modulation over the fundamental FP fringes that are intended to define the mode-locking frequency. This super-modulation can prevent mode-locking if the free spectral range of the parasitic cavity is small enough that too few modes fit inside of the interference maxima. The reflection also creates parasitic pulses that destabilize the laser by modulating the saturable absorber. An example lasing spectrum from a laser with high parasitic reflection impairment is shown in Figure 5.13. The laser is practically single-longitudinal-mode due to the multiple overlapping Fabry-Perot resonances, and is useless as a mode-locked laser.

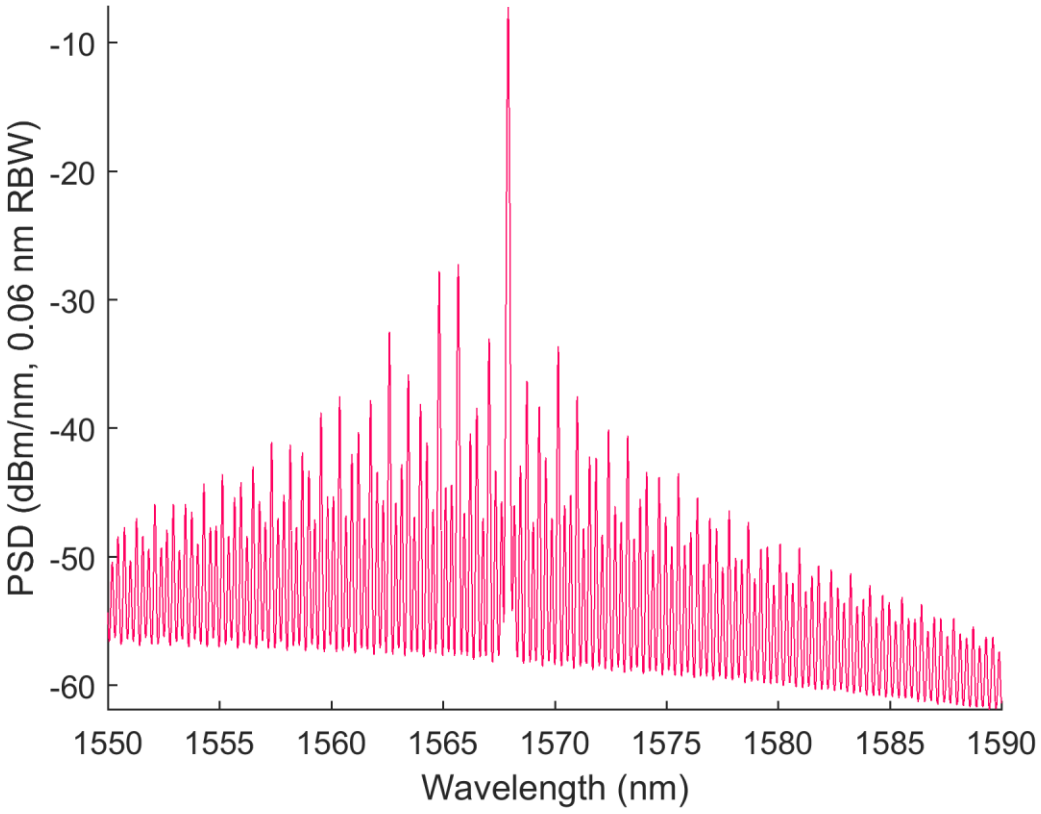

Figure 5.13: Lasing spectrum from a 3-section laser with ≈ -25 dB reflection at the heterogeneous transitions.

The minimum acceptable value for parasitic reflection depends on the application and on the length of the parasitic cavity. Longer parasitic cavities are more problematic than short cavities due to more frequent (in wavelength domain) interference nulls. Mode-locked lasers appear to be particularly vulnerable to parasitic reflection. The successful mode-locked lasers in this work all had parasitic reflections minimized to below −40 dB. Lasers with parasitic reflections higher than −27 dB would not mode-lock at all, and lasers with in-between values of reflection had impaired operating ranges and poor pulse width and noise performance.

The reflection value of a heterogeneous silicon/III-V transition was measured previously in [8] as −46 dB. This value is satisfactory for most laser applications. However, the device in [8] was all-passive, with the PL wavelength shifted down to 1480 nm to eliminate absorption. In addition, it is likely that the taper photoresist was overexposed and ashed back, which shortens the length of the structure compared to the as-drawn value, to reduce the tip size. This complicates metallization of the structure. It is also likely that the p-mesa dry etch was over-etched through the quantum wells, which, while attractive for reducing the size of the quantum well pattern, cannot be used in a high-yield process, as the etch rate of the AlGaInAs active region is extremely slow, requiring 45+ minute MHA etches. Very long dry etches in the UCSB MHA system have a strong correlation with micromasking and other dry etch failures.

Measurement of the taper reflection uses the method described in [25]. A 3-section laser is biased at its transparency current, then the ASE spectrum is captured using a lensed fiber and optical spectrum analyzer. A transmission matrix model of the 3-section laser is used to fit for the taper reflection. The loss and gain in the amplifier waveguide can be assumed to be

approximately zero because of the bias condition. The loss in the silicon waveguide, provided that the passive sections are short, can typically be ignored. The reflection from the facet can be assumed to be $R \approx 0.3$. This leaves only the taper loss and reflection. The taper loss itself is difficult to know accurately because of its spectral dependence and the clumsiness of the measurement technique used in Section 5.2.5. However, increasing loss should give the appearance of reduced reflection, since the field strength at the taper will be reduced by the absorption. If the researcher simply assumes that the loss is zero, then the worst-case, highest possible reflection can be measured. In this case, for good performing short tapers, the reflection is probably lower than what is indicated by this technique, but by only 0.4–2 dB (the loss of two transitions).

The taper-based heterogeneous transition has high index of refraction contrast, $\Delta n \approx 2$, as opposed to $\Delta n \approx 0.2$ in a regrown p-cladding offset quantum well InP-substrate laser, and so the reflection from the tip of the III-V taper at the termination can be problematic. The transition must be designed such that the light is fully transferred to the Si waveguide, and the tip is small enough that the mode field overlap with it is low. Initial simulation using the Eigenmode expansion and beam propagation methods of the reflection from the transition suggested that sub-1-μm tip size would be sufficient for −40 dB reflection. The p-mesa tip size was chosen to be 500 nm, which is the minimum feature size in UCSB's i-line projection lithography system. The initial active region layer design was the "Wide QW" design discussed in Section 5.2.2. Measurement of the reflection versus taper length is shown in Figure 5.14a for two different taper designs, the wide QW and narrow QW (Figure 5.12b). The first observation from the data in Figure 5.12a is that the reflection depends on the length of the taper, predictably being high for the 0 μm taper (which in this case was not angled). The decline

with respect to length is because the shorter tapers are less adiabatic, so the light is not fully transferred to the Si waveguide before the termination of the III-V waveguide at the taper tip. The reflection approaches an asymptote at about −25 dB for very long tapers. The second observation from Figure 5.12a is that the wide QW transition has significantly higher reflection, almost 10 dB in the worst case, and no dependence on length.

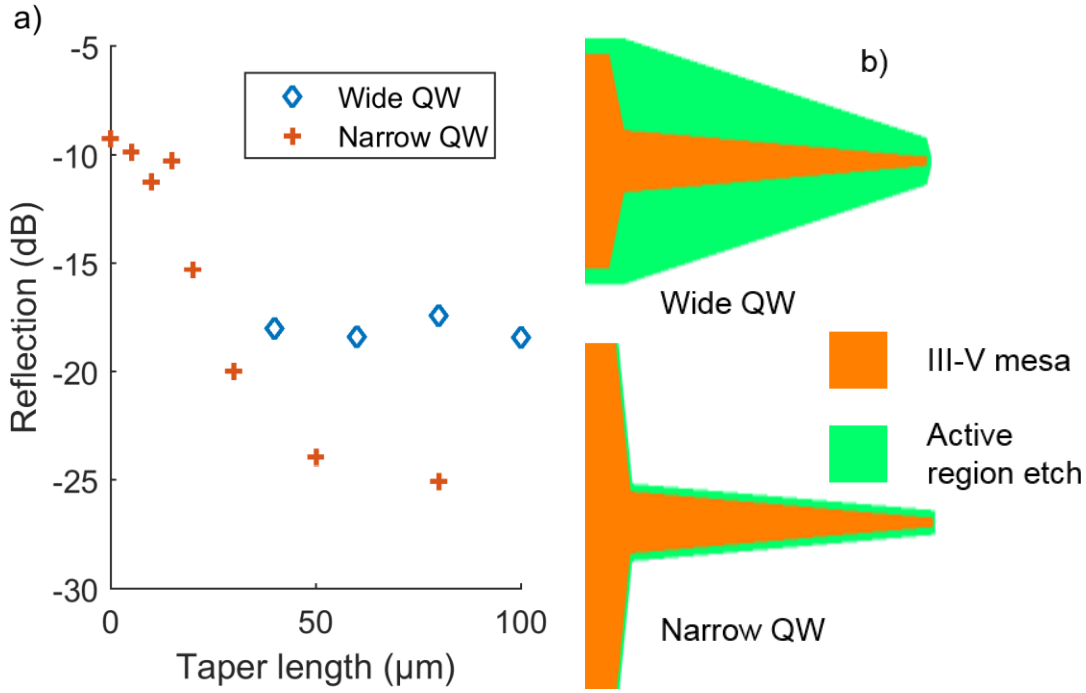

Figure 5.14: The impact of the quantum well pattern size on the taper reflection. (a) is the reflection versus the III-V taper length, and (b) is a plan view schematic showing the QW taper style. The p-mesa taper design was identical. These tapers used Epi E, which is the "High Index III-V" design in Figure 5.9.

This leads to the hypothesis that the active region taper is providing the transformation of the mode, and the wide QW taper is simply too abrupt, even at 100 μm length, due to the larger initial width of 14 μm (compared to 4 μm for the narrow QW taper). For this reason, the wide

QW design was abandoned, despite the slight advantage in LI characteristics shown in Figure 5.7a.

To test the impact of the p-InP tip size, a set of 3-section lasers with varying tip sizes was produced. This process was moved to 248-nm deep-UV lithography to achieve sub-500-nm features. Isolated lines can be produced below the resolution limit of the tool by over exposure, and so a range of p-InP tip sizes from 50 nm to 900 nm were produced with 20-µm-long narrow QW tapers. The reflection showed a surprising trend: 500 nm (the previous standard design) had the lowest reflection. Larger tip sizes predictably increase the reflection, but smaller tip sizes increase it as well. This confirms what was suggested by the wide-versus-narrow QW experiment: the reflection depends primarily on the active region dimensions. Note that the dimension plotted in Figure 5.15a is the width of the taper at the base. The best design was drawn at 300 nm on the mask, and is 500 nm at the base due to non-vertical etched sidewall.

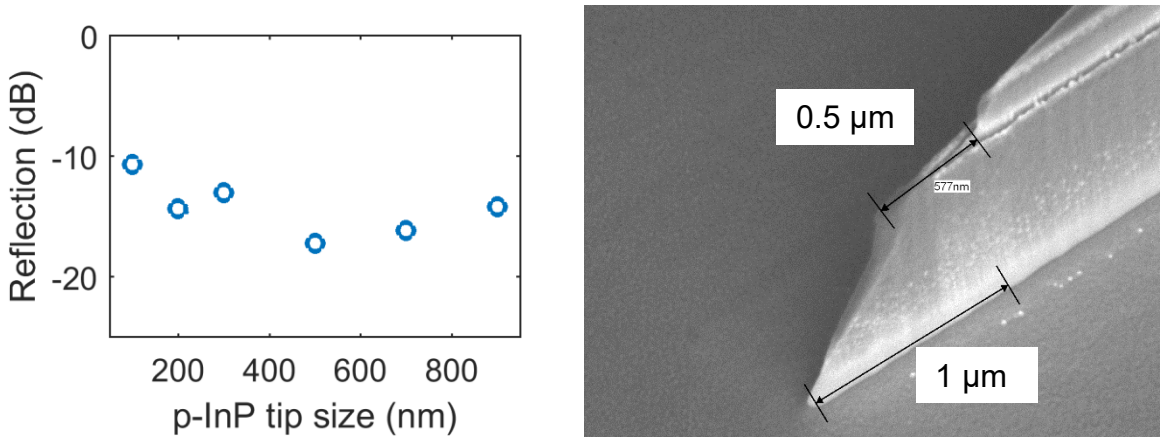

Figure 5.15: Taper tip size experiment. (a) shows the measured reflection versus the p-InP tip size. (b) shows the smallest taper, which was drawn as 50 nm but resolved at 85 nm at the top and 126 nm at the bottom due to mask erosion and non-vertical etch sidewall.

The horizontal asymptote at –25 dB in Figure 5.14a likely represents the feature shown in the QW confinement factor in Figure 4.9, where the mode has become evanescent in the III-V

layers and will no longer have increasing confinement factor in the silicon as the silicon waveguide is increased. Reducing the relative propagation constant of the III-V waveguide by reducing the thickness or index of refraction of the III-V waveguide core, similar to the approach taken for reducing the length of the taper in Section 5.2.4, can reduce the evanescent confinement in III-V. The same set of 3-section laser devices were fabricated using Epi H, which has lower index SCH (n = 3.38 vs. n = 3.45) and fewer quantum wells was fabricated and tested for reflection to be compared to the result for the narrow-QW lasers in Figure 5.14. These tapers also have the narrow QW design. The results of the experiment are shown in Figure 5.16. The low index epi design (Epi H, Table 4-4) shows lower minimum reflection and reaches the minimum value for shorter III-V tapers.

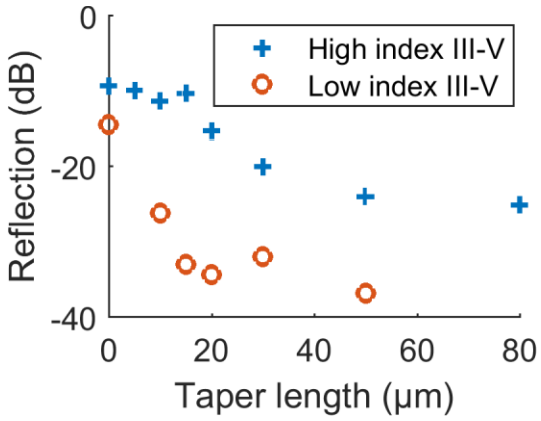

Figure 5.16: Taper reflections for high index (Epi E) and low index (Epi H) III-V designs.

Reducing the propagation constant of the III-V waveguide had a significant impact on the minimum reflection, reducing it from −25 dB to −36 dB. Reducing the p-InP tip size is unhelpful, and the active region taper tip size cannot be drawn smaller than 500 nm, as this is the optimum value for reflection and loss for the p-InP pattern. To attain a smaller active region tip size, the active region wet etch length can be extended to undercut the p-InP mesa. This can shrink the active region taper tip to below the size of the p-InP mesa, since the phosphoric acid

etch mixture (see Section 3.3) etches neither photoresist nor p-InP at a measurable rate. The reflection for the undercut taper is compared to the narrow QW design in Figure 5.17. Both sets of lasers have 300-nm-wide (as drawn, 500 nm at the base) p-InP taper tips and the Low Index III-V (Epi H) design. The lowest reflection value is −43 dB for the 30 μm-long taper design. Inexplicably, the reflection increases slightly for longer tapers. This could be explainable by decreasing loss in the longer tapers due to being more adiabatic, but Figure 5.9 shows that the change in loss due to increasing length beyond 30 μm should be below 0.1 dB, and the slope efficiency of the longer tapers was, as usual, lower than the 30 μm taper. It is possible that the longer tapers, which are very narrow over a longer absolute length of the taper, may be eroded by the wet etch and no longer as sharp.

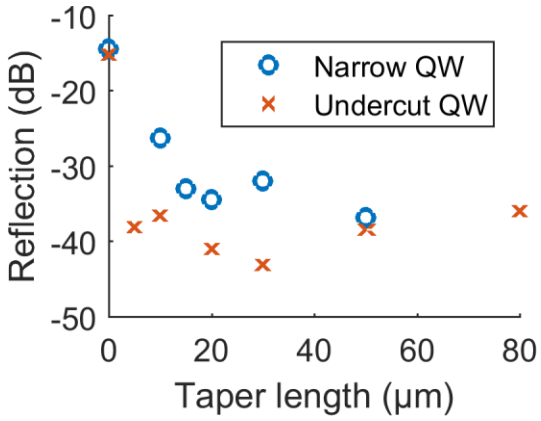

Figure 5.17: Taper reflections versus length for the undercut QW, compared to the narrow QW.

The tapers were undercut by etching the 1.3-μm-wide photoresist pattern (300-nm p-InP pattern plus 2 x 500-nm alignment tolerance overhang) for 1 minute and 30 seconds. The tip size underneath was intended to be dead sharp. Inspection of cleaved samples showed that this produced around 550 nm of undercut, so that should correspond to a 100-nm-wide taper tip in

the active region pattern. However, a FIB inspection should be performed on the actual device to confirm this.

The best transition reflection, with the low index III-V layers, 300-nm-as-drawn p-InP tip, 2-μm-wide silicon flare, and undercut QW active region design, demonstrated −43 dB reflection. It will be shown in the following section that this reflection comes from the n-layer transition, which in these designs was simply a 1.25 μm-long stub that was right underneath the p-InP taper, and so could not be separated from the main taper reflection spatially in the Fourier transform method.

An obvious omission from this section is the lack of accurate simulation data. As mentioned earlier, Eigenmode expansion did not produce accurate values for reflection, underestimating it by over 40 dB. The beam propagation method does not produce accurate simulations for very short tapers, which violate the paraxial beam approximation. Eventually, FDTD was found to be the closest to accurate.

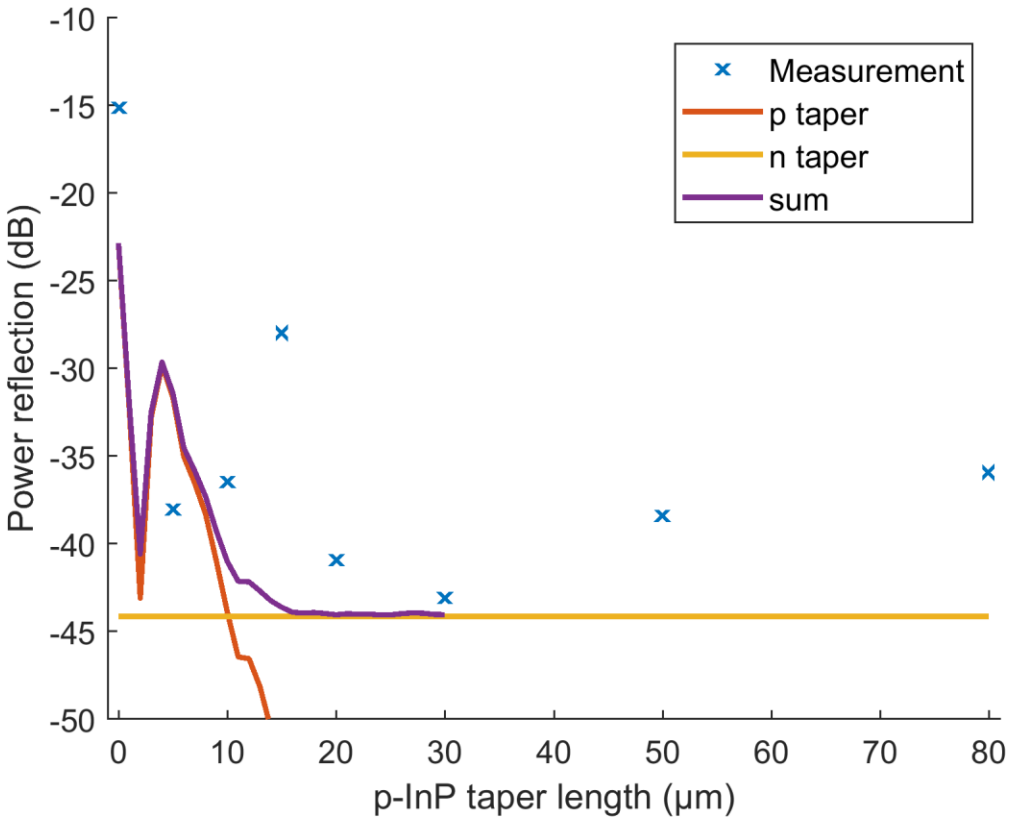

Figure 5.18: FDTD simulation of the undercut-style taper. Blue X symbols denote the measurement data. The red line indicates the simulated reflection from the p-mesa and active region taper only. The yellow line is the reflection from the n-layer transition (to be discussed in the next section), and the purple line is the total reflection from both transitions.

While the FDTD simulation is within an order of magnitude of the measured value in most cases, it does not accurately reproduce the position of the peak at 15 μm in the measurement, or the increase in reflection after 30 μm. This does cast some doubt on the measurement results from this section. The lasers all have the same dimensions (length, current channel width) and the same waveguide design, (1.5-μm wide and 250-nm-etch depth into 500-nm SOI device layer). Each data series in the reflection plots, i.e., all devices with the same color and symbol in a single figure, were co-fabricated on the same chip in close proximity to each other, so variation in fabrication from run to run and even from one part of the die to another should be

minimized. The variation in fringe depth of the parasitic cavity interference pattern super modulation induced by the reflection should represent variation in reflection, with the caveat that high loss designs may have higher reflection than indicated. Since Figure 5.11 does not show immense variation in slope efficiency, it can be assumed that the variation from loss from this oversight is only a few dB, at most. The differing active region etch designs, wide QW, narrow QW, and undercut QW, were fabricated on different chips, but the variation in reflection between those devices was so large that fabrication variation can be ruled out. Therefore, the conclusions drawn from this section, that individual designs are superior to others with respect to reflection, should be accurate, even if the quantitative value of the reflection is not.

5.4. N-layer transition

The n-InP contact layer must extend laterally from the III-V taper for electrons to be injected into the taper. Even though the p-InP taper is not fully pumped to the same current density as the amplifier section, it is still pumped enough that removing this injection completely will increase the loss considerably. The n-InP layers consist of a 110-nm-thick layer of InP, followed by a 5-layer superlattice of InGaAsP/InP (see Table 4-1). Typically, to uncover the passive Si devices to expose them to the cladding deposition, the n-InP is removed over most of the circuit. This requires a transition between the n-layer-covered waveguide and the uncovered silicon waveguide.

The design used in early publications was essentially an extremely short taper, 3-μm-wide at the beginning, 0.5-μm-wide at the end, and 1.2 μm in length, shown in Figure 5.19a. The original designer likely used Eigenmode expansion and assumed the reflection would be

negligible, but later expansion on the design in FDTD (see Figure 5.18) suggests otherwise. As with the p-InP mesa taper, too short taper length can increase the reflection drastically, so structure was widened at the base to 4 μm and lengthened to 20 μm, as shown in Figure 5.19b. Simulation of the reflection versus taper length for the Figure 5.19b taper is shown in Figure 5.20. The data point at 0 μm length indicates the reflection from the stub transition from Figure 5.19a. The reflection can be improved by as much as 4 dB by increasing the length.

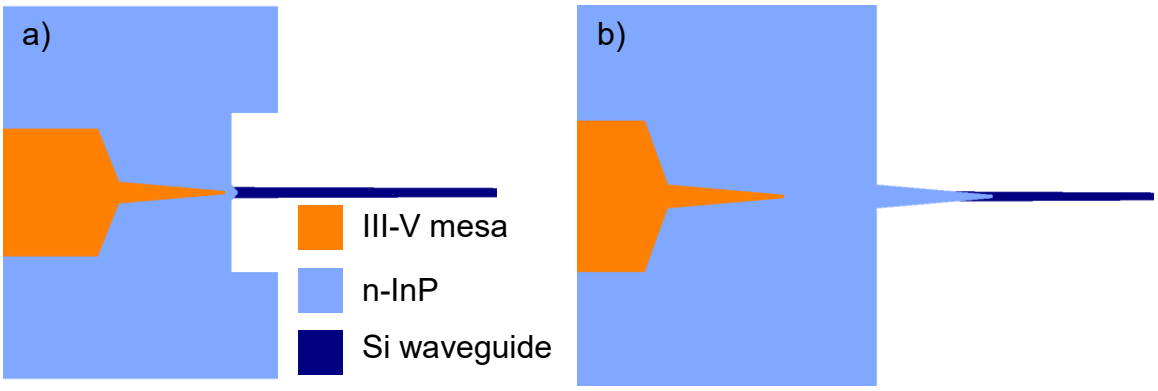

Figure 5.19: Plan view schematics of two n-layer transitions. (a) shows the original taper design. (b) shows the lengthened version.

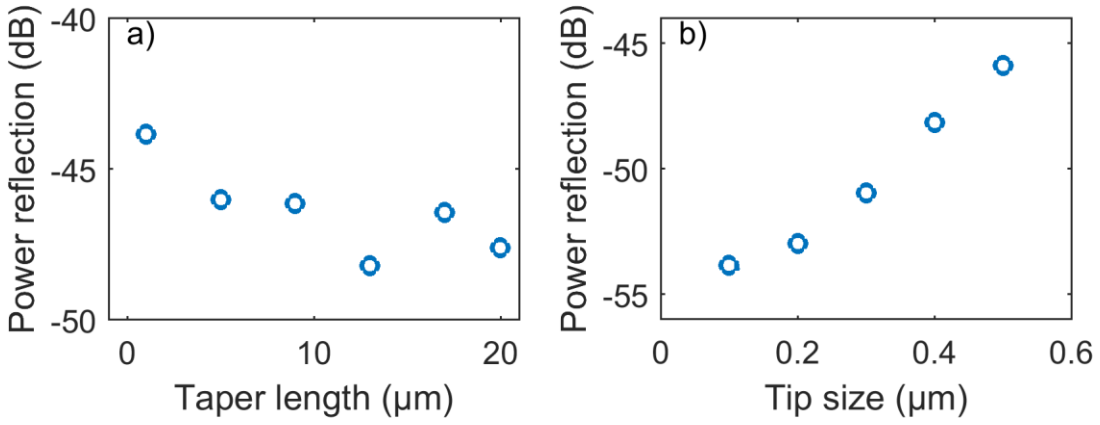

Figure 5.20: (a) Reflection versus length for the 4-μm-base 0.5-μm-tip n-InP taper. (b) Reflection for a 20-μm-long taper with various tip size. Reduction in tip reflection by another 8 dB could be possible with DUV lithography.

Combining the n-layer taper with the low-index, undercut QW, 2 μm Si flare, 20 μm-long, produced an extremely small reflection. To increase the sensitivity of the measurement, the 3-section laser was cut in half to form a 2-section laser. This increases the FSR, allowing the OSA to be operated at a numerically higher resolution bandwidth (e.g., 0.1 nm instead of 0.05 nm), which increases the sensitivity. The result of this measurement is shown in Figure 5.21 as the red line. The model, using −46 dB for the taper reflection, is shown as the blue line. The feature indicated by the numeral I is the Fabry-Perot resonance between the polished silicon facet and the polished heterogeneous facet. Numeral II indicates the position of the taper reflection. The source of the pair of side lobes on the main FP peak indicated by numeral III is unknown. They are present in pure FP single section lasers, so they are not caused by the taper. The forest of peaks near the DC indicated by IV are due to higher order mode emission into the deeply etched multimode silicon waveguide.

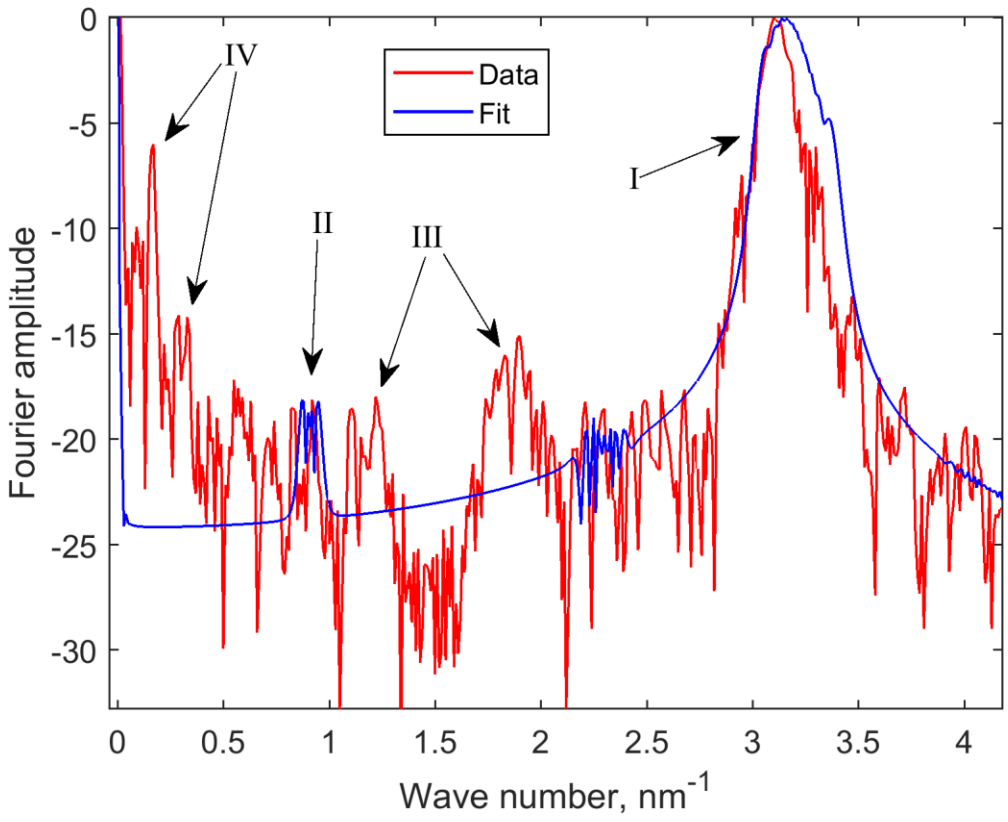

Figure 5.21: Fourier transform of a 2-section laser. The red line shows the FFT of the measured ASE data. The blue line shows the FFT of the matrix model fit. The Roman numerals indicate notable spectral features.

While the reflection peak has been reduced to below −40 dB, the higher order mode emission is quite high. This creates a super modulation on the output spectrum by forming a sort of unbalanced MZI in the passive waveguide section. Emission going out of the amplifier through the taper into the passive waveguide has some emission into a higher order mode. This mode has a different effective index than the fundamental mode. The two modes propagate in the passive waveguide section and reflect nearly equally from the facet mirror, returning to the taper tip. Due to the principle of optical reciprocity, the two modes would recombine into the fundamental mode, except that now a phase difference has accumulated by their transmission through the passive waveguide. At certain wavelengths, they are in the correct phase and will recombine into the fundamental mode in the amplifier waveguide, but at wavelengths where the modes do not have the appropriate phase, there will be loss. This creates a similar spectral modulation to a reflection. The FSR of the induced modulator will depend on the difference between the propagation constants of the two modes and the length of the passive waveguide section. This is depicted schematically in Figure 5.22.

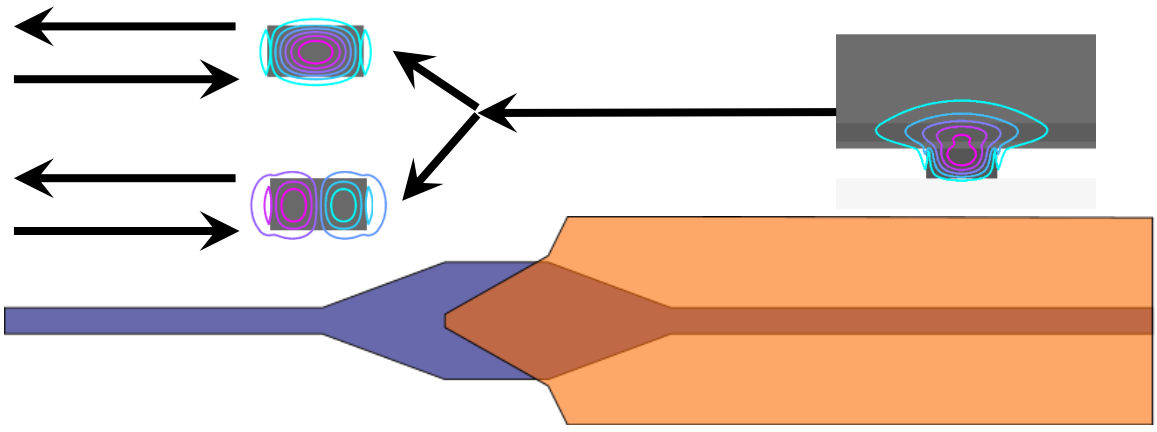

Figure 5.22: Schematic depiction of the multimoding interference effect.

A laser with 1-mm-long passive waveguide sections and likely large transmission into a higher order mode is shown in Figure 5.23. This is not quite as problematic as the high parasitic reflection laser Figure 5.13. There are a few groups of 2-4 modes, so mode-locking is possible. Short pulses will not be able to be generated from a laser like this, however, so the effect needs to be mitigated.

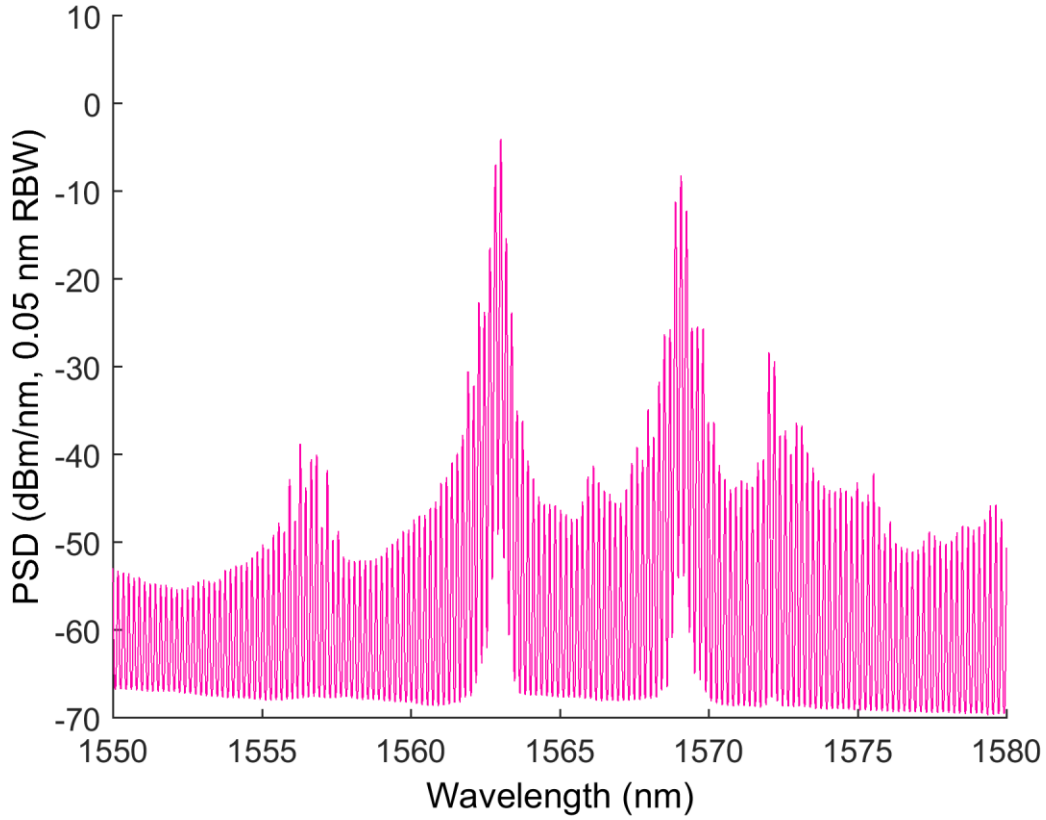

Figure 5.23: Lasing spectrum from a 3-section laser with low reflection (≈ −46 dB) but high transmission into a higher order mode (probably −15 dB)

Tapers intrinsically emit a small amount of higher order modes into multimode waveguides, even if the tip size approaches zero. This is because the condition that the normal component of the electric flux be equal across a boundary. Even if the taper tip is

infinitesimally small, the mode will be perturbed in the cladding around the taper tip (see Figure 5.2c and d for an example). The mismatched modes can then couple with radiation modes or higher order guided modes. The obvious solution would be to output into a fundamentally single mode waveguide. This is challenging since single-mode silicon waveguides are usually 220-nm thick, as opposed to the silicon used in this work which is 500 nm. At 220 nm, it is difficult to achieve low confinement in the III-V waveguide. Some groups have demonstrated 2-level silicon waveguides for this purpose [26], but the manufacturing complexity of these approaches is beyond what is available in this work. Shallow etching of the silicon waveguide less than 50% of the device layer thickness can also eliminate almost all of the higher order modes, and a bent partially etched waveguide will have high loss for the higher order modes, making it quasi single mode. Unfortunately, the directional coupler requires a fully etched waveguide for repeatable definition of the laser mirror reflectivity (see Section 6.2), so the tapers must be designed to produce functional mode-locked lasers with deeply etched multimode waveguides.

The source of the highest transmission into higher order modes, according to simulation, is misalignment of the n-layer taper to the underlying silicon waveguide. If the taper is not perfectly centered, then the even symmetry of the fundamental mode is broken and the overlap with the TE10 mode increases, as shown in Figure 5.24. This particular lithography is conducted in the i-line Autostep200 system, which typically has around 200 nm of misalignment. Transporting the process to the deep UV system, which has 20 nm of misalignment, would be one approach to dealing with this issue. However, during most of this work, the DUV system did not have an adequately thick photoresist for this process, and the wafers were often quartered before the n-layer step to mitigate risk to the individual dies.

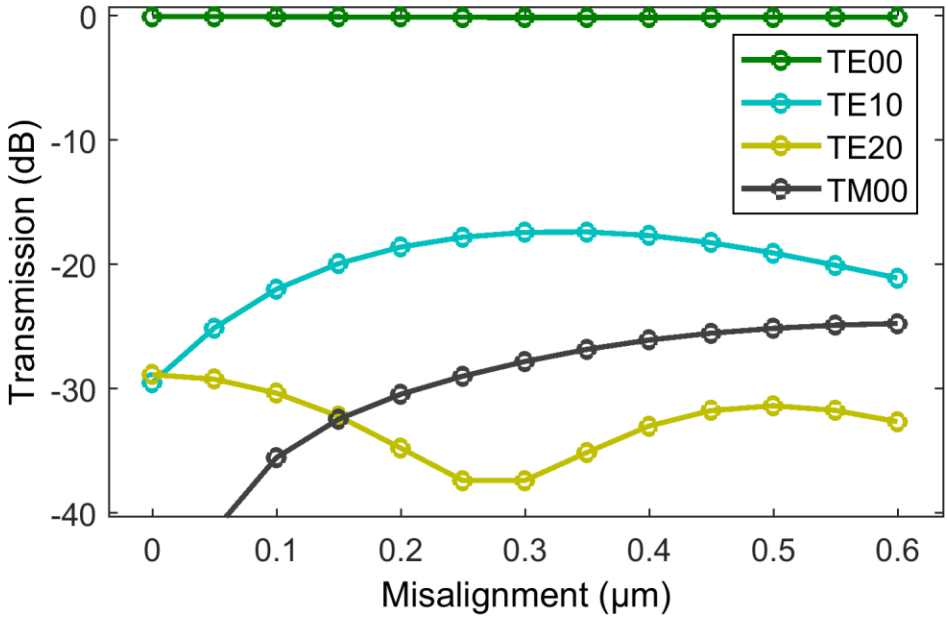

Figure 5.24: Transmission into guided higher order modes by the n-layer taper when it is not accurately aligned to the center of the silicon waveguide. Transmission as much as -17 dB into the TE10 mode is possible with only 300 nm of misalignment.

The solution, at least until the process can be transported to a system with better alignment accuracy, is to change the transition from a taper into a simple angled junction, as shown in Figure 5.25. The angled junction cannot be misaligned, and with proper selection of the angle, the parasitic reflection can be reduced to a level comparable to the taper.

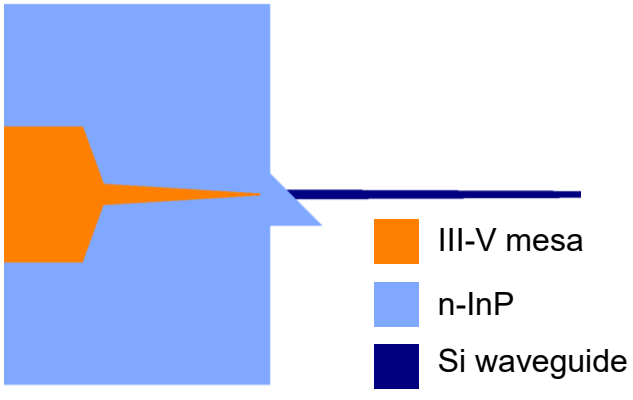

Figure 5.25: Schematic of the angled n-layer junction.

Optimization of the angle to minimize the transmission into higher order modes was carried out using FDTD. Figure 5.26a shows the higher order mode transmission from 0° up to 85°. Higher angles became too long for FDTD simulation due to the asymptote of the tangent function at 90°. Certain angles, such as 26°, have relatively high transmission into the TE01 mode, which is the most critical as it cannot be removed by the spline bend (see Section 6.3). The TE10 mode is gradually increasing with angle. A detail of the region around 45° degrees is shown in Figure 5.26b. The optimal point is 46°, although for some reason the researcher programmed 45° into his mask.

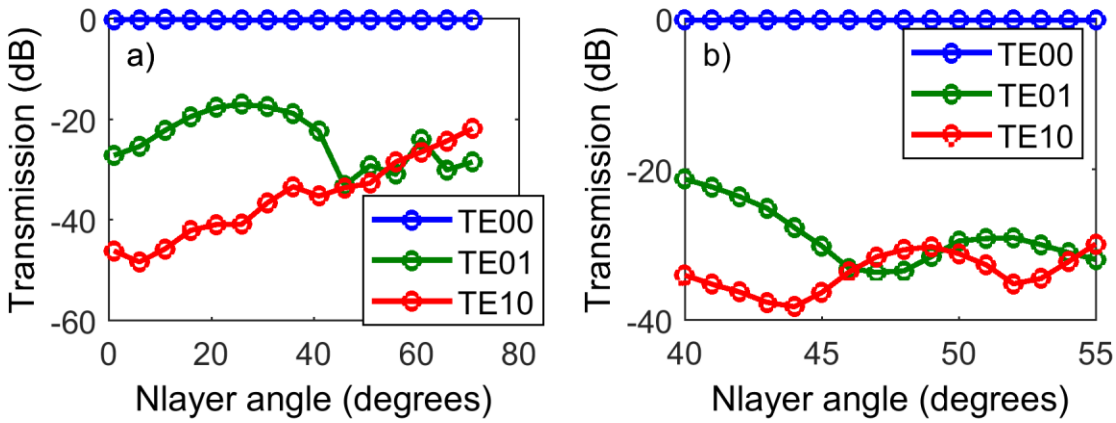

Figure 5.26: Transmission versus the angle of the n-layer junction. (a) is a wide range of angles and (b) is a closer look at near the optimum value of 46 degrees, when the sum of the two propagating higher order modes is minimized. The transmission into higher order modes is reduced to −30 dB (−33 dB into each higher order mode), an improvement of 13 dB over the typical misaligned n-layer taper.

Reflection must be considered as well. The n-layer taper reflection is low enough without much design effort, (Figure 5.20), and reflection is normally a more critical value than parasitic multimoding. Once again, FDTD is the only option for accurate simulation of reflection. Figure 5.27 shows the simulated reflection versus angle. While the reflection into the TE00 mode is

below −40 dB for all angles, there can be a significant reflection into the TE01 mode for angles below 15°.

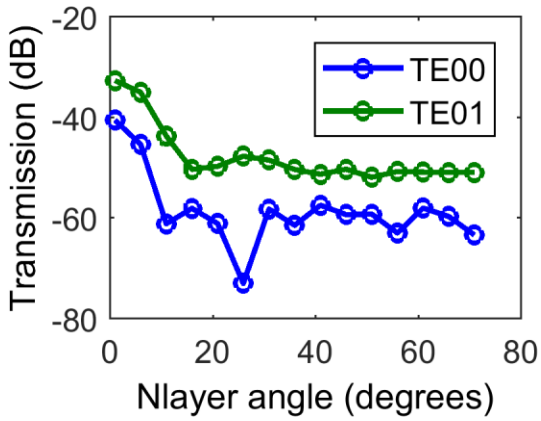

Figure 5.27: Reflection versus angle for the TE00 mode and the only propagating higher order mode with significant reflection, TE01. Reflections are both below −50 dB for all angles above 15°.

From this point forward, all of the laser test structures for transitions are fully integrated, as they were included in mode-locked lasers to be able to test the effect of the taper on mode-locking performance. Making them into 3-section lasers would be destructive, and so quantification of the reflection is no longer possible because there is no on-chip reference reflection, which is normally available from the flat polished facet. Lasers that were otherwise identical can still be compared, so one type of transition can be compared to another without quantification.

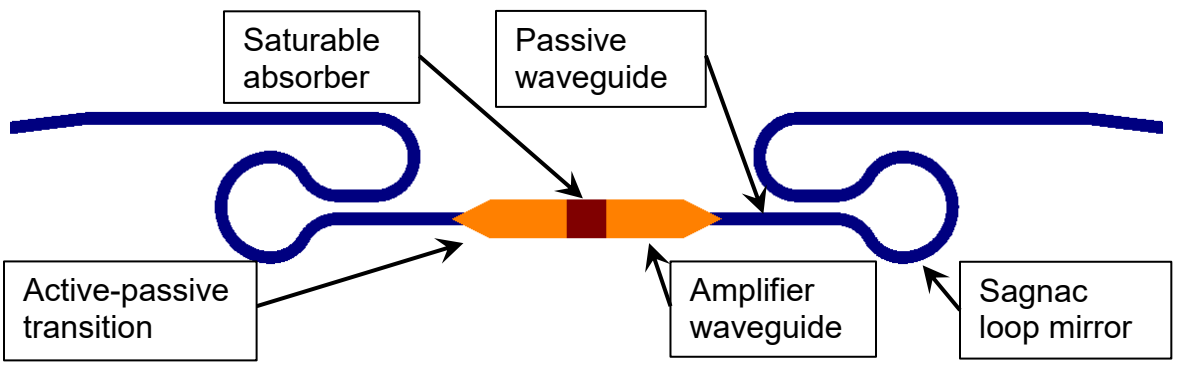

Figure 5.28: Schematic of the integrated laser presented in the following comparisons of heterogeneous transitions.

Two such devices, one with the n-layer taper of Figure 5.19b and another with the n-layer angle of Figure 5.25 were fabricated together, and the Fourier transforms of their ASE spectra are compared in Figure 5.29. The multi-mode interference peaks—shown at I—from the n-layer taper are stronger in amplitude than the mirror-to-mirror resonance, which the plot is normalized to. The mirror-to-mirror resonance is at ≈ 4000 μm and is not shown. The n-layer angle eliminates the higher order mode excitation down to the noise floor level, an improvement of 5-8 dB, depending on the mode. Unfortunately, the angled junction also has increased reflection, indicated by the symbol III. The increased reflection at II corresponds to the parasitic cavity between the low-reflection facet and the laser mirror. The cause for this variation was not determined but almost certainly is unrelated to the transition design.

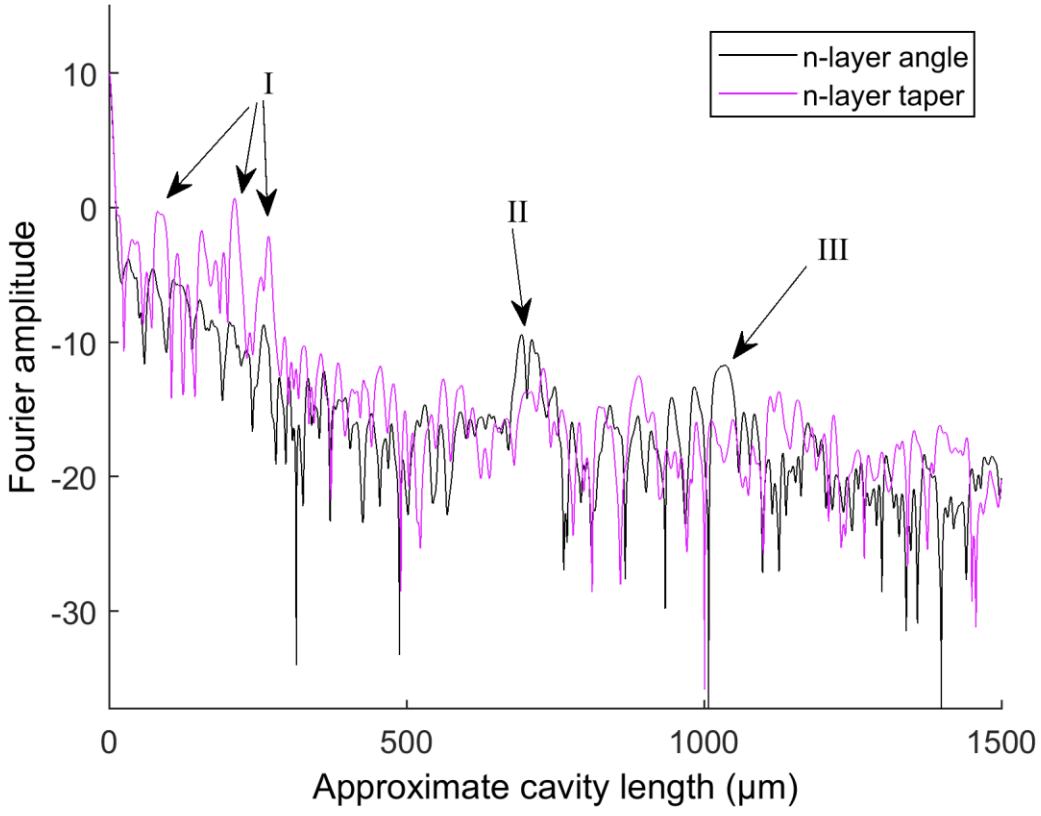

Figure 5.29: Comparison of the Fourier-transformed ASE spectra of two fully-integrated lasers, one with an angled n-layer transition (black) and the second with a tapered n-layer junction (magenta). The multimode interference peaks indicated by the symbol I are eliminated down to the noise floor by the n-layer angle, but the reflection is increased, as shown by the symbol III. The symbol II indicates the reflection between the angled facet and the laser mirror, which varied from device to device for an undiscovered reason.

The n-layer transition, despite its apparent simplicity, was the cause of failure for an entire run of mode-locked lasers (EPHI 4.1), which were particularly highly misaligned. For low reflection, the lowest value transition measured in this work used the n-layer taper, but those devices did not produce mode-locked lasers due to the multimode interference problem. Adopting the n-layer angle produced stronger mode-locking. If the misalignment in the n-layer taper could be resolved, for example by using the deep UV stepper, then it would have comparable performance with respect to multimode interference. In addition, if the constraint of requiring a deeply etched waveguide were removed, shallow etching resolves the multimode interference, even when the n-layer taper is used. According to the simulation in Figure 5.18, the reflection from the transition is limited by the n-layer transition. A shallow etched Si waveguide with a deep-UV lithography aligned and sized taper tip could achieve even better performance, in terms of both multimode interference and reflection, than what was demonstrated in this section.

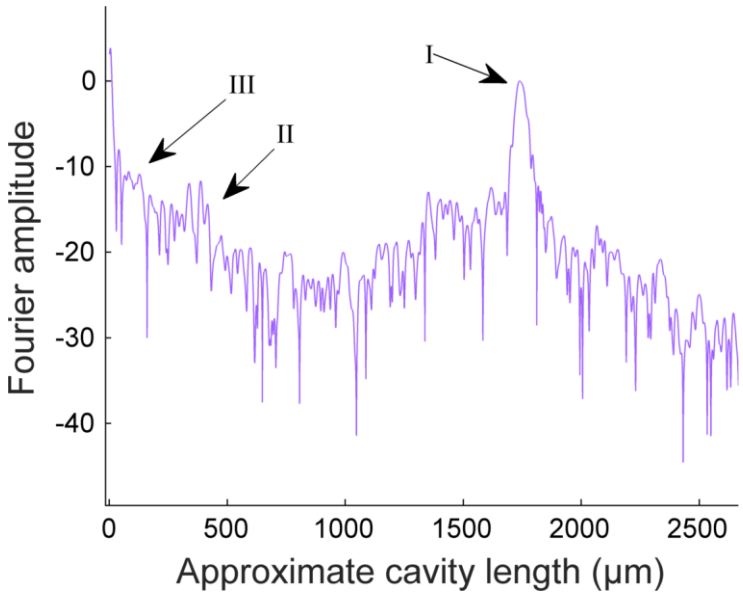

Figure 5.30: Fourier transform of a 3-section laser ASE output. The laser has a 245-nm-shallow etched Si waveguide and a taper-type n-layer transition. I denotes the Fabry-Perot resonance. II is the reflections between the taper and the polished Si facet. III shows the position of typical higher order mode interference, which was not present in this device.

The simulated loss is slightly higher in the n-layer angle (0.16 versus 0.06), but experimental investigation did not display a significant impact in the laser output power efficiency. Figure 5.31 shows the LI characteristic of two otherwise identical lasers that have the two designs. Near threshold the performance is practically identical. It has been suspected that the propagation loss in the n-InP is higher than predicted in literature due to residue or damage on the n-InP surface, and so it is possible that the shorter overall length of n-InP waveguide in the angle makes up for the increased passive loss.

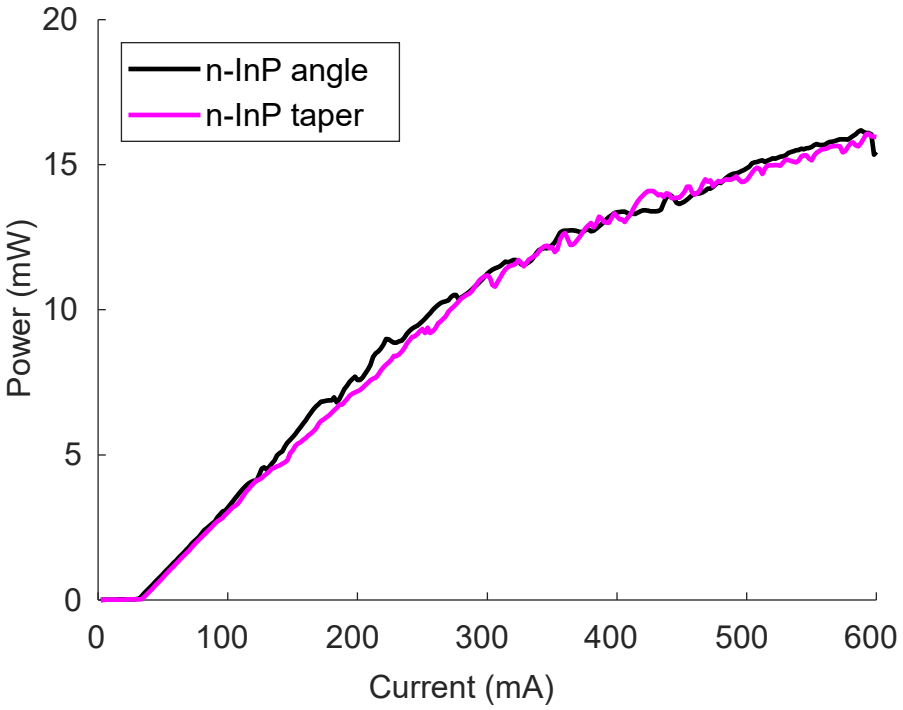

Figure 5.31: LI characteristic of two otherwise identical integrated lasers, one with the n-InP taper design (magenta) and the other with the n-InP angle design (black).

The n-InP transition, despite appearing to produce only a minor alteration of the mode profile, can still be detrimental to the laser performance if it is not designed properly. Basic linear tapers have adequate performance in the ideal case, but even small misalignment can generate an unacceptable amount of emission into higher order modes in the passive silicon waveguide. Adopting the angled transition design reduces the higher order mode emission by 15 dB in the worst-case misalignment and 4 dB in the best-case alignment compared to a taper. The reflection appears to increase slightly, but this is considered to be an acceptable compromise. Shifting the n-InP lithography to the deep UV lithography system could allow improved performance n-InP tapers by reducing the tip size and improving the alignment accuracy. A perfectly aligned 100-nm taper tip would likely be superior to the angled transition.

5.5. Conformal-index Taper

The p-type InP and active region taper initially presented major performance impairments for the laser due to high loss and high reflection (sections 5.2 and 5.3). Reduction of loss to below 1 dB was accomplished primarily by reducing the length of the taper to reduce longitudinal confinement factor and widening the silicon waveguide to reduce transverse confinement factor. Unfortunately, as an unintended side effect, these measures introduce parasitic higher order mode emission into the silicon waveguide, which supports a large number of higher order modes at 2-μm width and 500-nm thickness, regardless of the waveguide etch depth. Figure 5.32 shows the transmission into higher order modes versus the length of the III-V taper for the transition design in Table 5-1. Note that since this process works with thin photoresist, it has been done in the deep UV system, and so misalignment does not need to be considered.

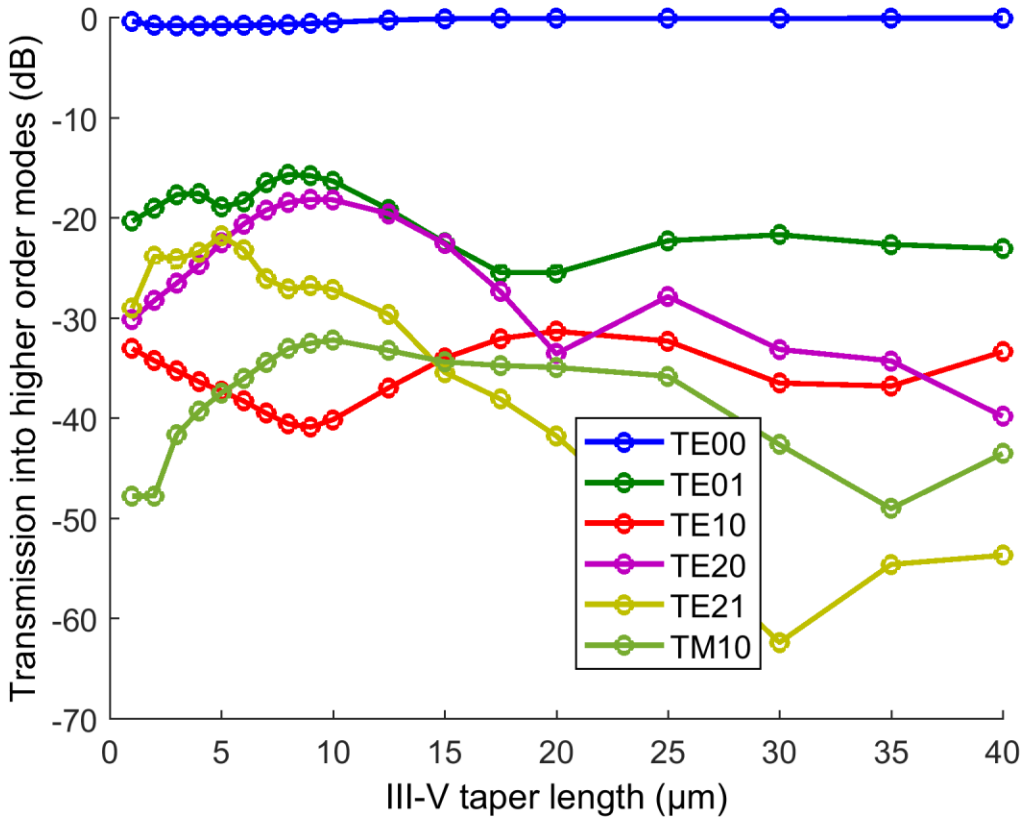

Figure 5.32: FDTD simulation of modal transmission for the low index III-V 2-μm flare undercut-QW taper into the 2-μm-wide silicon waveguide. Many modes are emitted, but TE10 and TE01 are significant in that they cannot be eliminated even down to reasonable waveguide widths.

Very short tapers, below 15 μm, emit a significant amount of power into the TE01 mode, as much as −15 dB. This is problematic for the operation of broad wavelength bandwidth laser devices because of the phenomenon illustrated in Figure 5.22. Lengthening the taper to 20 μm reduces the multimode emission to −25 dB, but further increase in length does not produce any more improvement because of the perturbation in the mode caused by the taper tip affecting the mode overlap in the waveguide after the termination. Note that the TE01 mode can be eliminated by etching the waveguide less than half of the device layer thickness (250 nm in this case), so this problem has reduced prominence if the need for a fully etched waveguide

can be eliminated. As discussed in Chapter 6, the single-step fully etched waveguide was deemed a necessity for repeatable laser mirror reflection.

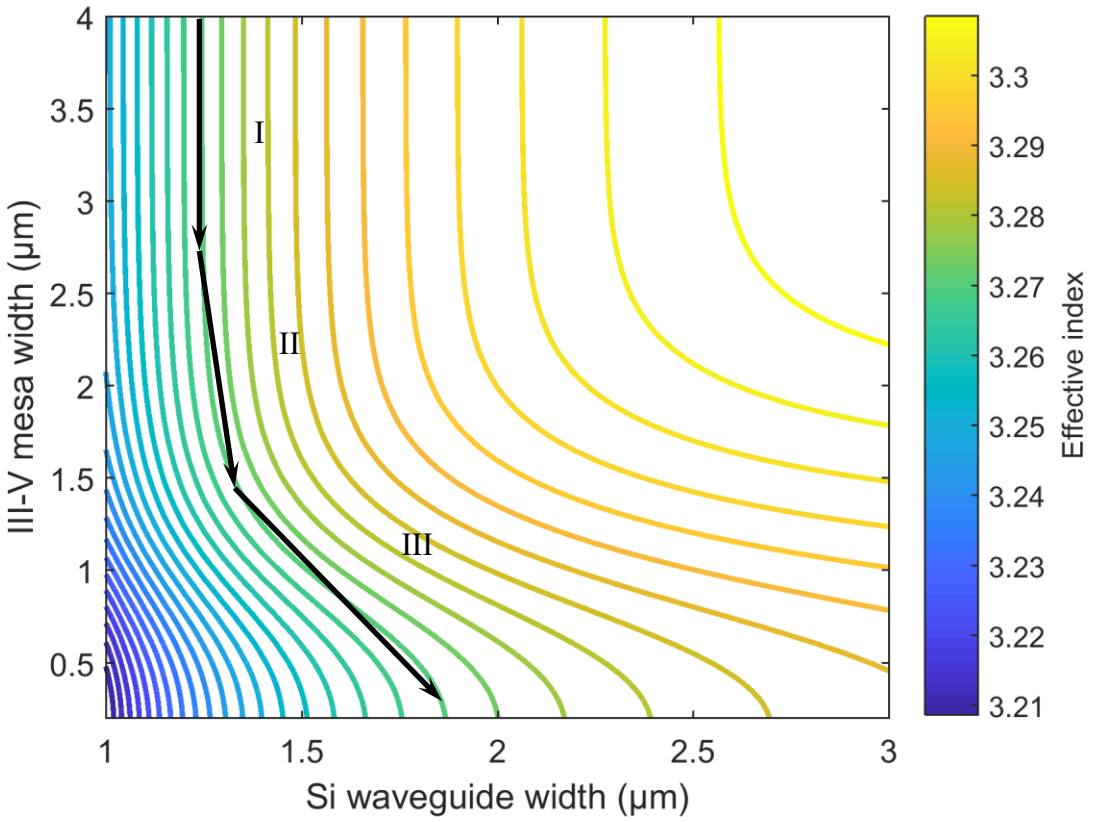

Figure 5.33: Heterogeneous waveguide effective index (contours) as a function of the width of the III-V mesa and the underlying silicon waveguide in the III-V taper section of the heterogeneous transition. The black lines represent the 3 linear taper sections in the conformal-index taper.

In an effort to produce a short taper that is more adiabatic, a new method for designing the transition was implemented. The width of the two waveguides in the III-V taper can be controlled independently, and so the mode profile can be transitioned gradually over the entire length of the transition, whereas the single taper designs often transform the mode fairly abruptly near the end of the structure. The concept is illustrated in

Figure 5.33. As the III-V mesa width decreases linearly in the propagation direction as it approaches the tip of the taper, the silicon waveguide width is varied to maintain the same modal effective index, making the transition more gradual. In the first section, I, the contours are vertical, signifying that the III-V waveguide is not affecting the mode strongly. Changing the silicon waveguide width here produces a large change in effective index, so the III-V waveguide is tapered and the Si waveguide stays the same width, 1.35 μm. This width was chosen because it is wide enough to have low confinement factor for the fundamental mode but low enough that the higher order mode in the amplifier waveguide is not guided (Figure 4.9). The second section, II, begins to involve both waveguides, so the silicon waveguide width increases from 1.35 to 1.45 μm to maintain the same effective index. In the third section, labeled III in

Figure 5.33, the effective index begins to vary rapidly with III-V index width, so the silicon waveguide also has its largest change in width to counteract the changing effective index from the end of the III-V waveguide, tapering from 1.45 to 1.85 μm.

The selected contour (starting at Si width 1.35 μm) was chosen assuming that the absorption in the taper began at the 4 μm-wide III-V mesa, since Figure 5.8 suggests that the contact is passivated at this width. 1.35 μm Si width gives a relatively minimal confinement factor for the low III-V index quantum well designs but is single mode in the amplifier section. Starting on a higher initial Si width contour requires a more drastic change in Si width in the third section, which required an increase in the overall length in simulation. Since the transmission simulations were very time consuming with FDTD and Eigenmode expansion (many modes in many slices in the 3-section taper), extensive exploration of the design space

was not done, so there is a possibility that a lower starting Si width contour may have better performance.

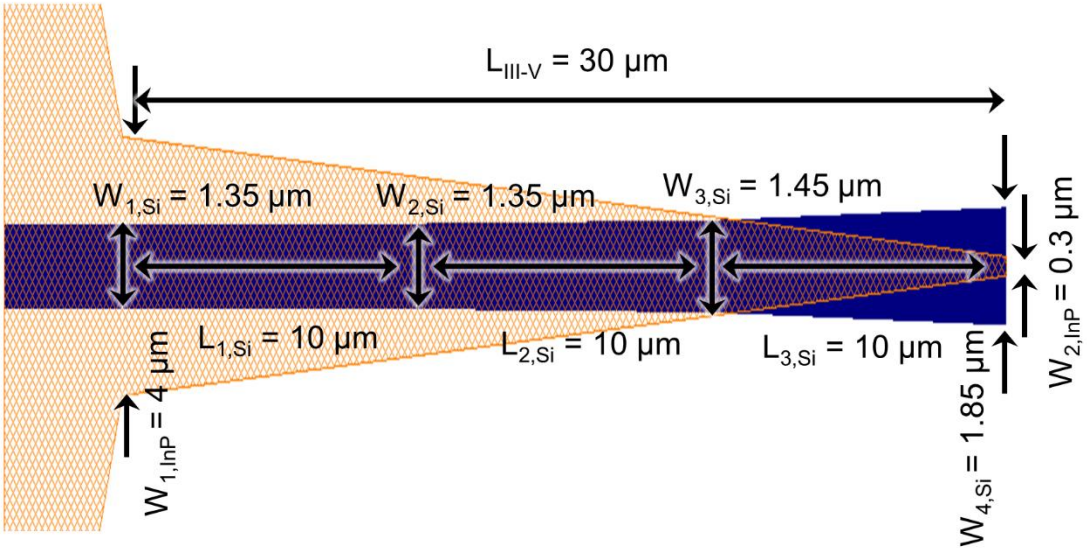

Figure 5.34: Plan view schematic of the conformal-index taper with the final dimensions.

The selected waveguide widths to follow the indicated contour are shown in Figure 5.34. The lengths of the three sections were optimized numerically, again using FDTD. The first section is the least critical, which can be inferred by the relatively constant effective index shown on segment I in

Figure 5.33. However, there is a reduction in the TE01 mode transmission up to 10 µm in length, which is shown in the simulation in Figure 5.35a. TE10 increases slightly, but the TE10 mode was ultimately attenuated by the spline curve loop mirror design (see Section 6.3) and is less of a problem. 10 µm was chosen for simplicity, but this section may be able to be shortened to decrease absorption. The simulation for segment II is shown in Figure 5.35b. The TE01 mode reaches below −30 dB at 10 µm. 10 µm was chosen in this case because the target was −30 dB or lower, and length should be minimized. Experimentally, the loss in the conformal-index taper was evidently lower than the simple 2-µm flare taper, so there may have been room

to increase this by another few micrometers to further reduce the TE01 mode. The last section, segment III, is shown in Figure 5.35c. As suggested in the index contour plot, this section is where the mode is transformed the most rapidly, so short tapers have higher than −20 dB transmission. It also contains the termination, so excessive length is not helpful to reduce the transmission after a certain point. 10 μm was the minimum transmission for TE01, and so the final design was 10 μm for all three sections.

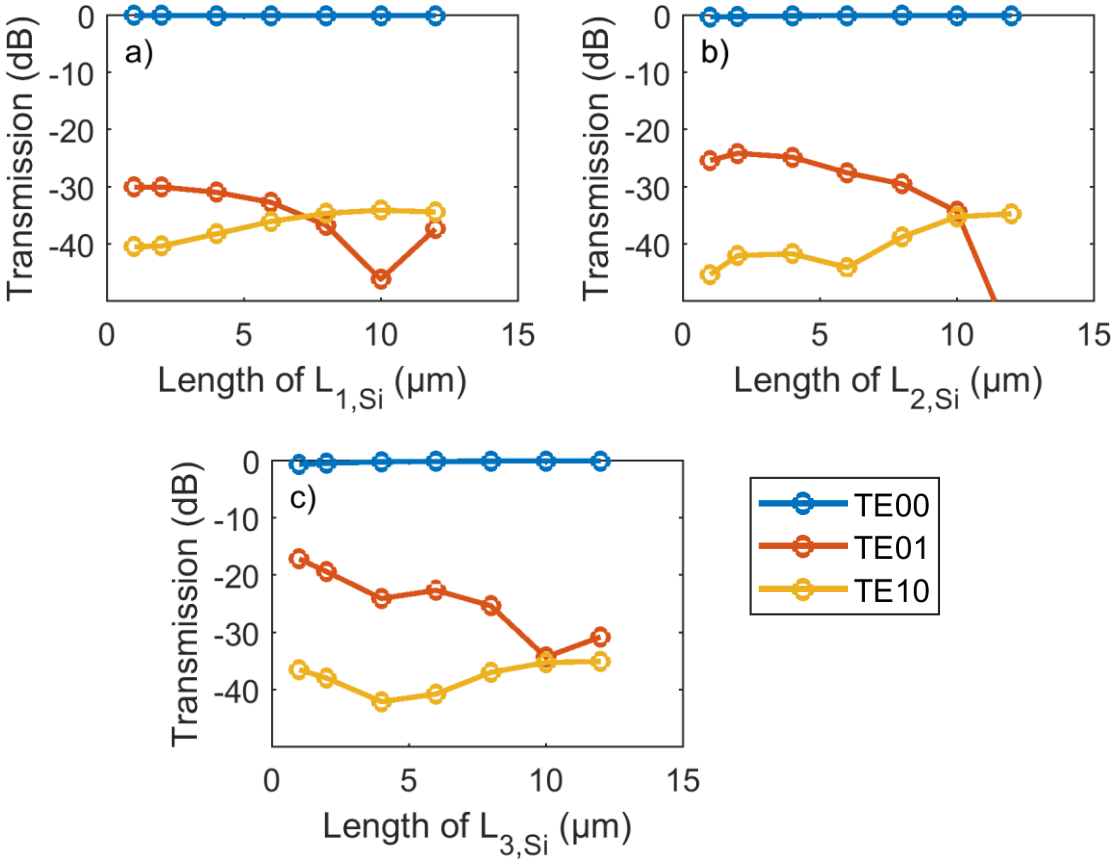

Figure 5.35: Transmission into the problematic propagating modes (those which are not eliminated in subsequent narrow Si waveguide sections) versus the length of the three sections in the 3-section conformal-index taper. (a) is the first section, $L_{1,Si}$ in Figure 5.34 (b) is the center section, $L_{2,Si}$ in Figure 5.34, and (c) is the tip section, $L_{3,Si}$ in Figure 5.34.

The 10, 10, 10 μm design was chosen before the discovery that the TE10 mode can be attenuated with later passive component designs. A further optimization of these lengths to trade off reduced TE01 for increased TE10 may be helpful for improving performance.

The performance of the precise design indicated in the Figure 5.34 schematic is shown in Figure 5.36, an FDTD simulation of the higher order mode emission for the 10, 10, 10 μm design. This is a 3-dimensional problem, and other combinations of lengths may exist; optimizing the three separately in as in Figure 5.35 may have only produced a local minimum. Given the computationally intensive nature of FDTD, experiments may be required for further optimization.

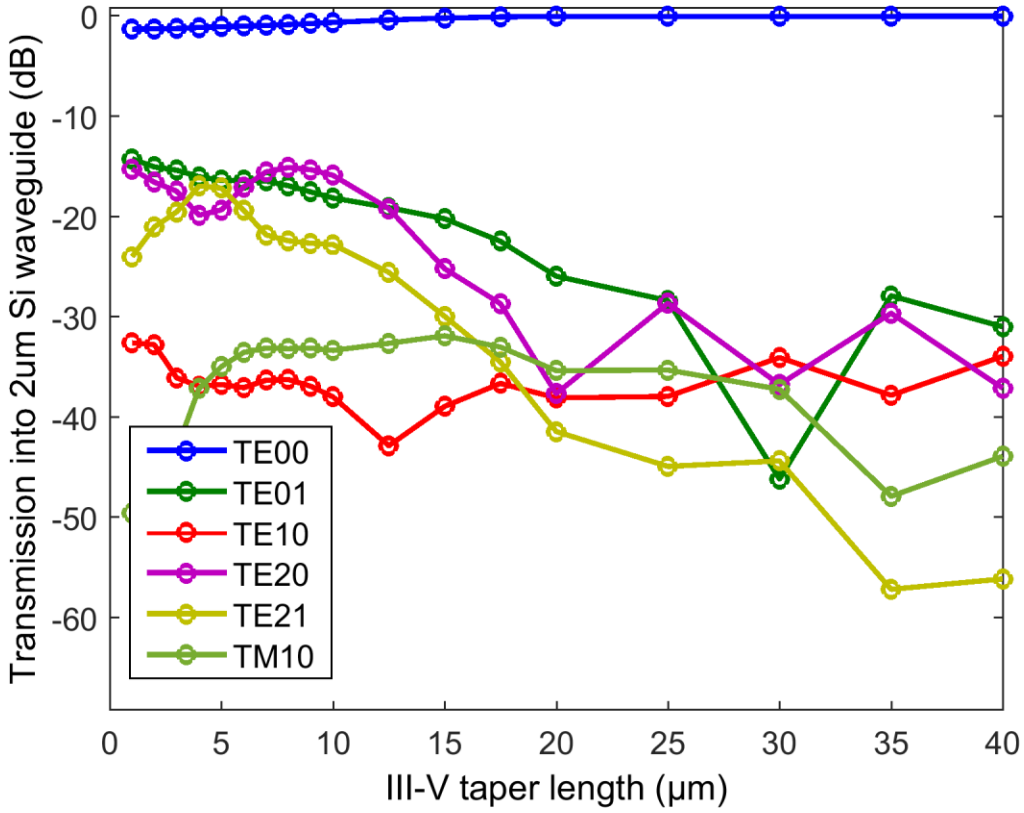

Figure 5.36: Transmission into higher order mode for the 3-section conformal-index taper.

Transmission two problematic modes, TE10 and TE01, is plotted together for the conformal-index taper with three equal length taper segments and the 20-μm-long taper with

the simple 2-μm flare. Both have the low-index III-V epi design. At 30 μm, the improvement in transmission in TE01 is improved by 20 dB, with a slight deterioration of the TE10 transmission of 3 dB. Ignoring the mysterious dip at 30 μm, the improvement at nearby lengths (25 and 35 μm) is still 6 dB.

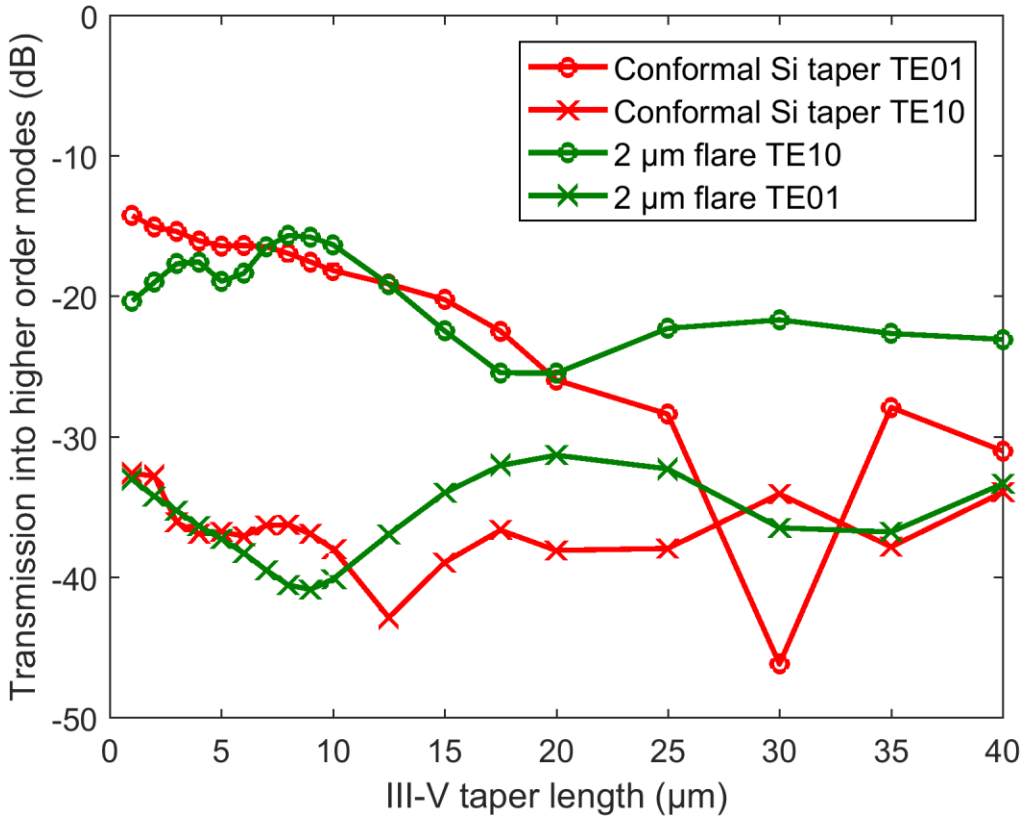

Figure 5.37: Comparison of the higher order mode emission versus length into the most disruptive TE10 and TE01 modes from the basic 2-μm flare (green) and the 3-section conformal-index taper (red).

The laser LI characteristics from integrated lasers with the different taper designs were fabricated to compare the performance of the different designs. Figure 5.38 compares two 15-μm-long tapers, one with the 2-μm-flare taper described in Table 5-1, and the other with the 3-section conformal-index taper with three 5-μm sections and the Si waveguide widths shown in Figure 5.34. The experiment shows a somewhat unexpected result, that the conformal-index

taper has lower loss as indicated by the lower threshold and higher slope efficiency. This is due partially to the fact that the amplifier flare from the gain section waveguide width to the beginning of the transition is less critical, having to increase from 0.85 μm to 1.35 μm in the 3-section taper instead of 2 μm in the basic taper, and that the conformal-index taper is more adiabatic at short lengths. As is normal for these comparisons, the two lasers were fabricated together on the same chip in close proximity to each other. Due to an oversight during mask layout, no 30-μm-long basic 2-μm flare designs were included on the mask.

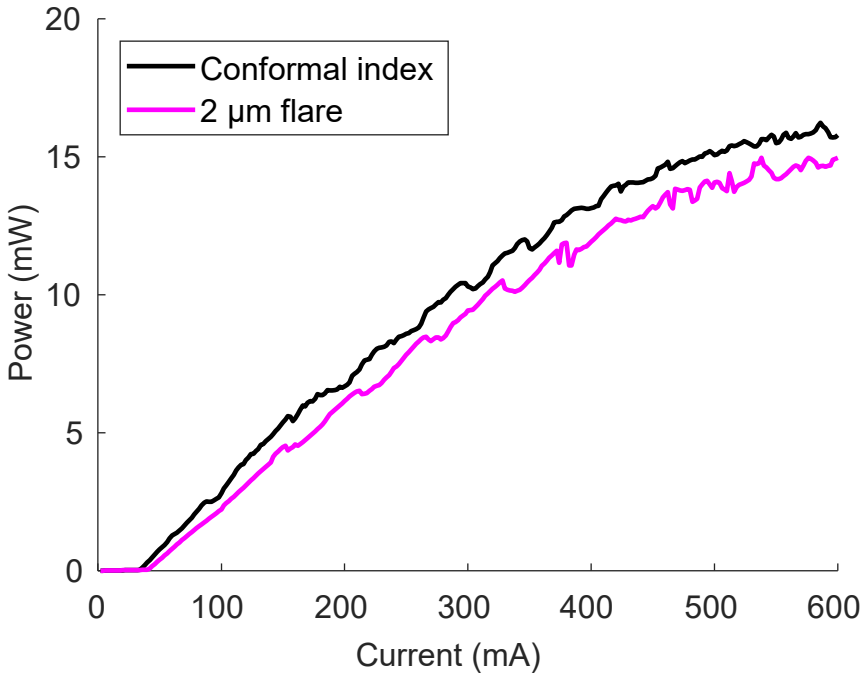

Figure 5.38: LI characteristics for two otherwise identical lasers with 15-μm-long III-V taper sections. The black line shows a 3-section conformal-index taper, while the magenta line shows a basic 2-μm flare taper.

Two different lengths of 3-section conformal-index taper were examined, 5-5-5 μm and 10-10-10 μm. As shown in Figure 5.39, there is only a slight difference in output power. Simulation suggests that the longer taper has lower transmission into higher order modes. This

contradicts the measurement result in Figure 5.11. This may be an indicator that the conformal-index taper has better performance in longer tapers as well, or that the difference in passive loss is higher for shorter tapers, which shifts the optimum point where passive loss and absorption are balanced out to a longer taper length. It may be worth experimentally exploring longer lengths as well.

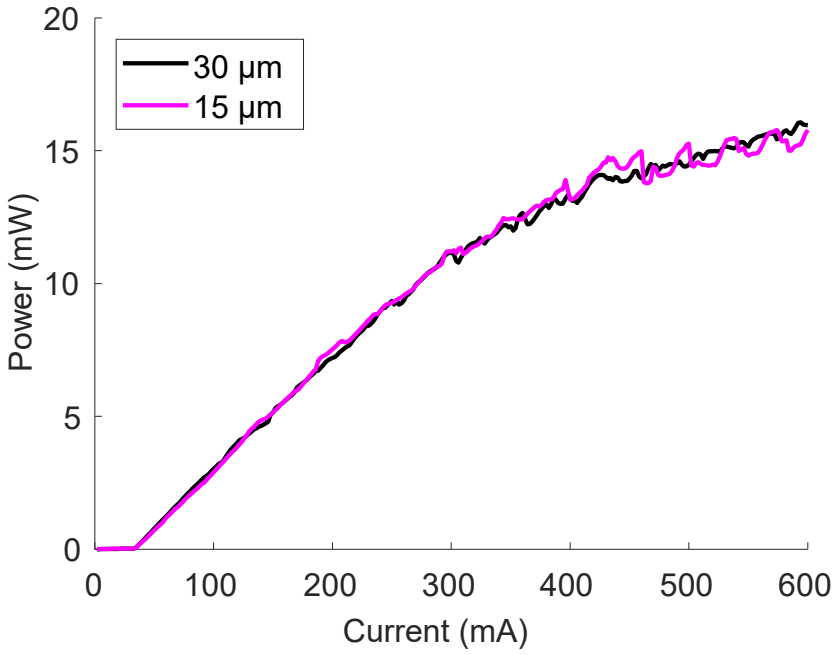

Figure 5.39: LI characteristics of two otherwise identical lasers with 3-section conformal-index tapers of differing lengths. The black curve shows a 30-µm III-V taper section, the 10-10-10 µm design shown in Figure 5.34, and the magenta curve shows a similar design (same Si waveguide widths) but with the segment lengths all 5 µm.

The 3-section conformal-index taper optimizes the twin waveguide design to produce a more gradual transition from the amplifier waveguide to the passive silicon waveguide. It provides 14 dB improvement in the highest multimode excitation compared to the basic 2-µm

flare developed in Section 5.2.1 as well as slightly higher output power, indicating that there is no penalty to loss in adopting this design.

5.6. Mode locking

Simulation of the impact of impairments with spectral dependence on the performance of mode-locked lasers is extremely difficult. Knowledge of the spectral dependence of the nonlinear gain and loss is required for accurate modeling of the mode-locking phenomenon, and extraction of this information from real devices is impractical. Up until this point, the transition optimization followed the assumption that better continuous wave (CW) performance would correspond to better mode-locking behavior, in terms of both pulse width and noise. Lasers with early transition designs, such as those yielding the output spectra in Figure 5.13 and Figure 5.23, had good CW output power, but poor CW wavelength spectra. These devices would not mode lock at all. Once the transition was optimized to the point that good CW performance in both power efficiency and spectral behavior was available, the devices would exhibit uniform mode locking over a wide range of bias conditions. At this point, the optimization can simply be conducted by experimentally comparing mode-locking characteristics.

The test structure used in this experiment is shown schematically in Figure 5.28. It has integrated Type 1 spline curve mirrors with angled output facets (see Section 6.1.3), a 10 GHz fundamental cavity with a 2000-μm-long amplifier section, including the 60-μm-long saturable absorber. The amplifier section waveguide has an 850-nm-wide silicon waveguide. They use Epi H, the 0.85% strain 3-QW laser epi with 1.2-μm band-gap wavelength SCH layers. Note

that the sub-1 ps results reported later in this work used the 1% strain 3-QW design and Type 2 spline curve mirrors. The experiment sought to answer the following questions:

- The 3-section conformal-index taper has lower parasitic multi-mode emission than the basic 2-μm-flare taper. Does this translate to better performance? If so, this could establish experimentally what the maximum tolerable level of higher order mode emission is.
- Shorter tapers generally have lower loss. What is the impact of shortening the taper on the mode-locking performance? Shorter tapers have higher reflection Figure 5.17. At what point is trade-off between lower loss and higher spectral parasitic impairment optimized for pulse width?
- The n-InP transition, similar to above, can be achieved with an angled junction for lower multimode emission, or a taper for lower reflection. Which one provides the optimal performance for mode-locked pulse width?

Figure 5.40 shows the minimum pulse width for four otherwise identical integrated lasers with different heterogeneous transition designs. The first pair of data points are a 15-μm-overall length basic taper with a 2-μm flare ("p: 15 μm basic, n: angled"), and a conformal-index 5-5-5 μm taper. Both have the angled n-InP transition. The basic taper had a minimum attainable pulse width of 3.5 ps, while the conformal-index taper was significantly better, with 2.7 ps. This is likely due to the 5 dB lower emission into the TE01 mode of the conformal-index taper, even at 15 μm. These lasers have the spline curve loop mirror, which filters the TE10 mode. So, the answer to the first bullet point is: lower higher order mode emission does translate to shorter pulses.

The second pair of devices are two 3-section conformal-index tapers, one 5-5-5 μm ("p: 15 μm conformal, n: angled") and the other 10-10-10 μm ("p: 30 μm conformal, n: angled"). These are identical other than the overall length of the III-V taper. There is a more marginal improvement in pulse width, from 2.7 ps for the 15 μm taper to 2.3 ps for the 30 μm taper. The answer, then, to the second bullet point, is that longer tapers produce slightly lower pulse width. In the case of these particular designs, as shown in Figure 5.39, there was no trade-off in terms of output power. It is likely worth exploring an even longer 3-section taper, especially the 2nd and 3rd segments.

The final pair of devices have identical p-III-V tapers, but one has the n-InP angle ("p: 30 μm conformal, n: angle") and the other has the n-InP taper ("p: 30 μm conformal, n: taper"). Surprisingly, this did not show as significant of an improvement as expected. The pulse width from the n-InP taper was 2.6 ps, and it only improved by 0.3 ps to 2.3 ps by changing to the angle. Evidently, the high transmission into TE10 (Figure 5.24) has less of an impact than expected, probably due to the mode filtering effect of the spline curve mirror. The curve for transmission into TE01 in the misaligned taper simulation was not shown because it was considered insignificantly small (> -40 dB). It would be worthwhile to repeat this experiment on polished facet FP mirror lasers to eliminate the effect of the spline curve mirror.

In any case, despite the uncertainty in the impact of which simulation output corresponds to better pulse width performance, in this ensemble of devices, the 10-10-10 μm conformal-index taper with the angled n-layer junction provided the shortest pulse width.

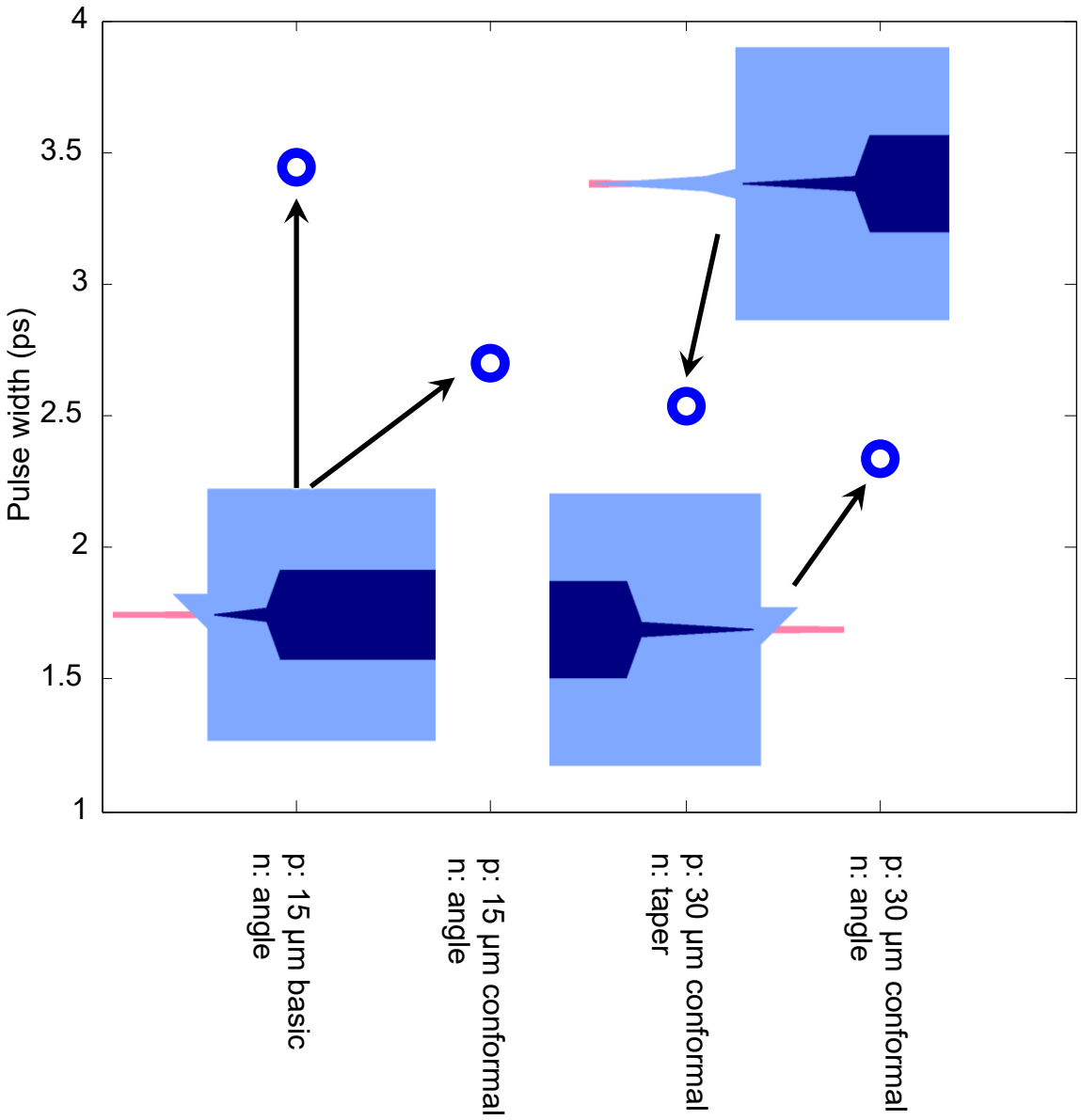

Figure 5.40: Shortest attainable pulse width for integrated mode-locked lasers with various heterogeneous transition designs.

In conclusion: all of the devices in Figure 5.40 produced reasonably short pulses, but it must be stressed that the majority of the lasers produced in the process of this dissertation failed to mode lock at all, either with a weak RF peak in the electrical spectrum analyzer, or mode-locking at the wrong frequency (usually at the FSR of the parasitic cavity between the

transition and the mirror). The heterogeneous transition was the single most difficult engineering problem that was overcome in the course of this work, principally due to the lack of accurate measurement techniques and simulation tools at the outset. The transition must have less than −40 dB reflection and less than −30 dB emission into higher order modes for short pulse mode-locking. Lower values would likely produce better performance.

References

[1] H. Park, Y. Kuo, A. W. Fang, R. Jones, O. Cohen, M. J. Paniccia, and J. E. Bowers, "A hybrid AlGaInAs-silicon evanescent preamplifier and photodetector," *Opt. Express*, vol. 15, no. 21, p. 13539, 2007.

[2] K. Takeda, T. Sato, T. Fujii, E. Kuramochi, M. Notomi, K. Hasebe, T. Kakitsuka, and S. Matsuo, "Heterogeneously integrated photonic-crystal lasers on silicon for on / off chip optical interconnects," *Opt. Express*, vol. 22, no. 2011, pp. 702–708, 2015.

[3] D. Liang, M. Fiorentino, S. Srinivasan, J. E. Bowers, and R. G. Beausoleil, "Low threshold electrically-pumped hybrid silicon microring lasers," *IEEE J. Sel. Top. Quantum Electron.*, vol. 17, no. 6, pp. 1528–1533, 2011.

[4] J. Van Campenhout, P. Rojo Romeo, P. Regreny, C. Seassal, D. Van Thourhout, S. Verstuyft, L. Di Cioccio, J.-M. Fedeli, C. Lagahe, and R. Baets, "Electrically pumped InP-based microdisk lasers integrated with a nanophotonic silicon-on-insulator waveguide circuit," *Opt. Express*, vol. 15, no. 11, p. 6744, 2007.

[5] Y. De Koninck, G. Roelkens, and R. Baets, "Design of a hybrid III-V-on-silicon microlaser with resonant cavity mirrors," *IEEE Photonics J.*, vol. 5, no. 2, 2013.

[6] B. Ben Bakir, N. Olivier, P. Grosse, S. Messaoudène, S. Brision, E. Augendre, P. Philippe, K. Gilbert, D. Bordel, J. Harduin, and J. Fedeli, "Electrically driven hybrid Si/III-V lasers based on adiabatic mode transformers," in *Proc. of SPIE*, 2010, vol. 7719, p. 77191F.

[7] P. Iii, "Adiabatic and multimode interference couplers on Adiabatic and Multimode Interference Couplers on," *IEEE Photonics Technol. Lett.*, vol. 18, no. 21, pp. 2287–2289, 2006.

[8] G. Kurczveil, P. Pintus, M. J. R. Heck, J. D. Peters, and J. E. Bowers, "Characterization of Insertion Loss and Back Reflection in Passive Hybrid Silicon Tapers," *IEEE Photonics J.*, vol. 5, no. 2, pp. 6600410–6600410, 2013.

[9] A. W. Fang, E. Lively, Y. Kuo, D. Liang, and J. E. Bowers, "A distributed feedback silicon evanescent laser," *Opt. Express*, vol. 16, no. 7, pp. 4413–4419, 2008.

[10] A. W. Fang, B. R. Koch, R. Jones, E. Lively, Di Liang, Ying-Hao Kuo, and J. E. Bowers, "A Distributed Bragg Reflector Silicon Evanescent Laser," *IEEE Photonics Technol. Lett.*, vol. 20, no. 20, pp. 1667–1669, Oct. 2008.

[11] M. L. Davenport, G. Kurczveil, M. J. R. Heck, and J. E. Bowers, "A hybrid silicon colliding pulse mode-locked laser with integrated passive waveguide section," *2012 IEEE Photonics Conf. IPC 2012*, vol. 3, pp. 816–817, 2012.

[12] D. T. Cassidy, "Technique for measurement of the gain spectra of semiconductor diode lasers," *J. Appl. Phys.*, vol. 56, no. 11, p. 3096, 1984.

[13] B. W. Hakki and T. L. Paoli, "Gain spectra in GaAs double−heterostructure injection lasers," *J. Appl. Phys.*, vol. 46, no. 3, p. 1299, 1975.

[14] N. M. Johnson, "Hydrogen passivation of shallow-acceptor impurities in p-type GaAs," *Phys. Rev. B*, vol. 33, no. 2, p. 1102, 1986.

[15] T. R. Hayes, W. C. Dautremont-Smith, H. S. Luftman, and J. W. Lee, "Passivation of acceptors in InP resulting from CH4/H2 reactive ion etching," *Appl. Phys. Lett.*, vol. 55, no. 1, p. 56, 1989.

[16] M. Moehrle, "Hydrogen passivation of Zn acceptors in InGaAs during reactive ion etching," *Appl. Phys. Lett.*, vol. 56, no. 6, pp. 542–544, Feb. 1990.

[17] P. S. Nandhra, R. C. Newman, R. Murray, B. Pajot, J. Chevallier, R. B. Beall, and J. J.

Harris, “The passivation of Be acceptors in GaAs by exposure to a hydrogen plasma,” *Semicond. Sci. Technol. April*, vol. 3, no. 4, pp. 356–360, 1988.

[18] T. Henderson, V. Ley, T. Kim, T. Moise, and D. Hill, “Hydrogen-related burn-in in GaAs/AlGaAs HBTs and implications for reliability,” *Int. Electron Devices Meet. Tech. Dig.*, 1996.

[19] S. A. Stockman, A. W. Hanson, S. M. Lichtenthal, M. T. Fresina, G. E. Höfler, K. C. Hsieh, and G. E. Stillman, “Passivation of carbon acceptors during growth of carbon-doped GaAs, InGaAs, and HBTs by MOCVD,” *J. Electron. Mater.*, vol. 21, no. 12, pp. 1111–1118, 1992.

[20] N. M. Johnson, C. Doland, F. Ponce, J. Walker, and G. Anderson, “Hydrogen in crystalline semiconductors,” *Phys. B Condens. Matter*, vol. 170, no. 1–4, pp. 3–20, Apr. 1991.

[21] E. E. Haller, “Hydrogen in Crystalline Semiconductors - III-V Compounds.pdf,” *Semicond. Sci. Technol.*, vol. 6, no. 2, pp. 73–84, 1991.

[22] S. J. Pearton, J. W. Corbett, and J. T. Borenstein, “Hydrogen diffusion in crystalline semiconductors,” *Phys. B Condens. Matter*, vol. 170, no. 1–4, pp. 85–97, Apr. 1991.

[23] T. I. Gromova, E. I. Davydova, M. B. Uspenskii, and V. A. Shishkin, “SEM evidence for near-surface carrier passivation by hydrogen in CH4/H2 reactive ion etched p-InP,” *Semicond. Sci. Technol.*, vol. 10, no. 4, pp. 2–6, 1994.

[24] J. Kreissl, M. Moehrle, A. Sigmund, R. Bochnia, P. Harde, and W. Ulrici, “Hydrogen passivation in InP:Zn resulting from reactive ion etching during laser stripe formation,” in *Conference Proceedings. 2000 International Conference on Indium Phosphide and Related Materials (Cat. No.00CH37107)*, 2000, pp. 142–145.

[25] Y. Barbarin, E. a J. M. Bente, C. Marquet, E. J. S. Leclère, J. J. M. Binsma, and M. K. Smit, “Measurement of reflectivity of butt-joint active-passive interfaces in integrated extended cavity lasers,” *IEEE Photonics Technol. Lett.*, vol. 17, no. 11, pp. 2265–2267, 2005.

[26] P. Dong, T.-C. Hu, T.-Y. Liow, Y.-K. Chen, C. Xie, X. Luo, G.-Q. Lo, R. Kopf, and A. Tate, “Novel integration technique for silicon/III-V hybrid laser.,” *Opt. Express*, vol. 22, no. 22, pp. 26854–61, 2014.

Chapter 6

Fully Integrated Lasers

A passive optical component, as opposed to an active component, is one that is incapable of controlling the optical transmission by means of an applied signal, such as an electrical drive current in a laser or voltage signal in a modulator. Passive components include simple waveguides to transport light from one part of the circuit to another, splitters, combiners, reflectors, wavelength filters, multiplexers and de-multiplexers, and polarization diversity devices like polarization rotators and splitters.

The promise of silicon photonics is principally considered to be its manufacturability: the ability to be produced inside the silicon electronics foundry infrastructure. This allows production at high volume and low cost to fulfill photonics applications that are projected to have extremely high demand, such as fiber optic transceivers for use in data center networks. However, it must be mentioned that the silicon-on-insulator platform produces outstanding passive components [1]. This is due to both the extremely high material quality of single-crystalline silicon, in terms of purity and density of defects, and the high refractive index contrast between the silicon and its cladding layers, typically silicon dioxide, which has n =

1.45, compared to n = 3.47 for silicon. This is in comparison to n = 3.38 in the AlGaInAs 1.2 μm band gap waveguide core, which is clad with n = 3.17 InP in the optimized heterogeneous amplifier. The increased index contrast allows for more compact devices, while the material quality and sophisticated silicon dry etch processing produces state of the art propagation loss as low as 0.5 dB/cm [2] at bend radii of a few micrometers. Waveguides made from InP alloys in practical circuits typically have propagation losses above 1 dB/cm and bend radii above 100 μm.

Based on this advantage, it can be presumed that the deterioration in performance compared to native substrate InP circuits caused by the heterogeneous transition–mainly the loss–can eventually be compensated in large-scale integrated circuits by the reduced loss, reduced size, and increased precision of silicon passive components.

6.1. The Silicon Passive Waveguide

As mentioned in Chapter 2, the silicon waveguide must be fully etched all the way to the buried oxide to guarantee repeatable and high yield performance of phase-sensitive components, particularly the directional coupler and distributed Bragg reflector mirrors. Accurate definition of the reflection and center wavelength of these components is crucial for producing high output power lasers. Unfortunately, this introduces some penalties. As the silicon thickness used in this work is 500 nm, the waveguide supports multiple transverse electric (TE) modes. In addition, the deeply etched waveguide typically has higher propagation loss than a similarly sized shallow etched waveguide.

6.1.1. Waveguide Basics

Partially etched silicon waveguides may have a single transverse TE mode if the etch depth is less than half of the thickness of the waveguide. Even if the waveguide is relatively large, for example 800 nm wide, the first higher order TE mode (TE10 typically) will not be strongly guided around bends, forming a quasi-single mode waveguide. A fully etched waveguide does not enjoy this advantage and must be very small to be single TE mode. 220-nm thick and 400-nm wide is commonly used. However, the heterogeneous transition requires thicker silicon, and the high yield fabrication process requires fully etching the silicon, so higher order TE modes will always be guided. For wider waveguides, there may be many guided higher order modes. Under ideal circumstances there is no coupling between the modes, since they are orthogonal to one another. In real integrated circuits, there can be fairly strong coupling between modes due to abnormalities like misalignment between layers or coherent backscattering [3].

Since a well-designed laser typically emits mainly into the fundamental TE00 mode, any higher order mode present in the circuit is considered a parasitic effect. These will be referred to in this text as “parasitic higher order modes,” and the act of generating them as “parasitic multimoding.” Parasitic multimoding creates interference and has a similar effect to parasitic reflection, in that it creates periodic nulls in the emission spectrum of the laser. In a tunable laser, this will create dead spots in the tuning map, and in multimode lasers it will reduce the emission bandwidth.

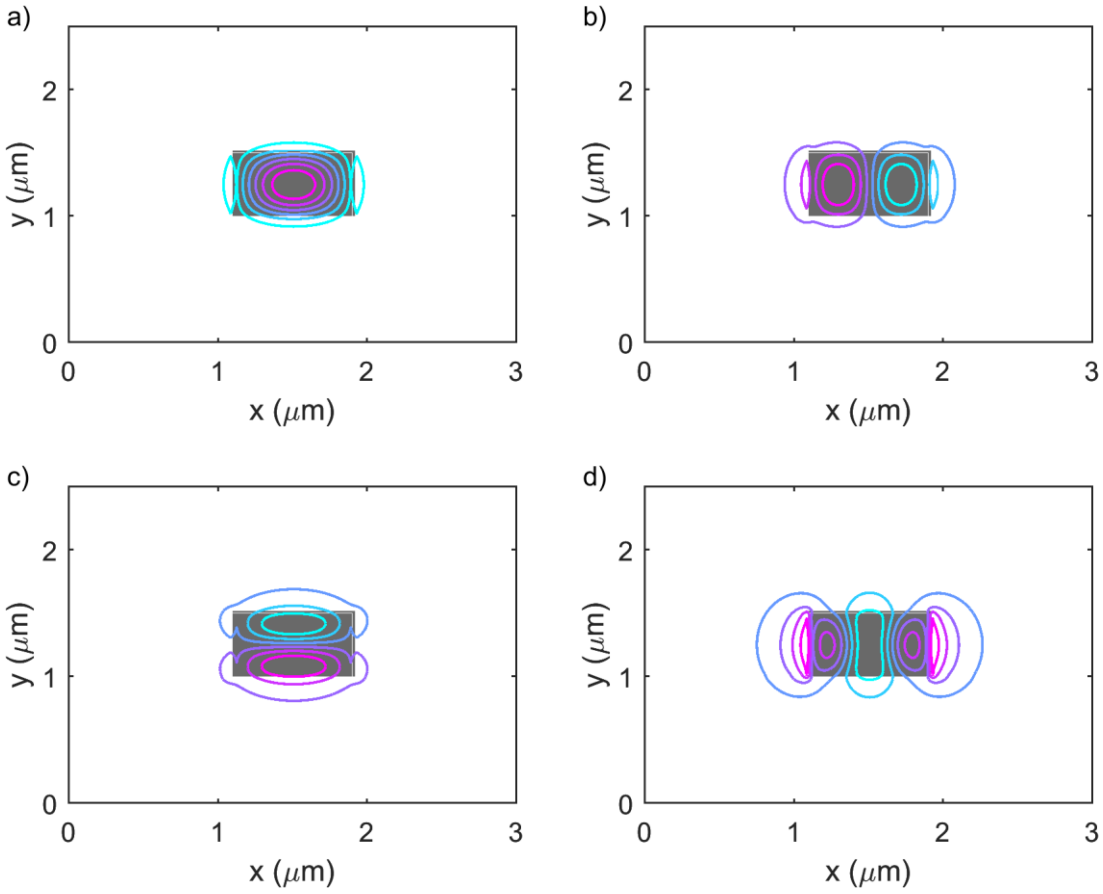

Figure 6.1: Mode field amplitudes of a) fundamental TE00, b) second order TE10, c) third order TE01, and d) fourth order TE20 modes. Amplitudes are contours, while the grayscale represents index, with darker being higher.

The higher-order modes that are of a concern in this platform are shown in Figure 6.1: (a) is the fundamental TE00 mode, which is desired, (b) is the TE10 mode, which is coupled to in bent to straight waveguide transitions and laterally misaligned photonic layers, (c) is the TE01 mode, which can be generated by misalignment, abrupt terminations of vertical photonic layers and bent-to-straight waveguide transitions, and (d) the TE20 mode, which couples with the TE00 mode in lateral tapers.

While the TE10 and TE20 modes can be avoided by narrowing the waveguide width to 400 nm or smaller, the propagation loss of the fully etched silicon waveguide increases

dramatically with decreasing waveguide width due to the electric field amplitude increasing at the rough waveguide sidewall [4]. Figure 6.2 a) shows the propagation loss of waveguides with varying width. This measurement was performed by fabricating straight waveguides with polished facets, and then measuring the wavelength transmission spectrum of the resulting Fabry-Perot resonator. Cassidy's mode sum minimum method was used to calculate the propagation loss from the extinction of the wavelength fringes [5], using reflection values calculated with the Eigenmode expansion method and shown in figure Figure 6.2b. Note that these were "post bond" waveguides, which have endured the full heterogeneous integration process.

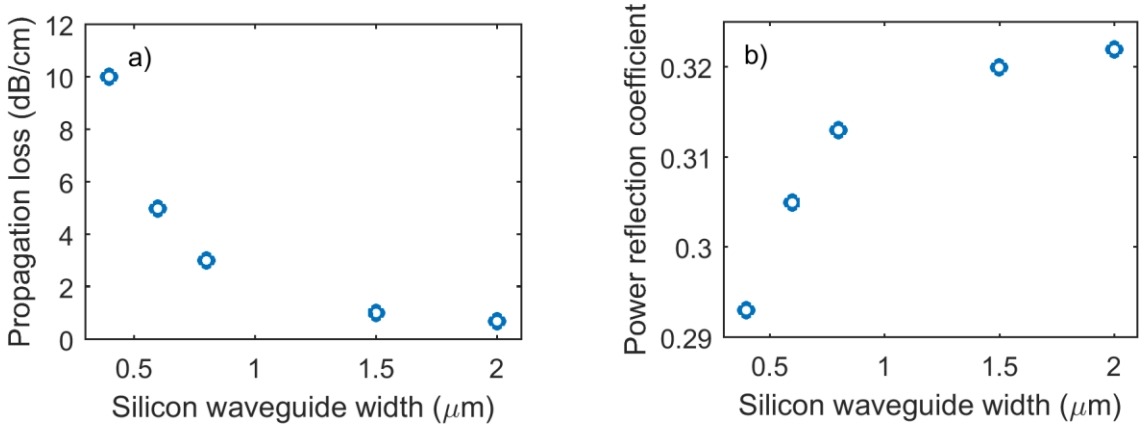

Figure 6.2: a) Propagation loss of deeply etched 500-nm-tall silicon waveguides of various width at 1550-nm wavelength and b) simulated reflection coefficients used in the calculation.

Given this information, it is clear that using a 400-nm waveguide to eliminate higher order modes will be very costly in terms of loss, as this waveguide has almost 10 dB/cm of propagation loss. Therefore, an 800-nm waveguide will generally be used for straight sections, such as the mode-locked laser passive waveguide, and the waveguide will be tapered to the 400-nm width only for bent waveguides to avoid the need for a waveguide offset. This can be accomplished with a relatively short lateral taper, as shown in Figure 6.4a. This simulation was

performed using the Eigenmode expansion method, with the TE00 mode of the 400-nm waveguide launched into the taper and the transmission into the modes of the 800-nm waveguide shown versus taper length in Figure 6.3b). Loss is relatively minimal for any length and the transmission into the strongest higher order mode, TE20, is below −40 dB for tapers longer than 15 μm. 25 μm was selected as to have a wide margin of error. There is only 0.001 dB of loss and −42 dB transmission into the higher order mode.

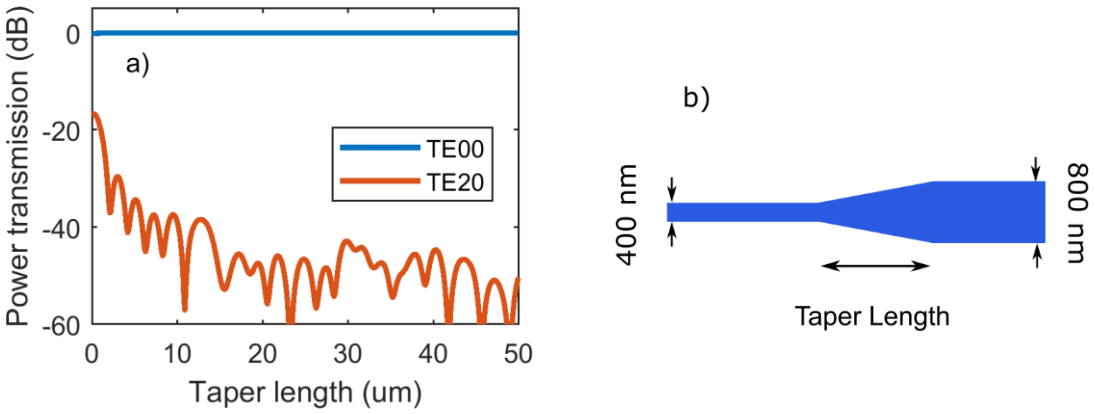

Figure 6.4: Transmission from the fundamental TE00 mode in the 400-nm waveguide into the TE20 mode of an 800-nm waveguide. TE20 has the strongest higher order mode emission for this structure.

6.1.2. Waveguide Bends

The fully etched waveguide does have one advantage: extremely small waveguide bend radius. This helps to offset the increased propagation loss in the 400-nm bent waveguide sections, since the length of the bends can be reduced. The 400-nm fully-etched waveguide can make 90° bends with less than 0.1 dB of bending loss down to bend radius as low as 2 μm, as shown in Figure 6.5 a), with the bend loss reaching 0 at 8-μm-bend radius. A very tightly bent waveguide can act as a mode filter, as the critical bend radius increases for increasing

mode order. The problematic TE10 mode is very lossy: a 2-μm-radius bent waveguide will have 3 dB/μm bending loss

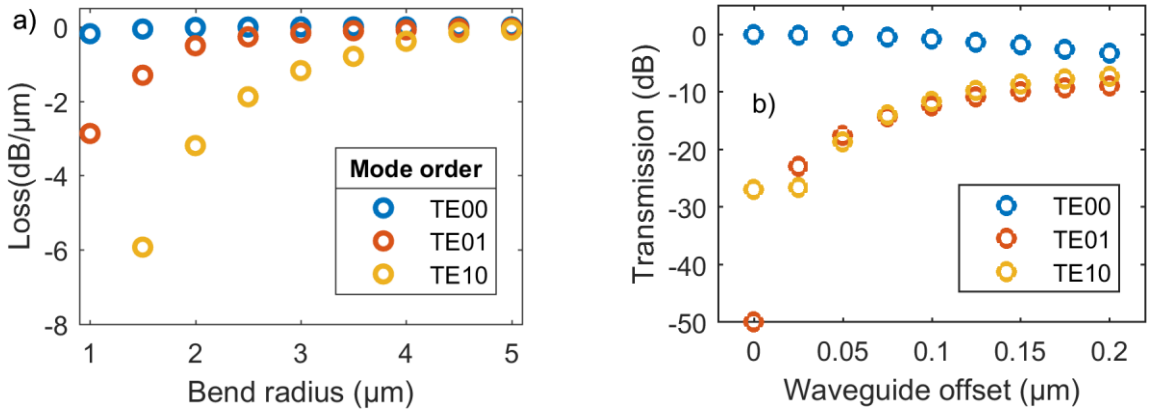

Figure 6.5: a) Bend loss for a 400-nm-wide fully etched waveguide at 1550-nm wavelength for the three guided modes. b) Transmission into multiple modes for an S-bend section with 25-μm bend radius versus waveguide offset

Unfortunately, because the waveguide still supports multiple transverse modes, the effect of the abrupt change in bend radius excites a higher order mode. Even with a relatively large 25-μm bend radius, there is still considerable excitation of the TE10 mode in an s-bend, in which the effect is exaggerated due to the transition from radius R to $-R$. Offsetting the two waveguides laterally at the junction does not reduce this effect and in fact worsens it, in addition to increasing the loss in the TE00 mode as shown in Figure 6.5b. Higher order mode transition must be below −30 dB, so this is unacceptable. For a 2-μm bend radius waveguide, the higher order mode excitation increases to −11 dB, and the loss of the TE00 mode increases to −0.35 dB. This level of multimode excitation is beyond what is tolerable.

The solution is to use an adiabatic bend, where the bend radius transitions gradually from infinity to the final bend radius. A common adiabatic bend is the Euler bend, where the curvature (defined as $k = 1/R$) decreases linearly along the length of the curve. The Euler bend,

like most adiabatic bends, is much longer than a circular bend with a similar radius. This is undesirable as it will increase the propagation loss of the bend in the narrow waveguide. Instead, the method of W. Bogaerts et al. was adopted [2]. This combines a natural 3rd order Bezier spline curve with a circular bend to produce an adiabatic bend with minimal penalty in length. A schematic representation of the spline/circle bend most commonly used in this work is shown in Figure 6.6 a). The red part of the curve signifies the circle, with a bend radius of 2 μm, while the black part represents the partial Bezier spline.

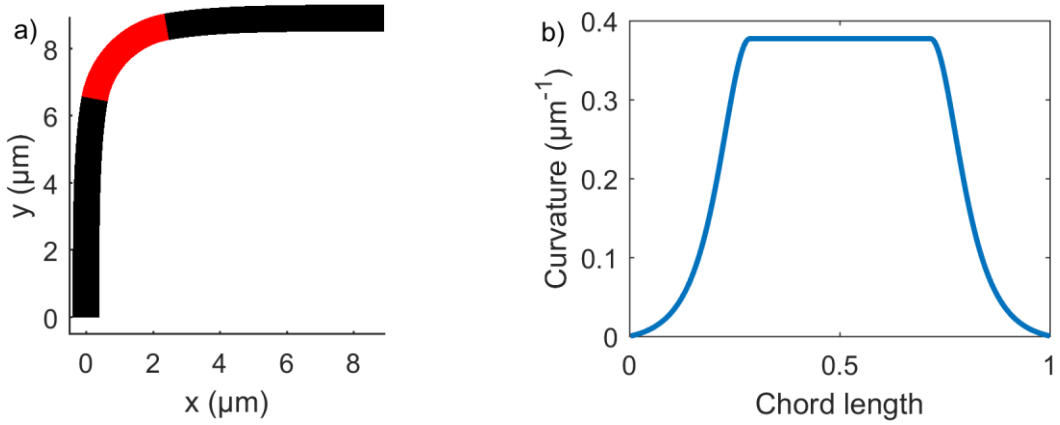

Figure 6.6 a) Scale representation of a 10 μm control point 25-degree coverage spline and 2-μm circular bend, and b) the curvature along the chord.

The spline/circle bend allows for simultaneously tighter bend radii and lower higher order mode excitation. Manipulation of the spline shape and coverage angle can result in a wide range of bend radii and device footprints. The higher order mode excitation is shown for three s-bend designs in Figure 6.7. The red marker is a pure circular bend. The spline/circular s-bends have 22.5° coverage of the curve relative to a 90° bend, meaning that the spline section remains the same as it is in the 90° bend, while the circular section has a reduced angular sweep to achieve the desired displacement in the s-bend. Simulation of these devices is very clumsy since it is impossible to draw them in most simulation tool design environments. Together with

the fact that the total angular bend, the spline angular coverage, the spline control points, and the minimum bend radius all factor into the performance of the bend, a fully rigorous design procedure was not performed. The first few devices investigated showed considerable improvement over the circular bend and then the simulation effort was abandoned. It is possible that an even lower mode excitation level and smaller footprint could be attained with a more thorough approach.

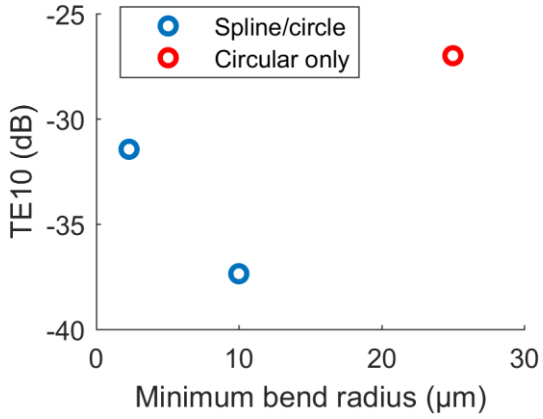

Figure 6.7: Simulated multimode excitation for various s-bend designs using FDTD

The fully etched 500-nm-thick silicon waveguide can produce loss below 1 dB/cm from wide waveguides, and bend radii below 10 μm from narrow spline/circular bends. The waveguide geometries can be combined on a single chip with short lateral tapers that have less than 0.01 dB of loss and better than −40 dB higher order mode excitation.

6.1.3. Low Reflection Edge Coupling

Integrated lasers, which by definition have the laser mirror on chip instead of relying on a cleaved or polished facet, must address the issue of the parasitic reflection from the facet forming a compound cavity between the facet and the laser mirror. Semiconductors typically have very high index of refraction, and silicon is no exception with n = 3.47. A very strong

Fresnel reflection occurs with the silicon-air interface. Even if index matching material is used to match the air to the index of the fiber mode, Δn = 2.02 still exists between the waveguide mode and the index matching material.

A common solution to this problem is to angle the waveguide relative to the facet. For wide multi-mode waveguides, the angled section can be thought of as a non-adiabatic taper—as it is only a few microns long—that couples the reflected power into higher order modes. Specific angles at particular wavelengths can couple over 99% of the power into higher order modes. If the wide waveguide facet is followed by a taper down to a narrower waveguide in which these higher order modes are not guided, then they are radiated, and the reflected power is lost. This effectively transforms the reflected power into loss. The addition of an anti-reflection coating designed to reduce the reflection into the higher order mode can reduce this loss.

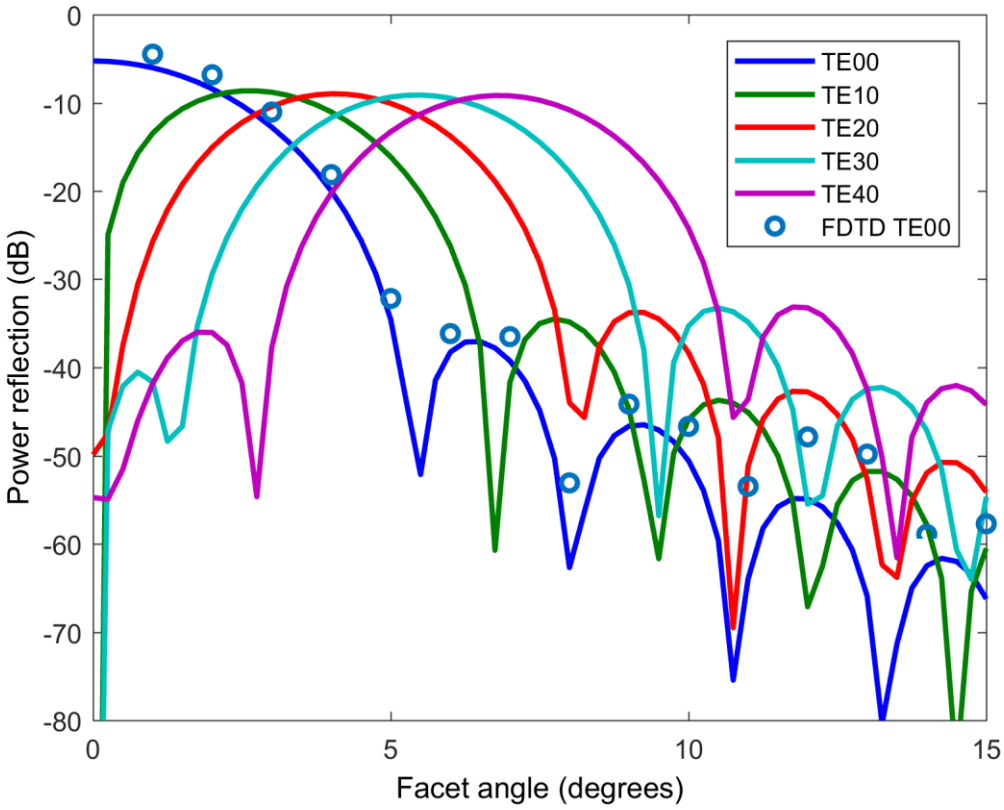

Figure 6.8: Simulated reflection into mode order for a 5-μm-wide angled facet. The lines are simulated using Eigenmode expansion, and the circles were simulated for only the TE00 mode in FDTD to double check the accuracy.

This effect is shown for an uncoated angled facet in Figure 6.8. The reflection for the fundamental mode decreases rapidly, but the reflection into the first higher order mode subsequently begins to increase. Higher angles transform the reflection into increasingly higher order modes. Due to refraction at the facet, the maximum angle is restricted to about 10 degrees, since very high angles relative to the normal of the facet are difficult to approach with a fiber for off-chip coupling. A simple Snell's law calculation reveals that 16 degrees is the critical angle for an air/silicon interface, but 11 degrees results in an output angle of 41.5 degrees, which is impossible to reach with a typical lensed fiber. 7 degrees happens to be a common angle, and there are many fiber positioner fixtures for this angle, so the author chose 7 degrees. However, this introduces −30 dB parasitic emission into the TE10 mode, which is guided in the 400-nm waveguide, and as mentioned earlier, transforms the higher order modes into loss. This loss totals about 2 dB, which is a significant amount of loss compared to the other components on the chip.

Applying an antireflection coating can reduce the loss by removing the reflection into the higher order mode. This coating needs to be designed using a 3D electric field simulation like FDTD or Eigenmode expansion, as the light emerging from the facet into the air is highly divergent. Plane wave approximations will yield a drastically incorrect film design, with a center wavelength error of over 100 nm. Thin films, 165 nm of Ta_2O_5 and 125 nm of SiO_2, were applied to the polished 5-μm-wide waveguide facet with ion beam deposition. The reduction in reflection is shown in Figure 6.9a. Finally, the waveguide is tapered from 5 μm to

400 nm over a length of 400 μm. This taper is lossy for the higher order modes, especially the TE20 mode, which is not guided. Figure 6.9b) shows the impact of the taper on the reflected light from the coated facet after tapering from 5 μm to 400 nm. The TE20 mode is not guided in the 400-nm-wide waveguide and so the blue curve shows the coupling from the TE20 mode into the TE00, since they both have even symmetry. The TE20 mode is strongly suppressed by the taper, while the TE10 mode, which is guided in the 400 nm waveguide, is only attenuated by 2 dB. For 8° angled facets, the reflection is below −50 for all modes, and below −60 for the TE00 mode. The reflection into the TE10 mode is the highest at −58 dB, but this is considered acceptable.

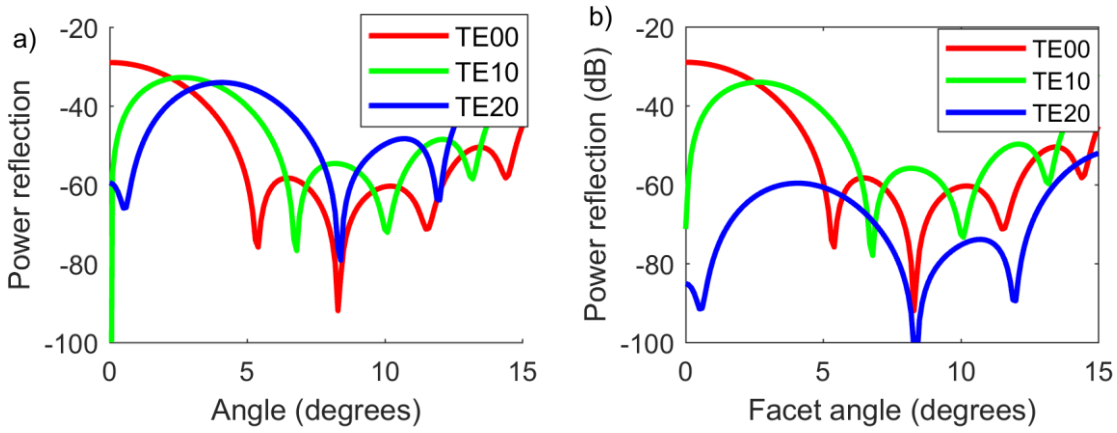

Figure 6.9: a) Antireflection coated angled facet, and b) the reflection of the coated facet after being transmitted through the taper down to 400 nm.

The antireflection coating has a wavelength minimum in reflection which is well known, and for flat facets normally the reflection value is below −40 dB for 10 nm of optical bandwidth. However, since the angled facet is naturally quite broadband, their combination allows the reflection to be below −40 dB for the S+C+L bands. This is shown in Figure 6.10. The coating is designed to reduce the TE10 reflection, and the different modes have different

wavelength minima. The chart in Figure 6.10 includes the loss of the taper, otherwise the TE20 reflection would be above −40 dB.

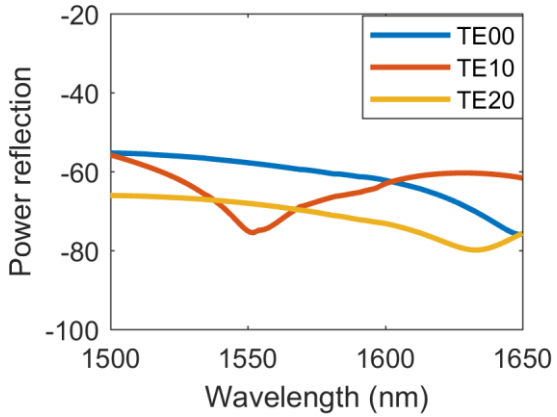

Figure 6.10: Reflection versus wavelength of the angled, coated, and tapered 5-μm-wide waveguide.

While this solution looks very good in simulation, measurements of the facet reflection using the spectral Fourier transform method [6] show that it is approximately −37 dB. The reason for this is unknown. It is possible that the thin film coatings have voids or particles, or that the polished waveguide facet is not planar. Another possibility is that the reflection is in the TM mode, which could be generated by the laser at low power levels. Increasing the angle to 10° to shift the reflection into TE30 and TE40 and undergoing an AFM inspection of the polished and coated facets are both a good direction to pursue. The performance of the current coating was adequate for high power mode-locked lasers, both in terms of reducing the insertion loss of the output facet and the parasitic reflection, but some spectral modulation from the angle facet is still visible. Improving the angle facet reflection could be a pathway to improved performance.

6.2. Directional Coupler

A directional coupler is a 4-port device which is used to split or combine electromagnetic signals. It has many uses in integrated photonic devices, such as splitting and combining light to form interferometric modulators. The main advantage of the directional coupler over other power splitter/combiners is that the coupling ratio can be controlled continuously from 0 to 1 by simply varying the length of the coupler, whereas other types of power splitter/combiners, for example multimode interference couplers (MMIs) and adiabatic couplers, must be redesigned for each desired splitting ratio. In addition, for lasers, the directional coupler is extremely desirable because it has very small parasitic reflection and parasitic multimode excitation, especially when compared to the MMI, which often has reflection above −30 dB reflection even in well-designed devices on the SOI platform. In addition, the MMI is inherently a multimode device, and when the injected signal is off the wavelength of peak transmission in the MMI it can excite higher order modes in the output waveguide, which is extremely undesirable in fully etched silicon waveguides. The adiabatic coupler has the advantage of extremely broad wavelength operation, with experimental demonstrations on SOI showing 100-nm bandwidth [7]. These splitter/combiners are much more complicated than the basic directional coupler, and the device in [7] had a shallowly etched waveguide–deeply etched adiabatic couplers often must be in excess of 500 μm in length, which increases the insertion loss and limits their application in laser cavities since the increased length introduces a free spectral range penalty.

The drawback of the directional coupler is that it has extreme sensitivity to dimensional variation, as the coupling ratio depends on the propagation constants of the two coupled modes

in the structure and on the degree of overlap between the un-perturbed modes of the structure, which has an exponential dependence on the coupler gap. The basic circular-bend-based directional coupler is shown in Figure 6.11a. It must be noted that the s-bends at the inputs and outputs of the device need to be considered in the design, because they must be beta-matched (so both ports on each side need to have the same bending radius) and because, as shown in Figure 6.11b, the profile of the symmetric mode shows significant perturbation because of the narrow gap. This requires transformation of the mode in the solitary waveguide into the shape of the mode in the coupled waveguide, so the curvature must be low enough that this is a gradual transition.

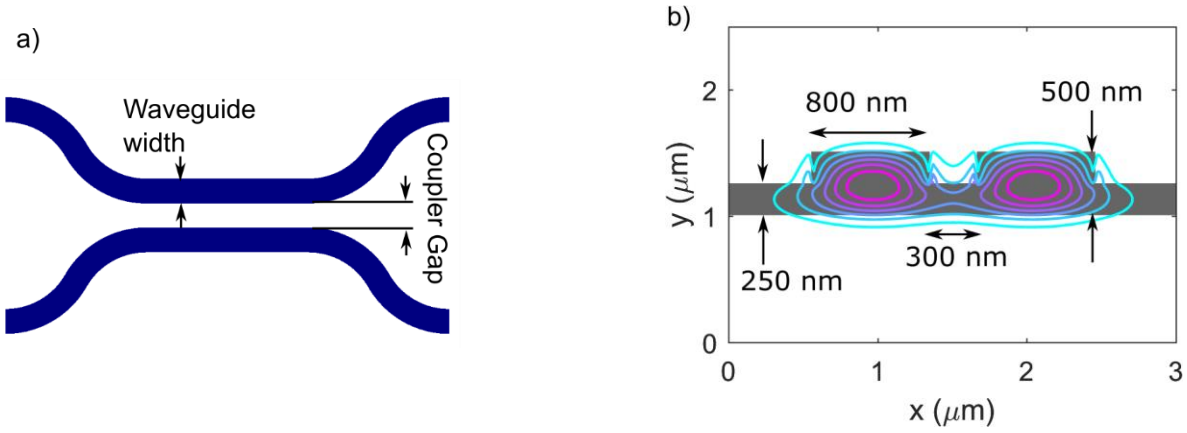

Figure 6.11: a) Plan view schematic of a directional coupler, and b) the cross section of a shallow directional coupler and mode contours of the lowest order symmetric mode overlaid on the to-scale cross section.

6.2.1. Shallow Directional Couplers

An initial attempt was made on early laser runs to use a shallow waveguide, but it was found that the directional coupler performance was too unpredictable based on normal fabrication tolerances. A simulation of the coupler shown in Figure 6.11b was performed using the Eigenmode expansion method and compared to similar couplers with 5% over etch and 5%

under etch, which is a reasonable assumption for achievable uniformity of a dry etch process. The variation in the power coupling coefficient introduced by +/− 5% etch depth is almost a factor of two. The results of this simulation are shown in Figure 6.12a).

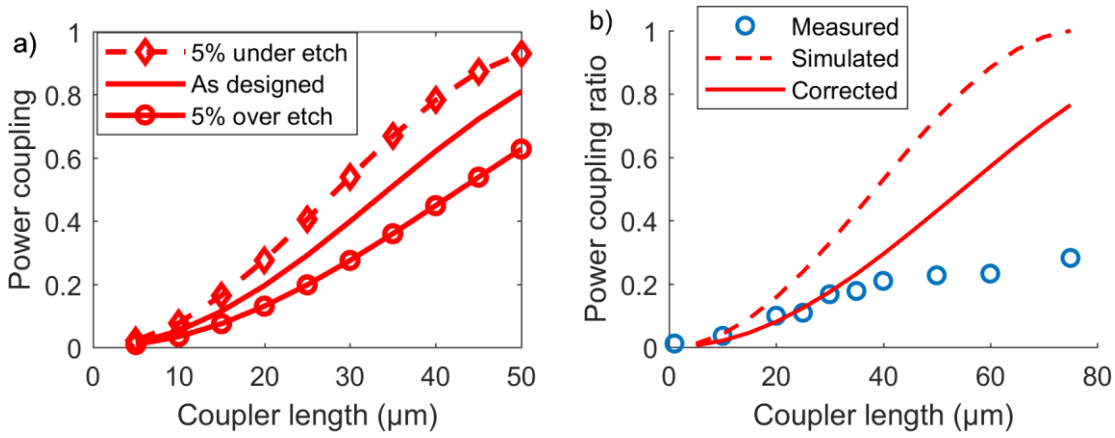

Figure 6.12: a) Simulation of process variation in power coupling of a directional coupler introduced by etch depth variation, and b) measurement data from shallow directional couplers.

The power coupling of the shallow couplers was then characterized by producing a set of devices with varying coupler length. These were fabricated in 500-nm-thick SOI with deep-UV lithography, and then diced, polished, and AR coated for testing. TE polarized light was launched into an input of the directional coupler with a lensed fiber, and the transmitted power at both output ports was collected with a second lensed fiber. The laser was swept across the C band and a digital IIR filter was used to remove residual FP ripple and multimode interference from inadvertently launching TM polarized light. The difference in power was used to calculate the splitting ratio. Additionally, a nearby straight waveguide was used as a reference to calibrate out the fiber-to-chip coupling losses to determine the insertion loss of the couplers.

The performance of the coupler did not match with expectations. The measured power coupling coefficient (Figure 6.12b, blue circles) was much less than the original design (Figure 6.12b, dashed red line). Even after accounting for the over etch, 345 nm instead of the intended 250 nm, and correcting the simulation (Figure 6.12b, solid red line) the measured power coupling (open circles) deviated from the simulation at longer coupler lengths. In addition, there was an average of 0.75 dB of excess loss in the couplers. Laser cavities using this shallow coupler design had very poor yield and output power, as will be discussed later in Section 6.3.

6.2.2. Fully Etched Directional Couplers

Due to the poor performance of the shallow waveguide directional coupler, it was abandoned in favor of a fully etched one. Fully etching the waveguide is highly repeatable as the $C4F_8/SF_6/Ar$ dry etch is highly selective, etching the buried silicon dioxide layer much more slowly than it etches silicon. Now the only source of dimensional variation should be the lithography linewidths, which can be practically controlled to within 2% in the UCSB fabrication facility thanks to the deep UV lithography system. However, because of the tighter confinement of the fully etched waveguide, the waveguide must be narrower to achieve reasonable coupling lengths. The goal of the directional coupler design is for the 50/50 coupling length to be sub-100 μm. According to [8], the mode width in the waveguide should be minimized to reduce the impact of linewidth variation on the coupling coefficient. The impact of the silicon waveguide core width on the mode width can be seen in Figure 6.13a. The mode of the 500-nm-tall and fully-etched silicon waveguides was calculated using the finite difference method, and the $1/e^2$ mode width was extracted for each waveguide width. In general, mode width tracks the width of the waveguide linearly while the waveguide width is above a certain critical width. Below this critical width, the mode width expands as the

waveguide becomes narrower, following an exponential trend as the mode enters the weakly guided regime. At this critical width, the two effects are acting in opposition and there is small variation of the mode width compared to the waveguide width. Since the coupling strength depends strongly on the overlap of the evanescent fields, directional couplers using this waveguide width should be less sensitive to fabrication induced linewidth variation. The coupler gap was chosen to be 400 nm as well. A smaller gap will reduce the coupling length exponentially but increases the difficulty of the lithography.

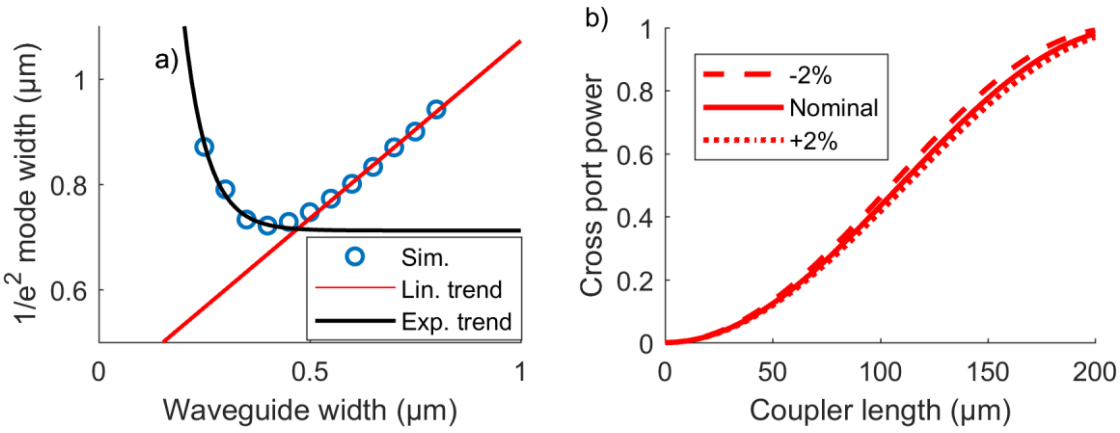

Figure 6.13: a) Simulation of the mode width in a fully etched 500-nm-tall silicon waveguide. Open blue circles represent simulation, while the lines are a linear trend line (red) and exponential trend line (black). b) Fabrication tolerance to linewidth variation of the 400-nm-wide 400-nm-gap fully-etched coupler.

After the introduction of the deep waveguide directional coupler, yield of lasers with cavities based on directional couplers increased dramatically. This includes the loop mirror mode-locked lasers as well as tunable single wavelength lasers based on coupled-ring-resonator mirrors. Because most of the lasers were working, focus on debugging the directional coupler was reduced and direct measurements of the coupling coefficient of the 400-nm-waveguide 400-nm-gap fully-etched coupler were not performed. Instead, the reflection of the

loop mirrors was measured from the laser output power. This will be discussed in Section 6.3. It was revealed during this investigation, once again, that the directional coupler did not produce as high-power reflection coefficient as it was designed for. This was found to be due to an air hole inside of the gap which was created by shadowing during the oxide cladding deposition, which is performed with reactive ion sputtering. Other researchers in the group attempted to resolve the problem with other deposition methods. It was found that the RIE PECVD machines create a similar air void.

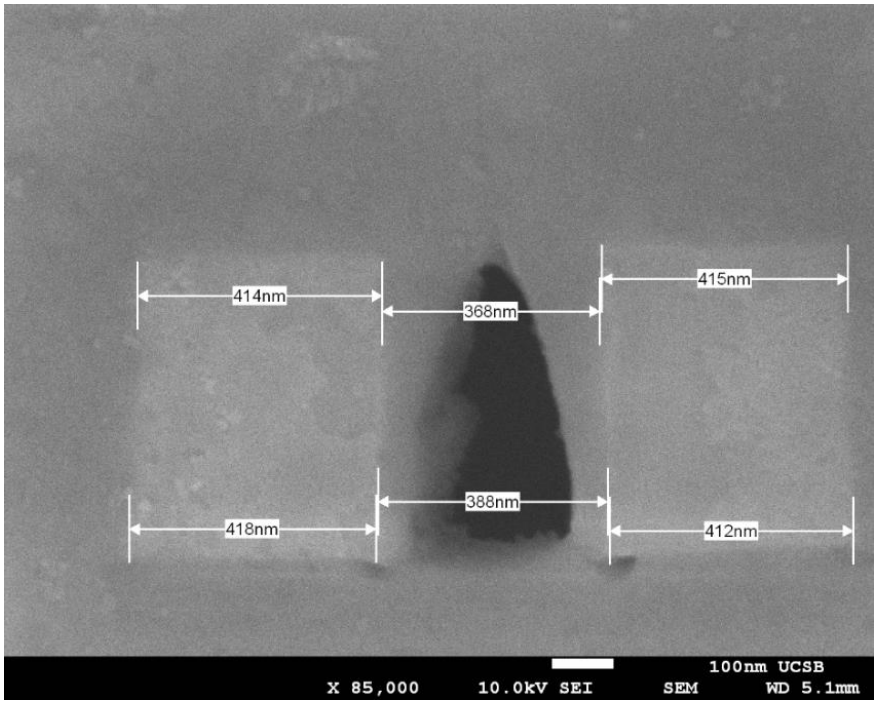

Figure 6.14: SEM image of the cross section of a fully etched directional coupler showing an air void in the coupler gap. Image courtesy of C. Zhang.

Simulation of the directional coupler with the air void added in show a considerable reduction in the coupling coefficient. The 50/50 coupling length is increased by 40 μm, as shown in

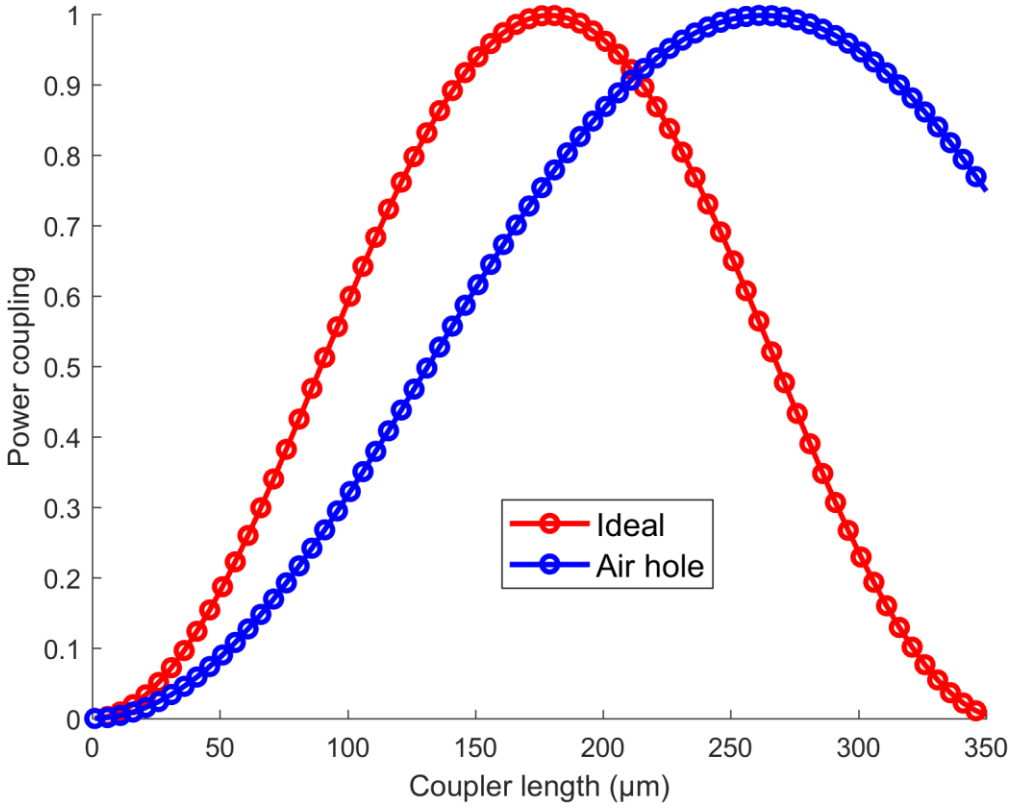

Figure 6.15. Measurements in the following section on loop mirror reflectors will show that this simulation is accurate when the air hole is included. More sophisticated high-pressure ICP PECVD systems can allegedly fill gaps such as these with oxide without forming a seam or hole. Unfortunately, the ICP PECVD system at UCSB (the Unaxis) does not produce good optical quality oxide films and contaminates the p-type InP with hydrogen, as discussed in Section 5.2.3. Since the performance of the couplers seem predictable when the air hole is considered, it was decided to simply compensate for it in the design and leave the process alone. As shown in Section 6.3, high performance laser reflectors can be produced with this design. In the future, it will probably be worthwhile to reduce the gap, since the coupler lengths are now longer than the desired 100 μm for 50/50 coupling.

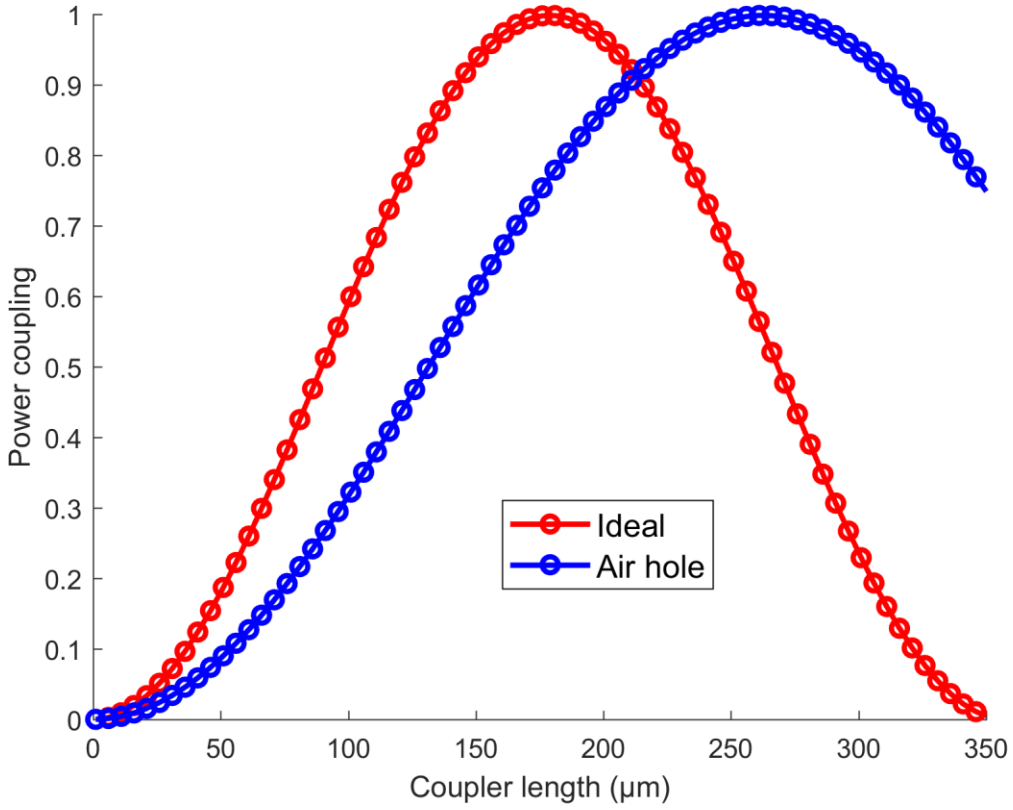

Figure 6.15: Directional coupler simulation at 1585-nm wavelength showing the impact of the air hole shown in Figure 6.14.

6.2.3. Future Designs

All of the fully etched waveguide devices described in this dissertation use the 400-nm gap/400-nm waveguide directional coupler design. Experience fabricating and testing these devices has led the author to consider changes to the design to improve performance. As explained earlier, the variation in mode width with respect to the change in waveguide width is minimized at 400-nm-waveguide width. But the coupler strength depends more on the width of the evanescent field in the gap, which only decreases in size with increasing waveguide width. In photolithography, changing the linewidth of the waveguide also affects gap; increasing exposure should narrow the waveguide (positive tone photoresist) and enlarge the

gap. Increasing coupler gaps should decrease the coupling strength exponentially. There is a point where the two effects are equal in strength and cancel each other out. This point turns out to be at 450-nm-waveguide width, just at the beginning of the deviation from the linear trend. The coupling variation introduced from the waveguide width and gap fabrication error is shown in Figure 6.16a. The errors cancel to nearly 0 over the entire range. The fabrication tolerance plot had to be enlarged to +/− 10% to show meaningful error. This trick only works at one wavelength and a specific combination of waveguide and gap; the critical mode width depends on wavelength, and after the linewidth variation becomes too large, the errors go out of balance.

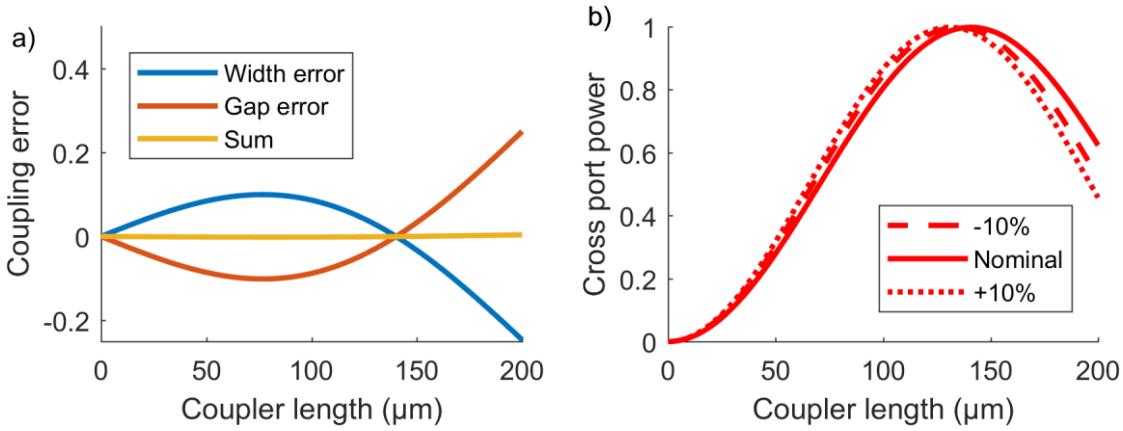

Figure 6.16: a) Coupling error introduced by the gap and width variation, and b) the fabrication tolerance of the 450-nm waveguide 300-nm gap directional coupler.

6.3. Loop Mirror

As discussed in Section 2.3.1, a broad-band reflector is desired for mode-locked laser mirrors. Broad-band Bragg gratings are available on silicon [9], but they are difficult to fabricate since

the period for a 1st order grating at 1550-nm wavelength on silicon is typically ~130 nm, depending on the waveguide geometry, which is below the resolution limit of the projection lithography systems available at UCSB and typically requires 192-nm immersion lithography or electron beam lithography, both of which are extremely expensive. The loop mirror was originally proposed in fiber optics as a nonlinear optical switch based on self-phase modulation [10], and was first demonstrated on silicon for use in Fabry-Perot interferometers [11], and are often referred to as Sagnac loop mirrors due to their similarity to the Sagnac interferometer.

6.3.1. Loop Mirror Design

The loop mirror is essentially a directional coupler with the two output ports connected via a loop of waveguide. This is shown schematically in Figure 6.17a). The power reflection of the device is given by the formula:

$$R = 4\tau k e^{-2\alpha L} \qquad 6.1$$

where R is the power reflection, κ and τ are the power coupling and transmission coefficients, L is the overall single-pass length of the device (directional coupler plus loop), and α is the propagation loss in the waveguide in cm^{-1}.

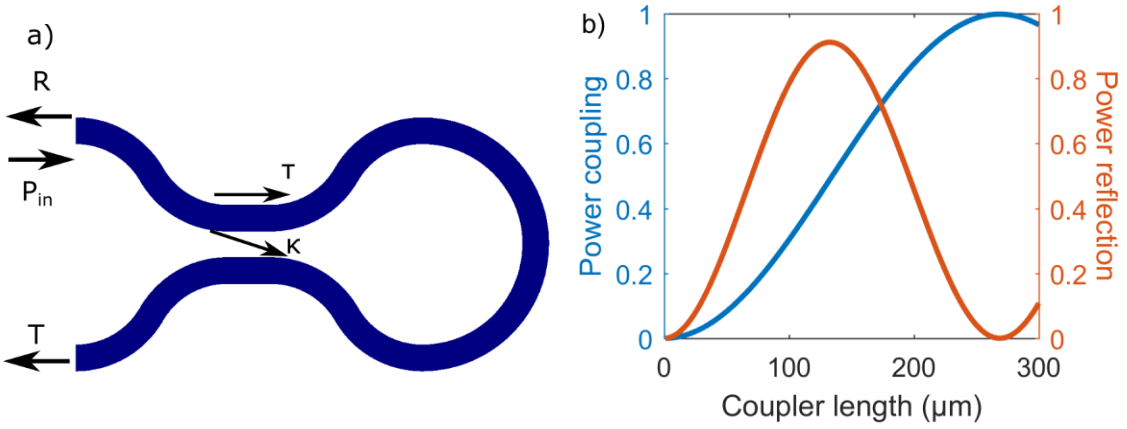

Figure 6.17: a) Schematic of the loop mirror, with R and T being the power reflection and transmission, P_{in} being the input power, and κ and τ being the power coupling and transmission coefficients of the directional coupler. b) Power coupling coefficient κ (blue) of the directional coupler and the resulting reflection (red). The waveguides are 400-nm tall, 500-nm thick, and have a 400-nm wide gap. The air hole of Figure 6.17 is included in the simulation.

Assuming 10 dB/cm as shown in Figure 6.2 for a 400-nm wide waveguide, using the calculated coupling coefficient from the 400-nm-waveguide 400-nm gap directional coupler, and assuming 60-μm single-pass length for the loop, the reflection versus directional coupler length can be calculated. This is shown in Figure 6.17b in red, compared to the coupling coefficient in blue. It can be seen that the maximum reflection is not equal to 1, which is due to the propagation loss being fairly high in the 400-nm-wide waveguide. Power reflection over 90% can be achieved even with this waveguide loss. Minimization of the length of the coupler and the length of the loop are therefore important for maintaining high reflection. Reduction of the loop to a length as small as 20 μm can be achieved by using very small bends; reduction of the directional coupler length can be achieved by reducing the width of the gap. 300 nm is practical with 248-nm lithography and would reduce the length of the coupler by about 60%.

The wavelength dependence of the loop mirror is fairly complicated and depends mainly on the wavelength dependence of the directional coupler. Directional couplers normally have their coupling coefficient increase with wavelength, as the mode expands out of the waveguide when the length is less than the coupling length (where $\kappa = 0.5$). When $\kappa > 0.5$, the through power begins to fall faster than the coupling power, resulting in the curved response versus wavelength for the 100% designed coupler seen in Figure 6.18. For lower reflection mirrors, the trend versus wavelength is nearly linear with increasing wavelength. This may actually

increase the laser operating bandwidth, as a laser designed at 1550 nm will have decreasing gain as the wavelength red-shifts, and the increasing reflection can compensate for this. In practice, quantum well mode-locked laser optical bandwidth is maximally 11 nm [12] due to homogeneous broadening in the gain material. Over this range, the worst-case variation in reflection is in the 50/50 mirror case, which only varies by 4.5%.

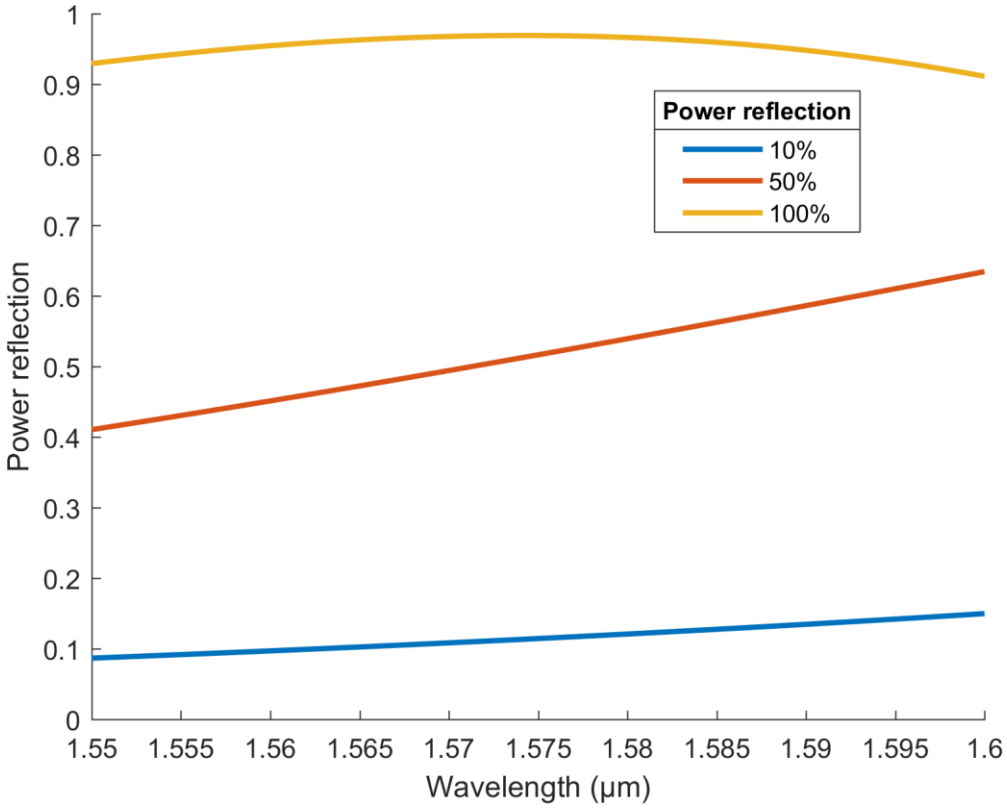

Figure 6.18: Wavelength dependence of the loop mirror power reflection for three different mirror designs with the target power reflection shown in the legend. The waveguides are 400-nm tall, 500-nm thick, and have a 400-nm wide gap. The air hole of Figure 6.17 is included in the simulation.

6.3.2. Measurement of Loop Mirror Lasers

Due to the inaccuracies of the passive directional coupler measurements introduced by fiber-to-chip coupling loss and inadequate polarization extinction in Section 6.2.1, and the difficulty projecting the performance of the passive splitting ratios onto the final laser performance, measurement of the loop mirror reflection was extracted directly from working integrated lasers. A specialized test structure was designed for this purpose, and is shown schematically in Figure 6.19. The device is a heterogeneous Si/III-V laser consisting of a flat polished silicon waveguide facet, with known reflectivity of 0.305 (Figure 6.2), a short passive 800-nm-wide 500-nm-thick waveguide, a heterogeneous amplifier based on the F-type epi shown in Table 4-3 and including two 20 μm linear P-taper linear N-taper heterogeneous transitions, then an 800-nm to 400-nm passive Si taper, followed by a circular-bend loop mirror as described in the previous section. The output of the loop mirror is directed to a low reflection angled facet as discussed in 6.1.3. This device is shown schematically in Figure 6.19.

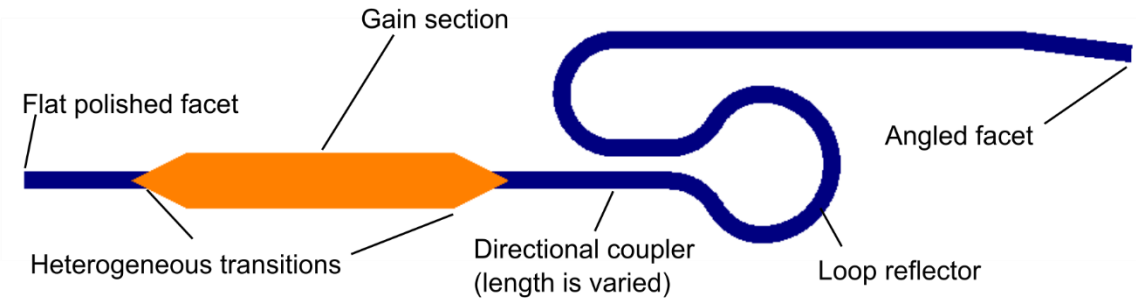

Figure 6.19: Loop mirror reflection test laser.

In total, 16 devices were fabricated, with directional coupler lengths of 16, 30, 42, and 88 μm. The devices were in groups of 4, each with a different waveguide width. For the purpose of this measurement, the waveguide width is inconsequential and so those devices are essentially repeats to improve the quality of the data.

The measurement was carried with two methods: The slope efficiency comparison method, and the threshold current comparison method. Slope efficiency comparison uses the difference in slope efficiency from the flat facet side and the loop reflector side to determine a ratio of the power reflection. Since the flat facet reflection is known accurately, the loop mirror reflection can then be determined. Threshold current comparison uses the gain-current relationship of the amplifier and the difference in threshold to determine the mirror loss, which, again, with the known flat facet mirror reflectivity, allows the calculation of the loop mirror reflection. The threshold method requires an additional test device, identical to the device in Figure 6.19 but with two flat facet mirrors instead of the loop mirror and a flat facet mirror.

The measurement of laser slope efficiencies was performed at 20°C using an integrating sphere to collect the power. The sphere has a 1.5" aperture, so it can be assumed that 100% of the power is collected. According to the formulation in [13], the ratio of the slope efficiencies η_{d1} and η_{d2} from either side of the device are related by:

$$\frac{\eta_{d1}}{\eta_{d2}} = \frac{F_1}{F_2}, \tag{6.2}$$

the value of which is known from the slope efficiency measurement. The F values are defined according to Equation 3.30 in [13] with some slight modifications:

$$F_1 = \frac{t_{\text{taper}}^2}{\left(1 - r_1^2\right) + \frac{r_1}{r_2}\left(1 - r_2^2\right)} \tag{6.3}$$

and

$$F_2 = \frac{t_{\text{taper}}^2 t_{\text{angle}}^2 t_{\text{LR}}^2}{\left(1-r_2^2\right)+\frac{r_2}{r_1}\left(1-r_1^2\right)}. \qquad 6.4$$

In this formulation, side 1 is the polished facet, and side 2 is the loop reflector. F_1, η_{d1}, and r_1 are the F value, slope efficiency, and field reflection coefficient for the polished mirror side, and F_2, η_{d2}, t_{LR}, and r_2 are the F value, slope efficiency, field transmission and reflection coefficients for the loop mirror side. t_{angle} is the field transmission coefficient for the angled facet, which is not antireflection coated and therefore has loss of approximately 2 dB due to the fact that the reflection is into the TE20 mode which is subsequently lost in the tapered silicon waveguide. The reflections from the angled facet and the heterogeneous transition are neglected as they are at least 2 orders of magnitude smaller than the mirror reflections, and t_{taper} is the transmission coefficient of the heterogeneous transition, which does not have to be assumed as it is shared between F value terms and will cancel. The equations can be combined as follows:

$$\frac{\eta_{d1}}{\eta_{d2}} = \frac{F_1}{F_2} = \frac{\left(\left(1-r_2^2\right)+\frac{r_2}{r_1}\left(1-r_1^2\right)\right)}{t_{angle}^2 t_{LR}^2\left(\left(1-r_1^2\right)+\frac{r_1}{r_2}\left(1-r_2^2\right)\right)}, \qquad 6.5$$

which must be solved numerically for r_2, the loop mirror reflectivity. The resulting data is shown in Figure 6.20 as black symbols.

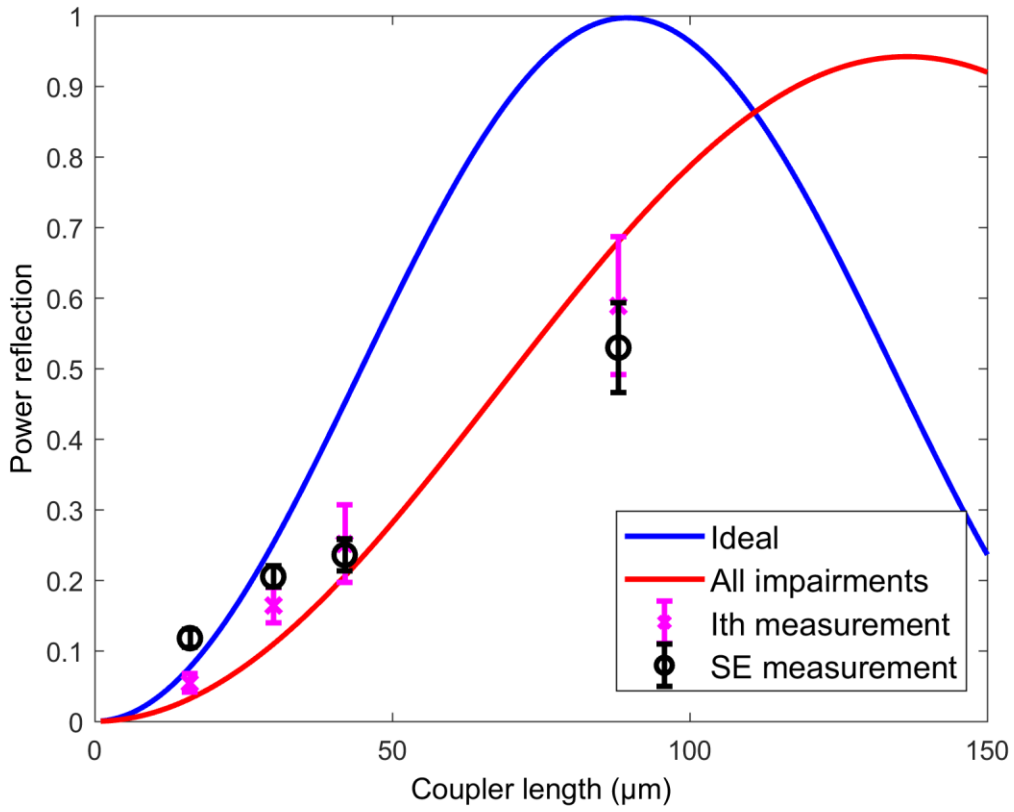

Figure 6.20: Measurement results for the loop mirror reflection (symbols) plotted with the simulation results (lines). The symbols represent the average value of 4 separate devices, and the error bar is the standard deviation. The "Ith measurement" refers to the method of extraction of reflection from comparing threshold current, and the "SE measurement" refers to the method of extracting reflection by comparing slope efficiency. The waveguides are 400-nm tall, 500-nm thick, and have a 400-nm wide gap. The air hole of Figure 6.17 is included in the "All impairments" simulation.

The second method, the threshold current comparison, uses an identical device (in this case they were the same lasers with the loop mirror polished away) without a loop mirror and Cassidy's method [5] to extract the gain coefficient g_0 and the modal device transparency current J_m (to avoid needing to determine the internal loss and injection efficiency). Then, Equation 4.7 can be written for each type of device:

$$\alpha_{\mathrm{m,polish}} = g_{0,\mathrm{J}}(\lambda)\ln\left(\frac{J_{\mathrm{th,polish}}}{J_{\mathrm{m}}(\lambda)}\right) \tag{6.6}$$

for the laser with two polished facets and

$$\alpha_{\mathrm{m,LR/polish}} = g_{0,\mathrm{J}}(\lambda)\ln\left(\frac{J_{\mathrm{th,LR/polish}}}{J_{\mathrm{m}}(\lambda)}\right) \tag{6.7}$$

for the laser with one polished facet and one loop reflector. The mirror loss terms for the two devices are:

$$\alpha_{\mathrm{m,LR/polish}} = \frac{1}{L_a}\ln\left(\frac{1}{r_1\, r_2}\right), \tag{6.8}$$

and

$$\alpha_{\mathrm{m,polish}} = \frac{1}{L_a}\ln\left(\frac{1}{r_1^2}\right), \tag{6.9}$$

where L_a is the length of the amplifier section, and $g_{0,\mathrm{J}}(\lambda)$ and $\mathrm{J_m}(\lambda)$ are both known from the gain measurement from the flat facets device. Note that $g_{0,\mathrm{J}}(\lambda)$ and $\mathrm{J_m}(\lambda)$ depend on wavelength, so the lasing wavelength of the loop mirror device must also be known. These equations can be solved algebraically or numerically for r_2, the loop mirror reflection. This value is plotted in Figure 6.20 as the pink X symbols showing the average value and the error bar showing the standard deviation of the four devices with each directional coupler design.

The values for the threshold current comparison are within the measurement error of the simulated value for the loop mirror after taking all directional coupler impairments into account–in this case, the air hole, the real line widths (434-nm waveguides, 386-nm gap), the difference in wavelength (couplers designed at 1585 nm, lasers lasing around 1565 nm), the waveguide propagation loss (10 dB/cm) and the sidewall angle (about 7 degrees). The air hole

is the major cause of difference between the ideal and impaired simulations. The slope efficiency comparison method is less accurate, most likely because the measurement ignores the wavelength variation of the slope efficiency that is introduced, and the loss of the angled facet may not be known accurately and is not a factor in the threshold comparison. This measurement suggests that the directional coupler can be simulated accurately provided that the real dimensions of the waveguides and the composition of the gap are known.

6.4. Impact of Passive Components on Mode Locking

The introduction of a passive waveguide and integrated mirror to a mode-locked laser diode must be done with extreme care to prevent the addition of parasitic interference through unintended reflection and multimode excitation, which can be seen in Figure 2.1. Waveguide loss, parasitic reflection, and multimode excitation can all impact the behavior of the mode-locked laser. Waveguide loss impacts the performance, reducing the continuous wave output power and therefore the pulse peak power. Reflection and multimoding degrade mode-locking performance by restricting the laser emission wavelength through the creation of interference fringes, which reduces the bandwidth available for short pulse formation, and by introducing secondary pulses inside the cavity that may destabilize the mode locking operation by bleaching the absorber or reducing gain from the main pulse. As discussed earlier in Chapter 2, the directional coupler-based loop mirror should in theory have no parasitic reflection and only introduce higher order modes at the bent-to-straight waveguide transitions. The waveguide loss is limited for millimeter scale waveguide sections as long as the waveguide width is wide for most of the propagation distance (see Figure 6.2). A 1-mm-long passive waveguide at 800 nm width and a 160-μm-length loop mirror at the 400-nm waveguide-width

should only add 0.36 dB of loss. While this is not insignificant, it should still allow for high power operation as long as other sources of loss in the cavity are minimized, and in the case of these lasers is typically smaller than the heterogeneous transition loss (see Section 5.2) and the amplifier waveguide propagation loss (see Section 4.3).

In the case of the best performing mode-locked laser designs, using the conformal-index p-InP taper and angled n-InP transition, the dominant source of parasitic reflection was from the angled facet, which has somewhat variable performance, and despite anti-reflection coating is still in the −30 dB range for the best devices and above −20 dB for the worst. Quantification is difficult due to the low value and the fact that there is no reference reflection on any of the mode-locked lasers.

The device designs available for comparison have the 30 μm conformal-index P-taper and the angled N-taper unless otherwise specified. All the active region lengths are 2000 μm. The passive waveguide sections vary in length to compensate for various directional coupler designs, but the total propagation length is designed to set the cavity length so that the repetition rate will be 10 GHz fundamental and 20 GHz in colliding-pulse mode-locking. The standard absorber length is 60 μm unless otherwise stated. Most of the lasers have 36-μm- and 80-μm-long directional couplers in their front and rear loop mirrors, corresponding to 15% and 50% power reflection, respectively. All the gain section waveguide widths in the following sections are 850 nm.

6.4.1. Cavity Reflection Optimization

To attain high output power and high wall plug efficiency, the reflection of the cavity mirrors must be carefully designed. As mentioned in Section 4.2, longer gain sections have an advantage in output power since the increased length of the mesa reduces both the electrical

and thermal resistances while the increased transparency current can be accommodated by reducing the thickness of the active region. Since the active region has higher loss than the passive section, this increases the overall loss in the cavity, which decreases the slope efficiency. The higher gain afforded by the longer gain section allows for lower reflection mirrors, which directly compensates for the increased loss. If the proper reflection can be maintained in the mirrors, high slope efficiency can be attained for devices with long gain sections, and the reduced electrical and thermal resistance will result in higher maximum output power. In typical applications, only power from one side of the device can be utilized. For this reason, it is beneficial to have a high reflection mirror on the laser back side (the one not emitting into the circuit) to reduce the threshold.

Empirical determination of this optimum is usually necessary, as the loss in the gain section is difficult to determine experimentally. According to the simulation in Figure 4.10, it is approximately 5 cm^{-1} in the 850-nm waveguide, which is 4.34 dB for a 2000-μm gain section and is the dominant source of loss in the cavity. For this experiment, circular loop mirrors with bend radii of 25 μm were employed. The rear mirror is designed for 50% power reflection, and the front mirror, from which the power was collected, has directional coupler lengths of 20 μm, 36 μm, and 80 μm, targeting 4%, 15%, and 50% power reflection. Measurement of the laser power was conducted by collecting power from the front side of the laser through an integrating sphere while the device is attached to a 20°C copper stage. The facet was terminated with a 5-μm flared angle facet and was antireflection coated, so the loss from the transformation of the reflection can be neglected. Figure 6.21a shows the maximum power attained by the three lasers, with the 4% mirror reaching 25 mW of output power, nearly double that of the 15% mirror. Figure 6.21b shows a detail of the LI curve near threshold, demonstrating the drawback

of reduced mirror reflectivity: increased threshold current. In the case of these devices, the threshold current is dominated by the modal transparency current, which is about 28 mA, so the penalty in wall plug efficiency is not significant, and the R = 4% power reflection mirror reaches 4.20%, compared to 2.25% for the R = 15% mirror. Further reduction of the reflection may increase the maximum output power to an even higher level, but introduces the risk of increased threshold current which will degrade wall plug efficiency.

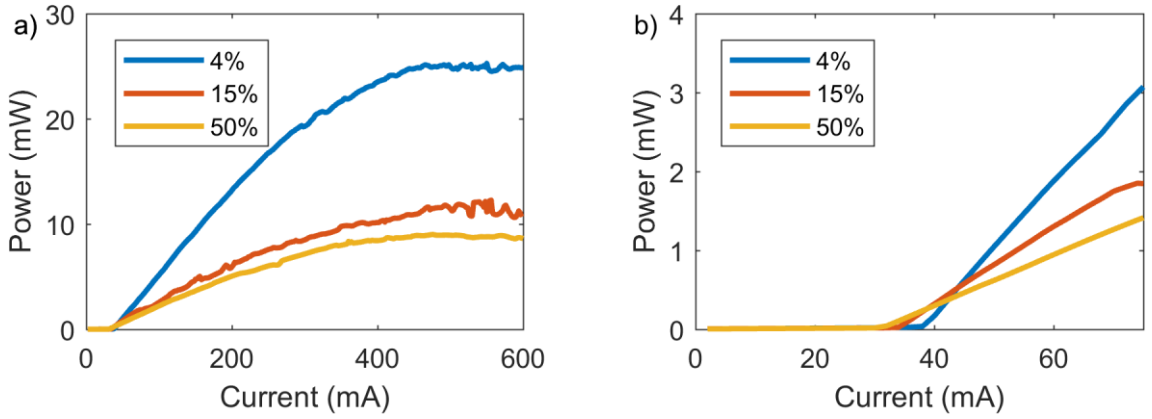

Figure 6.21: LI characteristic of the mirror reflectivity split. The rear mirror was designed for 50% power reflection in all three devices. The legend indicates the front mirror reflectivity. a) is the full current range showing the maximum power, and b) is a detail around threshold. The directional coupler waveguides are 400-nm tall, 500-nm thick, and have a 400-nm wide gap. The gain sections are 2000-μm long and have 850-nm wide waveguides in the amplifier section.

6.4.2. Spline Mirror Optimization

The spline/circular bend introduced in Section 6.1.2 was intended to reduce the footprint and therefore the propagation loss in the loop mirror by allowing tighter waveguide bends without introducing bend-to-straight transition loss and multimode excitation. The spline mirrors with good performance both had 10° coverage of 90° bends. For the s-bend, the spline

section was treated like a 90° bend, and the angle of the circular section was reduced to form a 45° bend. The u-turn at the end of the loop is a full natural spline. The two best performing splits were the Type 1 spline mirror with 5-μm control points, resulting in a minimum bend radius of 5 μm in the u-turn (by coincidence), and the Type 2 spline mirror with 3-μm control points and minimum bend radius of 3 μm. These mirrors are shown to scale with the 25-μm circular mirror in Figure 6.22. The difference in footprint is dramatic: the circular mirror occupies a square of 13,600 μm^2, while the type 1 and type 2 spline mirrors are 1,600 μm^2 and 720 μm^2, respectively, a reduction of 19 times for the Type 2 mirror. In addition, the propagation length through the loops are greatly reduced, from 217 μm for the circular mirror to 57 μm for the spline type 1 and 30 μm for the spline type 2 mirror.

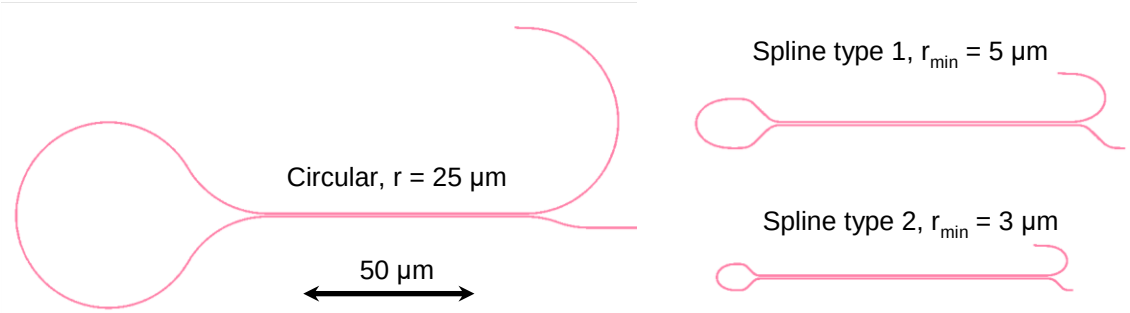

Figure 6.22: Size comparison of the circular bend loop mirror and the two spline loop mirrors.

The spline mirrors therefore have reduced propagation loss, which increases slope efficiency. Losses from bend-to-straight transitions are also eliminated. The 25-μm mirror has bent-to-straight transitions which add up to 0.2 dB loss, and the 217-μm loop of 400-nm waveguide has 0.217 dB of loss, for a total of 0.417 dB not including the directional coupler. The spline type 1 mirror, if it does indeed eliminate the transition loss, only has 0.057 dB of loss from the loops. Consequently, the slope efficiency of the spline loop mirrors is

considerably higher than the circular mirror lasers. This is shown in

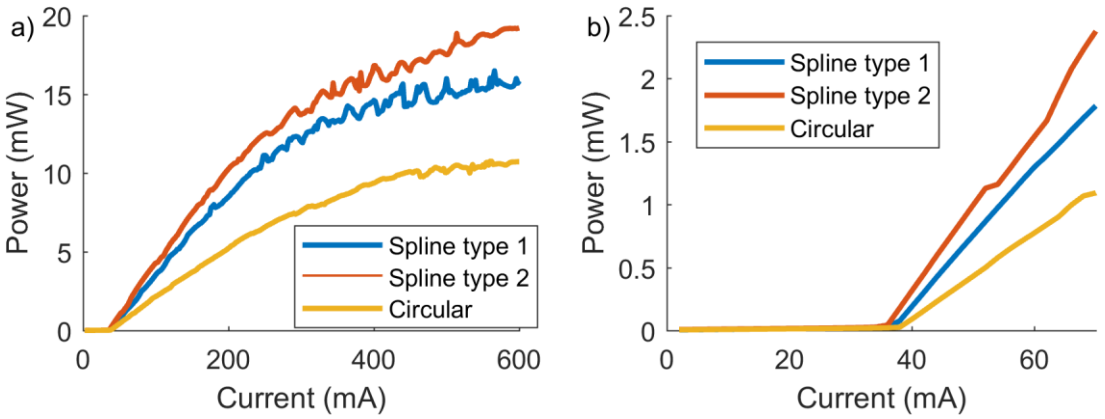

Figure 6.23a. The difference in output power is even higher than expected, leading the author to believe that the circular mirror device may have been impaired. Nevertheless, of the 4 repeats of each type of device that were available, these are the three with the highest performance.

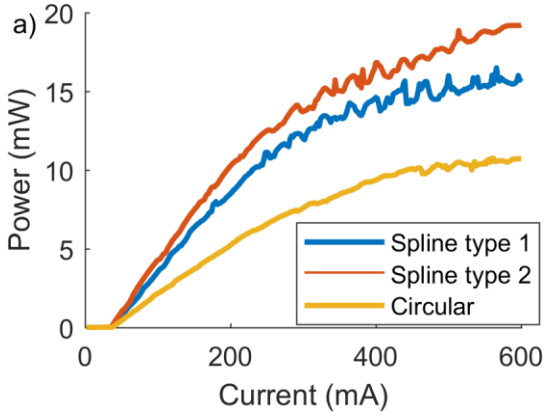

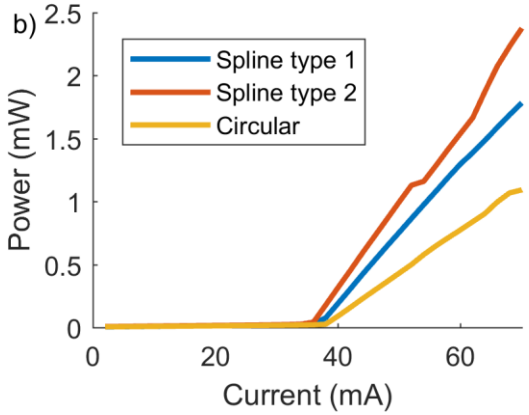

Figure 6.23b shows that the threshold follows the inverse trend of the slope efficiency, ruling out a potentially higher reflection in the circular loop mirror device, as this should have caused the threshold to decrease.

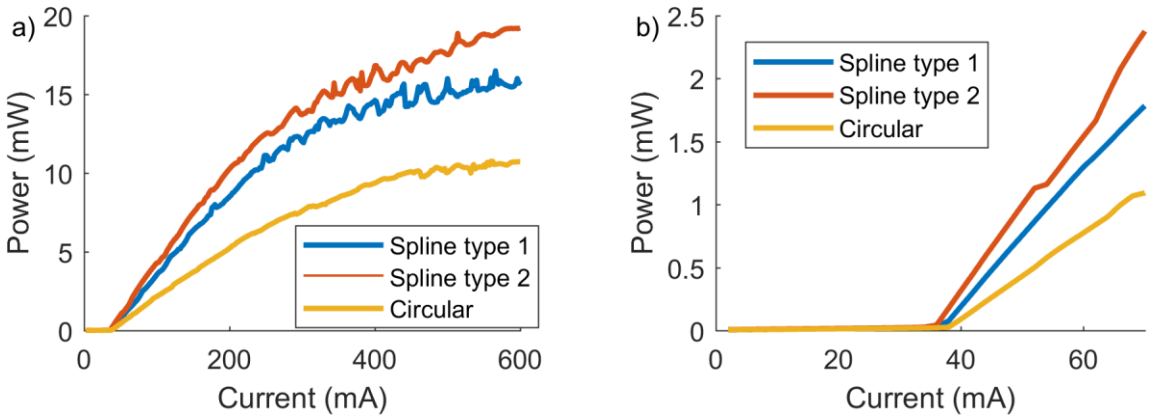

Figure 6.23: LI characteristic of the loop-mirror type split. The legend indicates the mirror type. a) is the full current range showing the maximum power, and b) is a detail of the threshold current. The directional coupler waveguides are 400-nm tall, 500-nm thick, and have a 400-nm wide gap. The gain sections are 2000-μm long and have 850-nm wide waveguides in the amplifier section.

Precise cavity optimization and reduction of losses is crucial for high output power integrated lasers, producing almost a factor of two increase in power for a finely optimized 4% mirror compared to an approximately optimized 15% mirror (which felt sufficiently low to the author at the time of the mask design). Reduction of passive losses by introducing the spline/circular bend into the loop mirror similarly provides an increase in output power, perhaps as much as 60% in this case. The lasers in Figure 6.23 have R = 15% mirrors, and could then reasonably produce 38 mW of output power with the R = 4% mirror. Increasing the back-mirror reflection to 90% would allow further reduction of the front mirror reflectivity, and so 40 mW, or 16 dBm, which is a common target for high power single wavelength lasers

in coherent transmission systems, should be attainable, bringing the heterogeneous silicon laser within the range of the state of the art of output power for InP-substrate lasers.

6.4.3. Mode Locking Results

The spline curve mirror was highly significant with regard to the passive mode locking performance. The multimode interference introduced by the higher order mode excitation creates groups of modes which are separated by 5-10 nm in wavelength, giving them slightly different repetition frequencies due to the high waveguide dispersion in the active region. Since they are not phase locked, the groups of modes create separate pulses, which drift away in time, due to dispersion, and prevent the mode-locked laser from reaching steady state pulsation. Mode-locked lasers produced with components that had −14 dB transmission into TE10 would only Q-switch mode lock because of this phenomenon. Even if the transmission can be reduced to −28 dB, as it was with the introduction of the angled n-layer taper (see Section 5.4), the mode comb can have its optical bandwidth limited by the mode interference. This increases the minimum attainable pulse width.

The spline loop mirror was introduced to address this limitation, firstly by reducing the multimode excitation at the bent-to-straight transition and, in the case of the Type 2 spline loop mirror, act as a mode filter by enabling extremely tight 3-μm-radius bends. Measurement of the pulse width shows that indeed there is a clear trend in relation to the mirror design, shown in Figure 6.24. The Type 2 spline loop mirror showed the lowest pulse width, at 909 fs, passively mode-locked. All three had their best pulse width near 88 mA bias current and −4.5 V absorber bias. The current shortest pulse on silicon is 3 ps, shown as a green line [14]. This laser was able to produce 98 mW of peak power, which is the highest of any fully integrated mode-locked laser diode around 20 GHz. For all fully integrated mode-locked laser

diodes around 20 GHz, the shortest pulse measured in the same way (with autocorrelation) is 1.06 ps [15]. Shorter pulses from fully integrated lasers exist at higher frequencies. One allegedly has a 640 fs pulse at 37 GHz [16], but did not report on chip peak power but is approximately 31 mW assuming 10 dB of fiber to-chip-coupling loss; additionally, there was evidently a miscalculation of their pulse width in the paper, and from their own Figure 8 it appears the FWHM of the autocorrelation trace is 2.87 ps, or a 1.86 ps $sech^2$ pulse width. The other claims 700 fs pulse width at 500 GHz [17], but it did not produce any extinction between pulses. The autocorrelation trace appears to be a sinusoid, and it has 43 mW of peak power. The passive pulse performance of the Type 2 spline mirror laser is the best of any silicon laser by a factor of 3. It is the best of any fully integrated mode-locked laser diode at 20 GHz as well, and compares favorably against all fully integrated mode-locked lasers. Only the integrated laser result reported in [18], at 30 GHz, is shorter. This paper did not report an output power.

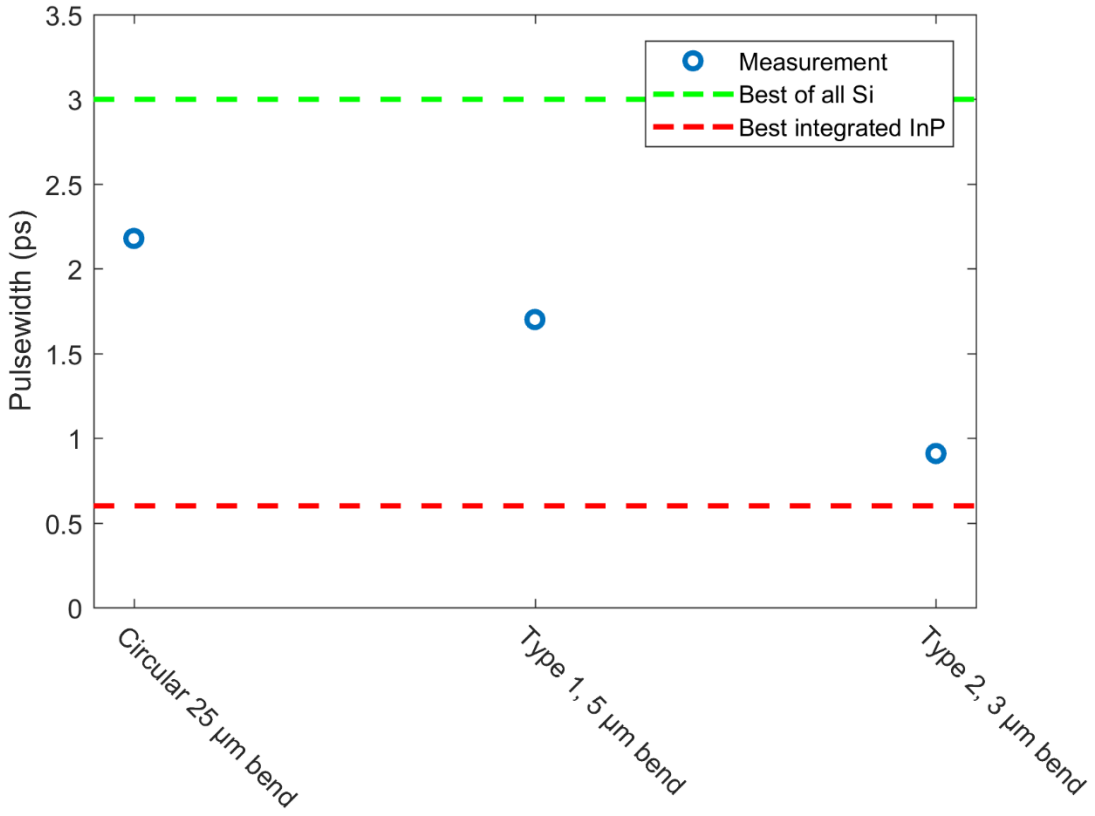

Figure 6.24: Narrowest passively mode-locked pulse widths from the mirror split block. The directional coupler waveguides are 400-nm tall, 500-nm thick, and have a 400-nm wide gap. The gain sections are 2000-µm long and have 850-nm wide waveguides in the amplifier section. The devices all have 15% power reflection front mirrors and 50% power reflection rear mirrors. All devices have 60-µm long saturable absorbers.

The autocorrelation trace of the best pulse is shown in Figure 6.25a, along with the full span of the electrical spectrum in Figure 6.25b. The autocorrelation shows good agreement with the expected hyperbolic secant squared fit, except for the pulse wings, which is expected in diode lasers since the pulse is not fully symmetric. The electrical spectrum displays a clean line at 20 GHz with no sign of amplitude modulation on the carrier frequency and only a very low level of carrier resonance fluctuations around 1 GHz. These fluctuations are 40 dB below

the 20 GHz peak, so they are not a major concern, but it is worth mentioning that some bias conditions that create longer pulses do not have any visible peaks except the 20 GHz peak.

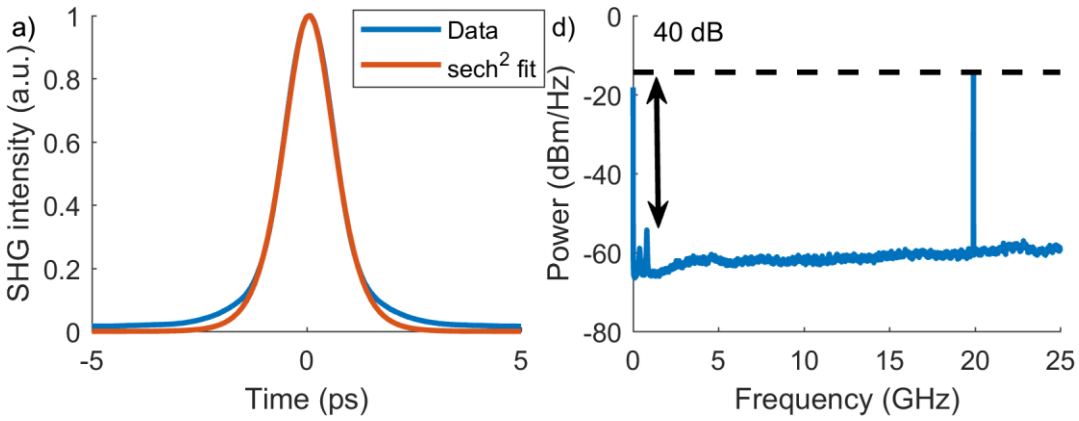

Figure 6.25: a) Autocorrelation trace of the 909-fs pulse from the type 2 spline mirror laser, b) electrical spectrum at the same bias condition. The directional coupler waveguides are 400-nm tall, 500-nm thick, and have a 400-nm wide gap. The gain section is 2000-μm long and has an 850-nm-wide waveguides in the amplifier section. The device has a 15% power reflection front mirror and 50% power reflection rear mirror. It has a 60-μm long saturable absorber. This device has a Type 2 spline curve mirror.

It should also be noted from Figure 6.25b that there is no measurable power fluctuation at 10 GHz, and in fact there was no bias condition for this laser that would produce an autocorrelation trace at 10 GHz. This is due to the extremely accurate matching of the passive cavity lengths and optimization of the absorber length to ensure strong time-domain extinction ratio. The optical spectrum is shown in Figure 6.26a, displaying a wavelength comb centered at 1575 nm and a side peak starting to emerge at 1562 nm. Figure 6.26b shows a detail of the fringes at 1571 nm, showing 25 dB suppression of the 10 GHz modes.

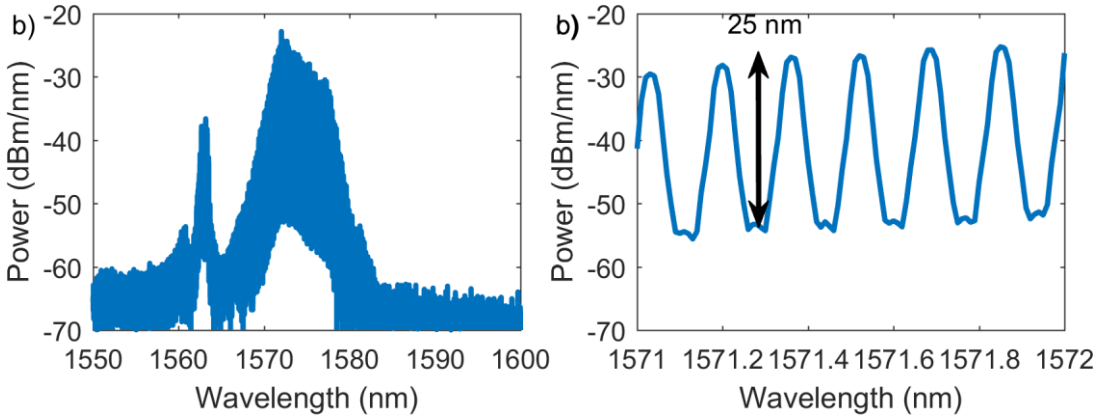

Figure 6.26: The optical spectrum from the 909-fs bias condition. a) Full span and b) detail showing suppression of the fundamental modes. The directional coupler waveguides are 400-nm tall, 500-nm thick, and have a 400-nm wide gap. The gain section is 2000-µm long and has an 850-nm wide waveguides in the amplifier section. The device has a 15% power reflection front mirror and 50% power reflection rear mirror. It has a 60-µm long saturable absorber. This device has a Type 2 spline curve mirror

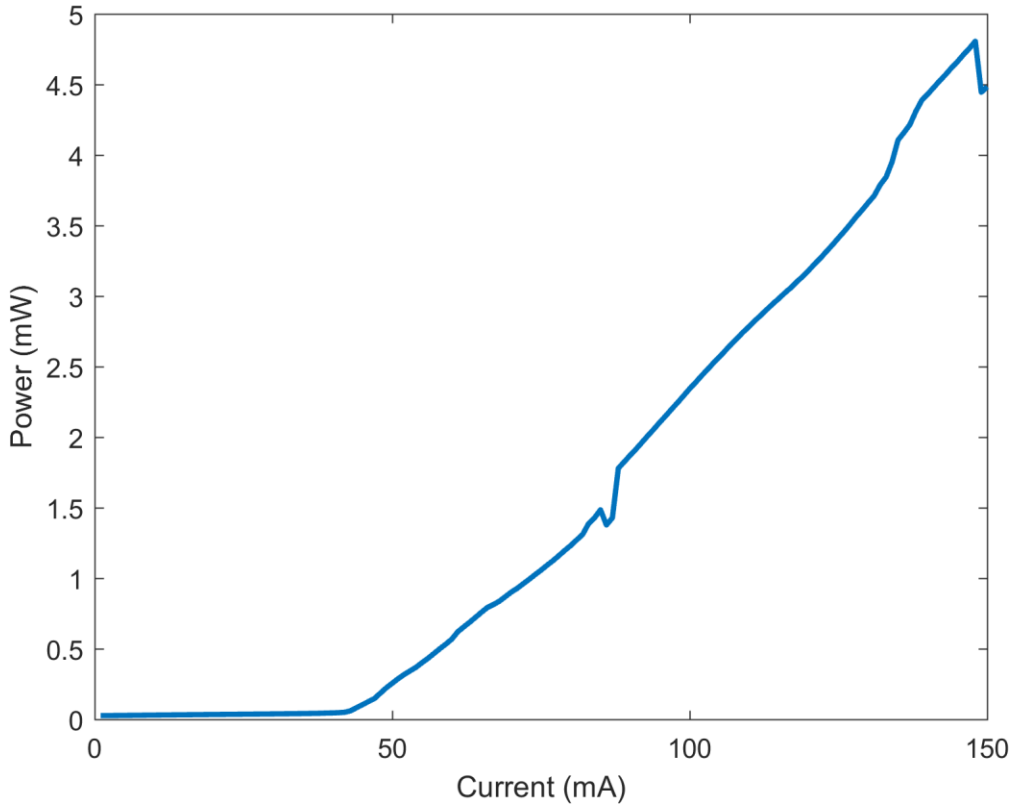

Figure 6.27: LI characteristic of the Type-2 spline curve laser under the absorber bias condition that produced the shortest pulse (−4.5 V). The bias current with the shortest pulse was 88 mA, which corresponds to 1.78 mW of continuous wave power. For a 909-fs pulse at 20 GHz, this gives a 98 mW peak power. The directional coupler waveguides are 400-nm tall, 500-nm thick, and have a 400-nm wide gap. The gain section is 2000-μm long and has an 850-nm wide waveguides in the amplifier section. The device has a 15% power reflection front mirror and 50% power reflection rear mirror. It has a 60-μm long saturable absorber.

The LI characteristic of the laser, taken with an integrating sphere from the low reflection front mirror side at −4.5 V absorber bias, is shown in Figure 6.27. The bias condition that produced the shortest pulse, 88 mA and −4.5V, can be seen to produce 1.78 mW of output power. This corresponds to 98 mW of peak power at 20 GHz.

The mirror design also had a significant impact on the RF linewidth. Pulses emitted into higher order modes may reach the absorber and partially saturate it, allowing more emission of amplified spontaneous emission. Removal of the higher order modes by the tight bends in the spline mirror eliminates this effect. The Type 1 spline mirror has the best performance, with a 3-dB linewidth taken from the measured data of 1.1 kHz, the second lowest reported value of any mode-locked laser diode without off-chip stabilization. The Type 2 spline mirror is slightly worse at 1.6 kHz, and the circular mirror is considerably worse at 4.0 kHz. The reduced linewidth enhancement factor of AlGaInAs [19] allows these devices to outperform any other mode-locked laser at 20 GHz, including many with much longer cavity lengths. Only one laser in literature has a lower linewidth [20], due to its 1-GHz repetition rate. The best published result on an InP substrate for RF linewidth is [21], with 2-kHz 3-dB linewidth. This is a cleaved-facet 10 GHz fundamental mode-locked laser. The spline loop mirror lasers are

able to out-perform this device because the reduced gain region length allowed by the integration of passive waveguides reduces the threshold, to 34 mA for the type 1 spline loop mirror, compared to around 100 mA in [21]. This improvement is only possible when extreme care is taken to avoid introducing parasitic effects from the active/passive transition and the other passive components.

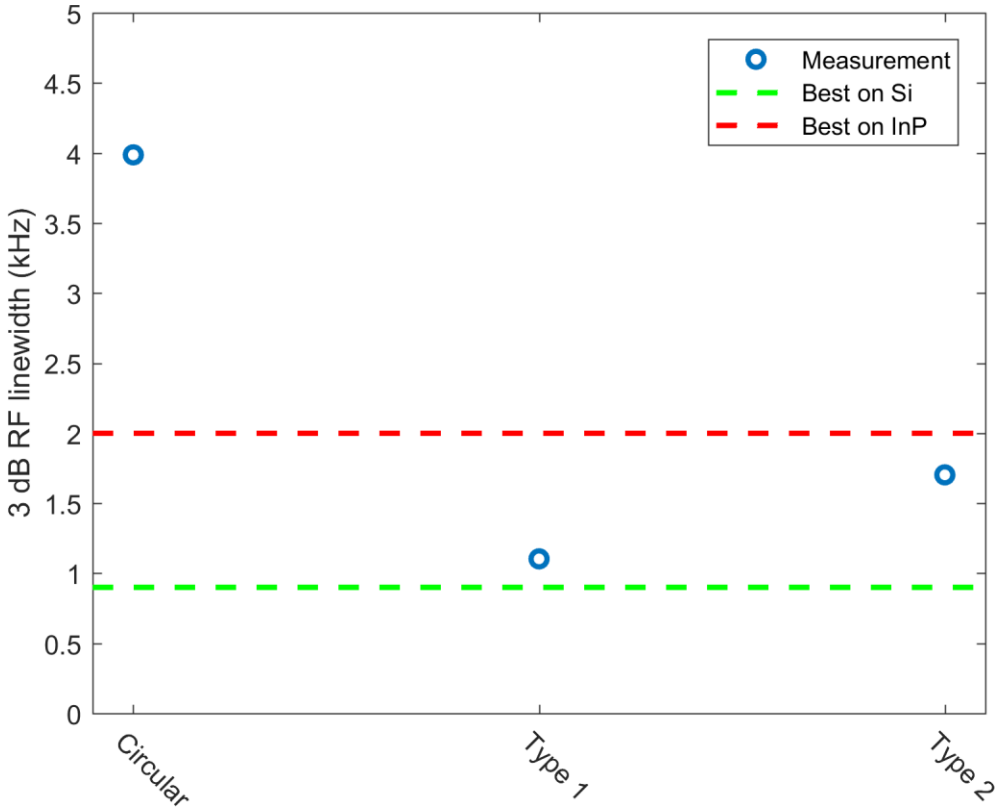

Figure 6.28: 3 dB RF linewidth of the three mirror designs (dots), with the previous best result on silicon shown as the green line and the previous best result on InP as a red line. The directional coupler waveguides are 400-nm tall, 500-nm thick, and have a 400-nm wide gap. The gain section is 2000-μm long and has an 850-nm wide waveguides in the amplifier section. The device has a 15% power reflection front mirror and 50% power reflection rear mirror. It has a 60-μm long saturable absorber.

A close look at the linewidths of all three devices is shown in Figure 6.29, with the data as dots and a Voigt fit as the solid line. Figure 6.30 shows the best performing device, the Type 1 spline loop mirror, over a wider range of frequency. While the Type 1 mirror has better performance, it must be admitted that given the small number of devices in the study and the difficulty of measuring these low levels of noise due to the slow jitter, the difference between the two may be within the error margin of the measurement.

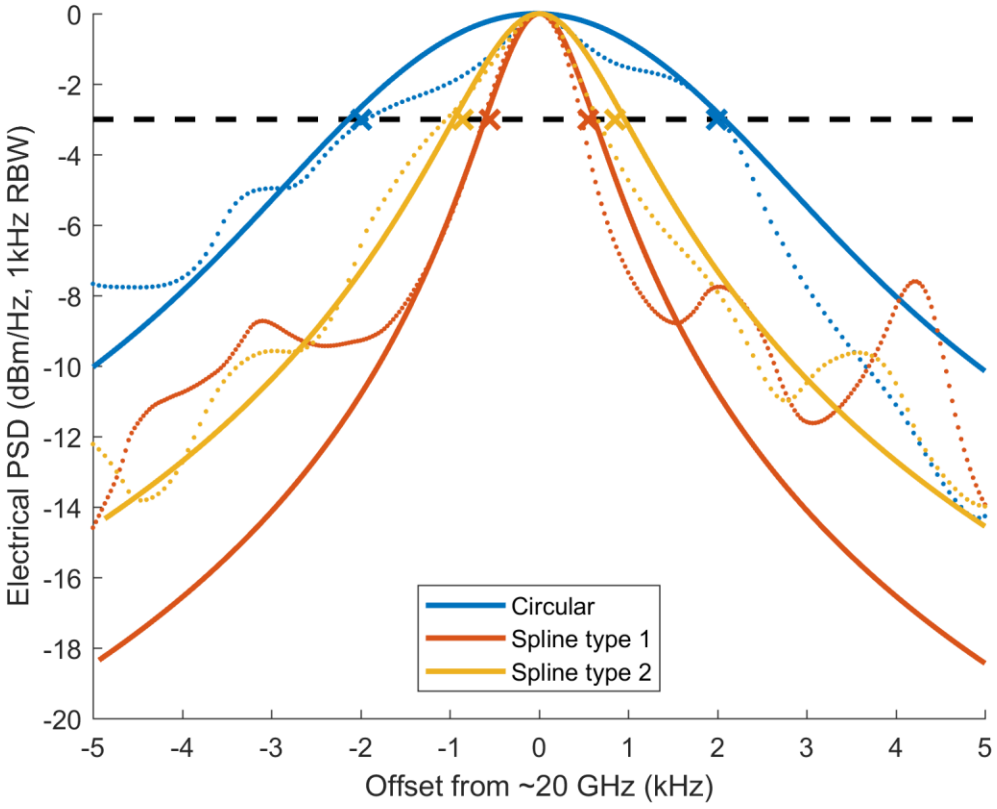

Figure 6.29: Data and Voigt fit curves for the three loop-mirror lasers. The directional coupler waveguides are 400-nm tall, 500-nm thick, and have a 400-nm wide gap. The gain section is 2000-μm long and has an 850-nm wide waveguides in the amplifier section. The device has a 15% power reflection front mirror and 50% power reflection rear mirror. It has a 60-μm long saturable absorber.

This measurement was extremely challenging, and the author must admit that a considerable proportion of the improvement may be related to improvement in measurement technique. The authors of [14] and [21] did not devote much space in their papers to the measurement technique, so it is unclear whether the data is comparable. These lasers, and all passively mode-locked lasers that the author has characterized, are unstable on low time scales. The RF peak frequency can be observed to shift back and forth across ~40 kHz or so at ~0.1 Hz speeds (referred to as "slow jitter"), so measurement of the RF spectrum with acquisition times longer than 100 ms will capture this as enlargement of the linewidth. Noise at these timescales is most likely related to technical noise such as vibration or changes in temperature. This is a fundamental limitation of using the RF linewidth as a gauge for the frequency noise of the laser. In an ideal case, the single-sideband phase noise would be used to characterize noise, however, the large amount of slow jitter prevents the analyzer from tracking the peak for close-in measurements of phase noise. It is probably possible to remove the slow jitter with low-speed electronic circuits, such as in [22], and a hermetic package would also reduce the impact of the environment on the technical noise.

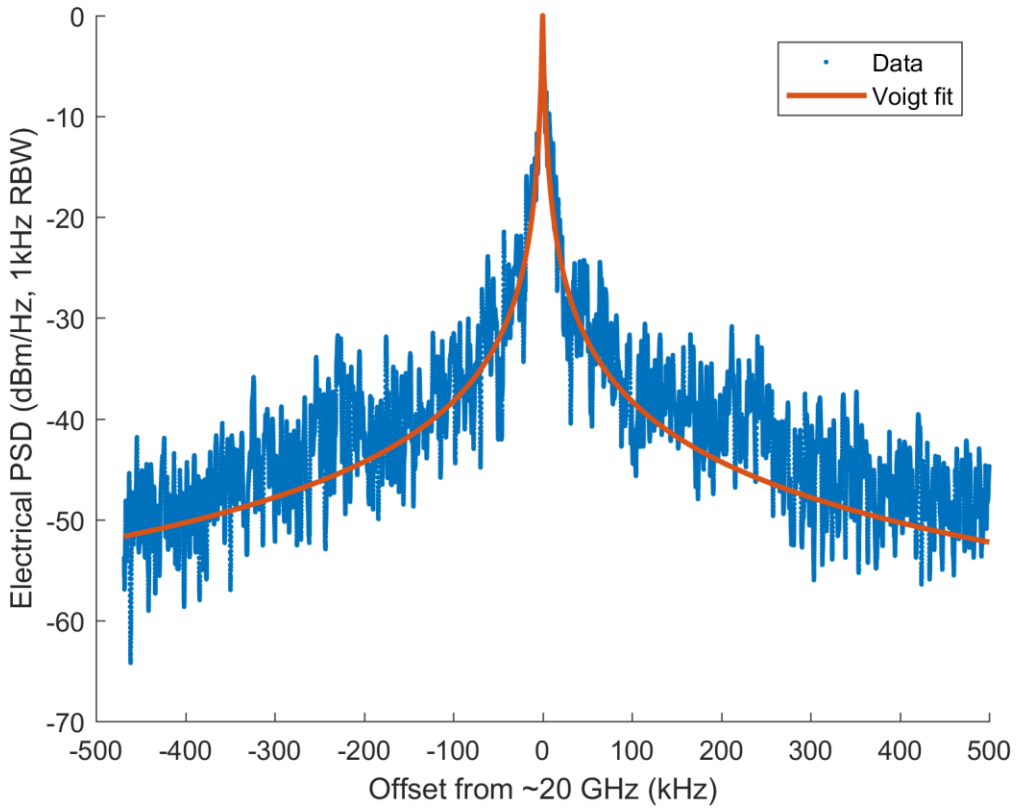

Figure 6.30: Wider span view of the Type 1 spline loop mirror, showing the absence of significant satellite peaks and the quality of the fit over a wider range. The directional coupler waveguides are 400-nm tall, 500-nm thick, and have a 400-nm wide gap. The gain section is 2000-µm long and has an 850-nm wide waveguides in the amplifier section. The device has a 15% power reflection front mirror and 50% power reflection rear mirror. It has a 60-µm long saturable absorber. This device has a Type 1 spline curve mirror.

Several significant measurement techniques had a large impact on the noise measurement. The most critical was the use of low-noise supplies to bias the laser. Computer programmable source-measure units that are commonly used for laser characterization (such as the Keithley 2400) have significant amounts of noise at 60 Hz from the AC frequency of the wall plug power, as well as a number of peaks up to 100s of MHz range. All of the noise measurements in this work use an ILX LDX-5620B battery powered laser diode driver, which is completely

disconnected from wall plug power, to bias the gain section and an HP E3610A power supply to bias the saturable absorber.

Since the absorber is reverse biased (using a linearized voltage supply), it is acting as a photodiode, and produces a significant amount of RF power; reading the microwave signal directly from the absorber instead of using a high-speed photodiode yields almost 20 dB higher RF power, in the −10 dBmV range. All of these low noise results come from the bias condition that produced the shortest pulse, so as a result, there is significant power in the 40-GHz harmonic. It must also be presumed that there is a powerful 60 GHz harmonic as well, and so the use of a 67 GHz GSG probe, a 67 GHz bias T, a 10 dB attenuator, and 67 GHz 50 Ω termination reduces destabilizing back-reflections from improper impedance matching.

A fast acquisition time is important to avoid integrating noise from the slow fluctuation. It is fairly evident from the electrical spectra in [14] and [21] that the use of a reduced number of trace points was employed to limit the acquisition time. Instead, for the measurement in this work, a digital FFT filter was used on time-domain data, allowing 30,000 points per trace with an acquisition time of only 125 ms.

Lastly, vibrational and thermal noises were managed by excessively taping fibers, shortening the lensed fiber sticking off the end of the boat to <1 mm, and enclosing the entire measurement setup in a metal shielded vibration isolating box on top of an air suspended optical table. The laser was not cooled for the noise measurement, since the switching of the temperature controller involves large currents and large *dI/dT*, and introduces a sinusoidal variation in the temperature of the stage that, even though less than 0.01°C, still influences the pulse train frequency in the near kHz range. Instead, the laser was enclosed in its box and left forward biased for 1 hour to allow the laser and the stage to reach equilibrium temperature

before taking the noise measurement. This temperature was typically about 25°C, while room temperature in the lab was 23°C.

6.5. Full Integration: Conclusion

Typical fully-integrated mode-locked laser diodes have degraded performance when compared to simple cleaved facet lasers (Figure 1-5), but this is due to the addition of parasitic effects that are introduced by the integrated components. If these parasitic effects are properly managed, performance of fully integrated lasers can exceed cleaved facet lasers, thanks to the addition of passive waveguides that have reduced dispersion and loss, and do not increase the laser threshold by enlarging the gain section.

The mode-locked lasers illustrated in this chapter represent the state of the art. They exceed the performance of integrated lasers with similar repetition rates, with the shortest pulse at 20 GHz at 909 fs and the second shortest pulse of any integrated laser. The Type 1 spline loop mirror, with a 1.1 kHz RF line width, has the second lowest linewidth ever reported for any mode-locked laser diode, and by far the lowest at 20 GHz. Using the small (~10 MHz) frequency tunability available by adjusting the bias conditions, low-speed electronic feedback should be able to correct for the slow jitter. The narrow linewidth is required for use as a carrier signal in microwave transmission systems [23]. This, combined with the short pulse, permits the statement that these lasers now represent the state of the art of fully integrated mode-locked laser diodes.

References

[1] K. Okamoto, “Progress and technical challenge for planar waveguide devices: Silica and silicon waveguides,” *Laser Photonics Rev.*, vol. 6, no. 1, pp. 14–23, 2012.

[2] W. Bogaerts and S. K. Selvaraja, “Compact Single-Mode Silicon Hybrid Rib/Strip Waveguide With Adiabatic Bends,” *IEEE Photonics J.*, vol. 3, no. 3, pp. 422–432, Jun. 2011.

[3] F. Morichetti, A. Canciamilla, C. Ferrari, M. Torregiani, A. Melloni, and M. Martinelli, “Roughness induced backscattering in optical silicon waveguides,” *Phys. Rev. Lett.*, vol. 104, no. 3, pp. 1–4, 2010.

[4] K. K. Lee, D. R. Lim, H.-C. Luan, A. Agarwal, J. Foresi, and L. C. Kimerling, “Effect of size and roughness on light transmission in a Si/SiO2 waveguide: Experiments and model,” *Appl. Phys. Lett.*, vol. 77, no. 11, p. 1617, 2000.

[5] D. T. Cassidy, “Technique for measurement of the gain spectra of semiconductor diode lasers,” *J. Appl. Phys.*, vol. 56, no. 11, p. 3096, 1984.

[6] Y. Barbarin, E. A. J. M. Bente, C. Marquet, E. J. S. Leclère, J. J. M. Binsma, and M. K. Smit, “Measurement of reflectivity of butt-joint active-passive interfaces in integrated extended cavity lasers,” *IEEE Photonics Technol. Lett.*, vol. 17, no. 11, pp. 2265–2267, 2005.

[7] H. Yun, W. Shi, Y. Wang, L. Chrostowski, and N. A. F. Jaeger, “2×2 adiabatic 3-dB coupler on silicon-on-insulator rib waveguides,” in *Photonics …*, 2013, vol. 8915, p. 89150V.

[8] C. R. Doerr, M. Cappuzzo, E. Chen, A. Wong-Foy, L. Gomez, A. Griffin, and L. Buhl, “Bending of a planar lightwave circuit 2 x 2 coupler to desensitize it to wavelength,

polarization, and fabrication changes," *IEEE Photonics Technol. Lett.*, vol. 17, no. 6, pp. 1211–1213, Jun. 2005.

[9] M. Gnan, G. Bellanca, H. M. H. Chong, P. Bassi, and R. M. De La Rue, "Modelling of photonic wire Bragg gratings," *Opt. Quantum Electron.*, vol. 38, no. 1–3 SPEC. ISS., pp. 133–148, 2006.

[10] N. J. Doran and D. Wood, "Nonlinear-optical loop mirror.," *Opt. Lett.*, vol. 13, no. 1, pp. 56–58, 1988.

[11] X. Sun, L. Zhou, J. Xie, Z. Zou, L. Lu, H. Zhu, X. Li, and J. Chen, "Tunable silicon Fabry-Perot comb filters formed by Sagnac loop mirrors.," *Opt. Lett.*, vol. 38, no. 4, pp. 567–9, 2013.

[12] J. Van Campenhout, W. M. J. Green, S. Assefa, and Y. a Vlasov, "Low-power, 2 x 2 silicon electro-optic switch with 110-nm bandwidth for broadband reconfigurable optical networks.," *Opt. Express*, vol. 17, no. 26, pp. 24020–24029, 2009.

[13] S. W. Corzine and M. Mashanovich, *Diode Lasers and Photonic Integrated Circuits*. 2012.

[14] S. Keyvaninia, S. Uvin, M. Tassaert, Z. Wang, X. Fu, S. Latkowski, J. Marien, L. Thomassen, F. Lelarge, G. Duan, G. Lepage, P. Verheyen, J. Van Campenhout, E. Bente, and G. Roelkens, "III–V-on-silicon anti-colliding pulse-type mode-locked laser," *Opt. Lett.*, vol. 40, no. 13, p. 3057, Jul. 2015.

[15] V. Moskalenko, S. Latkowski, S. Tahvili, T. de Vries, M. Smit, and E. Bente, "Record bandwidth and sub-picosecond pulses from a monolithically integrated mode-locked quantum well ring laser," *Opt. Express*, vol. 22, no. 23, p. 28865, 2014.

[16] W. Lai, Y. Cheng, C. Yao, D. Zhou, J. Bian, L. Zhao, and J. Wu, "A high-power tapered

and cascaded active multimode interferometer semiconductor laser diode," *J. Semicond.*, vol. 32, no. 5, p. 54007, May 2011.

[17] S. Arahira, S. Oshiba, Y. Matsui, T. Kunii, and Y. Ogawa, "500 GHz optical short pulse generation from a monolithic passively mode-locked distributed Bragg reflector laser diode," *Appl. Phys. Lett.*, vol. 64, no. 15, pp. 1917–1919, 1994.

[18] J. S. Parker, A. Bhardwaj, P. R. A. Binetti, Y. Hung, C. H. Lin, and L. A. Coldren, "Integrated 30GHz passive ring mode-locked laser with gain flattening filter," *Conf. Dig. - IEEE Int. Semicond. Laser Conf.*, vol. 1, no. 805, pp. 3–4, 2010.

[19] D. P. Sapkota, M. S. Kayastha, and K. Wakita, "Analysis of linewidth enhancement factor for compressively strained AlGaInAs and InGaAsP quantum well lasers," *Opt. Quantum Electron.*, vol. 45, no. 1, pp. 35–43, Jan. 2013.

[20] Z. Wang, K. Van Gasse, V. Moskalenko, S. Latkowski, E. Bente, B. Kuyken, and G. Roelkens, "A III-V-on-Si ultra-dense comb laser," *Light Sci. Appl.*, vol. 6, no. 5, p. e16260, May 2017.

[21] L. Hou, M. Haji, J. H. Marsh, and A. C. Bryce, "10 GHz AlGaInAs/InP 1.55 μm passively mode-locked laser with low divergence angle and timing jitter.," *CLEO SI*, vol. 19, no. 26, pp. B75-80, 2011.

[22] L. Gianfrani, A. Castrillo, E. Fasci, G. Galzerano, G. Casa, and P. Laporta, "Offset-frequency locking of extended-cavity diode lasers for precision spectroscopy of water at 1.38 μm.," *Opt. Express*, vol. 18, no. 21, pp. 21851–21860, 2010.

[23] A. J. Seeds, "TeraHertz photonics for communications," *Conf. Opt. Fiber Commun. Tech. Dig. Ser.*, vol. 33, no. 3, pp. 579–587, 2014.

Chapter 7

Conclusion and Outlook

This work has successfully demonstrated an advancement in the state of the art of mode-locked laser diodes. Heterogeneous integration of ultra-fast recovery time and low linewidth enhancement factor AlGaInAs gain material with low loss, high linearity and low footprint silicon on insulator waveguides has allowed the production of the second shortest pulse ever from a fully integrated all-on-chip mode-locked laser diode at 909 fs, after [1].

The stability of the microwave pulse train of these lasers under passive mode-locking is superior to any laser at 20 GHz, integrated or otherwise, with its 1.1 kHz 3 dB microwave linewidth. Only a single laser has demonstrated lower, at 900 Hz [2]; it is also a heterogeneous silicon laser, and has a 1 GHz repetition rate. Since linewidth decreases rapidly with decreasing repetition rate, it is expected that the technology in this work would be superior if the repetition rate was comparable, thanks to the clear benefit of the AlGaInAs gain material with respect to linewidth.

The full price of integration has been paid by the inclusion of the heterogeneous active-passive transition, integrated mirrors, and angled facet off-chip coupling, so the laser is now

ready for use in an integrated circuit. It is also possible to incorporate integrated structures to improve performance of the mode-locked laser, provided that the parasitic reflection and multimode emission of these structures can be reduced to an acceptable level (−40 dB for parasitic reflection and −30 dB for parasitic multimode emission).

7.1. Thesis Summary

The work in this dissertation encompasses a wide range of laser engineering and optimization. The lasers using the technology level at the beginning of this effort in had 1-2 milliwatts of maximum power and extreme difficulty with device yield. Normally, despite attempting to examine different device designs, only a single laser out of dozens across multiple dies would mode-lock. Considerable effort was spent increasing the manufacturing yield so that experimental comparisons could be made between laser designs, as detailed in Chapter 3. In the final run of lasers, 92% of mode-locked lasers were lasing, with 75% producing measurable pulses and high extinction RF peaks.

As the manufacturing yield improved, correction of device design deficiencies became more straightforward, as larger data sets make it easier to adapt simulation tools to produce accurate data. In cases where quantitative simulation results are difficult to obtain, such as quantum well design, yield and uniformity–particularly from chip to chip–are critical for advancing the laser performance. Uniform fabrication (and design of experiment) allowed steady development of the epitaxial layers and amplifier waveguide. Figure 7.1 shows the advancement in laser output power of mode-locked lasers operated as continuous wave lasers, with the absorber biased at the gain section voltage.

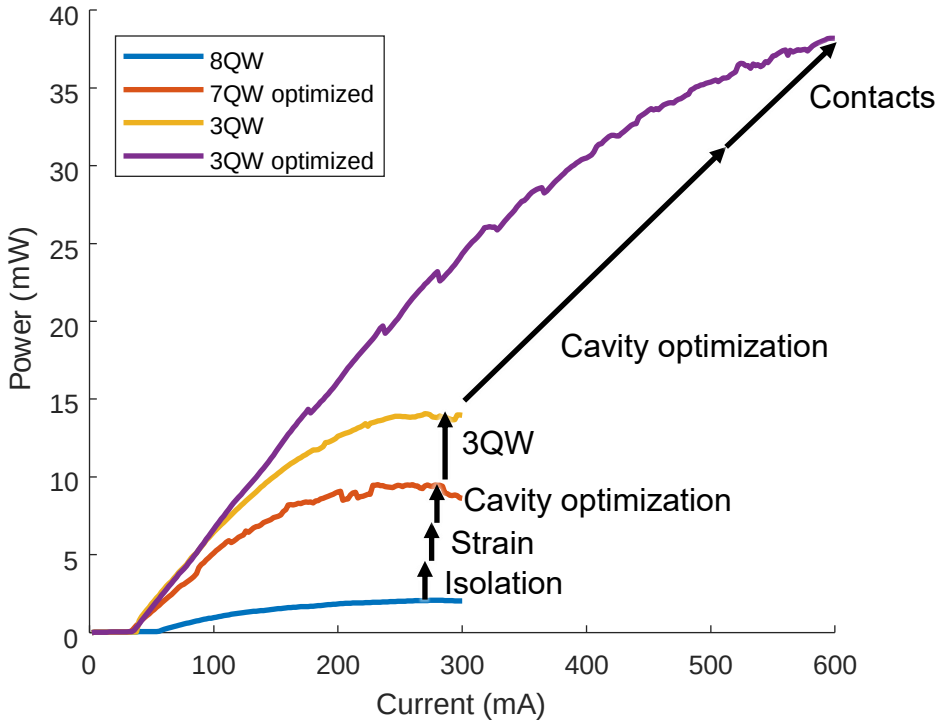

Figure 7.1: LI characteristics for 4 generations of fully integrated heterogeneous Si/III-V mode-locked lasers.

The blue line is an early integrated mode-locked laser. It used a 10-µm-long isolation section, which was excessive and was adding 3 dB of loss each (6 dB total) and had almost 100 kΩ resistance. Reducing the length of the isolation section to 1 µm eliminated the loss while maintaining 10-kΩ resistance. Increasing the strain to 1% in the quantum well reduced the propagation loss from 30 cm^{-1} to 8 cm^{-1}. It was the first to use the Sagnac loop reflector. The power reflection was 60% on both sides, immense overkill for the 1 mm-long 8 QW amplifier. Reduction of the mirror reflection ("cavity optimization") to 25% increased the slope efficiency. These three factors combined to produce the red curve: the threshold was reduced by half and the slope efficiency increased by double, increasing the output power by five times.

The introduction of the 3 QW epi, with the same cavity design, produced a modest increase in slope efficiency due to reduced overlap with the hole population in the quantum well, shown as the yellow curve in Figure 7.1. Another adjustment to the cavity design—this time an increase in the gain section length to 2 mm, a reduction in front mirror reflectivity to 4%, and an increase in the back-mirror reflectivity to 50%—produced similar slope efficiency. Thanks to the reduced thermal and electrical resistance from the larger 3 QW amplifier and improvement in the p-contact by eliminating hydrogen-containing processes, the operating current at which self-heating rolls over the slope efficiency to 0 W/A was more than doubled from 250 mA to 600 mA. The power from this laser is displayed as the purple curve. This laser had a maximum output power of 38 mW at 20°C, the highest of any published heterogeneous III-V/Si laser.

The mode-locking performance was also initially abysmal. The first fully integrated lasers would not mode-lock at the designed frequency (20 GHz), instead operating at 30 GHz, which was the fundamental frequency of the parasitic cavity formed between the heterogeneous transition and the laser mirror; others would mode-lock at 10 GHz, despite being designed for colliding pulse mode locking. Some of the final laser designs using the circular loop mirror had extremely accurate frequency definition: the device shown in Figure 7.2 was only 50 kHz away from 20 GHz. Mode-locked lasers are slightly frequency tunable (few MHz) by adjusting the bias conditions; however, this device was biased for optimum performance, and had a 2.34 ps pulse and 7.5 kHz linewidth at the bias condition shown in Figure 7.2. As an aside, the shortest pulse width lasers, using the spline curve mirror, mode-locked at 19.8 GHz, likely due to an error computing the length of the spline sections.

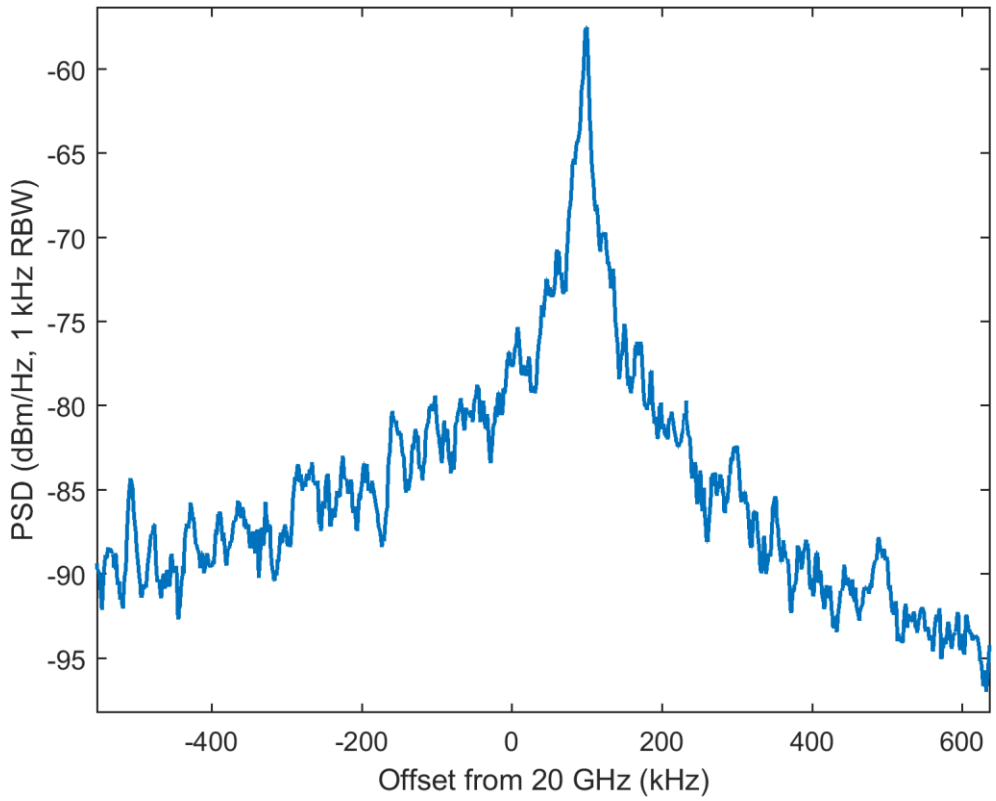

Figure 7.2: ESA spectrum of a 20.00006-GHz mode-locked laser, showing 7.5-kHz linewidth as it was producing at 2.34-ps pulse

Optimization of the heterogeneous transition for low loss, low reflection, and low higher-order mode emission was critical to produce high power continuous wave lasers. Most importantly, the reduction in parasitics allowed experimental optimization of the mode-locked lasers, since the earlier designs did not produce sane results. The most important aspects of the design were the length, since long tapers in the transition had high loss due to differential pumping, and the tip size of the active region, which affected the reflection much more than the p-mesa taper. Finally, the adoption of the 30-μm conformal-index taper and angled n-layer were important for eliminating parasitic multimode interference.

The laser mirror was also important for high performance. While the early designs were not as disastrous for the mode-locking performance, as there is less to go wrong with a passive

silicon directional coupler and waveguide loop, accurate definition of the mirror reflection can make the difference between a record-high 38 mW output power laser and a 150-mA threshold current laser where Auger recombination eats all the electrons because the current density is too high. The discovery of the air-hole in the directional coupler, and subsequent adaptation of the simulation, made the difference for high output power and low threshold lasers. Finally, the introduction of the spline curve loop mirror—to reduce loss in the narrow 400-nm waveguide—produced an unexpected boost in pulse width and noise, thanks to the mode filtering effect of the tightly bent narrow waveguide.

The ultimate lowest pulse width came from a laser with the spline curve mirror, specifically the tightly bent Type 2 design, with a 3-μm minimum bend radius. The fully optimized laser used the best epi so far (the 1% strain 3-quantum well Epi J) and the best transition design (30-μm conformal index taper with angled n-layer) and produced a 909-fs pulse. This is the second-lowest pulse from a fully-integrated on-chip mode-locked laser. A comparison of this device to other fully integrated lasers in literature is shown in Figure 7.3.

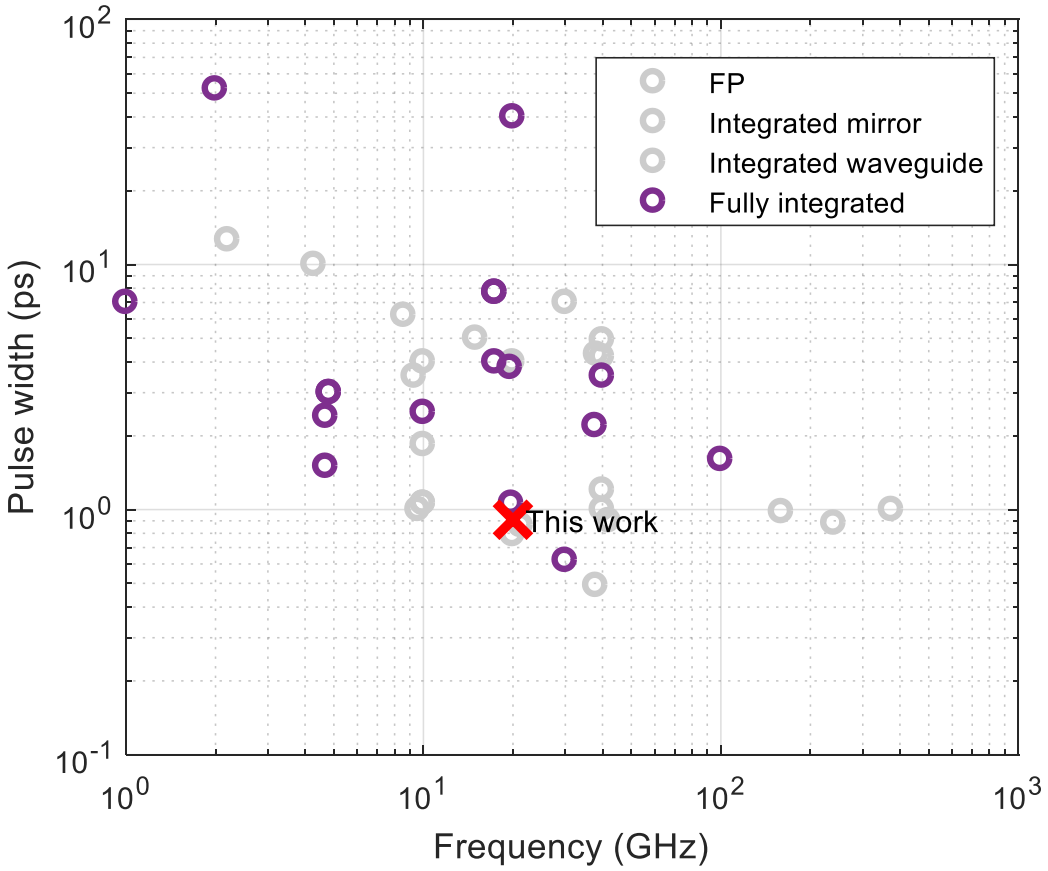

Figure 7.3: Pulse width of fully integrated all on-chip mode-locked laser diodes at 1.55 μm. See Chapter 1 for references.

It should be noted that the other two fully integrated femtosecond pulse lasers, [1] and [3], are both racetrack-style lasers, which typically have poor output power due to the inability to optimize the cavity direction. Neither paper reported the output power. [1] wrote in his dissertation that the laser had −6 dBm of fiber-coupled power; [3] showed unpublished LI curves at a conference presentation with −10 dBm of fiber-coupled power. Presuming that neither experimenter was using a wildly inappropriate lensed fiber coupler, the laser from this dissertation comfortably outstrips them in peak power, and in has the highest peak power from

any fully integrated laser at 20 GHz, as shown in Figure 7.4. [1] and [3] could not be included in this comparison because they did not report the on-chip power of their lasers.

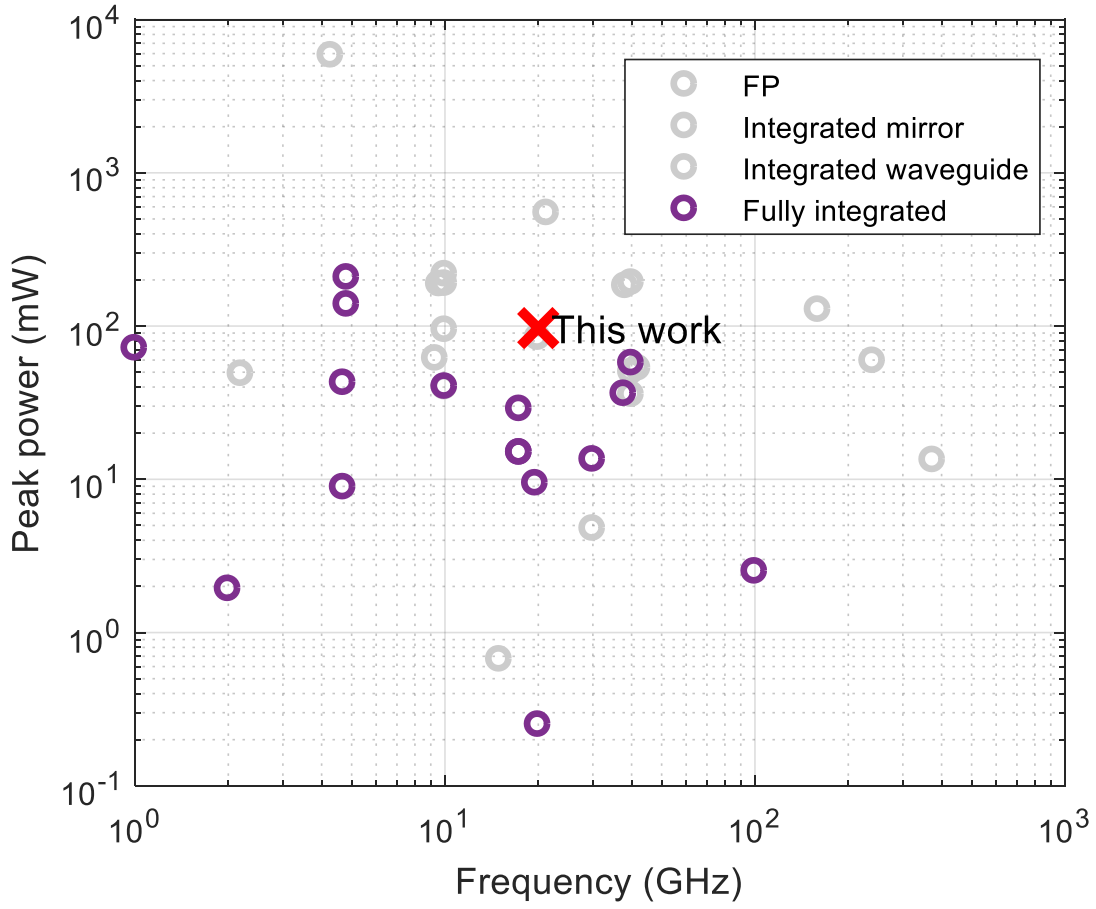

Figure 7.4: Peak power for fully integrated on-chip mode-locked laser diodes at 1.55 μm. See Chapter 1 for references.

The selection of AlGaInAs for the quantum well material (see Section 2.1) was a great advantage for the RF linewidth. In addition, the low-loss silicon waveguide is also clearly beneficial, as the other two outstanding fully integrated results are also heterogeneous silicon/III-V lasers [2][4]. The 1.1 kHz linewidth demonstrated in this work is by far the lowest at 20 GHz, and beats the nearest competitor at that frequency by a factor of 120, as shown in Figure 7.5.

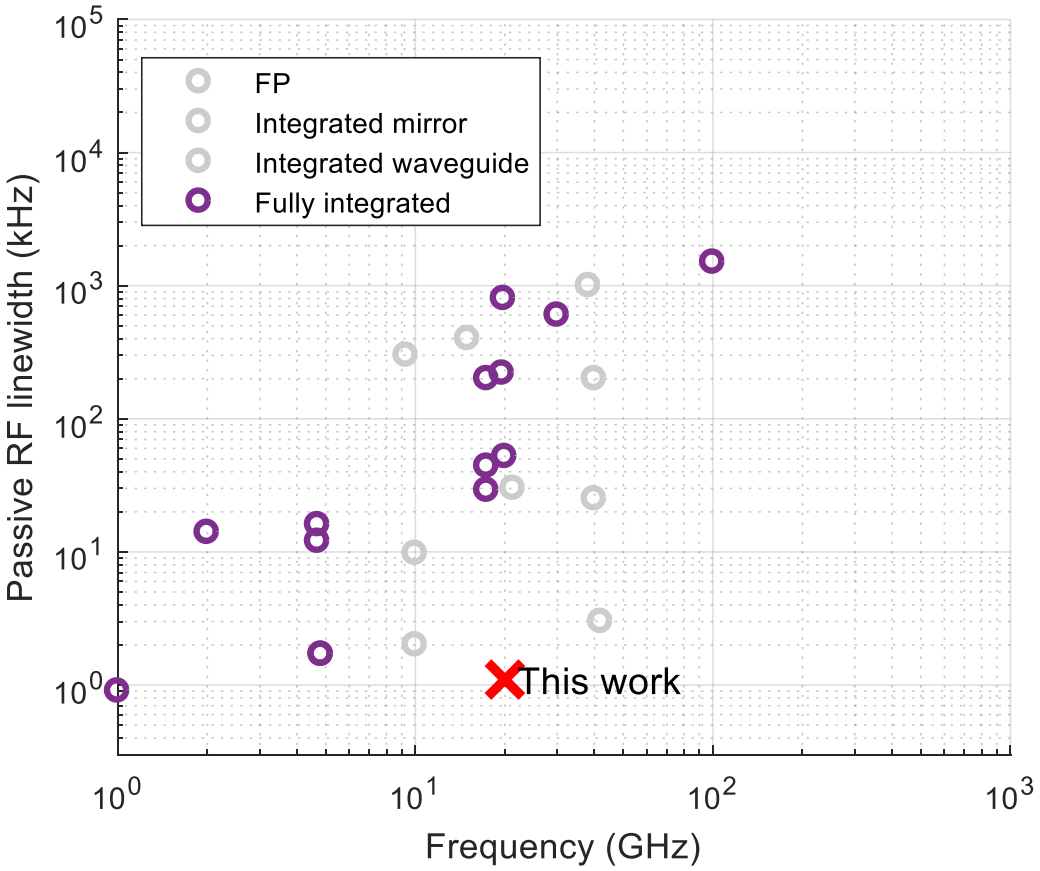

Figure 7.5: 3 dB RF linewidth for fully integrated on-chip mode-locked laser diodes at 1.55 μm. See Chapter 1 for references.

7.2. Future Work

Fully integrated mode-locked laser diodes are limited to pulse widths above 600 fs [1], even for outstanding examples. Semiconductor gain media can support optical bandwidth of 60-nm or more (see Figure 4.15), which, assuming that a transform-limited pulse can be produced, should allow pulse widths below 50 fs. In-plane amplifiers with off-chip external cavities have been able to demonstrate pulse widths of 200 fs [5], and vertical-external cavity lasers

(VECSELs), using optical pumping, have shown peak power of 4.35 kW [6]. These types of devices use bulk-optic or fiber-optic components to form the laser cavity and have the advantage of higher performance than their integrated counterparts—particularly passive components like waveguides and splitters—and the availability of prism and diffraction based dispersion compensation. The optically pumped VECSEL has the advantage of better thermal management due to the lack of ohmic self-heating that limits maximum output power in electrically pumped laser diodes. The pulse width of in-plane mode-locked laser diodes is thought to be limited by self-phase modulation and dispersion [7] in the amplifier waveguide, and so VECSELs and external cavity lasers with mostly passive fiber or air cavities and dispersion compensation do not suffer from these effects.

The lasers in this work have 909 fs minimum pulse width and 98-mW peak power. While these are excellent results when compared to other fully-integrated in-plane lasers, they are fairly lackluster when compared to 200 fs and 165 W pulses of [5]. The best quantum well C-band in-plane laser, with a 490-fs pulse, [8] likely represents the difference in quality between integrated cavity mirrors and cleaved facet mirrors. The spline-curve Sagnac loop mirror could have improved bandwidth and loss; it currently uses a directional coupler and a narrow deeply etched waveguide with 10 dB/cm loss. Implementation of a broad-band coupler, like an adiabatic directional coupler, and a state-of-the-art silicon waveguide with sub-1 dB/cm loss and only one guided transverse TE mode, may help improve the power and bandwidth of the devices in this work to be comparable to cleaved-facet lasers.

The difference between the lasers in this work and the shortest pulse fully integrated laser, 900 fs vs 600 fs, is likely due to the superiority of the active-passive transition in [1], which uses an offset-quantum-well waveguide with regrown p-InP cladding and does not suffer from

the high-index-contrast induced parasitics resulting from the taper-based heterogeneous transition in this work.

Finally, the lasers in this work produced short pulses only at very low bias current, around 90 mA, while they exhibited the highest continuous-wave power at over 600 mA, up to ten times higher than the power level at 90 mA bias.

A surface plot of the pulse width for various bias conditions is shown in Figure 7.6. The dark blue patch around −4 V and 80 mA, indicated by the symbol I, is the regime where the shortest pulses were produced, and despite the low continuous wave power at this bias condition demonstrated the highest peak power because of the short pulse. Figure 7.7, row I, shows a broad orderly optical spectrum (I-a), a 50-dB extinction ratio peak at 20 GHz in the electrical spectrum (I-b), and a 1-ps time-domain pulse autocorrelation trace, shown as a blue line, with a very good sech^2 fit, shown as red dashes (I-c). As the operating current is increased to 140 mA, in region II, the optical spectrum narrows (II-a) and two mode groups appear on the shoulder of the central mode group. This is likely due to intra-cavity power in the parasitic higher order TE01 mode increasing beyond the saturable absorber's ability to suppress it. The laser is still stably mode-locked at 20 GHz (II-b), but the pulse is broadened to 6 ps due to the reduced optical bandwidth available. Finally, in region III, one of the parasitic multimode induced side mode groups has reached threshold and is lasing (III-a). This destabilizes the pulse train, and begins to introduce significant amplitude modulation around 1 GHz as the laser begins to Q-switch mode-lock (III-b). The pulse enlarges further to 10 ps, and a ripple appears on the autocorrelation trace (III-c) from high-frequency beating between the two groups of modes.

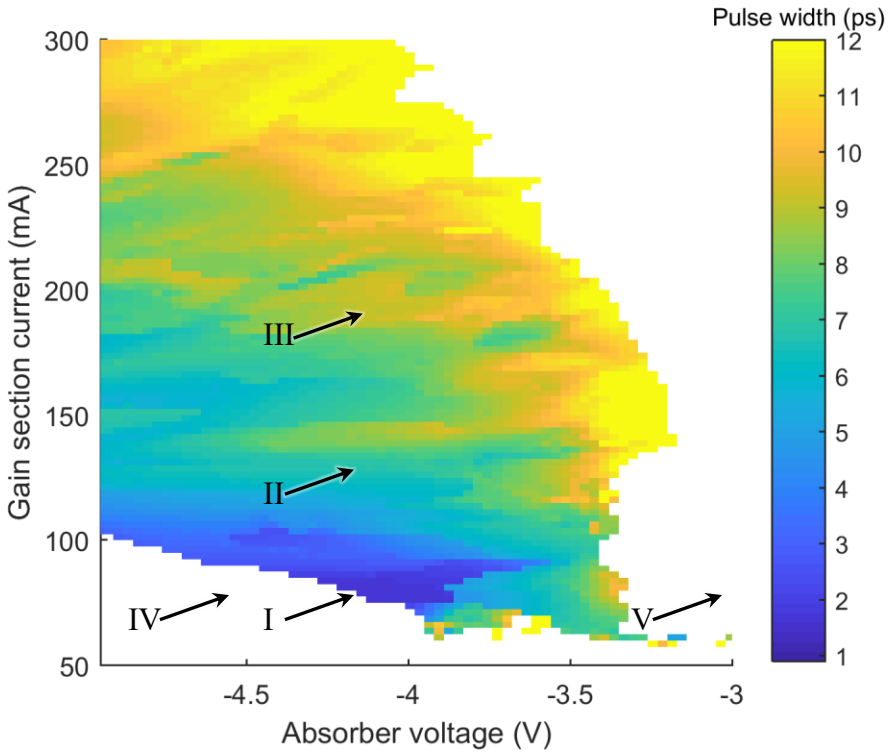

Figure 7.6: Pulse width versus operating conditions for an Epi J laser with Type 2 spline curve mirror and the conformal index, angled n-layer transition. The spectra and autocorrelation traces for the regions indicated by I, II, III, IV, and IV are shown in Figure 7.7.

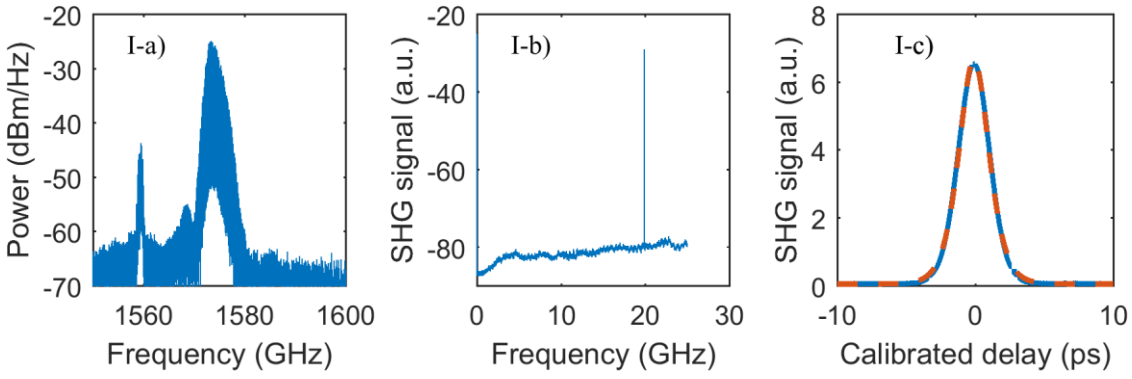

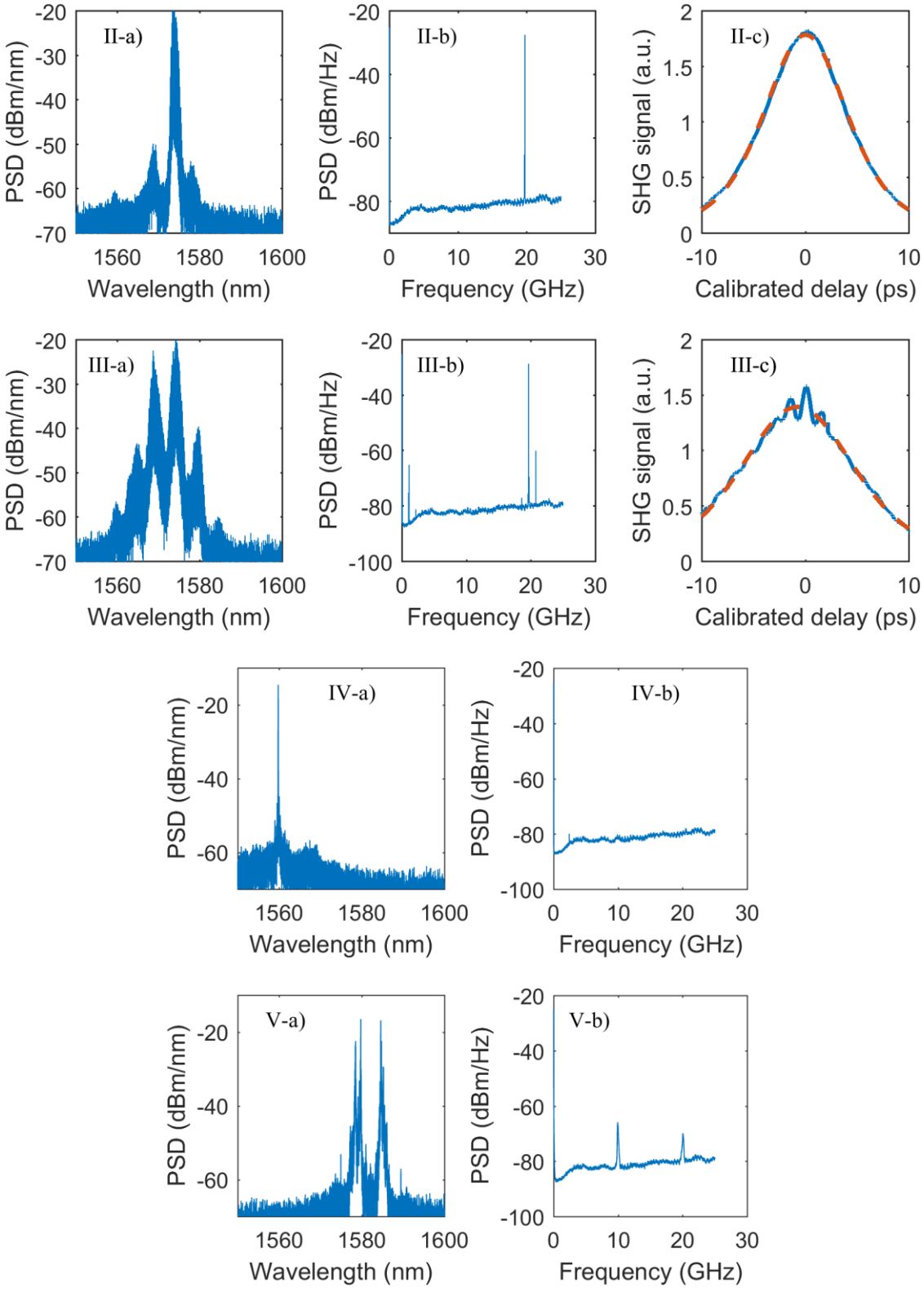
II-a)
II-b)
II-c)
III-a)
III-b)
III-c)
IV-a)
IV-b)
V-a)
V-b)
PSD (dBm/nm)
PSD (dBm/Hz)
SHG signal (a.u.)
Wavelength (nm)
Frequency (GHz)
Calibrated delay (ps)

Figure 7.7: Optical spectra (a), electrical spectra (b), and autocorrelation traces (c) for the regions indicated in Figure 7.6. Region I shows the ultra-fast pulse region, II shows an intermediate pulse width, and III shows a very long pulse. Region IV shows a condition where excessive loss in the highly reverse biased absorber reduces intra-cavity power to below the level required for spectral hole burning to broaden the mode comb. Region V shows a condition where the absorber loss is too low to suppress CW lasing. In the c) column, the blue line is the measurement trace and the red dashed line is a sech^2 fit.

Increasing the absorber reverse bias to help suppress the parasitic higher order mode spectral modulation is possible in theory, but as explained in Section 4.6.2, reverse bias below −5 V, especially at higher gain section bias current, would destroy the absorber contact. Reduction of the parasitic higher order mode emission to below −40 dB should eliminate the spectral modulation, or reduce it sufficiently that the 20-dB deep null between the mode groups disappears, which would reduce the spectral narrowing effect and eliminate the THz mode beating from the autocorrelation trace (III-c). Increasing the mode filtration from the spline curve mirror by tightening the bend or introducing a single-transverse-TE-mode waveguide would also be helpful. Eliminating this effect should allow the mode-locked laser to continue to produce sub-1 ps pulses up to 200 mA, which should produce a 5-times increase in peak power.

Evidence also points to the conclusion that higher confinement factor, either transverse Γ_{xy} or longitudinal Γ_z, could improve the pulse width by allowing lower (more negative) bias voltage on the saturable absorber. Region IV in Figure 7.6 has the ultra-fast current bias, but larger negative reverse bias. The laser is still lasing, but the loss in the absorber has increased to the point that the round-trip gain is no longer sufficient to create enough intra-cavity power

to broaden the mode comb through spectral hole burning (IV-a), so the laser becomes single longitudinal mode and mode-locking is impossible. An increase in the confinement factor in the quantum well, Γ_{xy}, allows the pulse to be shortened (section 4.6.1), but this increases the propagation loss and lower slope efficiency, so an increase in Γ_z by lengthening the gain section relative to the overall cavity length would be more efficient. Region V shows the laser when the absorber reverse bias is insufficient to fully extinguish continuous wave power between pulses. It has a weak amplitude modulation (V-b) but does not form a mode comb (V-a); the absorber cannot suppress parasitic pulses from reflection multimode emission, so the continuous wave spectrum is quite impaired.

Increasing the gain section length would also increase the total loss, as the amplifier waveguide has 16 dB/cm loss compared to the passive waveguide which has 2 dB/cm loss. Adjustment of the front mirror reflectivity may then be possible to return the slope efficiency to the level of the 2-mm amplifier length, and self-heating should then decrease as the resistance and thermal conductivity will be improved for the longer amplifier. The record high power heterogeneous laser shown in Figure 7.1 as the purple line had a circular loop mirror, as the test structures to optimize mirror reflectivity used the at-the-time proven design. It used an R =0.04 power reflection mirror, while the spline curve mirrors were all R = 0.15 power reflection. Given the improvement in loss for the spline curve mirror, a 20% improvement in slope efficiency can be expected by incorporating it instead of the circular mirror (see Section 6.3). The increase in gain section length will then reduce the output power as the total internal loss increases; this can be tuned back out by reducing the reflection of the front mirror to R = 0.02. Then, the increased maximum operating current should bring the maximum CW power to nearly 70 mW, which is competitive with state-of-the-art integrated lasers on InP substrates.

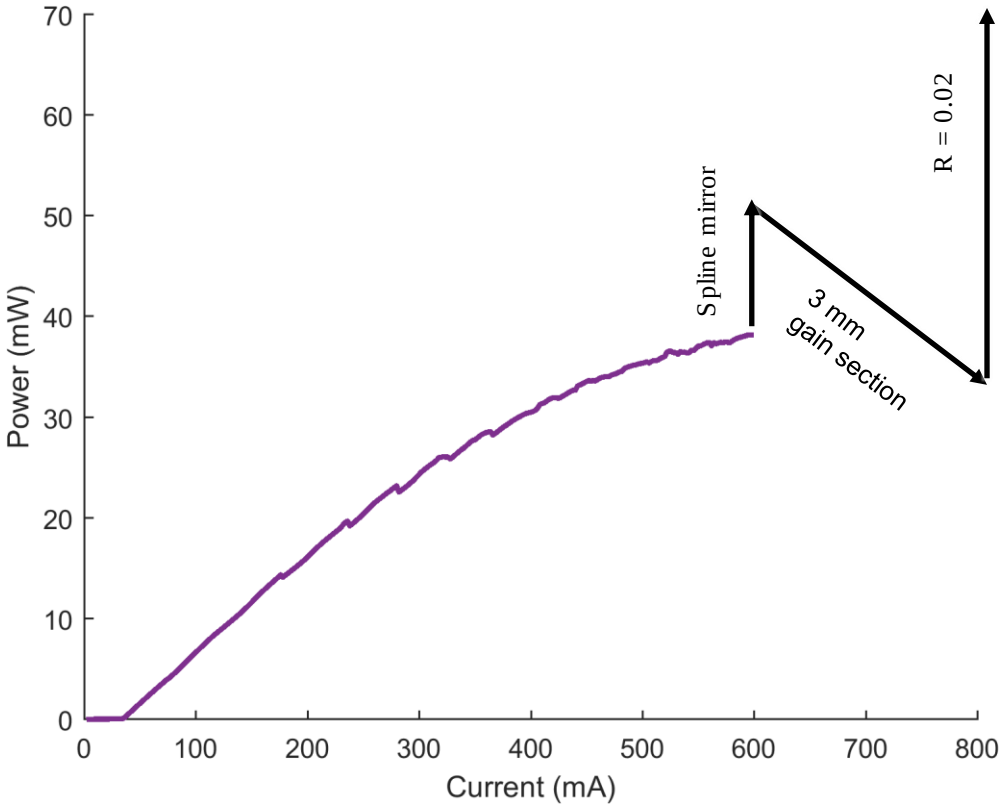

Figure 7.8: The low reflection front mirror laser from Figure 7.1, with hypothetical improvements to the design to maximize output power.

In addition, the rear mirrors were $R = 0.5$. Increasing this reflection to the maximum value ($R \approx 0.9$) for the Sagnac loop mirror would allow a further reduction in the front mirror reflectivity. This is a much riskier design, but it could be a path to over 100 mW output power.

Thanks to the capability to integrate different confinement factor amplifier waveguides on a single chip, or even in a single device with lateral tapers (Figure 4.9), there may be a further combination of amplifier waveguide confinement factor, for example, the $\Gamma_{xy} = 0.035$, 700-nm-wide waveguide in the saturable absorber to have the shortest length to minimize parasitic capacitance, with the 1.4-μm $\Gamma_{xy} = 0.01$ waveguide in the amplifier to reduce loss and self-phase modulation.

These complex designs strain the predictive power of existing mode-locked laser models, and the requirement to re-optimize the cavity design for each waveguide design presents difficulty in optimizing this type of device experimentally, since now the amplifier waveguide, absorber waveguide, mirror reflectivity, absorber length, and amplifier length create a 5-dimensional problem. Further improvement will also require advancement in modeling.

7.3. Final Word

While the effort required to produce this level of performance was considerable, it only represents the beginning. Devising nominally sufficient components on the emerging heterogeneous silicon/III-V platform allowed for the production of state-of-the-art integrated mode-locked lasers, and also revealed the path forward to eclipse existing technologies by optimization of the multi-dimensional design space of the heterogeneously integrated laser cavity.

Integration with a passive SOI waveguide introduces the ability to integrate these lasers with many other devices based on the SOI platform, such as modulators, filters, detectors, and even MEMS devices, provided that the devices sharing the mode-locked laser waveguide have sufficiently well engineered parasitic reflection and multi-mode emission.

The output power and optical bandwidth of these devices is still insufficient for most applications that bulk and fiber optic mode-locked lasers are used for today, even if the improvements outlined in Section 7.2 result in a 500-fs pulse with 100 mW of output power. This still only corresponds to 10 W of peak power; reduction in the repetition rate could reasonably increase it further, but beyond 1 W two-photon absorption will begin to limit output power. Therefore, it is likely that these devices will find applications where their outstanding

passive stability, high repetition rate, and low physical footprint make the use of larger and more power-hungry fiber lasers impractical. The two integrated circuits proposed in Section 1.1 are good examples of this type of application: the microwave channelizer as part of, for example, an electronic warfare suite on a remotely operated aircraft, or the integrated gas spectrometer as a toxic gas sensor inside of a spacecraft. However, in their current form, the lasers have limited application. The 20 GHz repetition rate was selected for use in the DARPA E-PHI program. Both the microwave channelizer and a dual comb spectroscope require low repetition rate, since the repetition rate defines the system resolution. Reduction of the repetition rate is easy to accomplish with a silicon waveguide, since the loss can be comparatively low, such as in [2]. Integration with a silicon nitride waveguide, such as in [9], would be a path to sub-1 GHz repetition rate. Use in a coherent millimeter wave transmission system, which would take advantage of the narrow RF linewidth, will require an increase in the repetition rate to 100 GHz or above. This would normally degrade the linewidth, as shown in Figure 2.2. Using harmonic mode-locking, such as [10], can maintain the linewidth of a long cavity at high repetition rates. The flexibility of heterogeneous integration allows for multiple epi wafer designs to be integrated seamlessly on a single chip, with C-band, O-band [11], mid-infrared [12], and 2.0-μm lasers already demonstrated [13], makes it an ideal candidate for this type of device, which may require a specific non-telecom wavelength range to detect certain gas species.

The existence of the mode-locked laser devices and thorough characterization and description of their design contained in this dissertation will open the door to exploratory research into a new class of mode-locked-laser-based heterogeneous integrated circuits.

References

[1] J. S. Parker, A. Bhardwaj, P. R. A. Binetti, Y. Hung, C. H. Lin, and L. A. Coldren, "Integrated 30GHz passive ring mode-locked laser with gain flattening filter," *Conf. Dig. - IEEE Int. Semicond. Laser Conf.*, vol. 1, no. 805, pp. 3–4, 2010.

[2] Z. Wang, K. Van Gasse, V. Moskalenko, S. Latkowski, E. Bente, B. Kuyken, and G. Roelkens, "A III-V-on-Si ultra-dense comb laser," *Light Sci. Appl.*, vol. 6, no. 5, p. e16260, May 2017.

[3] V. Moskalenko, S. Latkowski, S. Tahvili, T. de Vries, M. Smit, and E. Bente, "Record bandwidth and sub-picosecond pulses from a monolithically integrated mode-locked quantum well ring laser," *Opt. Express*, vol. 22, no. 23, p. 28865, 2014.

[4] S. Keyvaninia, S. Uvin, M. Tassaert, Z. Wang, X. Fu, S. Latkowski, J. Marien, L. Thomassen, F. Lelarge, G. Duan, G. Lepage, P. Verheyen, J. Van Campenhout, E. Bente, and G. Roelkens, "III–V-on-silicon anti-colliding pulse-type mode-locked laser," *Opt. Lett.*, vol. 40, no. 13, p. 3057, Jul. 2015.

[5] P. J. Delfyett, G. Alphonse, W. Ceislik, L. Florez, N. Stoffel, T. Gmitter, and N. Andreadakis, "200-fs optical pulse generation and intracavity pulse evolution in a hybrid mode-locked semiconductor diode-laser/amplifier system," *Opt. Lett.*, vol. 17, no. 9, p. 670, May 1992.

[6] K. G. Wilcox, A. C. Tropper, H. E. Beere, D. A. Ritchie, B. Kunert, B. Heinen, and W. Stolz, "4.35 kW peak power femtosecond pulse mode-locked VECSEL for supercontinuum generation," *Opt. Express*, vol. 21, no. 2, p. 1599, Jan. 2013.

[7] G. P. Agrawal and N. A. Olsson, "Self-phase modulation and spectral broadening of optical pulses in semiconductor laser amplifiers," *Quantum Electron. IEEE J.*, vol. 25,

no. 11, pp. 2297–2306, 1989.

[8] L. Hou, M. Haji, J. H. Marsh, and A. C. Bryce, “490 fs pulse generation from a passive C-band AlGaInAs / InP quantum well mode-locked laser,” *Opt. Lett.*, vol. 37, no. 5, pp. 773–775, 2012.

[9] M. Piels, J. F. Bauters, M. L. Davenport, M. J. R. Heck, and J. E. Bowers, “Low-loss silicon nitride AWG demultiplexer heterogeneously integrated with hybrid III-V/Silicon photodetectors,” *J. Light. Technol.*, vol. 32, no. 4, pp. 817–823, 2014.

[10] S. Srinivasan, A. Arrighi, M. J. R. Heck, J. Hutchinson, E. Norberg, G. Fish, and J. E. Bowers, “Harmonically Mode-Locked Hybrid Silicon Laser With Intra-Cavity Filter to Suppress Supermode Noise,” *IEEE J. Sel. Top. Quantum Electron.*, vol. 20, no. 4, pp. 8–15, Jul. 2014.

[11] S. R. Jain, M. N. Sysak, G. Kurczveil, and J. E. Bowers, “Integrated hybrid silicon DFB laser-EAM array using quantum well intermixing,” *Opt. Express*, 2011.

[12] A. Spott, M. L. Davenport, J. Peters, J. T. Bovington, M. J. Heck, and J. E. Bowers, “A CW Mid-infrared Hybrid Silicon Laser at Room Temperature,” *IEEE Photonics Conf.*, pp. 2–3, 2014.

[13] A. Spott, M. Davenport, J. Peters, J. Bovington, M. J. R. Heck, E. J. Stanton, I. Vurgaftman, J. Meyer, and J. Bowers, “Heterogeneously integrated 2 . 0 μ m CW hybrid silicon lasers at room temperature,” vol. 40, no. 7, pp. 1480–1483, 2015.